Establishment of a model for self-assembly processes in biological systems

Dissertation

zur Erlangung des akademischen Grads

Doktor der Naturwissenschaften

Dr. rer. nat.

von

Benjamin Hämisch

geboren am 30.09.1990

in Bad Driburg

Paderborn

Juni 2022

Die vorliegende Arbeit wurde im Zeitraum von Februar 2017 bis Juni 2022 im Fachbereich für Physikalische Chemie der Fakultät für Naturwissenschaften der Universität Paderborn unter der Betreuung von Prof. Dr. Klaus Huber angefertigt.

Prüfungsausschuss:

Prof. Dr. Klaus Huber	Erstgutachter
Prof. Dr. Simon Ebbinghaus	Zweitgutachter
Prof. Dr. Thomas Kühne	
Prof. Dr. Sabine Fechner	Vorsitz

Tag der Einreichung:	21.06.2022
Tag der mündlichen Prüfung:	25.07.2022

Hiermit erkläre ich, die vorliegende Dissertationsschrift selbständig verfasst zu haben. Die dazu genutzte Literatur, zu Hilfeleistungen herangezogene Institutionen sowie Beiträge anderer Personen zu dieser Arbeit werden im Rahmen der Dissertationsschrift vollständig angegeben bzw. kenntlich gemacht.

Paderborn, Juni 2022

Benjamin Hämisch

Danksagung

An erster Stelle möchte ich meinen Dank an meinen Doktorvater Prof. Dr. Klaus Huber richten. Er hat mich viele Jahre meines Akademikerlebens begleitet und war stets ein äußerst hilfreicher Diskussionspartner und ich habe Ihn als Betreuer sehr wertgeschätzt. Vielen Dank für all die hilfreichen Gespräche, für die enorme Unterstützung und die maßgeblichen Denkanstöße.

Ich bedanke mich bei Prof. Dr. Simon Ebbinghaus für die Übernahme des Zweitgutachters und für die produktive gemeinsame Kooperation. Seinem Mitarbeiter Roland Pollak gebührt ein weiterer Dank, die Zusammenarbeit in Braunschweig hat mir sehr viel Spaß bereitet und war äußerst erkenntnisreich.

Ich möchte mich auch bei Prof. Dr. Oliver Strube für die zahlreichen erfolgreichen Diskussionen rund um das Thema Fibrinogen bedanken. Unsere Kooperation brachte nicht nur zwei erfolgreiche Publikationen hervor, sondern bildete während meiner Masterarbeit zugleich auch den Grundstein für meine akademische Laufbahn. In diesem Kontext gilt ein besonderer Dank an Anne Büngeler. Sie ist eine kompetente Kollegin und gute Freundin zugleich, danke dass du immer ein offenes Ohr für mich hattest.

Allen Kollegen des Arbeitskreises von Prof. Dr. Huber möchte ich meinen Dank aussprechen. Ich habe mich von Tag eins an gut aufgenommen gefühlt, ihr habt mich lange Zeit meines Lebens begleitet und wart maßgeblich am Erfolg meiner Abschlussarbeiten sowie meiner Promotion beteiligt. Danke Markus, Marina, Nico Schmidt, Nico Carl, Kate, Fabian, Leon und Wenke!

Auch meinen ehemaligen Kommilitonen Cüneyt, Dennis und Simon möchte ich für die unvergessliche Studentenzeit danken. Die Praktikumsvorbereitungen in der Cafete sowie die lustigen Abende der Chemikerfeten sind nur zwei von unzähligen schönen Erinnerungen.

Abseits des Universitätslebens möchte ich auch meinen Freunden meinen Dank aussprechen. Ihr habt mich stets unterstützt und habt für den nötigen Ausgleich während der Doktorandenzeit gesorgt. Ohne solch ein Rückgrat wäre vieles nicht möglich gewesen. Danke Meike, Patrick, Tobias, Andreas und Rahel!

Abschließend möchte ich meiner Familie danken. Vielen Dank, dass ihr immer für mich da seid und ich stets auf eure Unterstützung zählen kann. Ohne euch wäre ich nicht dort, wo ich jetzt bin, ihr seid mein größtes Glück.

Zusammenfassung

Das Ziel der vorliegenden Arbeit ist die Etablierung eines Modellsystems basierend auf dem Farbstoff Pseudoisocyaninchlorid (PIC) zur Untersuchung von Aggregationsprozessen in Biosystemen mit Hinblick auf Crowding-Effekte. PIC weist viele ähnliche Eigenschaften auf, die auch in Proteinen wiederzufinden sind. PIC weist, wie zahlreiche Proteine, eine marginale Wasserlöslichkeit auf, außerdem besteht PIC aus einer Mischung von hydrophilen und hydrophoben Bereichen, welche die Selbstassemblierung in einer Vorzugsrichtung ermöglichen. Im Falle von PIC wird das Produkt der Selbstassemblierung J-Aggregat genannt, welche bei gegebener Konzentration gebildet werden, sobald die Aggregationstemperatur unterschritten wird. Dabei handelt es sich um fibrilläre Strukturen, ähnlich wie die Aggregate von amyloidogenen Proteinen.

Um den Mechanismus der Bildung von J-Aggregaten sowie deren Struktur zu untersuchen, wurde sich in dieser Arbeit der statischen und dynamischen Lichtstreuung bedient. Die Bestimmung der Konzentrationsabhängigkeit der Aggregationstemperatur sowie die Charakterisierung der Bildung von PIC Oligomeren wurde mit UV-Vis Spektroskopie untersucht. Um Crowding-Effekte, und somit die zelluläre Situation, zu simulieren wurden vier verschiedene Stoffe genutzt, Triethylenglycol (TEG), Polyethylenglycol (PEG), Ficoll 400 sowie Sucrose. Ergänzend wurden *in vivo* Experimente in HeLa-Zellen in Kooperation mit dem Arbeitskreis Ebbinghaus in Braunschweig durchgeführt. Um das volle Potential des Modellsystems PIC auszuschöpfen, wurde außerdem eine Methode entwickelt, um die Probenzusammensetzung von PIC oberhalb und unterhalb der Aggregationsschwelle zu quantifizieren. Dies ermöglicht die Beschreibung der Konzentrationen von Monomeren, Oligomeren ($N \leq 3$) und J-Aggregaten.

Zusätzlich wurde die Selbstassemblierung von Fibrinogen in Abwesenheit von Thrombin mittels zeitaufgelöster statischer und dynamischer Lichtstreuung analysiert, als ein Beispiel für Aggregationsphänomene in biologischen Systemen. Dabei konnte gezeigt werden, dass der Mechanismus der Selbstassemblierung einer Koagulation entspricht, welche abhängig von der Ionenstärke entweder reaktions- (DLCA) oder diffusionslimitiert (DLCA) ist. Dabei werden globuläre Strukturen gebildet Die Einführung des synthetischen Crowders Ficoll 400 führt zu einer beschleunigten Aggregation.

Abstract

The scope of the present work is the establishment of a model system based on the dyestuff pseudo isocyanine chloride (PIC) as a tool to investigate self-assembly processes in biological systems with special regard to crowding effects. PIC has many similar properties which can also be found in proteins. PIC, as well as various proteins, exhibits a marginal solubility in water together with a mixture of hydrophilic and hydrophobic spots, which enables the self-assembly in a preferred direction. In case of PIC, the product of self-assembly is called J-aggregate, which are found at a given concentration when the aggregation temperature is undershoot. They are characterized as fibrillar structures, similar to the aggregates originated from amyloidogenic proteins.

Investigation of the mechanistic features of J-aggregate formation as well as the characterization of the aggregate structure has been done with static and dynamic light scattering. Determination of the concentration dependency of the aggregation temperature together with the characterization of the formation of PIC oligomers has been carried out with UV-Vis spectroscopy. To simulate crowding effects, and therefore simulate a cellular environment, four different chemicals were used, triethylene glycol (TEG), polyethylene glycol (PEG), Ficoll 400 and sucrose. Complementing this, *in vivo* experiments in HeLa cells were conducted in cooperation with the working group Ebbinghaus in Braunschweig. To exploit the full potential of PIC as a model system, a method was developed to quantify the sample composition of PIC above and below the aggregation threshold. This method enables the description of the concentration of monomers, oligomers ($N \leq 3$) and J-aggregates.

The transition to a biological relevant system was established with the analysis of the protein fibrinogen. The self-assembly of fibrinogen in the absence of thrombin was investigated with time-resolved static and dynamic light scattering. It could be shown that the underlying mechanism of the self-assembly is classified as a coagulation, which is either limited by reaction (RLCA) or by diffusion (DLCA), depending on the ionic strength. Globular structures are generated. Introduction of the synthetic crowder Ficoll 400 lead to an accelerated aggregation.

List of Abbreviations

AFM	Atomic force microscopy
ASA	Water-accessible surface area
BSA	Bovine serum albumin
DLCA	Diffusion-limited colloid aggregation
DLS	Dynamic light scattering
DMSO	Dimethyl sulfoxide
DPBS	Dulbecco's phosphate-buffered saline
DSC	Differential scanning calorimetry
FRET	Förster resonance energy transfer
IAPP	Islet amyloid polypeptide
PEG	Polyethylene glycol
PIC	Pseudo-isocyanine chloride
PII	Pseudo-isocyanine iodide
RLCA	Reaction-limited colloid aggregation
RVI	Regulatory volume increase
SLS	Static light scattering
TEG	Triethylene glycol
TR	Time-resolved
UV-Vis	Ultraviolet-Visible

Table of Contents

Zusammenfassung **vii**

Abstract **viii**

List of Abbreviations **ix**

1. Introduction and Objective **1**

1.1 Introduction 1

1.2 Objective 5

1.3 References 8

2. Synopsis **11**

2.1 The self-assembly of fibrinogen 11

2.2 Oligomeric solutions of PIC 13

2.3 The mechanism of J-aggregate formation 15

2.4 The aggregated regime 17

2.5 The impact of crowding on the self-assembly of PIC 20

2.6 Relevance for *in vivo* systems - the HeLa cells 23

2.7 Self-assembly of fibrinogen under crowded conditions 24

2.8 References 25

3. Coauthors' Contribution **26**

4. Self-Assembly of Fibrinogen in Aqueous, Thrombin-Free Solutions of Variable Ionic Strengths **28**

5. Mechanism and equilibrium thermodynamics of H- and J-aggregate formation from pseudo isocyanine chloride in water **51**

6. Thermodynamic Analysis of the Self-Assembly of Pseudo Isocyanine Chloride in the Presence of Crowding Agents **83**

7. Self-Assembly of Pseudo-Isocyanine Chloride as a Sensor for Macromolecular Crowding In Vitro and In Vivo **100**

8. Self-Assembly of Fibrinogen in the presence of Ficoll 400 **127**

9. List of Publications **129**

1. Introduction and Objective

1.1 Introduction

The self-assembly of proteins in biological systems is a highly complex field and thus offers a plethora of interesting scientific problems. Self-assembly processes perform crucial tasks in living systems, for example the formation of the cytoskeleton of cells via actin, tubulin and intermediate filament proteins.[1] It can also be harmful, mostly in terms of amyloidogenic diseases, like for instance the imbalance of β-Amyloid production and clearance. This imbalance leads to neurotoxic aggregates[2], which is related to Alzheimer's disease.[3]

Fibrinogen is a prominent example for a protein whose aggregates are connected to a pivotal mechanism protecting the organism or if it occurs at the wrong time in the wrong place can be harmful to it. Fibrinogen is a glycoprotein which consists of two identical D-domains and a central E-domain[4]. Each of the fibrinogen halves is composed of three subunits α, β and γ which are connected via disulfide-bridges in the central E-domain. N-termini of all subunits are located in the central E-domain. The protein is present in the blood stream with a concentration of around 2 to 6 g/L.[5] Small angle x-ray scattering experiments revealed a rod-like structure of fibrinogen in buffered solution with an approximate length of 45 nm and a diameter of 9 nm.[5] Fibrinogen plays an important role in the formation of blood clots, an essential process for the survival of vertebrates.[6] In case of a tissue damage, the glycoprotein is activated via a complex cascade of interconnected reactions.[7] A key step of the cascade is the cleavage of the N-termini of the α and β chains via the enzyme thrombin which establishes the conversion from fibrinogen to fibrin.[8] This cleavage creates possible binding sites on fibrin, enabling the non-covalent self-assembly towards protofibrils which align to rope-like fibrils.[9] In a final step of the clot formation, covalent binding between fibrin is induced via the enzyme factor XIIIa[10], leading to a network of interconnected fibrin molecules, which closes the tissue damage. However this can also be harmful as locally non-specific formation of fibrin clots can cause strokes or thrombosis.[11]

It is known that fibrinogen can undergo self-asssembly under certain conditions also in the absence of thrombin, as for instance in the presence of specific metal ions or by ozone oxidation.[12,13] Those generated aggregates may also facilitate accidential non-desired formation of clots. Therefore, it is of great interest to elucidate the mechanisms of aggregate formation of fibrinogen, also in the absence of thrombin.

A better understanding of the accidental self-assembly of proteins within biological systems in general opens up the possibility to gain better knowledge on diseases associated with the products of those self-assembly processes. Investigations of biological systems are highly complex and are accompanied with an enormous parameter space, such as pH, concentration, temperature, the presence of different proteins or other components aside from the target protein, which makes it hard to reproduce[14] processes with those systems and causes distinct discrepancies between *in-vivo* measurements and observations from *in-vitro* experiments.[15,16] This complexity of protein systems, together with the sophisticated handling of proteins, creates a need for model systems similar to protein systems but more robust. One promising approach is the use of a dyestuff as a protein substitute. The specific pattern of hydrophobic spots, ionic groups and residues suited to form H-bond can be found in both substance classes, together with a marginal solubility in water. Those features are predominantly responsible for self-assembly processes, leading to fibrillar structures with long range ordering in at least one direction.[17]

The cationic dyestuff pseudo isocyanine chloride (PIC) is a promising candidate. The molecular structure of PIC is shown in **Figure 1.1**. PIC was firstly investigated by Jelley[18,19] and Scheibe[20,21]. It shows a sharp absorbance peak at 573 nm as soon as aggregates are formed in solution. The formation of aggregates, which are called J-aggregates, is induced by a temperature drop with the aggregation temperature being decreased the lower the concentration of PIC is. The aggregation threshold can be seen in **Figure 1.1** for PIC in aqueous solution and in 0.01M NaCl solution. Samples which are kept above the respective threshold do not exhibit J-aggregates. The addition of sodium chloride shifts the aggregation threshold to lower concentrations. A physical reasoning for this shift is still absent. However, one has to keep in mind that introduction of sodium chloride does not only lead to an increased ionic strength, but also adds one of the reactants of the aggregation process. Thus, determination of the origin of the shift requires a detailed study with a focus on the separation of the various impacts triggering an aggregation. It was observed that use of other salts ($NaClO_4$, $NaNO_3$) leads to precipitation of the dyestuff without any J-aggregates being formed (data not shown). A similar effect is observed when dissolving the iodide analogue of PIC in water[22].

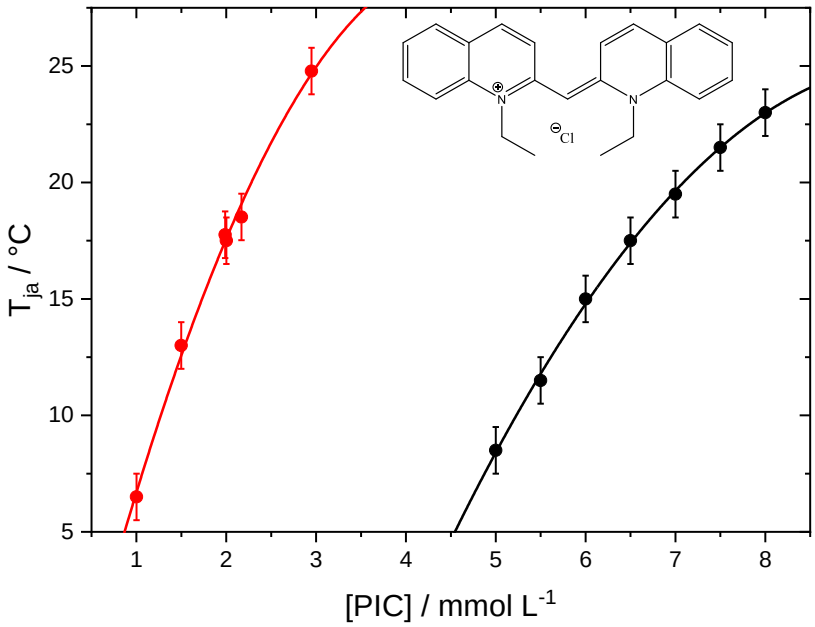

Figure 1.1: The phase diagram of pseudo-isocyanine chloride (PIC) in aqueous solution (black) and in 0.01M NaCl (red) together with the structural formula of PIC.

Aside from J-aggregates, other species are present in solution, denoted as H-aggregates. The difference between those two types of aggregates lies in the way monomers align within the aggregates and in the size of the aggregates. In J-aggregates the monomers tend to overlap their π-systems in a tilted head-to-end alignment, as also proposed by the most recent structure model from von Berlepsch et al.[23] derived from x-ray diffraction experiments. In contrast, monomers within an H-aggregate are more aligned in a face-to-face manner. The differences in the mode of alignment of molecules within those aggregates is also the reason of the shift in absorption peaks of those species in relation to the monomer peak, as it was quantified with the exciton model[24]. Beside the structural differences, H-aggregates are occurring as oligomers while the number of monomers within a J-aggregate exceeds several hundred. Fidder and Wiersma[25] stated 100 monomers as a lower limit while investigation of the annihilation of single excitons, performed by Sundström et al.[26], suggest an aggregation number in the regime of $2 \cdot 10^4$ to $5 \cdot 10^4$.

Kopainsky was one of the first who established an absorption spectrum of dimeric H-aggregates[27]. Absorption measurements at low temperatures, conducted by Cooper, revealed additional shoulders at the peak around $\lambda < 483$ nm, which are indicating H-aggregates of higher degree of oligomerization[28]. He calculated theoretical molecular exciton

shifts of trimers, tetramers and pentamers, which were found to be in agreement with experimental results. The observed shoulder peaks can indeed be attributed to H-aggregates with N > 2. Isolated spectra of these species are not published by now.

Having identified PIC as a suitable candidate to represent a protein-like substitute, one further important aspect has to be considered for developing model systems to study protein aggregation. In general, *in-vitro* experiments are carried out under physiological conditions in terms of pH, ionic composition and strength. These conditions already mimic the environment in living systems sufficiently enough to provide first insights and, in some cases, qualitatively reproduce data from *in-vivo* experiments.[29,30] Nevertheless, the major part of findings on protein aggregation indicates a lack of physiological relevance because the complexity in a living cell is mostly neglected.[31] When studying the properties of proteins in solution, a low concentration of the target protein is chosen in order to be in line with the situation in living systems, usually in a concentration regime from 1 to 10 g L^{-1}. The occurrence of other components, such as proteins or salts, is not being considered which is one of the reasons for deviations to *in vivo* experiments. The concentration range of all other components within a cell accounts to around 300 to 400 g L^{-1}.[32] Hence, while the concentration of the target protein can be considered as diluted, the overall concentration of solid content leads to non-negligible intermolecular interactions. This state is named crowded instead of concentrated since many different macromolecules attribute to the solid content.[31] T. C. Laurent was one of the first linking the behaviour of crowded solutions to volume exclusion and verified it by solubility assays with various proteins in the presence of polysaccharides.[33] P. Ross and A. P. Minton[34] successfully modelled the non-ideality of concentrated hemoglobin solution based on a hard-sphere model, underlining the effect of volume exclusion. However, application of this hard sphere model onto a similar system, namely the decrease in solubility of sickle cell hemoglobin via addition of myoglobin, lead to predictions which were not in agreement with experimental data.[35] Thus, correlating the problem solely on volume exclusion is not adequate.[36]

Further studies also underline the importance of taking crowding effects into account when investigating biosystems. Dextran for example enhances amyloid formation of C-II[37] and promotes the formation of actin filaments.[38] The oligomerization of fibrinogen can be accelerated with addition of bovine serum albumin (BSA) while tubulin oligomerizes preferably in the presence of Dextran.[39] Polyethylene glycole (PEG) is commonly used as a

synthetic crowder, promoting for example the dimer formation of pyruvate dehydrogenase[40,41] but has no effect on the self-assembly of myoglobin.[42] However, crowding does not only accelerate reactions but can also supress them, as it is shown by Gao et al with IAPP as the target protein.[43]

1.2 Objective

The objective of the present thesis is to establish the dyestuff pseudo-isocyanine chloride (PIC) as a novel model system to mimic protein aggregation in crowded media. For this purpose, a better understanding of the oligomerization and aggregation of PIC and its accompanied mechanisms is needed. Thus, the key questions resolve around the quantification of equilibrium states in terms of sample compositions, the kinetics of H-aggregate oligomerization and its role as a precursor for PIC aggregation as well as the mechanism of J-aggregate formation itself. Once progress on the self-assembly of pure PIC has been established, synthetic crowding agents, which are typically used in literature, are applied in *in vitro* experiments to affect this self-assembly. The observed effects on the aggregation of PIC are analysed with respect to its thermodynamic driving forces. For this purpose, data evaluation methods, commonly used in the context of protein aggregation, are applied. *In vivo* experiments of PIC in living cells are finally conducted to complement the previous findings on the effect of synthetic crowding agents.

Beside the analysis of the PIC system, a biological system and its susceptibility towards crowding agents shall also be elucidated, namely the aggregation of the bioprotein fibrinogen in the absence of thrombin, covered in **Chapter 4**. Whereas the thrombin-catalysed self-assembly of fibrinogen is already described in great detail in literature, there is not much known on the self-assembly proceeding from fibrinogen without thrombin involved. It is already shown in literature that fibrinogen itself is prone to aggregation under distinct circumstances, such as a low ionic strength[44] or the presence of multivalent metal cations[12]. Fibrinogen-based particles offer great potential in applications in medicine, such as acting as a scaffold to promote cell adhesion for example. For this purpose, key questions have to be answered which address the mechanism of particle formation derived from fibrinogen, the controllability of the process and how changes in parameters could possibly affect the outcome of particle formation. These questions shall be answered with the help of combined

time-resolved static and dynamic light scattering. Scattering data at different solution conditions were recorded and interpreted with appropriate mechanistic models with the target to establish a correlation between solution conditions and the accompanied alterations in the kinetics. Furthermore, the morphology of the generated fibrinogen aggregates shall be characterized and compared to the morphology of fibrin fibrils. The presented data shall provide the groundwork for establishing fibrinogen related bioparticles as a promising material in various medical applications. To bring this chapter in line with crowding effects, additional experiments are conducted where fibrinogen is introduced to synthetic crowding agents. The presentation of those experiments is done in **Chapter 8**.

As already indicated in the Introduction, the dyestuff PIC has the potential to be a protein substitute to investigate crowding effects on the generation of protein aggregates. **Chapter 5** shall elucidate the basic principles of PIC oligomerization and aggregation, which are necessary to fully utilize PIC as a model system for protein aggregation. The key questions to be answered in this chapter address the underlying mechanism of PIC aggregation and how the equilibrium situations above and below the aggregation threshold can be described. There are already numerous important findings on the topic published, such as the presence of oligomers, which are called H-aggregates, above the aggregation threshold[27], the appearance of the spectrum of dimers[45] and a structure model of J-aggregates[23]. Characterizations of J-aggregates and their formation in diluted solution was also investigated[46]. With **Chapter 5**, these findings shall be complemented regarding the mechanism of J-aggregate formation. Furthermore, it will be shown how spectra of oligomers with a degree of oligomerisation greater than 2 can be established and how an isolated spectrum of J-aggregates can be obtained. Additionally, a procedure will be developed to estimate the content of J-aggregates at a given temperature and PIC concentration with help of the aggregation threshold.

Successively, the focus turns toward the introduction of crowding agents into the PIC system. The chemical similarities of dyestuffs and proteins, namely the specific pattern of chemical groups and a marginal solubility in water, which leads to the capability to form fibrillar structures, make dyestuffs a potential protein substitute to investigate aggregation patterns in biological systems. Crowding is an important parameter when studying those aggregation phenomena. Therefore, **Chapter 6** shall elucidate how various synthetic crowders, which are frequently used in literature to mimic cellular crowding, affects the tendency of the dyestuff PIC to form J-aggregates. Questions around the thermodynamic driving forces of crowding

effects on J-aggregate formation of PIC shall be answered, to enable the quantification of either amplification or suppression of the formation of aggregates. The validity of well-established concepts of thermodynamic principles, which are usually applied on chemical reactions, folding reactions, or self-assembly processes of proteins, shall be proven now for the self-assembly of PIC in order to furthermore underline the similarities of various dyestuffs and proteins. Additionally, it should be verified whether principles from synthetic polymerizations can be applied also to the self-assembly of PIC. Findings on this question shall strengthen the knowledge regarding the mechanism of self-assembly of PIC.

Since it was proven that synthetic crowding agents do have an impact on the self-assembly of PIC, a follow-up question is how PIC behaves under natural crowding in a cell. This question shall be tackled in **Chapter 7**, together with further clarifications on how addition of crowding agents alters the aggregation threshold of PIC and how the presence of crowding agents changes the equilibrium above the aggregation threshold. The previously mentioned natural crowding is investigated with the help of *in vivo* experiments in HeLa cells. Here, it is of interest whether PIC is able to penetrate cells, whether aggregation is also occurring within cells and how cells infiltrated with PIC react to osmotic stress. The results strongly underline that PIC can possibly be used as a crowding sensor in cellular environments.

The purpose of **Chapter 8** is to extend the findings on the self-assembly of fibrinogen in the absence of thrombin (**Chapter 4**) with insights on how crowding affects this self-assembly process. Aggregation experiments were conducted with the crowding agent Ficoll 400. It should be clarified whether this biosystem show similar reactions towards the presence of crowding agents as the dyestuff PIC.

1.3 References

[1] B. Alberts, A. Johnson, J. Lewis, M. Raff, K. Roberts, P. Walter, *Molecular Biology of the Cell*, Garland Science, New York, **2002**.

[2] B. A. Yankner, L. K. Duffy, D. A. Kirschner, *Science (80-.).* **1990**, *250*, 279.

[3] D. J. Selkoe, *Annu. Rev. Cell Biol.* **1994**, *10*, 373.

[4] R. F. Doolittle, *Annu. Rev. Biochem.* **1984**, *53*, 195.

[5] K. Lederer, R. Hammel, *Die Makromol. Chemie* **1975**, *176*, 2619.

[6] J. W. Weisel, R. I. Litvinov, *Blood* **2013**, *121*, 1712.

[7] R. G. Macfarlane, *Nature* **1964**, *202*, 498.

[8] H. A. Scheraga, M. Laskowski, *Adv. Protein Chem.* **1957**, *12*, 1.

[9] W. Krakow, G. F. Endres, B. M. Siegbl, H. A. Schekaga, *J. Mol. Biol.* **1972**, *71*, 95.

[10] R. A. S. Ariëns, T. S. Lai, J. W. Weisel, C. S. Greenberg, P. J. Grant, *Blood* **2002**, *100*, 743.

[11] B. Blombäck, *Thromb. Res.* **1996**, *83*, 1.

[12] F. S. Steven, M. M. Griffin, B. S. Brown, T. P. Hulley, *Int. J. Biol. Macromol.* **1982**, *4*, 367.

[13] M. A. Rosenfeld, V. B. Leonova, M. L. Konstantinova, S. D. Razumovskii, **2009**, *74*.

[14] J. R. Brender, J. Krishnamoorthy, M. F. M. Sciacca, S. Vivekanandan, L. D'Urso, J. Chen, C. La Rosa, A. Ramamoorthy, *J. Phys. Chem. B* **2015**, *119*, 2886.

[15] G. B. Ralston, *J. Chem. Educ.* **1990**, *67*, 857.

[16] A. P. Minton, *Curr. Opin. Biotechnol.* **1997**, *8*, 65.

[17] A. M. Morris, M. A. Watzky, R. G. Finke, *Biochim. Biophys. Acta - Proteins Proteomics* **2009**, *1794*, 375.

[18] E. E. Jelley, *Nature* **1936**, *138*, 1009.

[19] E. E. Jelley, *Nature* **1937**, *139*, 631.

[20] G. Scheibe, L. Kandler, H. Ecker, *Naturwissenschaften* **1937**, *25*, 75.

[21] G. Scheibe, L. Kandler, H. Ecker, *Naturwissenschaften* **1937**, *25*, 474.

[22] H. Stegemeyer, F. Stöckel, *Ber. Bunsenges. Phys. Chem.* **1996**, *100*, 9.

[23] H. von Berlepsch, C. Böttcher, L. Dähne, *J. Phys. Chem. B* **2000**, *104*, 8792.

[24] M. Kasha, H. R. Rawls, M. A. El-Bayoumi, *Pure Appl. Chem.* **1965**, *11*, 371.

[25] H. Fidder, D. A. Wiersma, *Phys. Rev. Lett.* **1991**, *66*, 1501.

[26] V. Sundström, T. Gillbro, R. A. Gadonas, A. Piskarskas, *J. Chem. Phys.* **1988**, *89*, 2754.

[27] B. Kopainsky, J. K. Hallermeier, W. Kaiser, *Chem. Phys. Lett.* **1981**, *83*, 498.

[28] W. Cooper, *Chem. Phys. Lett.* **1970**, *7*, 73.

[29] G. Calloni, S. Zoffoli, M. Stefani, C. M. Dobson, F. Chiti, *J. Biol. Chem.* **2005**, *280*, 10607.

[30] Z. Ignatova, L. M. Gierasch, *Biochemistry* **2005**, *44*, 7266.

[31] R. J. Ellis, *Trends Biochem. Sci.* **2001**, *26*, 597.

[32] S. B. Zimmerman, S. O. Trach, *J. Mol. Biol.* **1991**, *222*, 599.

[33] T. C. Laurent, *Biochem. J.* **1963**, *89*, 253.

[34] P. D. Ross, A. P. Minton, *J. Mol. Biol.* **1977**, *112*, 437.

[35] P. D. Ross, A. P. Minton, *Biochem. Biophys. Res. Commun.* **1979**, *88*, 1308.

[36] A. P. Minton, *Mol. Cell. Biochem.* **1983**, *55*, 119.

[37] D. M. Hatters, A. P. Minton, G. J. Howlett, *J. Biol. Chem.* **2002**, *277*, 7824.

[38] C. Rosin, P. H. Schummel, R. Winter, *Phys. Chem. Chem. Phys.* **2015**, *17*, 8330.

[39] G. Rivas, J. A. Fernandez, A. P. Minton, *Biochemistry* **1999**, *38*, 9379.

[40] H. J. Bosma, G. Voordouw, A. De Kok, C. Veeger, *FEBS Lett.* **1980**, *120*, 179.

[41] L. W. Nichol, A. G. Ogston, P. R. Wills, *FEBS Lett.* **1981**, *126*, 18.

[42] J. Wilf, A. P. Minton, *BBA - Protein Struct.* **1981**, *670*, 316.

[43] M. Gao, K. Estel, J. Seeliger, R. P. Friedrich, S. Dogan, E. E. Wanker, R. Winter, S. Ebbinghaus, *Phys. Chem. Chem. Phys.* **2015**, *17*, 8338.

[44] R. Gollwitzer, W. Bode, H. E. Karges, *Thromb. Res.* **1983**, 41.

[45] M.-L. Horng, E. L. Quitevis, *J. Chem. Educ.* **2000**, *77*, 637.

[46] B. Herzog, K. Huber, H. Stegemeyer, *Langmuir* **2003**, *19*, 5223.

2. Synopsis

2.1 The self-assembly of fibrinogen

Fibrinogen is a glycoprotein which is present in living systems, and which plays a crucial role in the blood clotting process. It forms fibrillar structures via catalysis of thrombin and builds up the matrix to immobilize blood platelets to stop bleeding by wound sealing. Knowledge of the reaction cascade of blood clotting is well-established in literature. Therefore, the present work starts with an investigation of the self-assembly of fibrinogen in the absence of thrombin. It is known that fibrinogen is prone to aggregation at ionic strengths lower than physiological conditions[1]. We conducted a set of light scattering experiments to investigate how the self-assembly of fibrinogen is affected by the ionic strength. In general, the lower the ionic strength is, the stronger and faster the self-assembly proceeds, as it can be seen in **Figure 2.1**.

The weight averaged molar mass went through an increase of three orders of magnitude in the first 10 minutes of the process at an ionic strength of *[I]* = 7 mM, while at *[I]* = 60 mM only an increase of one order of magnitude was observed over the course of 60 minutes. The size parameters R_g and R_h tended to be bigger at low ionic strengths, but the overall structural features of the aggregates were not affected by the final ionic strength, which can be seen in the evolution of the structure-sensitive parameter ρ. At the end of the process a value of $\rho < 1$ was observed, regardless of the ionic strength. This value indicates the growth of dense, globular structures. This globular structure stays in contrast with the morphology of fibrin-fibers.[2]

In a next step the kinetics of the self-assembly of fibrinogen was quantified. For this purpose, the coagulation theory from von Smoluchowski was applied[3]. The model fits well to experimental data recorded at ionic strengths lower than 60 mM. At those low ionic strengths, the process is diffusion-limited (DLCA) with the characteristic coagulation time t_c decreasing with decreasing ionic strength. At an ionic strength of *[I]* = 60 mM, a slight modification of the kinetic model had to be applied to be in line with experimental data. This modification took a crossover from a diffusion-limited process to a reaction-limited process (RLCA) into account.

Application of this modified model showed that at high ionic strengths, the modified model fits better to experimental data than the non-modified approach, therefore suggesting a shift from DLCA to RLCA once the ionic strength gets high enough.

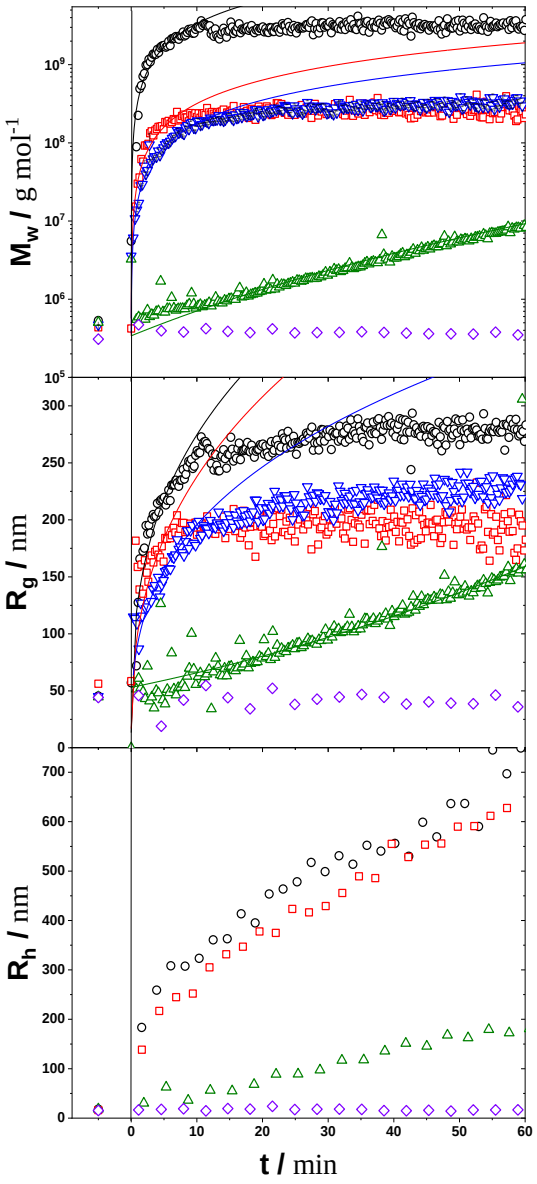

Figure 2.1. Evolution of the weight averaged molar mass M_w, radius of gyration R_g and hydrodynamically effective radius R_h of growing fibrinogen aggregates as a function of time t. Data are recorded at 25 °C and at a concentration of NaCl of 7 mM (black circles), 14 mM (red squares), 30 mM (blue inverted triangles), 60 mM (green triangles) and 100 mM (purple rhombs).

Since the self-assembly of fibrinogen takes place in the blood, thus in a crowded environment, effects of crowding should be considered in the investigation of the process. It is this task with which the Thesis shall be closed. However, the main focus is to investigate the impact of crowding on a synthetic model system. Thus, in the following chapters the findings on the aggregations of PIC and effects of crowders on the aggregation of PIC shall be elucidated. The key questions to be answered are how the sample composition can be described above the aggregation threshold. Can the newly gained information on the situation above the threshold

be used to describe the sample composition below the threshold? Here, it is of high interest to find a way to quantify the content of J-aggregates. Furthermore, the mechanism of the formation of J-aggregates shall be elucidated. This only will enable us to adequately investigate how synthetic crowding does affect the assembly of PIC towards oligomers and J-aggregates.

2.2 Oligomeric solutions of PIC

Cyanine based dyestuffs are in general capable of forming macromolecular-like structures, denoted as J-aggregates, and oligomers, denoted as H-aggregates. The tendency to undergo self-assembly correlates with the size of the van der Waals surfaces and the freedom of torsional motions within the molecule, which was used by Wörz et al.[4] to categorize dyestuffs into three classes based on their steric attributes: I) loose, II) compact and III) crowded. The latter has such a low aggregation propensity that even oligomerization is hindered. PIC itself was not classified in this work but it is relevant to know that oligomerization of PIC does occur and seems to be strongly connected to the formation of J-aggregates.[5] Therefore, it is necessary to describe the system as a whole with all its species and constituents involved to fully unleash the potential of PIC being a model system for aggregation phenomena in biological systems.

A major advantage of PIC is that absorption characteristics of PIC samples are directly related to the sample composition, as the absorption patterns of the different PIC species are distinguishable. Various efforts to extract the isolated absorption spectra of the oligomers were already conducted, resulting in a monomer and dimer spectrum.[5,6] Unfortunately, this does not suffice to fully describe the system above the regime where monomers and small oligomers prevail. Accordingly, the present thesis succeeded to establish an additional trimer spectrum above the threshold of J-aggregation, based on the same principles which were used to determine the dimer spectrum. All relevant spectra to describe the sample composition above the aggregation threshold are shown in **Figure 2.2**.

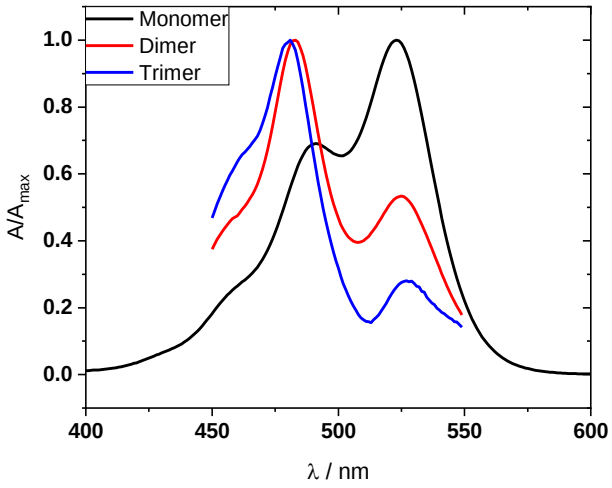

Figure 2.2. Absorption spectra of different PIC species present in solution. The monomer spectrum (black) was measured at *[PIC]* = 3µM, the dimer spectrum (red) was established by Horng et al..[6] Estimation of the trimer (blue) is carried out in the present work.

For simplification purposes, it was assumed that this trimer spectrum represents all oligomers with N ≥ 3. Another outcome during establishing the trimer spectrum was the temperature dependence of the associated trimerization constant K_T. Together with the temperature dependence of the dimerization constant, established by Neumann et al.[7], this enabled us to quantify the sample composition of PIC above the threshold of J-aggregation in terms of monomers, dimers and trimers. At a constant concentration, the monomer content decreases with decreasing temperature while the trimer content increases. Surprisingly, the relative concentration of dimers is not dependent on the concentration of PIC and on the temperature and amounts to ~17% of the overall concentration. Another feature of this multicomponent system is that state points right on the aggregation threshold exhibit the same relative sample composition, regardless of the overall PIC concentration.

Light scattering experiments in the regime prior to aggregation showed no angular dependence and a nearly constant weight averaged molar mass M_w of 890 ± 20 g mol^{-1} indicating the sole presence of monomers and small oligomers. With the previously determined sample composition, a theoretical value of M_w = 850 ± 70 g mol^{-1} can be calculated, being in good agreement with the value experimentally determined by light scattering.

2.3 The mechanism of J-aggregate formation

Description of the sample composition below the threshold of J-aggregation requires a few introductory words on the mechanism of the self-assembly of PIC to J-aggregates. In general, it is of interest to determine whether such an aggregation follows a stepwise growth or whether the process is better described with a monomer addition mechanism. This has not been fully answered by now. Daltrozzo et al.[8] treated the formation of J-aggregates as a crystallization process with PIC being a slightly soluble salt and found a good agreement between experimental results and the proposed model. Herzog et al.[9] did light scattering measurements on aggregated PIC samples. Their findings on the characteristics of growing J-aggregates revealed that initiation and growth of aggregates happens steadily during the process, with the consequence of a constant increase in the number of fully developed aggregates. All these results from literature already suggests a monomer addition process rather than stepwise growth.

The insight gained in the present thesis gives further hints on the underlying mechanism of J-aggregate formation. Dynamic light scattering experiments at the onset of aggregation revealed a pronounced bimodality in the correlation functions. Evaluation of these correlation functions gave two hydrodynamic radii, amounting to 0.5 nm and 90 nm with both remaining constant throughout the whole regime where evaluation of the bimodality was possible. The small species can be attributed to monomers or oligomers while the big species represents J-aggregates. This persisting distinction supports a monomer addition process. In case of a stepwise growth, as the alternative mechanism to monomer addition, a broad monomodal correlation function is to be expected, as it was observed in the context of the self-assembly of fibrinogen [see Chapter 4].

Beside the hydrodynamic radii of the species, one is also able to extract the intensity weighted weighing factors b_i during the phase, where bimodal correlation functions are observed. These weighing factors can be used to split the overall scattering signal into the contributions of both present species. The contribution of J-aggregates to the scattering signal was then re-evaluated, which lead to a constant radius of gyration of R_g = 188 nm, shown in **Figure 2.3**. This again underlines the presence of fully developed J-aggregates right at the beginning of the self-assembly, which indicates a monomer addition process. Determination of a radius of

gyration of non-aggregated PIC was not possible, since the contribution of non-aggregated PIC did non exhibit an angular dependency, as it can be seen in **Figure 2.3 A)**.

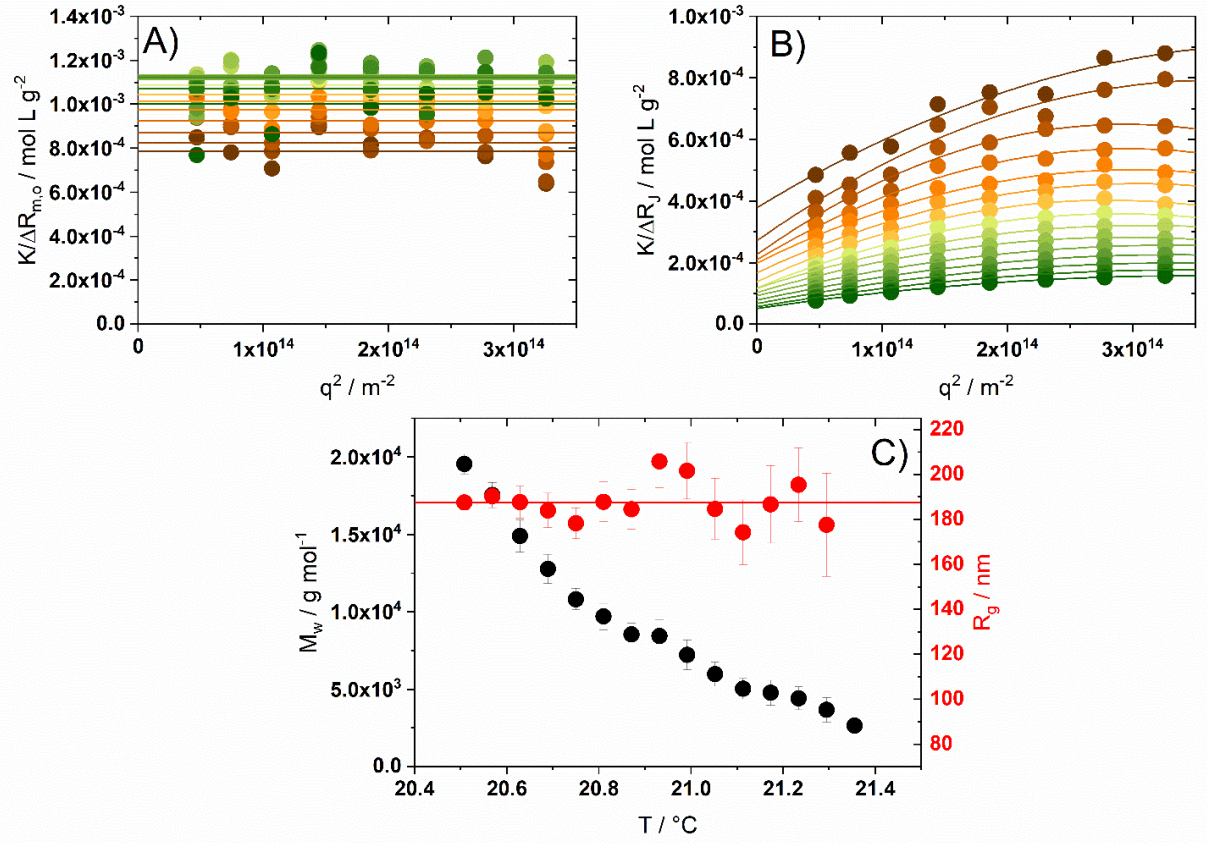

Figure 2.3. Evaluation of the scattering contribution of J-aggregates at the onset of aggregation. A) Scattering curves of J-aggregates and of B) oligomers/monomers with $\Delta R_i(q) = \Delta R(q) \cdot b_i(q)$. The color index goes from brown to green and represents different temperatures from 21.3 °C to 20.5 °C. C) Results of the data analysis of the scattering curves of J-aggregates shown in B) with a dummy concentration of 1 g/L. The increase in M_w with decreasing *T* indicates an accumulation of J-aggregates. The radius of gyration is constant and amounts to R_g = 188±2 nm.

The formation of J-aggregates is induced by a decrease in temperature, triggering further nucleation of J-aggregates instead of the growth of already existing aggregates. This aspect was verified with simulating scattering curves and comparing the outcome with experimental results. It was shown that the increase in mass weighted molar mass M_w and in radius of gyration R_g during aggregation is solely a consequence of a change in concentrations of monomers/oligomers and J-aggregates [see Chapter 5 Figure S5.12].

If the self-assembly of J-aggregates follows a monomer addition process, application of the ceiling temperature approach suggests itself and offers the opportunity to approximate the

thermodynamic parameters ΔH^0 and ΔS^0 governing J-aggregate formation. The underlying equation is the following:

$$\frac{1}{T_{ja}} = \frac{\Delta S^0}{\Delta H^0} + \frac{R \cdot \ln([PIC])}{\Delta H^0} \tag{2.1}$$

In eq 2.1, T_{ja} is the ceiling temperature here also denoted as the aggregation temperature, ΔS^0 the standard aggregation entropy, ΔH^0 the standard aggregation enthalpy, and *[PIC]* the equilibrium concentration of the active species in the formation process. The outcome of the analysis depends on the choice of active species. In a first approach, all species were considered as active building units, namely PIC monomers, and oligomers. In a second approach, only monomers were treated as the active species. It is conceivable that participation of monomers only in the formation of J-aggregates, thus with H-aggregates being inactive and acting as a monomer reservoir, is probably more favoured than co-aggregation with H-aggregates. In order for H-aggregates to be active, the tilt angle between monomers within an H-aggregate has to change to be in line with the tilt angle present in J-aggregates.[10] This change in tilt angle is probably energetically disfavoured, which thus makes self-assembly based on only monomers more energy efficient because here, no change in tilt angle is necessary beforehand. Both choices were discussed, the standard aggregation enthalpy is insensitive to the choice of the active species and amounts to -22 kJ mol^{-1}. The change in the standard entropy increases from -35 J mol^{-1} K^{-1} to -23 J mol^{-1} K^{-1} when only monomers are active.

Independently of the chosen active component, application of the ceiling temperature approach has an additional benefit. It enables us to estimate an equilibrium constant of J-aggregate formation, which is inversely proportional to the equilibrium concentration of active species. This occurrence can be used to estimate the concentration of J-aggregates, which is discussed in the next chapter.

2.4 The aggregated regime

The tendency of PIC to form J-aggregates is best described with a threshold curve (see **Figure 1.1**). At sufficiently low temperatures or high concentrations, the threshold is surpassed, and J-aggregates start to form. Thus, all state points below the threshold curve exhibit J-aggregates. Furthermore, it is found that the location of the threshold curve is dependent on the sodium chloride content. An increase of the sodium chloride content at a given

temperature is accompanied with a decrease in PIC concentration needed to form J-aggregates, resulting in a shift of the threshold curve to lower PIC concentrations. In the context of *in vivo* aggregation in HeLa cells, a Leibovitz solution was used as the solvent for PIC, which is a nutritious solution for cells and contains around 140 mM sodium chloride. Here, an even more pronounced shift of the threshold curve is observed, so that PIC concentrations in the sub-mM regime are already sufficient to show aggregation.

The development of the sample composition below the threshold curve is crucial to fully describe the aggregation of PIC. For this purpose, the system was treated as a system with one species being "non-aggregated" PIC with a concentration $[PIC]_{m,o}$, consisting of equilibrated monomers, dimers and trimers and the other species being J-aggregates with a concentration c_J. Furthermore, it was assumed that the temperature dependence of the equilibrium constants of dimerization $K_D(T)$ and trimerization $K_T(T)$, which were determined above the threshold curve, i.e. in the state free of J-aggregates, do not change when surpassing the threshold curve. Then, the concentration $[PIC]_{m,o}$ can be estimated with the equilibrium constant of aggregation $K_J = 1/[PIC]_{m,o}$. Accordingly, the concentration of J-aggregates c_J is the difference of the total PIC concentration c_{tot} and $[PIC]_{m,o}$.

This approach does not only enable the quantification of the sample composition below the aggregation threshold, but also allows the estimation of a J-aggregate spectrum. For this purpose, the contribution of monomers/oligomers on the absorbance is subtracted from experimental spectra of aggregated samples so that the resulting excess absorbance can be fully assigned to J-aggregates. The excess absorbance from J-aggregates is then normalized with the J-aggregate concentration, which have been done with twelve different spectra. It was the outcome of the analysis that after normalization, the resulting twelve J-aggregate spectra exhibited a satisfactory overlay, underlining the validity of the approach. Comparison of the averaged full J-aggregate spectrum with the monomer spectrum shows that the two peaks at $\lambda = 483$ nm and $\lambda = 523$ nm are redshifted in the J-aggregate spectrum. This occurrence is in line with calculations by Briggs who established theoretical bandshape functions for monomers and J-aggregates[11].

Knowledge of the concentrations of oligomeric species and J-aggregates was applied on the evaluation of data from light scattering experiments in pure water. With the assumption, that the scattering contribution of monomers/oligomers is negligible compared to the contribution

of J-aggregates, an approximation of the molar mass of J-aggregates M_J becomes accessible. Its value amounts to $1.48 \pm 0.07 \cdot 10^6$ g mol^{-1} and compares well with the value of $2.55 \cdot 10^6$ g mol^{-1} measured by Herzog et al.[9] in 0.01 M NaCl solution.

As already stated in the previous chapter, the increase in M_w and R_g with decreasing temperature in the aggregated regime seems to be solely a consequence of an increase in J-aggregate concentration c_J on the expense of monomers/oligomers. To verify this origin of the increase in M_w and R_g, scattering curves were simulated and the outcome was compared to experimental data. The simulation was conducted in the following way: a bimodal system was assumed, with J-aggregates and non-aggregated PIC being the species present in solution. In general, the scattering intensity, expressed as the excess Rayleigh ratio ΔR, of a solution containing different entities can be described with following equation:

$$\Delta \mathrm{R(q)} = \sum_i K_i \cdot c_i \cdot M_i \cdot P_i(q \cdot R_{g,i}) \qquad (2.2)$$

In eq. 2.2 $\Delta R(q)$ is the excess Rayleigh ratio as a function of the scattering vector q, K_i the optical constant, c_i the concentration in g/L, M_i the molar mass, $R_{g,i}$ the radius of gyration and $P_i(q)$ the form factor of species i. The form factor of non-aggregated PIC (index 1) can be assumed to equal 1 over the whole angular regime because of its small size. The molar mass of non-aggregated PIC was experimentally determined as M_1 = 890 g mol^{-1} by light scattering experiments with samples where J-aggregates are absent. For J-aggregates (index 2), the form factor of a rod was assumed. The radius of gyration $R_{g,2}$ = 188 nm was also obtained via light scattering by extracting the contribution of J-aggregates on the overall scattering signal and evaluate this contribution (see Chapter 2.3). As just indicated, the molar mass of J-aggregates $M_2 = M_J$ amounts to $1.48 \cdot 10^6$ g mol^{-}. The concentrations c_i of the two components were inferred from the phase diagram established in pure water (Chapter 5). To summarize, the parameters required in eq. 2.2 were taken from two sources. Light scattering experiments before and right at the onset of aggregation, where bimodality was observable, provided M_1 of non-aggregated PIC and $R_{g,2}$ of J-aggregates. With the approach to calculate concentrations based on the aggregation threshold, M_2 of J-aggregates and the concentrations c_1 and c_2 were accessible. With all these parameters, eq. 2.2 can be used to calculate the excess Rayleigh ratio of mixed samples containing non-aggregated PIC and J-aggregates, establishing scattering curves expressed as $Kc/\Delta R$, and re-evaluating the resulting scattering curves to obtain the radius of gyration R_g and the mass averaged molar mass M_w of the samples. As it

can be seen in **Figure 2.4**, M_w and R_g derived from simulated scattering curves nicely reproduce the trends from experimental data. This outcome does not only show how beneficial simulations of scattering data can be, but it also underlines the accuracy of the concentrations estimated with help of the aggregation threshold. Therefore, it also shows the validity of this estimation method, described in Chapter 2.4.

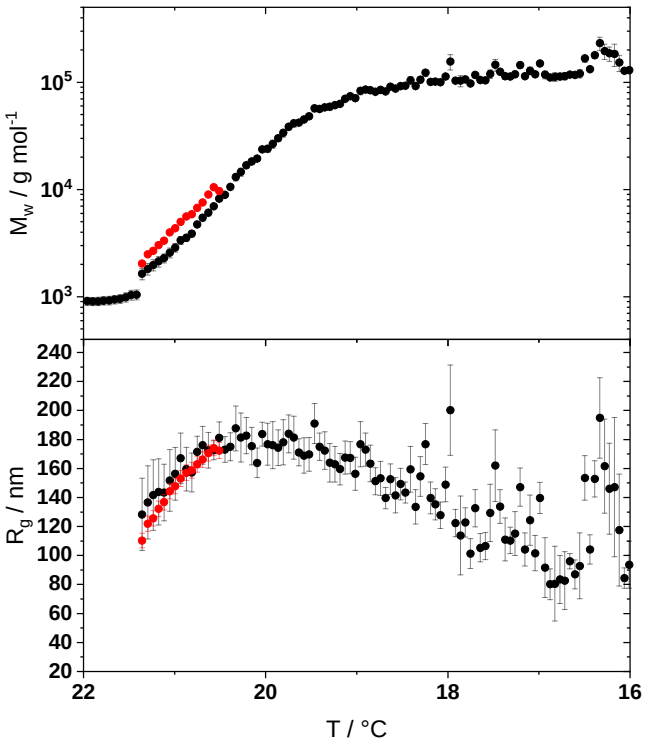

Figure 2.4. Temperature dependent evolution of the weight averaged molecular mass M_w and the radius of gyration R_g from a light scattering experiment (black) with *[PIC]* = 7 mM. The red spheres represent values for M_w and R_g obtained from the evaluation of simulated scattering curves.

2.5 The impact of crowding on the self-assembly of PIC

The previous chapters offer an overview of the PIC system with its features above and below the aggregation threshold. All those findings are based on aqueous samples without any additives involved. The findings shall now act as a reference system for the investigation of the effect of introducing crowding agents to the PIC system. For this purpose, four different, commonly used, synthetic crowding agents were probed *in vitro*, namely polyethylene glycol (PEG) with a molar mass of 400 g mol^{-1}, triethylene glycol (TEG), sucrose and Ficoll 400 with a molar mass of $4 \cdot 10^5$ g mol^{-1}. Ficoll 400 itself is a synthetic, high branched, globular copolymer

of sucrose and epichlorohydrin. It shall be the target of the present sub-chapter to summarize the most important findings on samples of PIC, which were exposed to these crowding agents.

A change in the tendency to form J-aggregates is best captured with establishment of a phase diagram. This has been done for all four crowders at different concentrations. Introduction of the ethylene glycol oligomers PEG and TEG led to a drop of the aggregation threshold towards lower temperatures, with the drop being more pronounced the higher the crowder concentration was. Thus, PEG and TEG are inhibiting the formation of J-aggregates. Addition of Ficoll 400 was accompanied with a strong increase in aggregation temperature, thus promoting the formation of J-aggregates. Unfortunately, no clear correlation between the aggregation temperature and the overall concentration of Ficoll 400 could be established. Sucrose, as the dominating monomer of Ficoll 400, did not have an impact on the self-assembly of PIC, regardless of the used concentration. These contrasting effects of Ficoll 400 and sucrose indicate that the globular structure of Ficoll 400, and therefore the volume exclusion, is the origin of the increase in aggregation temperature.

The effect on the oligomerisation to H-aggregates by addition of crowding agents was not explicitly quantified but qualitative statements can be made based on the observed differences in UV-Vis spectra. In general, the ratio of the distinct peaks at λ = 483 nm and λ = 523 nm give a first estimate on dominating species in solution, with the peak at λ = 483 nm representing dimers and the peak at λ = 523 nm representing monomers. Addition of either TEG or PEG led to a shift towards monomers, indicated by a shift in ratios in favour of the monomer peak at λ = 523 nm. Addition of sucrose did not significantly change the ratios of the two peaks, meaning that the sample composition is not altered by sucrose and is comparable to the sample composition in pure water. The impact of Ficoll 400 on the sample composition could not be established with this set of experiments. At the given temperature, addition of Ficoll 400 led to a downshift of the aggregation threshold towards lower temperatures, so that a peak arised at λ = 573 nm, which represents the presence of J-aggregates.

In a next step, the underlying thermodynamic parameters were investigated for the purpose of understanding the different driving forces of inhibition or promotion of J-aggregate formation. When investigating stabilizing or destabilizing effects of solutes on proteins with regard to folding or aggregation processes, usage of the *m*-value as a quantifying parameter

is a well-established method[12]. The *m*-value is the derivative of the free energy change of the process ΔG^0_{obs} observed with species 2, for example a folding process, with respect to the solute molality m_3 of species 3, as shown in the following equation:

$$m - value = \frac{\partial \Delta G^0_{obs}}{\partial m_3} = -RT \cdot \frac{\partial \ln(K_{obs})}{\partial m_3} \tag{2.3}$$

Thus, the value allows to make statements on whether interactions of the target molecule (species 2) with solutes (species 3) are of attractive or repulsive nature. Application of this method on a system where a change in solubility of species 2 is observed with addition of a crowder/additive (species 3) has the advantage that the m-value corresponds the chemical potential derivative μ_{23} which can be easily calculated with data of solubility measurements based on the following equation:

$$\mu_{23} = -RT \left(\frac{\delta \ln m_{2,ss}}{\delta m_3}\right)_{\mu_2} = m - value \tag{2.4}$$

In eq. 2.4 PIC corresponds to the target component denoted component 2. Hence, $m_{2,ss}$ is the molal concentration of PIC at its solubility limit and m_3 is the molal concentration of the crowder. This translation of the m-value to μ_{23} enabled us to apply the following procedure. We treated the system as a solubility problem, with the phase diagrams of PIC representing solubility limits and J-aggregates being the precipitate. The chemical potential derivative μ_{23} can then be calculated based on eq 2.4. In general, the sign of μ_{23} indicates whether interactions between additive and PIC are of attractive or repulsive nature, in relation to interactions with water. With sucrose, which did not exhibit any measurable effects on J-aggregate formation, the lowest negative value for μ_{23} was measured which amounts to -160 ± 60 cal mol^{-1} molal^{-1}. Addition of TEG and PEG led to μ_{23} = -290 ± 30 cal mol^{-1} molal^{-1} and μ_{23} = -690 ± 40 cal mol^{-1} molal^{-1}, respectively. These negative values indicate attractive interactions between TEG/PEG and PIC and explain the inhibitory effect of those crowding agents on the formation of J-aggregates. Preferential attractive interactions with crowder compared to water lead to an accumulation of crowding agents on the periphery of PIC, thus blocking possible binding sites for self-assembly. Consequently, the monomeric state of PIC is energetically favoured at temperatures which would lead to aggregation in pure water.

The value of μ_{23} amounts to $2.1 \cdot 10^6 \pm 1.6 \cdot 10^6$ cal mol^{-1} molal^{-1} when Ficoll 400 was present in solution. The positive sign indicates a depletion of Ficoll 400 from the surface of PIC. But, given

the fact that Ficoll 400 is much larger in size than a PIC molecule and the determined value for μ_{23} being around 3 orders of magnitudes larger than typical values for μ_{23}, the depletion of Ficoll 400 from the surface of PIC being the sole reason for the observed crowding effect most probably oversimplifies the situation. In order further investigate the crowding effect of Ficoll 400, the scaled particle theory[13] was applied. This theory enables the estimation of changes in activity coefficients for a given equilibrium reaction based on the presence of volume excluding macromolecules. Application of the scaled particle theory revealed that the shift in aggregation temperature can quantitatively be described with volume exclusion effects. Hence, the promoting effect of Ficoll on the self-assembly of PIC is probably originated in the volume exclusion of Ficoll together with repulsive interactions between PIC and Ficoll.

The correlation of μ_{23} with the water accessible surface area of the target molecule shall be emphasized in this context. It is shown by Knowles et al.[14] that this correlation can be used to predict m-values based on empirical data. The key features of the approach of Knowles et al.[14] are that each functional group has an empirically established group interaction potential for a specific solute, that the resulting contribution of the group interaction on the m-value directly scales with the water accessible surface area of the respective functional group and that the overall m-value is the sum of all contributions. It was shown that this empirical estimation of μ_{23} can successfully be performed with the PIC system, leading to results which are comparable with results determined with eq. 2.4.

2.6 Relevance for *in vivo* systems - the HeLa cells

Since the PIC system showed a promising response on synthetic crowding agents, it is also of great interest to see whether natural crowding within a cell induces similar responses. Therefore, *in vivo* experiments in HeLa cells were conducted in the context of a cooperation with the group of Professor Ebbinghaus in Braunschweig. The supernatant of the HeLa cells was enriched with PIC at a low enough concentration, so that formation of J-aggregation in the solution was absent. Then, fluorescence microscopy images were recorded over a period of time. As it can be seen in **Figure 2.5** the fluorescence signal within the cells increases over time, corresponding to an accumulation of PIC in the cells as J-aggregates. Interestingly, fluorescence was only observed within the cells. Furthermore, during the initial stages of aggregation, J-aggregates are assembled uniformly within the cell, as indicated by the detected fluorescence signal which was homogenously distributed over the whole cell.

Nevertheless, after some time has passed, aggregates seemed to accumulate rather in the nucleus than in the cytoplasm, as the fluorescence signal in the nucleus got stronger compared to the signal in the cytoplasm. Regarding the temporal evolution of the integrated fluorescence signal seen in **Figure 2.5**, there is a linear increase of the fluorescence signal with a plateau being reached after around 30 minutes.

These experiments verified that the formation of J-aggregates is also altered in a naturally crowded environment such as a cell. This circumstance opens up the possibility to use PIC as an easy-to-handle crowding sensor in biological systems.

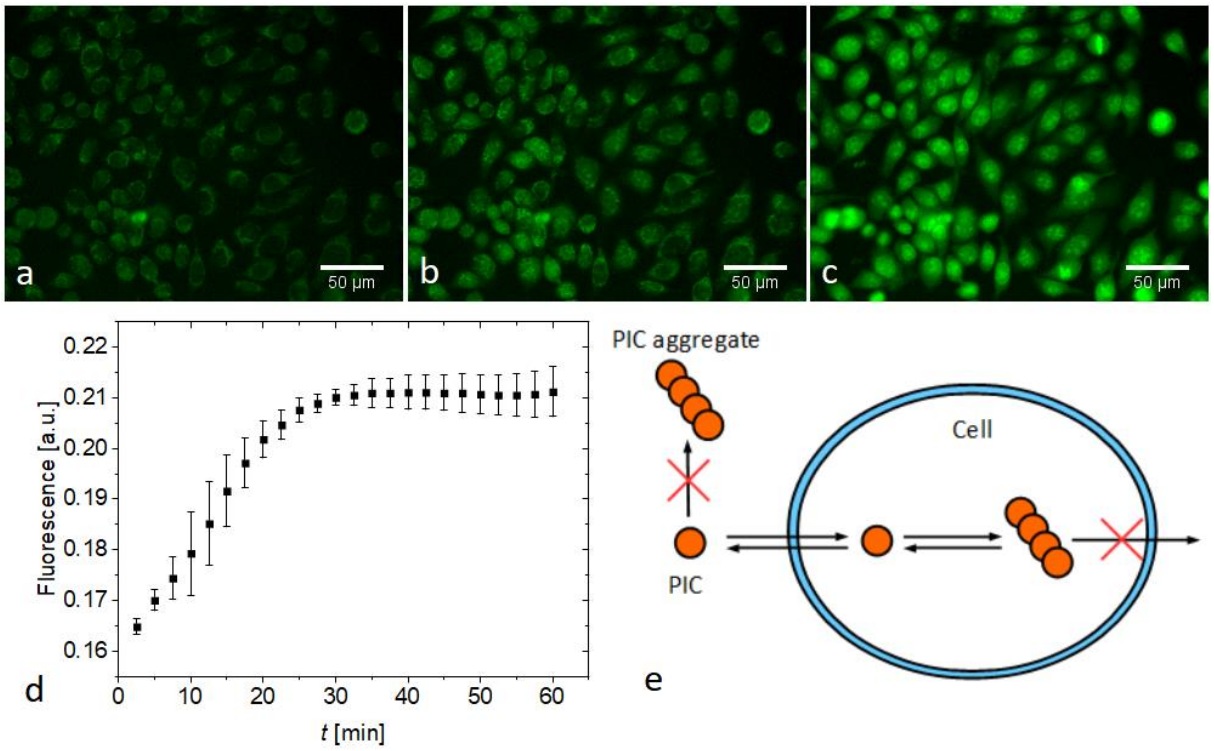

Figure 2.5: a-c) Exemplary fluorescence images of PIC aggregation in HeLa cells at 21°C a) 2.5 min b) 10 min c) 40 min after addition of PIC. Scale bar 50 µm. d) Aggregation kinetics of PIC measured by the cell-averaged fluorescence intensities. Three independent measurements were performed, and data shown as mean ± s.d. e) Model for PIC aggregation inside cells.

2.7 Self-assembly of fibrinogen under crowded conditions

The self-assembly of fibrinogen in the absence of thrombin was investigated and key features of its mechanism and kinetics has been elucidated (Chapter 2.1). Furthermore, it was shown that the dyestuff PIC can be used as a suitable model system for protein aggregation, especially for investigating crowding effects on the self-assembly (Chapters 2.2-2.6). It is the

aim of the final chapter of this thesis to show how addition of Ficoll 400, a crowding agent which was previously investigated in the context of the PIC system, alters the self-assembly of fibrinogen. Light scattering experiments on fibrinogen samples, which were exposed to Ficoll 400, revealed that the self-assembly of fibrinogen is strongly accelerated due to the crowder. Especially at the onset of the self-assembly, the process is much faster than in the absence of crowding agents. Qualitatively, the promoting effect of Ficoll 400 on fibrinogen is comparable to the one on the PIC system. There, a shift of the aggregation threshold towards lower temperatures has been observed, which is equivalent to an acceleration of self-assembly.

2.8 References

[1] R. Gollwitzer, W. Bode, H. E. Karges, *Thromb. Res.* **1983**, 41.

[2] R. F. Doolittle, *Annu. Rev. Biochem.* **1984**, *53*, 195.

[3] M. v. Smoluchowski, *Zeitschrift für Phys. Chemie* **1918**, *92*, 129.

[4] O. Wörz, G. Scheibe, *Zeitschrift fur Naturforsch. - Sect. B J. Chem. Sci.* **1969**, *24*, 381.

[5] B. Kopainsky, J. K. Hallermeier, W. Kaiser, *Chem. Phys. Lett.* **1981**, *83*, 498.

[6] M.-L. Horng, E. L. Quitevis, *J. Chem. Educ.* **2000**, *77*, 637.

[7] B. Neumann, P. Pollmann, *Phys. Chem. Chem. Phys.* **2000**, *2*, 4784.

[8] E. Daltrozzo, G. Scheibe, K. Gschwind, F. Haimerl, *Photogr. Sci. Eng.* **1974**, *18*, 441.

[9] B. Herzog, K. Huber, H. Stegemeyer, *Langmuir* **2003**, *19*, 5223.

[10] M. Kasha, H. R. Rawls, M. A. El-Bayoumi, *Pure Appl. Chem.* **1965**, *11*, 371.

[11] J. S. Briggs, *Zeitschrift für Phys. Chemie* **1971**, *75*, 214.

[12] E. J. Guinn, L. M. Pegram, M. W. Capp, M. N. Pollock, M. T. Record, *Proc. Natl. Acad. Sci. U. S. A.* **2011**, *108*, 16932.

[13] H. Reiss, H. L. Frisch, J. L. Lebowitz, *J. Chem. Phys.* **1959**, *31*, 369.

[14] D. B. Knowles, I. A. Shkel, N. M. Phan, M. Sternke, E. Lingeman, X. Cheng, L. Cheng, K. O'Connor, M. T. Record, *Biochemistry* **2015**, *54*, 3528.

3. Coauthors' Contribution

This section specifies the contribution of co-authors to the articles in chapter 4, 5, 6 and 7. The first author is fully responsible for all parts of the work not addressed here.

Chapter 4

Anne Büngeler perfomed and evaluated AFM experiments and assisted the light scattering experiments.

Dr. Charlotte Kielar assisted the AFM experiments and contributed to the discussion and interpretation of the results.

PD Dr. Adrian Keller contributed to the discussion and interpretation of the results.

Univ.-Prof. Dr. Oliver Strube contributed to the discussion and interpretation of the results and to writing the publication.

Prof. Dr. Klaus Huber contributed to the discussion and interpretation of results and to writing the publication.

Chapter 5

Prof. Dr. Klaus Huber contributed to the discussion and interpretation of results and to writing the publication.

Chapter 6

Rolland Pollak performed and evaluated the DSC experiments.

Prof. Dr. Simon Ebbinghaus contributed to the discussion and interpretation of results.

Prof. Dr. Klaus Huber contributed to the discussion and interpretation of results and to writing the publication.

Chapter 7

Roland Pollak performed and evaluated the *in vivo* experiments and contributed to the interpretation of the results from these experiments.

Prof. Dr. Simon Ebbinghaus contributed to the interpretation of the results from *in vivo* experiments and provided drafts for the paragraph referring to those experiments.

Prof. Dr. Klaus Huber contributed to the discussion and interpretation of the results and to writing the publication.

4. Self-Assembly of Fibrinogen in Aqueous, Thrombin-Free Solutions of Variable Ionic Strengths

Reprinted with permission from *Langmuir*, **2019**, *35*, 12113-12122. Copyright 2019 American Chemical Society.

DOI: 10.1021/acs.langmuir.9b01515

Link to publication: https://pubs.acs.org/articlesonrequest/AOR-KgkZ8q2sXBuSG3JAAT6g

LANGMUIR Article
Cite This: Langmuir 2019, 35, 12113−12122 pubs.acs.org/Langmuir

Self-Assembly of Fibrinogen in Aqueous, Thrombin-Free Solutions of Variable Ionic Strengths

Benjamin Hämisch,[†] Anne Büngeler,[‡] Charlotte Kielar,[§] Adrian Keller,[§] Oliver Strube,[‡] and Klaus Huber*[,†]

[†]Physical Chemistry, [‡]Biobased and Bioinspired Materials, and [§]Technical and Macromolecular Chemistry, Paderborn University, 33098 Paderborn, Germany

Supporting Information

ABSTRACT: Fibrinogen not only forms fibrin networks if assisted by thrombin but also exhibits self-assembly in dilute aqueous solutions in the absence of thrombin. It could be shown that self-assembly can be triggered in a controlled way by diluting the ionic strength set to a value of 0.14 M NaCl in the starting solutions. The present work unravels the mechanism of this self-assembly process by means of a combination of time-resolved multiangle static and dynamic light scattering and atomic force microscopy. Analysis was carried out as a function of the ionic strength adjusted by the drop in ionic strength and at variable salt compositions at a given final ionic strength. Composition was varied by changing the ratio of NaCl and phosphate buffer. The self-assembly induced by the drop of the ionic strength depends on the final value. The lower the final ionic strength gets, the faster is the self-assembly process. The variation of the salt composition at a given ionic strength has only a marginal effect, which depends on the ionic strength. The self-assembly obeys a step-growth process, where any intermediate cluster can coalesce with any other cluster. Interpretation of the data with a kinetic model based on the approach of von Smoluchowski follows a diffusion-limited cluster aggregation at ionic strength values lower than 30 mM. At an ionic strength of 30 mM, the model has to take into account a size dependence of the rate constant, and at 60 mM a transition is observed to a reaction-limited cluster aggregation.

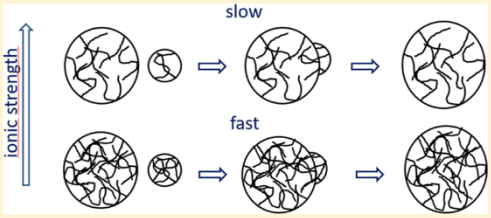

INTRODUCTION

Fibrinogen is a glycoprotein with the formula $(A\alpha B\beta\gamma)_2$. It plays a crucial role in the formation of blood clots, a pivotal process for the survival of vertebrates.[1,2] Pairs of Aα, Bβ, and γ chains are interconnected by covalent disulfide linkages close to their respective N-terminal ends, thereby establishing the central E-domain. From this E-domain the chains of each pair extend via stiff coiled coil segments toward opposite directions where the corresponding C-terminal ends of the three chains form two outer nodules, the D-domains. Fibrinogen, having itself a molar mass of 340 kD, establishes the monomeric unit of fibrin networks, which is at the center of late-stage hemostasis. The polymerization process is initiated by a thrombin-catalyzed cleavage of fibrinopeptides A and B at the N-terminal ends of the Aα and Bβ chains in the central E-domain of the fibrinogen molecule leading to the active monomers denoted fibrin. This triggers polymerization toward double-stranded protofibrils where two D-domains of one strand attach to a central E-domain of the other strand aligned in a parallel way. The resulting protofibrils aggregate laterally to thicker ropelike filaments and at the same time form branching points. During and after this self-assembly of fibrin, adjacent fibrin units are interconnected by means of factor XIII, which catalyzes covalent bond formation between γ chains from neighboring D-domains. Such covalent cross-linking transforms the assembly into chemical polymers with a considerable mechanical stability. Variation of the ionic strength by means of increasing the concentration of NaCl increases the clotting times and decreases the width of the fibrin filaments of the networks and with it the finally reached turbidities.[3−5] With increasing content of NaCl, the resulting network gets denser, with shorter mesh sizes but also with thinner filaments, with the latter causing the decrease in optical density. A comparative study of the impacts of NaCl and NaF attributed these trends to a specific interaction of Cl^- ions with fibrin monomers, thereby impairing lateral aggregation of protofibrils.[6,7] Other chaotropic ions like I^- or ClO_4^-, which like Cl^- bind water weakly, exhibit similar influences on the formation of fibrin networks.[6] In a more recent study, Kurniawan et al.[8] demonstrated that the family of anions showing such trends[3−6] also includes (4-(2-hydroxyethyl)-1-piperazineethanesulfonic acid) and related buffers.

Whereas the thrombin-catalyzed formation of fibrin networks has been investigated in great detail, much less is known on the self-assembly of the precursor fibrinogen, taking place in the absence of thrombin. Dialysis of bovine fibrinogen solutions in phosphate buffer against a buffer of low ionic strength induced formation of fibrils with a morphology closely

Received: May 22, 2019
Revised: August 20, 2019
Published: August 23, 2019

ACS Publications © 2019 American Chemical Society

DOI: 10.1021/acs.langmuir.9b01515
Langmuir 2019, 35, 12113−12122

related to that observed with thrombin-induced fibrin networks.[9] In line with this modulating effect of buffer, fibrinogen solutions without buffer reveal large fibrinogen aggregates, whereas corresponding solutions with buffer are stable, revealing small oligomers of fibrinogen molecules at the most. Noteworthy, such aggregates could be redissolved by addition of buffer.[10] Addition of multivalent transition metal cations may also trigger aggregation of fibrinogen. Steven et al.[11] distinguished three groups of multivalent metal cations, differing in their strength to induce aggregation of fibrinogen. Finally, Becker induced a self-assembly process of fibrinogen by incubating fibrinogen solutions in a phosphate-KCl−KCN buffer at pH 6.6 and T = 0 °C and found evidence for the formation of nonlinear, globular aggregates, which grow via a monomer addition mechanism.[12] This behavior differs from the results published by Gollwitzer et al.[9] though one has to take into account the difference in inducing the aggregation process applied by the two approaches.

Networks of fibrinogen have considerable relevance for the development of advanced biomaterials. Acting as a scaffold, it may promote cell adhesion or host and nucleate biominerals. Complete absence of thrombin will considerably facilitate medical applications of such materials as it would avoid possible interference of incompletely removed thrombin with the blood system where it is applied. In the light of such benefits, it is highly desirable to supplement the incomplete and fragmentary knowledge on self-assembly of fibrinogen in the absence of thrombin.

To fill this gap of knowledge, the present work reports a fundamental study on the self-assembly of fibrinogen. In a joint application of time-resolved static and dynamic light scattering (SLS/DLS) and atomic force microscopy (AFM), we analyze the effect of varying contents of NaCl and phosphate buffer on the initial stages of the self-assembly of fibrinogen in aqueous solution, free of thrombin. Complete dissolution of fibrinogen prior to the initiation of self-assembly is achieved by the use of an aqueous solution of fibrinogen in 140 mM NaCl. Self-assembly is triggered by decreasing the ionic strength of the fibrinogen solution. In more detail, two different routes shall be applied. In one route, the NaCl concentration of 140 mM is diluted to varying final values, enabling us to analyze the process as a function of the drop in ionic strength given by the final concentration of NaCl. In a second route, a drop of the ionic strength from 140 mM NaCl to 60 mM (or 30 mM) is applied with the low ionic strength state corresponding to a salt mixture at variable compositions. As a second salt, simple sodium phosphate buffer is applied, leading to variable values of chloride/phosphate ratios at a constant ionic strength of 60 mM (or 30 mM). Bivalent phosphate ions are slightly more kosmotropic than chloride ions. The second route is expected to give an answer to the question of whether aggregation is solely triggered by the drop in ionic strength or whether the ion species have an additional influence on the initiation. The results will provide new insight into the mechanism of fibrinogen self-assembly in dilute aqueous buffer solutions in the absence of thrombin and will help shed light on the extent to which mechanistic aspects observed for the thrombin-activated formation of fibrin networks can be transferred to the self-assembly of fibrinogen in the absence of thrombin. Such knowledge may also open new roads for the formation of fibrinogen-based scaffold materials free of thrombin.

EXPERIMENTAL SECTION

Materials. Fibrinogen, extracted from bovine plasma, was obtained from Sigma-Aldrich (Germany, Munich). As specified by the supplier, the fibrinogen contained 75% protein (with the amount of clottable protein being larger than 75% of the total protein), 10% sodium citrate, and 15% sodium chloride, with all percentages given by weight. The fibrinogen was used as received and was stored at −20 °C. A standard solution of sodium phosphate with a concentration of 500 mM and a pH of 6 from Cayman Chemical Company (Ann Arbor) was used as a buffer and was stored at 4 °C. Sodium chloride with a purity of 99.8% was obtained from Esco (Germany, Hannover). All samples were prepared with purified water, which was provided by a water purification system of the type Ultraclear TWF from Evoqua Water Technologies GmbH (Pittsburgh), leading to a conductivity of 0.055 μS/m.

Sample Preparation for Light-Scattering Measurements. First, a starting solution with a protein concentration of 0.75 g/L was prepared. Concentration values for fibrinogen were based on the total amount of protein throughout the present work. The background electrolyte in all but one case was 140 mM NaCl. Then, 10 mg of fibrinogen parent material and 81.2 mg of sodium chloride were dissolved in 10 mL of purified water while stirring at 400 rpm for 20 min, leading to a solution with a pH of 6.6. Light-scattering experiments were performed at a constant fibrinogen concentration of 0.075 g/L at an ionic strength [I] varied in the regime of 7 mM < [I] < 100 mM. All aggregation experiments were triggered by a dilution of a starting solution of fibrinogen by a factor of 10 with an electrolyte solution with the appropriate composition. To prepare the experiment at a final ionic strength of 7 mM, the dilution step to the final concentration based on a factor of 10 forced us to apply a background electrolyte of 70 mM NaCl as a starting point. The electrolyte solutions used to dilute the starting solution to trigger aggregation were prepared in the same way for all samples. One preparation is exemplarily illustrated in the Supporting Information (S1). All investigated samples are summarized in Table 1.

Table 1. Ion Composition of the Investigated Solutions[a]

[I]/mM	[NaCl]/mM	$[I]_{Ph}$/mM	analysis method
7	7		LS
14	14		LS
30	30		AFM/LS
30	22.5	7.5	LS
30	15	15	AFM/LS
60	60		AFM/LS
60	30	30	LS
60	14	46	AFM/LS
100	100		LS

[a]The third column shows the contribution of the phosphate buffer $[I]_{Ph}$ to the total ionic strength [I].

All values specified for the concentration of NaCl and for the ionic strength [I] of solutions investigated in the present work refer to the added amounts of phosphate buffer and/or NaCl only. Specification of absolute values of [NaCl] and [I] would require additional consideration of the small amount of NaCl and of sodium citrate introduced by the supplied fibrinogen parent material. However, the contribution of NaCl and sodium citrate from the fibrinogen parent material to the ionic strength of the solution after dilution amounts to 0.26 and 0.24 mM, respectively, and can be safely neglected.

Samples for light scattering were prepared in cylindrical quartz cuvettes from Hellma with a diameter of 24 mm. Prior to any measurement, the cuvettes were cleaned by continuously injecting freshly distilled acetone from below for 15 min to eliminate dust contamination. To condition the filter (0.45 μm, PES-membrane, Acrodisc Supor), the first 2 mL of the starting solution of fibrinogen was filtered and discarded. Subsequently, 1 mL of the starting solution was filtered into the light-scattering cuvette with the preconditioned

DOI: 10.1021/acs.langmuir.9b01515
Langmuir 2019, 35, 12113−12122

sterile filter. Ten measurements of the starting solution were recorded to characterize the initial state of fibrinogen at [NaCl] = 140 mM. Successively, the solution was diluted with 9 mL of electrolyte solution, which leads to a dilution of the fibrinogen and sodium chloride concentration of the starting solution by a factor of 10. To this end, the 9 mL of the electrolyte solution was filtered with a preconditioned filter (0.45 μm, MCE-membrane, Chromafil A-20/25) into the scattering cell containing 1 mL of the fibrinogen starting solution. Filtration of the electrolyte solution into the scattering cell triggered aggregation and defined time zero of a time-resolved light-scattering experiment. The first data point measured for a time-resolved light-scattering run could be usually recorded 20−30 s after time zero.

Time-Resolved Combined Dynamic and Static Light Scattering (DLS/SLS). Light-scattering measurements were carried out with an ALV/CGS-3/MD-8 multidetection system from ALV-Laservertriebsgesellschaft (Germany, Langen). A He−Ne laser was used as a light source, with a wavelength of λ_0 = 632.8 nm and a power of 35 mW. The cell housing with the toluene bath was equilibrated at 25 °C with an external thermostat throughout all measurements. The instrument includes an array of eight detectors with an angle of 8° between two neighboring detectors. The whole system covers an angular range of $30° \le \theta \le 86°$, which corresponds to a q-range in water of $6.8 \times 10^{-3} \le q \le 18 \times 10^{-3}$ nm^{-1} with

$$q = \frac{4\pi n}{\lambda_0}\sin\left(\frac{\theta}{2}\right) \tag{1}$$

being the momentum transfer, n = 1.332 (at T = 25 °C) being the refractive index of water, θ being the scattering angle, and λ_0 being the laser wavelength in vacuum. The time resolution of a time-resolved SLS/DLS experiment was 10 s, corresponding to the time required to record an angular-dependent SLS/DLS data set. To prove reproducibility of the time-resolved light-scattering experiments, two additional runs were carried out at an ionic strength of [NaCl] = 14 mM and are shown in the Supporting Information (S2), providing also a qualitative insight into the implication on the uncertainty of the resulting coagulation time t_c from model fits to time-resolved M_w data.

Treatment of Scattering Data. Static light scattering provides the excess Rayleigh ratio ΔR_θ of the solute

$$\Delta R_\theta = \mathrm{RR}_{\theta,\mathrm{std}}\left(\frac{r_{\theta,\mathrm{sol}} - r_{\theta,\mathrm{solv}}}{r_{\theta,\mathrm{std}}}\right) \tag{2}$$

with $\mathrm{RR}_{\theta,\mathrm{Std}}$ being the absolute Rayleigh ratio of toluene used as standard and with $r_{\theta,\mathrm{sol}}$, $r_{\theta,\mathrm{solv}}$, and $r_{\theta,\mathrm{std}}$ being the measured scattering signals of the solution, the solvent, and toluene, respectively. Data evaluation was carried out in two different ways. At low ionic strength (final values of 7, 14, and 30 mM), data were treated with the Guinier approximation[13]

$$\ln\left(\frac{Kc}{\Delta R_\theta}\right) = \ln\left(\frac{1}{M_w\, e^{(-R_g^2 q^2/3 + Bq^4)}}\right) \tag{3}$$

where the factor $B{\cdot}q^4$ is introduced to take into account a bending of the scattering curves. At the highest ionic strength (60 mM), scattering data were evaluated with the Guinier[13] and Berry approximation[14]

$$\left(\frac{Kc}{\Delta R_\theta}\right)^{0.5} = \left(\frac{1}{M_w\left(1 - \frac{1}{6}R_g^2 q^2\right)}\right)^{0.5} \tag{4}$$

leading to concurrent results, with the Berry approximation[14] yielding slightly smaller uncertainties. In eqs 3 and 4, c is the mass concentration and K is the contrast factor

$$K = \frac{4\pi^2 n^2}{N_A \lambda^4}\left(\frac{\mathrm{d}n}{\mathrm{d}c}\right)^2 \tag{5}$$

which is calculated with Avogadro's number N_A and the refractive index increment of fibrinogen in water. A value for the differential refractive index increment of $\mathrm{d}n/\mathrm{d}c$ = 0.187 mL/g was extrapolated from known values[15] via the Cauchy relationship. It has to be mentioned that the obtained values for M_w and R_g have to be considered as apparent because measurements could not be extrapolated to the infinite dilution limit. The concentration-dependence of eq 3 and 4 cannot be measured during a time-dependent light-scattering experiment. Fortunately, the investigated concentrations were extremely low, and an effect of interparticle interactions could be neglected.

Dynamic light scattering gives access to the field correlation function $g_1(\tau)$, which was treated in two alternative ways. A cumulant analysis[16] was carried out by plotting the logarithm of $g_1(\tau)$ versus the relaxation time τ

$$\ln(g_1(\tau, q)) = C - \Gamma(q)\tau + \frac{\mu_2}{2\Gamma^2}\tau^2 \tag{6}$$

with C being a constant. The initial slope of the fit gives the mean inverse relaxation time of diffusive modes $\Gamma(q)$. A plot of $\Gamma(q)$ versus q^2 gives the z-averaged diffusion coefficient D_0 as the slope at q = 0.

$$D_0 = \lim_{q\to 0}\frac{\delta(\Gamma(q^2))}{\delta q^2} \text{ with } \Gamma(q) = D_z(q)q^2 + C_D R_g^2 q^4 \tag{7}$$

C_D is a shape-sensitive constant. No concentration dependence of D_0 was considered for the same reason as mentioned in the context of eqs 3 and 4.

The Stokes−Einstein relationship transforms the translational diffusion coefficient into a hydrodynamically effective radius R_h

$$R_h = \frac{k_b T}{6\pi\eta D_0} \tag{8}$$

where k_b is the Boltzmann constant, T is the temperature in Kelvin, and η is the dynamic viscosity of the solvent.

The size parameters R_g and R_h can be used to derive the structure-sensitive parameter ρ.

$$\rho = \frac{R_g}{R_h} \tag{9}$$

The value of ρ depends on the shape of the present entities in solution. Typical values are ρ = 0.77 for compact spheres, $1.2 < \rho < 1.6$ for polymer coils, and $\rho > 2$ for cylindrical or rodlike particles.[17,18]

Furthermore, a power law of R_g versus M_w was applied to gain further information about the mechanism of aggregation and about the structure of the growing entities.

$$R_g \sim M_w^{\alpha} \tag{10}$$

Values of α for self-similar structures of spheres, Gaussian polymer coils, and infinitely thin rods are 0.33, 0.5, and 1, respectively.[19] It could be shown that the value for α based on M_w and R_g developed by time-resolved SLS bears information not only about the structure of the growing particles but also about the mechanism of growth of those particles.[19]

Sample Preparation for Atomic Force Microscopy. Cover glass slides with a diameter of 15 mm Carl Roth (Germany, Karlsruhe) were cleaned with a mixture of NH_3 (25%)/H_2O_2 (35%)/H_2O at a ratio of 1:1:5 (v/v/v) for 5 min at 80 °C and washed with ultrapure water prior to its use as AFM substrates. Samples for AFM measurements were prepared analogous to the sample preparation for light-scattering experiments. The final compositions of the investigated samples can be found in Table 1.

For each measurement, 1 mL of the fibrinogen solution was filtered into a glass vial with a sterile 0.45 μm filter (Acrodisc Supor), which has anti-protein-binding properties accomplished by its hydrophilic polyethersulfone membrane. The glass vials had the same size and shape as the light-scattering cuvette. To start the aggregation, 9 mL of a desired salt solution was filtered to the fibrinogen solution with a 0.20 μm syringe filter consisting of cellulose mixed ester (Chromafil

DOI: 10.1021/acs.langmuir.9b01515
Langmuir 2019, 35, 12113−12122

A-20/25). In each case, 100 μL of the bulk solution was taken 2 min after induction of aggregation and was placed on a precleaned glass slide. After an adsorption time of 2 min, the glass slide was rinsed with ultrapure water to terminate further adsorption. Then, the measuring cell was filled with 1 mL of ultrapure water and was added directly to the AFM to start the measurement. In all cases, the first image of the adsorbed fibrinogen aggregates was recorded approximately 5 min after terminating the aggregation process by washing with ultrapure water.

AFM Imaging. AFM imaging was performed using a JPK NanoWizard ULTRA Speed equipped with USC-F0.3-k0.3 cantilevers (NanoWorld). Measurements were performed in a liquid cell filled with 1 mL of ultrapure water. For all samples, AFM images were measured with a scan size of 2×2 μm^2. Images were recorded at 512 px × 512 px and a 10 Hz line rate, corresponding to 51.5 s per frame. High-speed imaging was employed to minimize the impact of possible artefacts resulting from exposure to water such as structural rearrangements or desorption of aggregates. The images were analyzed using Gwyddion open source software.[20]

Fitting Procedure. Fitting of time-resolved light-scattering data with the kinetic model was done with Software Origin2018b from Originlab. The Levenberg−Marquardt algorithm was used as a least-squares method. A nonweighted fit has been used. Application of a weighted fit by weighting each data point with the inverse of its squared standard error ($1/\sigma_i^2$) from the analysis of angular-dependent SLS/DLS data was considered as an alternative weighting procedure. It resulted in the same trends for the fit parameters without leading to a better overall performance of the model (for details, see S3 of the Supporting Information).

Kinetic Model. To interpret time-resolved data from SLS with a kinetic model, von Smoluchowski's coagulation theory[21] provides a suitable starting point. In this approach, the rate equation describing the concentration variation of particles with a degree of aggregation of i fibrinogen molecules per particle is given by

$$\frac{d[n_i]}{dt} = -\sum_{j=1}^{\infty} k_{i,j}[n_i][n_j] + \frac{1}{2}\sum_{j=1}^{i-1} k_{j,i-j}[n_j][n_{i-j}] \tag{11}$$

with $[n_i]$ being the molar concentration of particles consisting of i fibrinogen molecules. The first term on the right side of eq 11 describes the consumption of i-mers and the second term describes the formation of i-mers in the course of coagulation steps, where both contributions are controlled by a rate constant $k_{i,j}$, given by

$$k_{i,j} \sim (D_i + D_j)(R_i + R_j)P_{i,j} \tag{12}$$

In eq 12, D_i and R_i represent the diffusion coefficient and size of the interacting i-mer, respectively, and $P_{i,j}$ is a size-dependent probability for a collision event of an i-mer with a j-mer leading to coalescence of the two particles. In an approach applied by Modler et al.[22] to the assembly of phosphoglycerate kinase and later transferred to the assembly of β-amyloid by Carrotta et al.,[23] a homogeneous function of the overall mass of the interacting assemblies was adopted for the rate constant

$$k_{ai,aj} \sim a^{\lambda} k_{i,j} \tag{13}$$

Given that the size dependence of the two terms in brackets in eq 12 cancel according to $D_i + D_j \approx 1/R_h$ and $R_i + R_j \approx R_g$ so that $(D_i + D_j)(R_i + R_j) \approx \rho$, the only size dependence of the rate constant is introduced by $P_{i,j}$ and is recovered in the term a^{λ} of eq 13. In the limit of a diffusion-controlled reaction, where λ in eq 13 approaches 0, the resulting evolution of the mass with time is given by[22]

$$M_w(t) = M_0\left(1 + \frac{2t}{t_c}\right) \tag{14}$$

where M_0 is the molar mass of a fibrinogen molecule and t_c is the characteristic coagulation time. For a size dependence of $k_{i,j}$ captured by λ, in eq 13, eq 14 turns into

$$M_w(t) = M_0\left(1 + \frac{2t}{t_c}\right)^z \tag{15}$$

with $z = 1(1 - \lambda)$. Equation 15 establishes the crossover between two limiting cases, where $\lambda = 0$ corresponds to the case of a diffusion-limited cluster aggregation (DLCA) and $\lambda = 1$ to the case of a reaction-limited cluster aggregation (RLCA) expressed as

$$M_w(t) = M_0\, e^{t/C} \tag{16}$$

with C being a constant determined by the specific features of the RLCA.[21] Once R_g obeys a power law function of the assembly mass with a characteristic exponent α, the kinetic model can alternatively be fitted to

$$R_g(t) = \frac{R_{g0}}{M_0} M_w(t)^{\alpha} \tag{17}$$

with R_{g0} representing the radius of gyration at the initial state of the respective assembly process. Values smaller than 1/3 for α were always replaced by a value of 1/3 because smaller values represent nonphysical growth. Due to the fact that the scaling laws did not extend to the monomeric unit of 340 kD, where we have cylindrically shaped fibrinogen, we had to extrapolate fictitious values for the radius of the monomer R_{g0} to be used as a suitable prefactor in eq 17. Depending on the ionic strength, those values were fixed at R_{g0} = 55 nm (60 mM), at R_{g0} = 30.1 nm (30 mM), at R_{g0} = 16.2 nm (14 mM), and at R_{g0} = 10.7 nm (7 mM). The uncertainties indicated in Tables 2−4 for the model parameters result from the fits to the respective time-resolved data. Further uncertainties result from repeating experiments (S2 of the Supporting Information) or switching from nonweighted to weighted model fits (S3 of the Supporting Information).

Table 2. Fits to Data Measured at Variable NaCl Concentrations in the Absence of Phosphate Buffer

[NaCl]/mM	t_c/min M_w-data	t_c/min R_g-data	z M_w-data
	eq 14, $0 < t < 8$ min		
7	0.002 ± 0.00003	0.0021 ± 0.00008	1
14	0.0208 ± 0.0006	0.015 ± 0.0012	1
30	0.0369 ± 0.0008	0.068 ± 0.006	1
	eq 15[a]		
30	0.0017 ± 0.00003	0.0054 ± 0.0002	0.66
60	159 ± 0.3	166 ± 0.8	5.8

[a]The fit to data at [NaCl] = 30 mM included the time regime of $0 < t < 20$ min, and the fit to the data at [NaCl] = 60 mM included the entire time regime investigated.

Table 3. Fits to Data Measured at an Ionic Strength of 30 mM at Variable Contributions from the Phosphate Buffer [I_{ph}]

[I_{ph}]/mM	t_c/min M_w-data	t_c/min R_g-data	z M_w-data
	eq 14, $0 < t < 8$ min		
15	0.061 ± 0.0011	0.071 ± 0.0044	1
7.5	0.04 ± 0.004	0.07 ± 0.009	1
0	0.037 ± 0.0008	0.068 ± 0.0055	1
	eq 15, $0 < t < 20$ min		
15	0.011 ± 0.0001	0.0195 ± 0.0006	0.77
7.5	0.0037 ± 0.0001	0.0099 ± 0.0056	0.71
0	0.0017 ± 0.00003	0.0054 ± 0.0002	0.66

RESULTS AND DISCUSSION

Model-Independent Data Analysis. As was outlined in the literature,[9] lowering the salinity of fibrinogen solutions

DOI: 10.1021/acs.langmuir.9b01515
Langmuir 2019, 35, 12113−12122

Table 4. Fits to Data Measured at an Ionic Strength of 60 mM at Variable Contributions from the Phosphate Buffer [I_{ph}]

eq 15, 0 < t < 80 min (route 1)				
[I_{ph}]/mM	t_c/min M_w-data	t_c/min R_g-data	z M_w-data	$\chi^2 M_w$-data
45	31.7 ± 0.14	31.4 ± 0.8	2.25	9.69×10^{11}
30	43.6 ± 0.2	41.8 ± 0.5	2.41	4.8×10^{11}
0	159 ± 0.3	166 ± 0.8	5.8	2.38×10^{11}
eq 16, 0 < t < 30 min (route 2)				
	C/min M_w-data	C/min R_g-data		
45	12.7 ± 0.07	12.2 ± 1.5	-	2.98×10^{10}
30	14.7 ± 0.16	13.8 ± 0.7	-	4.29×10^{10}
0	15.7 ± 0.16	17.9 ± 0.7	-	3.85×10^{10}
eq 15, 30 < t < 80 min (route 2)				
	t_c/min M_w-data	t_c/min R_g-data	z	$\chi^2 M_w$-data[a]
45	31.5 ± 0.4	28.9 ± 0.4	1.17	1.39×10^{12}
30	36.5 ± 0.4	34.9 ± 0.6	1.29	7.4×10^{11}
0	144.8 ± 0.5	144 ± 0.9	4.25	3.87×10^{11}

[a]The values of χ^2 refer to the entire time regime including the fit with eq 16, 0 < t < 30 min.

triggers self-assembly of fibrinogen. We thus first analyzed the self-assembly of fibrinogen initially dissolved in aqueous solution with 140 mM NaCl. Those solutions were diluted with water at variable ionic strengths to achieve different finite concentrations of NaCl. Figure 1 illustrates the trend of the weight averaged molar mass M_w of the scattering particles from TR-SLS, the corresponding variation of the radius of gyration R_g from TR-SLS, and of the hydrodynamically effective radius R_h from TR-DLS. At all experiments, analysis of the initial state prior to lowering the salt content revealed values of $2.7 \leq M_w \leq 5.3 \times 10^5$ g/mol for the weight averaged molar mass, 34 nm $\leq R_g \leq$ 56 nm for the radius of gyration, and values of 15.5 nm $\leq R_h \leq$ 18.9 nm for the hydrodynamic radius. Those values have to be compared with literature data, which is M_w = 340 kD for the weight averaged molar mass and R_g = 12.2 nm for the radius of gyration in aqueous solution at pH 6.4 with a fibrinogen concentration of 6.1 g/L[24] and $D = 2.31 \times 10^{-11}$ m^2/s (R_h = 10.5 nm) for the diffusion coefficient measured at 25 °C in 100 mM NaCl with 10 mM phosphate buffer.[25] Although the experimental values lie in the regime of those expected from existing data, R_g and R_h are slightly larger than these values. The discrepancy indicates the existence of a small fraction of aggregates already in the starting solution. As it is outlined in the Supporting information (S4), DLS data can in fact be decomposed into two parts. One part, attributed to the fast mode, reveals R_h = 12 nm, which can unambiguously be assigned to the fibrinogen monomer. Accordingly, the slower mode stems from a small fraction of aggregates.

Dilution of [NaCl] from 140 to 100 mM reveals essentially constant molecular parameters, thereby ruling out any significant aggregation of fibrinogen during the first day after dilution. Only after a decrease of [NaCl] from 140 to 60 mM a noticeable aggregation is observed, which is further promoted with decreasing [NaCl].

Additional insight can be expected from a discussion on the shape-sensitive ratio $\rho = R_g/R_h$. Figure 2 summarizes the trends of ρ versus time at variable [NaCl]. Values characterizing the initial state prior to dilution of the ionic strength are all above 2. Such values are typical for structurally anisometric entities as is the case for the fibrinogen monomer. However, in the present experiments, those values are affected if not governed by the small fraction of aggregates already existing in the starting solutions. In the case of [NaCl] = 100 mM, ρ remains well above 2, indicating no substantial change in shape, in

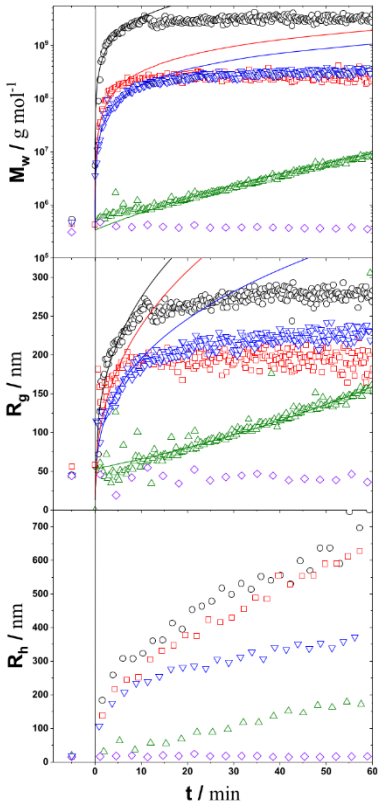

Figure 1. Evolution of the weight averaged molar mass M_w, radius of gyration R_g, and hydrodynamically effective radius R_h of growing fibrinogen aggregates as a function of time t. Data are recorded at 25 °C and at concentrations of NaCl of 7 mM (black circles), 14 mM (red squares), 30 mM (blue inverted triangles), 60 mM (green triangles), and 100 mM (purple rhombus). The lines represent fits based on eq 14 (7 mM < [NaCl] < 30 mM) to data in the regime of 0 < t < 8 min and eq 15 ([NaCl] = 60 mM) to all data. To provide a clear overview on all trends of M_w versus time t, a logarithmic scale has been selected in the topmost plot, unlike the corresponding linear representations in Figures 4 and 5.

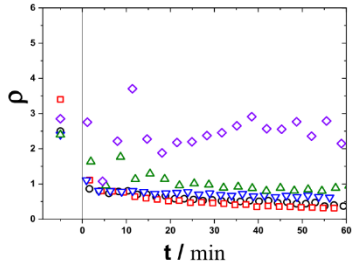

Figure 2. Evolution of the shape-sensitive ratio $\rho = R_g/R_h$ of growing fibrinogen aggregates as a function of time t. Data are recorded at 25 °C and at concentrations of NaCl of 7 mM (black circles), 14 mM (red squares), 30 mM (blue inverted triangles), 60 mM (green triangles), and 100 mM (purple rhombus).

DOI: 10.1021/acs.langmuir.9b01515
Langmuir 2019, 35, 12113−12122

agreement with the stability of the fibrinogen monomer at such high [NaCl]. Once a significant self-assembly is observed, the value drops to final values in the regime of $0.5 < \rho < 0.9$. Noteworthy, the drop in ρ appears to be more gradual at higher NaCl concentration.

Such low values are observed for compact particles with a distinct surface ($\rho = 0.78$) and for compact particles with shells of lower density ($\rho < 0.78$) and are significantly smaller than ρ of polymer coils with $1.2 < \rho < 1.6$ depending on chain flexibility, polydispersity, and solvent quality.[17]

Formation of homogeneous, rather compact particles is further confirmed by the exponent observed from plots of R_g versus M_w. If self-similar objects occur as intermediates during the self-assembly, power laws of the form shown in eq 10 can be expected for correlations of the radius of gyration with the weight averaged molar mass of the growing particles revealing exponents α characteristic for the particle shape and its growth mechanism. In the case of rods, polymers with a random walk structure, and homogeneous spheres, the exponent α adopts values of 1, 1/2, and 1/3, respectively. If growth occurs according to a step-growth process, as is the case for a polycondensation in polymer chemistry, the exponent retrieved by eq 10 corresponds to exactly the values just mentioned. If, however, the growth process obeys a monomer addition mechanism, half of the topologically expected exponent is observed,[19,26] that is, 1/2, 1/4, and 1/6 for rods, polymer coils, and spheres, respectively. As is shown in Figure 3, the values are close to 1/3 in all cases where a significant

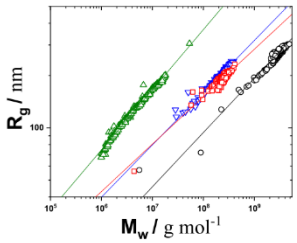

Figure 3. Correlations of weight averaged molar mass with radius of gyration in comparison to a power law behavior following eq 10. Data are recorded at 25 °C and at concentrations of NaCl of 7 mM (black circles), 14 mM (red squares), 30 mM (blue inverted triangles), and 60 mM (green triangles). The exponents of the power law are $\alpha = 0.29$ (7 mM), $\alpha = 0.28$ (14 mM), $\alpha = 0.29$ (30 mM), and $\alpha = 0.38$ (60 mM).

particle growth is observed. This value is thus compatible with two different modes of interpretation. In the case of a monomer addition process, a value close to $2 \times (1/3) = 0.66$ would still be compatible with polymer coils with excluded volume ($\alpha = 0.6$) corresponding to the shape of self-avoiding walks.[27]

However, structures with a density distribution similar to polymer coils would reveal values of $1.2 < \rho < 1.5$ for the structure-sensitive ratio ρ, which are much larger than the experimentally found values. If we assume a step-growth process, the exponent suggests structures with homogeneous density, like spheres or cubes. The experimental values for the structure-sensitive ratio of $0.5 < \rho < 0.9$ are closer to the theoretically predicted value of a sphere of $\rho = 0.78$ than to values of $1.2 < \rho < 1.6$ typical for particles with similar density distributions as those of polymer coils. This evidence for a step-growth process motivated us to perform a detailed interpretation of the present data with a suitable kinetic model, which is explained in detail in the Experimental Section.

Prior to this model analysis, the question shall be answered on whether the observed initiation of aggregation can be attributed to the drop in ionic strength or whether initiation also depends on the nature of the specific salt used at the lowered level of ionic strength. Three different salt compositions were analyzed at ionic strengths of 60 and 30 mM in the same way as just presented for various final concentrations of NaCl. The three compositions are established with contributions of 0, 25, and 50% stemming from phosphate buffer at [I] = 30 mM and 0, 50, and 75% at [I] = 60 mM. A detailed outline of the ionic compositions can be found in the Experimental Section. Figure 4 shows the trend

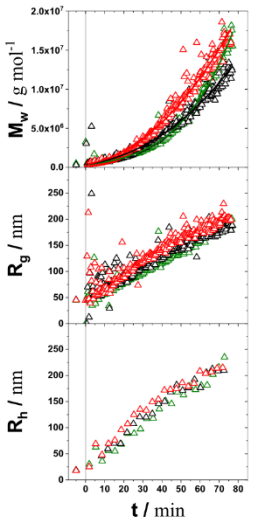

Figure 4. Evolution of the weight averaged molar mass M_w, radius of gyration R_g, and hydrodynamically effective radius R_h of growing fibrinogen aggregates as a function of time t. All data have an ionic strength of 60 mM but vary in the contribution from the phosphate buffer: 0 mM (green triangles), 30 mM (black triangles), and 45 mM (red triangles). The lines represent fits based on eq 15.

of M_w, R_g, and R_h at an ionic strength of 60 mM. None of the compositions show a remarkable deviation from the trend observed in pure 60 mM NaCl. The same feature is demonstrated in Figure 5 at an overall ionic strength of 30 mM. In full accordance with the impact observed already with the corresponding drop of [NaCl] from 60 to 30 mM in the case of pure NaCl, all three compositions at 30 mM show a similar enhancement of the aggregation process compared with the respective growth processes observed at 60 mM.

The ratio of R_g to R_h systematically approaches $0.7 < \rho < 0.8$ (Figure 6). As already noticed in the series with pure NaCl as the background salt, ρ seems to exhibit a more gradual decrease as the ionic strength increases, that is, as the process gets slower. Whereas at an ionic strength of 30 mM, a final value of $0.6 < \rho < 0.9$ is reached almost instantaneously upon lowering the ionic strength, it takes 20 min of aggregation to reach this value at an ionic strength of 60 mM.

Exponents from correlations between the radius of gyration and molar mass of the growing aggregates are all close to 1/3 (Figure 7). However, the appearance of a shift of the correlations of R_g versus M_w varying with the ionic strength

DOI: 10.1021/acs.langmuir.9b01515
Langmuir 2019, 35, 12113−12122

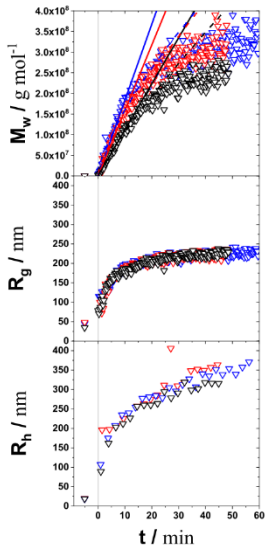

Figure 5. Evolution of the weight averaged molar mass M_w, radius of gyration R_g, and hydrodynamically effective radius R_h of growing fibrinogen aggregates as a function of time t. All data have an ionic strength of 30 mM but vary in the contribution from the phosphate buffer: 0 mM (blue inverted triangles), 7.5 mM (red inverted triangles), and 15 mM (black inverted triangles). The lines represent fits based on eq 14 at 0 min < t < 8 min (compact lines) and eq 15 at 0 min < t < 20 min (dashed lines).

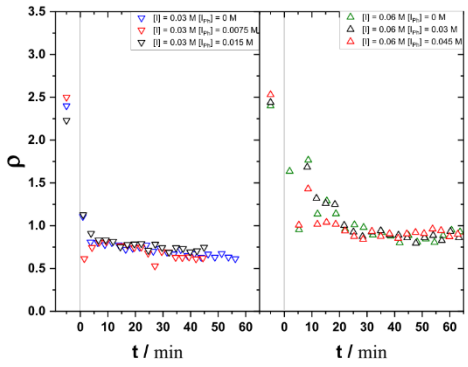

Figure 6. Evolution of the shape-sensitive ratio $\rho = R_g/R_h$ of growing fibrinogen aggregates as a function of time t. Data to the left have an ionic strength of 30 mM at variable contributions of the phosphate buffer: 0 mM (blue inverted triangles), 7.5 mM (red inverted triangles), and 15 mM (black inverted triangles). Data to the right have an ionic strength of 60 mM at variable contributions of the phosphate buffer: 0 mM (green triangles), 30 mM (black triangles), and 45 mM (red triangles).

can be observed. As is shown in Figures 3 and 7, only curves recorded at the same ionic strength overlay. Curves from different ionic strengths all reveal power laws with the same exponent but are shifted to higher values of M_w as the ionic strength where aggregation took place decreases. At a given aggregate size, the mass of the corresponding aggregate decreases with increasing ionic strength (Figures 3 and 7). Two causes are considered for such a shift. One possible cause is a distinct equilibrium concentration of nonconsumed monomers. Increasing the fraction of nonconsumed monomers

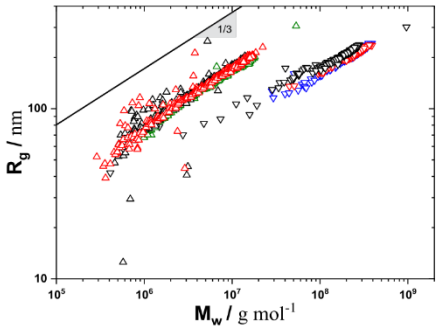

Figure 7. Correlations of weight averaged molar mass with radius of gyration in comparison to a power law behavior with an exponent of α = 1/3. Data to the left have an ionic strength of 60 mM at variable contributions of the phosphate buffer: 0 mM (green triangles), 30 mM (black triangles), and 45 mM (red triangles). Data to the right have an ionic strength of 30 mM at variable contributions of the phosphate buffer: 0 mM (blue inverted triangles), 7.5 mM (red inverted triangles), and 15 mM (black inverted triangles).

in a mixture of monomers and aggregates would decrease the weight averaged mass of the corresponding ensemble. Such a trend has in fact been observed for the formation of metal–organic frameworks.[28] Accordingly, a decrease in [NaCl] would increase the aggregate fraction and along with this increase M_w at a distinct size. Existence of a significant equilibrium concentration of monomers would keep the mode of monomers as a second mode in DLS, as aggregation proceeds. As is indicated in the Supporting Information, all measured correlation functions were monomodal (S5). Above all, the presented data suggest a growth via a step-growth mechanism and not via monomer addition. An equilibrium concentration of monomers in such a case would require transformation of the monomers to an inactive, nonaggregating species as a competing reaction. Thus, the coincidence of a power law obeying eq 10 with an exponent close to 1/3 together with the lack of monomers demonstrated by DLS excludes this possible explanation of the shifts of $R_g \sim M_w^{\alpha}$. The other possible cause for the shift of the power laws is the mass density within the aggregates depending on the ionic strength of the medium. This cause cannot be ruled out but can be made fully compatible with the step-growth process of particles of homogeneous density. To this end, we adopt the following structure for those particles. The coalescing particles are composed of highly branched filaments of fibrinogen. As the value of the ionic strength decreases, the branching density within the coalescing particles increases, thereby nicely explaining the shift of M_w to higher values at a given size R_g of the particles (Scheme 1). Values of ρ < 0.8 further support such branched structures with a homogeneous mass density.

To directly verify that fibrinogen indeed forms spherical particles under such low-salt conditions, we have turned to AFM. As expected from the light-scattering experiments, the AFM images in Figure 8 reveal the formation of rather well-defined particulate aggregates instead of fibrils at an ionic strength of 30 mM. At an increased ionic strength of 60 mM, however, particle assembly is significantly weaker, resulting in fewer and smaller particles, which is again in agreement with the in situ data discussed above. Furthermore, at an ionic strength of 30 mM, the presence of phosphate seems to have a small effect, as the particles appear slightly smaller.

DOI: 10.1021/acs.langmuir.9b01515
Langmuir 2019, 35, 12113–12122

Scheme 1. Postulated Coagulation Mechanism of Fibrinogen[a]

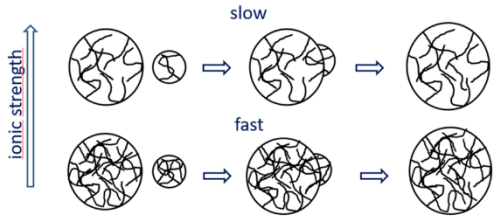

[a]A decrease in ionic strength is accompanied by an increase in branching density. The overall topology of the generated aggregates does not change with ionic strength.

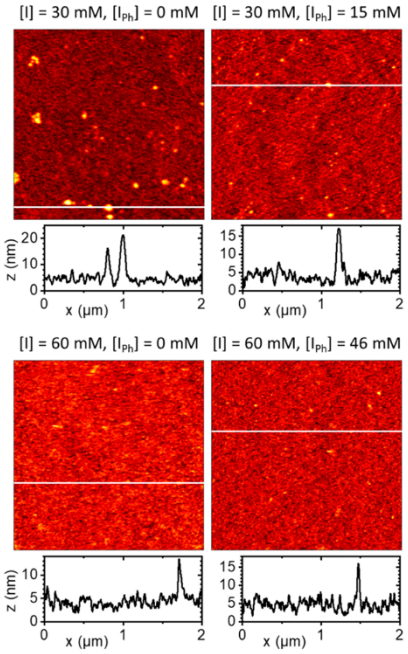

Figure 8. AFM images ($2 \times 2\ \mu m^2$) of fibrinogen aggregates adsorbed to glass slides after 2 min of incubation in bulk solution having ionic strengths [I] of 30 mM (upper row) and 60 mM (lower row) and different phosphate contents [I_{Ph}] as indicated. The corresponding height profiles below the images were taken along the white lines indicated in the images. The images have the same z-scales as the height profiles. Note that the interactions with the glass surface cause the aggregates to collapse, resulting in flattened instead of spherical particles.

Application of a Kinetic Model. As is indicated by Figures 1, 4, and 5, the weight averaged molar mass M_w of the growing aggregates during the initial time period obeys a linear dependence on time t at all ionic strengths except for [NaCl] = 60 mM. This linear correlation suggests an application of eq 14 corresponding to a DLCA process as described originally by von Smoluchowski.[21] Only in the case of [NaCl] = 60 mM, a more elaborate procedure based on eqs 15 and 16 had to be applied. Once mass values could be translated into values of radii of gyration R_g, the respective trends of R_g versus time were also fitted with one out of eqs 14, 15, or 16 in combination with eq 17 in the regime where the power law is valid.

A fit of eq 14 to the data recorded at ionic strengths of [NaCl] = 7, 14, and 30 mM in fact revealed a satisfactory description of the experiments with characteristic coagulation times t_c (Figure 1). Since the process was completed already after 10 min at the two lowest NaCl concentrations and was linear only within the first 8 min at an NaCl concentration of 30 mM, fits were restricted to the regime of $0 < t < 8$ min at those NaCl concentrations. An overview of the resulting t_c is presented in Table 2.

As expected, the fits to M_w and R_g yield consistent values. A significant elongation of the coagulation time t_c is observed with increasing ionic strength, revealing t_c = 0.002 min ([NaCl] = 7 mM), t_c = 0.021 min ([NaCl] = 14 mM), and t_c = 0.037 min ([NaCl] = 30 mM) for particle mass M_w versus time t. The trend in t_c indicates a significant slackening of the coagulation process with increasing concentration of NaCl. This deceleration is also manifested in the fact that at 30 mM, the fit can for the first time be extended to a much longer time period extending to 20 min, yet with eq 15 instead of eq 14 because eq 15 by means of $z > 1$ only can account for the convex gradient of $M_w(t)$ observed at 30 mM. At 60 mM NaCl, the process further slowed down, thus prohibiting application of the simple DLCA approach via eq 14 even during the first 8 min (Figure 1). As is shown in Figure 1 and Table 2, application of the modified coagulation approach (eq 15) revealed a value for t_c of 159 min and for z of 5.8, which indicates a significant retardation of the coagulation process compared with the one at 30 mM and a strong dependence of the rate constant on the particle size expressed by an exponent of $\lambda = 1 - 1/5.8$ in eq 13.

A closer look at the variation of the salt composition at constant ionic strength reveals only marginal variations. For the fits applied within 0 min $< t <$ 8 min at the overall ionic strength of 30 mM (Table 3), coagulation times t_c gradually decrease from 0.061 to 0.037 min for M_w with decreasing phosphate buffer content and lie in the same order of magnitude for R_g. Fits are represented in Figure 5. For fits extended to the first 20 min, a decrease of t_c from 0.011 to 0.0017 min accompanied by a decrease in z from 0.77 to 0.66 indicates the same feature of a marginal acceleration of the coagulation as the phosphate buffer content is gradually replaced by NaCl.

At an ionic strength of 60 mM, coagulation further slowed down, and the quality of the data made possible meaningful fits covering the entire time regime accessible. Two different alternative routes were applied for such a fit, with both routes almost equally suitable to account for the upturn of $M_w(t)$ toward longer times t. Route 1 is a fit with eq 15 to the trend of M_w versus t revealing a coagulation time t_c in connection with the additional parameter $z > 1$ with z determining the strength of the upturn in $M_w(t)$. Route 2 subdivides the process into two succeeding time periods, an initial period where the RLCA approach (eq 16) is applied and a final period where the modified coagulation approach eq 15 is used. This requires selection of a transition point at a distinct time t_t beyond which RLCA is no longer valid and eq 15 has to be applied instead. With both routes, in a first set of iterations, R_g and M_w-data were fitted with z being a fit parameter. The resulting values of z were then averaged, and the fit was repeated with z being fixed at the averaged value.

Application of route 1 based on the modified von Smoluchowski coagulation eq 15 gives a fairly long coagulation time t_c of 159 min in combination with z = 5.8 in pure NaCl.

DOI: 10.1021/acs.langmuir.9b01515
Langmuir 2019, 35, 12113−12122

This compares with coagulation times of 31.7 min < t_c < 43.6 min and exponents z close to 2.3 for the two solutions where phosphate buffer contributed to the overall ionic strength. Results are summarized in Table 4 and Figure 4. The decrease of t_c and z clearly indicates a gentle acceleration of the process as the content of phosphate buffer increases. Despite a considerable variation of z, the values are in all cases larger than 1, which is a clear signature of a particle-size-dependent rate constant increasing during a growth process according to eq 13 with exponents in the regime of $0.5 < \lambda < 1$.

Application of route 2 interprets the strongly bent first period with an RLCA process. The resulting parameters (Tables 4 and S6 of the Supporting Information), established with the RCLA approach for the first 30 min, are all close together covering a regime of 12.7 min < C < 15.7 min and again indicate the gentle acceleration with increasing content of phosphate buffer. During the second period, the solution with pure NaCl reveals a much larger coagulation time of t_c = 145 min than the solutions including phosphate buffer at the ionic strength of 60 mM, however, accompanied by also a much larger exponent z = 4.25. The two cases including phosphate buffer result in 31.5 min < t_c < 36.5 min and z values close to 1. The physical meaning of the simultaneous drop in t_c and z reflects an acceleration of the process in line with the trend retrieved from the initial period.

Hence, both routes consistently reveal a crossover to a reaction-controlled process. Although a comparison of the χ^2-values from route 1 and route 2 in Table 4 indicates a slightly better fit performance of route 1, and direct comparison of a fit of eq 15 with eq 16 to the trend of $M_w(t)$ of the first 30 min outlined in Table S5 of the Supporting Information show an insignificantly better performance of eq 15 during this initial period, the RLCA approach is considered to perform equally well as the modified von Smoluchowski approach.

■ CONCLUSIONS

The present work investigated the self-assembly of fibrinogen in saline solutions free of thrombin. Self-assembly was triggered by a drop of the ionic strength from an initial value of 140 mM NaCl to a final and lower value established by a mixture of NaCl and phosphate buffer. Interpretation of the growth process of fibrinogen assemblies at variable ionic strengths and at variable compositions of the added salt revealed the following trends. Increasing the final value of the ionic strength decelerated the particle growth process, which can be captured by an increasing coagulation rate in terms of a diffusion-limited von Smoluchowski process,[21−23] denoted DLCA. This trend is similar to the one observed for the thrombin-catalyzed polymerization of fibrin,[3−5] suggesting that the attachment of monomers may be similar for the self-assembly of fibrinogen and for the polymerization of fibrin. The deceleration of the self-assembly with increasing ionic strength can be explained as follows. Increasing the ionic strength lowers the sticking probability of approaching particles. This may be due to either (i) a regulation of an electrostatically driven strong binding caused by a strong electrostatic screening or (ii) a binding caused by a specific interaction that is blocked by one or more of the ionic species establishing the screening salt. At an ionic strength of 60 mM, the processes turned into an RLCA process during its initial period. Replacement of part of the NaCl by phosphate buffer slightly decelerated the process at the overall ionic strength of 30 mM. This trend is inversed at the ionic strength of 60 mM.

If the results are compared with the findings in the literature, analogies and differences become clear. In agreement with the electron micrographs published by Becker,[12] the aggregates have a homogeneous density distribution. However, we could not recover a monomer addition mechanism as was identified by Becker,[12] who retrieved this information from analytical gel filtration, which showed a decreasing amount of monomeric fibrinogen as time progressed.

The power law behavior of the correlation between the size and mass of the growing particles, which only became accessible with the time-resolved multiangle light scattering, revealed an additional significant insight into the self-assembly process. In all cases, an exponent close to 1/3 is observed, which for a given step-growth process indicates a structure with homogenous density for the growing particles.[19,26] The ratio of $\rho = R_g/R_h$ lying in the range of $0.8 > \rho > 0.5$ is in full agreement with growing particles having a homogeneous density and an exponent of 1/3. However, in case a step-growth process is carried out with sticky hard spheres as constituent units, fractals with an exponent for eq 10 of 1/2.05 are expected for the RLCA limit and 1/1.75 for the DLCA limit.[29] The fact that the exponent values in the present work are close to 1/3 and thus significantly smaller than 1/2 point to more homogeneous structures than anticipated for a process with sticky hard spheres. This supports the interpretation that the process follows a step-growth mechanism where the reacting particles coalesce rather than interconnect via sticky hard sphere sites. The shift of the power laws $R_g \sim M_w^{\alpha}$ toward lower values of M_w as the ionic strength of the hosting medium increases can be brought in line with the coalescence of particles by assuming the following scheme. The coalescing particles are formed of cross-linked fibrinogen fibrils establishing a network-like microgel. Aggregation induced at a lower ionic strength would then be based on the coalescence of microgel particles, which have a higher branching density. Scheme 1 illustrates this aspect schematically. To conclude, self-assembly process in thrombin-free solutions obeys a step-growth process based on the coalescence of particles. This strikingly differs from the mechanism of thrombin-catalyzed polymerization of fibrin, which forms protofibrils and stronger fibrils[30] first with cross-linking only occurring at later stages of the process.

■ ASSOCIATED CONTENT

Supporting Information

The Supporting Information is available free of charge on the ACS Publications website at DOI: 10.1021/acs.langmuir.9b01515.

Exemplary calculation of the ionic strength for a salt mixture, reproducibility of time-resolved light-scattering experiments at [NaCl] = 14 mM, weighted versus nonweighted model fits, characterization of the initial state of fibrinogen, mode analysis of DLS data during the aggregation process, fitting process of the sample with [I] =60 mM based on RLCA (PDF)

■ AUTHOR INFORMATION

Corresponding Author

*E-mail: klaus.huber@upb.de.

ORCID

Oliver Strube: 0000-0002-4357-8473

Klaus Huber: 0000-0001-7512-206X

DOI: 10.1021/acs.langmuir.9b01515
Langmuir 2019, 35, 12113−12122

Author Contributions

The manuscript was written through contributions of all authors. All authors have given approval to the final version of the manuscript.

Notes

The authors declare no competing financial interest.

■ REFERENCES

(1) Doolittle, R. F. Fibrinogen and Fibrin. *Annu. Rev. Biochem.* **1984**, *53*, 195−229.

(2) Weisel, J. W.; Litvinov, R. I. Mechanisms of Fibrin Polymerization and Clinical Implications. *Blood* **2013**, *121*, 1712−1719.

(3) Ferry, J. D.; Morrison, P. R. Preparation and Properties of Serum and Plasma Proteins. VIII. The Conversion of Human Fibrinogen to Fibrin under Various Conditions. *J. Am. Chem. Soc.* **1947**, *69*, 388−400.

(4) Carr, M. E.; Gabriel, D. A.; McDonagh, J. Influence of Ca2+ on the Structure of Reptilase-Derived and Thrombin-Derived Fibrin Gels. *Biochem. J.* **1986**, *239*, 513−516.

(5) Weisel, J. W.; Nagaswami, C. Computer Modeling of Fibrin Polymerization Kinetics Correlated with Electron Microscope and Turbidity Observations: Clot Structure and Assembly Are Kinetically Controlled. *Biophys. J.* **1992**, *63*, 111−128.

(6) Di Stasio, E.; Nagaswami, C.; Weisel, J. W.; Di Cera, E. Cl- Regulates the Structure of the Fibrin Clot. *Biophys. J.* **1998**, *75*, 1973−1979.

(7) Missori, M.; Papi, M.; Maulucci, G.; Arcovito, G.; Boumis, G.; Bellelli, A.; Amiconi, G.; De Spirito, M. Cl- and F- Anions Regulate the Architecture of Protofibrils in Fibrin Gel. *Eur. Biophys. J.* **2010**, *39*, 1001−1006.

(8) Kurniawan, N. A.; Peters, G. W. M.; Koenderink, G. H.; Rosalina, T. T.; van Kempen, T. H. S.; van de Vosse, F. N.; Vos, B. E.; Sonneveld, S.; Jansen, K. A. Buffers Strongly Modulate Fibrin Self-Assembly into Fibrous Networks. *Langmuir* **2017**, *33*, 6342−6352.

(9) Gollwitzer, R.; Bode, W.; Karges, H. E. On The Aggregation of Fibrinogen Molecules. *Thromb. Res.* **1983**, *29*, 41−53.

(10) Kim, S. H.; Haimovich-Caspi, L.; Omer, L.; Yu, C. M.; Talmon, Y.; Wang, N. H. L.; Franses, E. I. Stability and State of Aggregation of Aqueous Fibrinogen and Dipalmitoylphosphatidylcholine Lipid Vesicles. *Langmuir* **2007**, *23*, 5657−5664.

(11) Steven, F. S.; Griffin, M. M.; Brown, B. S.; Hulley, T. P. Aggregation of Fibrinogen Molecules by Metal Ions. *Int. J. Biol. Macromol.* **1982**, *4*, 367−369.

(12) Becker, C. M. Bovine Fibrinogen Aggregates: Electron Microscopic Observations of Quasi-Globular Structures. *Thromb. Res.* **1987**, *48*, 101−110.

(13) Guinier, A. *Small-Angle Scattering of X-rays*; John Wiley & Sons, Inc., 1955.

(14) Berry, G. C. Thermodynamic and Conformational Properties of Polystyrene. I. Light-Scattering Studies on Dilute Solutions of Linear Polystyrenes. *J. Chem. Phys.* **1966**, *44*, 4550−4564.

(15) Scheraga, H. A.; Laskowski, M. The Fibrinogen-Fibrin Conversion. *Adv. Protein Chem.* **1957**, *12*, 1−131.

(16) Koppel, D. E. Analysis of Macromolecular Polydispersity in Intensity Correlation Spectroscopy: The Method of Cumulants. *J. Chem. Phys.* **1972**, *57*, 4814−4820.

(17) Burchard, W. Static and Dynamic Light Scattering from Branched Polymers and Biopolymers. *Adv. Polym. Sci.* **1983**, *48*, 1−124.

(18) Schmidt, M. Combined Integrated and Dynamic Light Scattering by Poly(Γ-Benzyl Glutamate) in a Helicogenic Solvent. *Macromolecules* **1984**, *17*, 553−560.

(19) Liu, J.; Rieger, J.; Huber, K. Analysis of the Nucleation and Growth of Amorphous CaCO by Means of Time-Resolved Static Light Scattering Analysis of the Nucleation and Growth of Amorphous CaCO 3 by Means of Time-Resolved Static Light Scattering. *Langmuir* **2008**, 8262.

(20) Nečas, D.; Klapetek, P. Gwyddion: An Open-Source Software for SPM Data Analysis. *Cent. Eur. J. Phys.* **2012**, *10*, 181−188.

(21) von Smoluchowski, M. Versuch Einer Mathematischen Theorie Der Koagulationskinetik Kolloider Lösungen. *Z. Phys. Chem.* **1918**, *92*, 129−168.

(22) Modler, A. J.; Gast, K.; Lutsch, G.; Damaschun, G. Assembly of Amyloid Protofibrils via Critical Oligomers — A Novel Pathway of Amyloid Formation. *J. Mol. Biol.* **2003**, *2836*, 135−148.

(23) Carrotta, R.; Manno, M.; Bulone, D.; Martorana, V.; San Biagio, P. L. Protofibril Formation of Amyloid β-Protein at Low PH via a Non-Cooperative Elongation Mechanism. *J. Biol. Chem.* **2005**, *280*, 30001−30008.

(24) Lederer, K.; Hammel, R. Größe Und Gestalt Des Fibrinogenmoleküls, 2. Röntgenkleinwinkelstreuung an Verdünnten Lösungen. *Makromol. Chem.* **1975**, *176*, 2619−2639.

(25) Palmer, G. R.; Fritz, O. G.; Hallett, F. R. Quasielastic Light-Scattering Studies on Human Fibrinogen and Fibrin. I. Fibrinogen. *Biopolymers* **1979**, *18*, 1647−1658.

(26) Liu, J.; Pancera, S.; Boyko, V.; Shukla, A.; Narayanan, T.; Huber, K. Evaluation of the Particle Growth of Amorphous Calcium Carbonate in Water by Means of the Porod Invariant from SAXS. *Langmuir* **2010**, *26*, 17405−17412.

(27) Flory, P. J. The Configuration of Real Polymer Chains. *J. Chem. Phys.* **1949**, *17*, 303−310.

(28) Saha, S.; Springer, S.; Schweinefuß, M. E.; Pontoni, D.; Wiebcke, M.; Huber, K. Insight into Fast Nucleation and Growth of Zeolitic Imidazolate Framework-71 by in Situ Time-Resolved Light and X-Ray Scattering Experiments. *Cryst. Growth Des.* **2016**, *16*, 2002−2010.

(29) Weitz, D. A.; Huang, J. S.; Lin, M. Y.; Sung, J. Limits of the Fractal Dimension for Irreversible Kinetic Aggregation of Gold Colloids. *Phys. Rev. Lett.* **1985**, *54*, 1416−1419.

(30) Janmey, P. A.; Bale, M. D.; Ferry, J. D.; Erdile, L. Kinetics of Fibrin Oligomer Formation Observed by Electron Microscopy. *Biochemistry* **1983**, *22*, 4336−4340.

DOI: 10.1021/acs.langmuir.9b01515
Langmuir 2019, 35, 12113−12122

Supporting Information

Self-Assembly of Fibrinogen in Aqueous, Thrombin Free Solutions of Variable Ionic Strength

Benjamin Hämisch,[†] *Anne Büngeler,*[‡] *Charlotte Kielar,*[§] *Adrian Keller,*[§] *Oliver Strube*[‡], *Klaus Huber,*[*, †]

[†]Physical Chemistry, Paderborn University, 33098 Paderborn, Germany

[‡]Biobased and Bioinspired Materials, Paderborn University, 33098 Paderborn, Germany

[§]Technical and Macromolecular Chemistry, Paderborn University, 33098 Paderborn, Germany

Author Information:

Corresponding Author *Email: klaus.huber@upb.de

This document consists of 12 pages, 6 figures and 5 tables.

This material is available free of charge via the internet at http://pubs.acs.org.

S1. Exemplary calculation of the ionic strength for a salt mixture

According to the data sheet provided by the supplier the used sodium phosphate buffer solution contains 60 mM Na_2HPO_4 and 440 mM NaH_2PO_4. Thus, the ionic strength of the given solution is:

$$I = \frac{1}{2}(60\ mM \cdot 2^2 + 120\ mM \cdot 1^2 + 440\ mM \cdot 1^2 + 440\ mM \cdot 1^2) = 620\ mM \quad \text{(S1)}$$

After diluting a starting solution of fibrinogen tenfold, it has an ionic strength of 14 mM stemming from the NaCl content. The solution for dilution contains NaCl and sodium phosphate buffer with appropriate proportion to reach the desired ionic strength of the final solution in which aggregation is analysed. Accordingly, for the final fibrinogen solution with [I] = 60 mM and [I_{Ph}] = 30 mM, the solution for dilution requires an ionic strength contributions of 10/9*16 mM from NaCl and 10/9*30 mM from the sodium phosphate solution with the factor 10/9 taking into account the dilution. Therefore, one mL of the sodium phosphate solution was diluted with 17.6 mL water, leading to an ionic strength of 620 mM/18.6 = 33.3 mM. NaCl was then added to this solution until a concentration of 17.78 mM is reached.

S2. Reproducibility of time-resolved light scattering experiments at *[NaCl]* = 14 mM

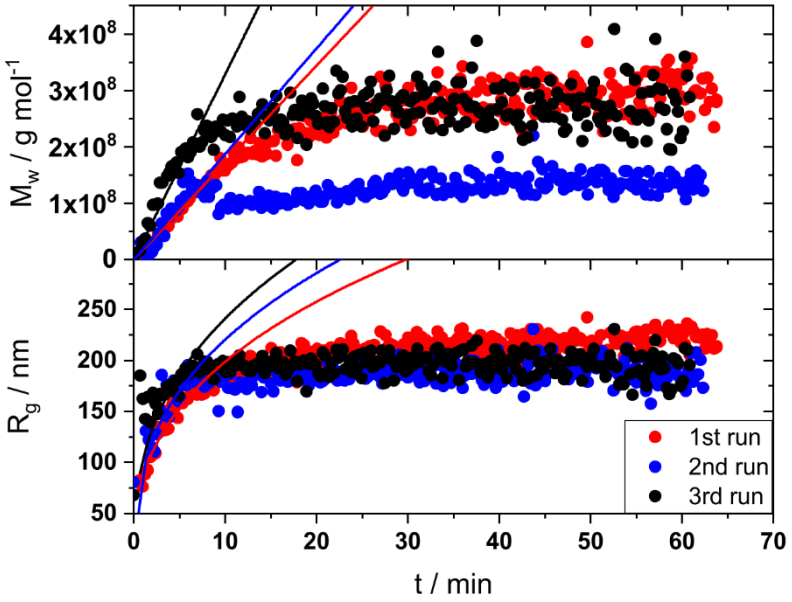

Figure S1. Evolution of the weight averaged molar mass M_w (top) and the radius of gyration R_g (bottom) as a function of time for three independent runs at a final ionic strength of *[NaCl]* = 14 mM. The 1st run is the one shown in the manuscript.

Table S1. Obtained coagulation times from the fits shown in Figure S1.

Sample	t_c / min M_w-data	t_c / min R_g-data
[I] = 14 mM – 1st run	0.021 ± 0.001	0.015 ± 0.001
[I] = 14 mM – 2nd run	0.035 ± 0.003	0.019 ± 0.001
[I] = 14 mM – 3rd run	0.039 ± 0.002	0.025 ± 0.001
Average	0.032 ± 0.008	0.02 ± 0.004

S3. Weighted versus non-weighted model fits

Table S2. Fits to M_w-data measured at an ionic strength of 60 mM at variable contribution from the phosphate buffer $[I_{ph}]$.

$[I_{ph}]$ / mM	t_c / min	z	t_c / min $\chi^2_{reduced}$	z $\chi^2_{reduced}$	χ^2	$\chi^2_{reduced}$
eq 15, 0 < t < 80 min (route 1)						
45	31.7 ± 0.14	2.25	80.2	3.9	9.69E11	20.7
30	43.6 ± 0.2	2.41	94	3.9	4.8E11	6.4
0	159 ± 0.3	5.8	120	4.6	2.38E11	29.4
eq 16, 0 < t < 30 min (route 2)						
	C / min		C / min $\chi^2_{reduced}$		χ^2	$\chi^2_{reduced}$
45	12.7 ± 0.07		12.9		2.98E10	8.9
30	14.7 ± 0.16		15.1		4.29E10	6.2
0	15.7 ± 0.16		15.3		3.85E10	91.7
eq 15, 30 < t < 80 min (route 2)						
	t_c / min	z	t_c / min $\chi^2_{reduced}$	z $\chi^2_{reduced}$	χ^2 [a)]	$\chi^2_{reduced}$
45	31.5 ± 0.4	1.17	44.6	1.41	1.39E12	4.9
30	36.5 ± 0.4	1.29	52.6	1.6	7.4E12	3.8
0	114.8 ± 0.5	4.25	234.9	6.3	3.87E11	34.2

[a)] The values of χ^2 refer to the entire time regime including the fit with eq 16, 0 < t < 30 min.

Alternatively to the non-weighted fit a weighted fit was applied to the data recorded at an ionic strength of 60 mM, which minimizes

$$\chi^2_{reduced} = \frac{1}{n}\sum_{i=1}^{n}\frac{(O_i - C_i)^2}{\sigma_i^2} \qquad \text{(S2)}$$

with n the number of data points, O_i the observed value of data point i, C_i the value calculated from the fit for that data point and σ_i the experimental uncertainty of O_i from SLS data evaluation.

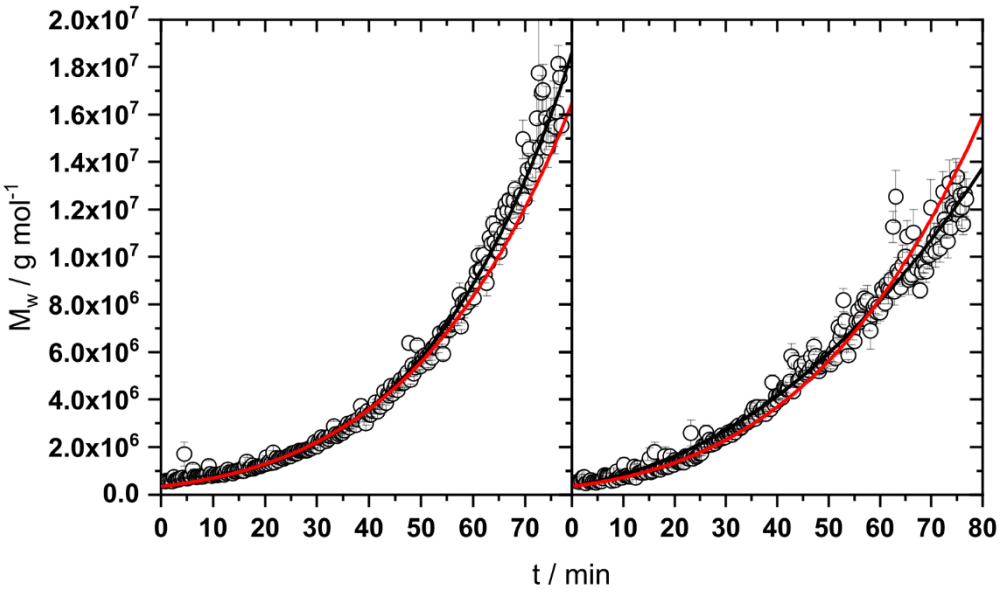

Figure S2. Non-weighted fit versus weighted fit based on eq 15 to the evolution of the weight averaged molar mass M_w of growing fibrinogen aggregates as a function of time *t* at 0 mM phosphate buffer (left) and 30 mM phosphate buffer (right). The curves represent non-weighted fits (black curves) and weighted fits with minimizing $\chi 2_{reduced}$ (red curves). The corresponding fit parameters can be found in Table S2.

S4. Characterization of the initial state of fibrinogen

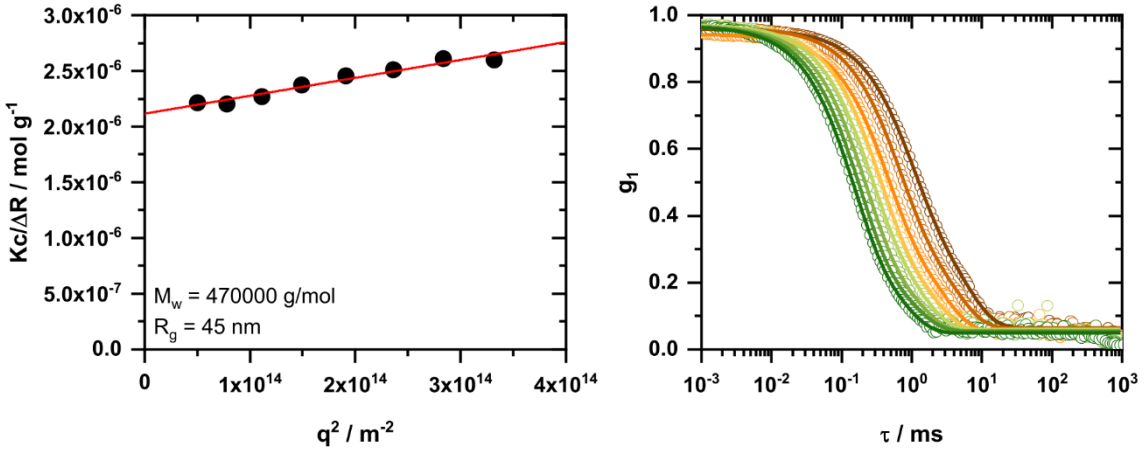

Figure S3. Data evaluation of static (left) and dynamic (right) light scattering of the initial stage prior to dilution of the sample with *[I]* = 30 mM and $[I_{ph}]$ = 0 mM. The autocorrelation function g_1 was fitted with eq S3.

Table S3. Characterization of all starting solutions prior to dilution by SLS/DLS.

Sample	M_w / 10^5 g mol^{-1}	R_g / nm	R_h / nm
[I] = 7 mM	5.3 ± 0.04	45.4 ± 1.3	18.1 ± 0.8
[I] = 14 mM	4.4 ± 0.09	56.2 ± 7	16.3 ± 0.7
[I] = 30 mM ; $[I_{Ph}]$ = 0 mM	4.7 ± 0.06	45 ± 2.1	18.6 ± 0.8
[I] = 30 mM ; $[I_{Ph}]$ = 7.5 mM	2.7 ± 0.08	48.5 ± 4.5	19.7 ± 1.3
[I] = 30 mM ; $[I_{Ph}]$ = 15 mM	4.2 ± 0.16	34.8 ± 8	18.9 ± 0.6
[I] = 60 mM ; $[I_{Ph}]$ = 0 mM	5 ± 0.05	44.7 ± 1.7	18.4 ± 1.4
[I] = 60 mM ; $[I_{Ph}]$ = 30 mM	3.1 ± 0.09	45.7 ± 5.3	18.7 ± 0.9
[I] = 60 mM ; $[I_{Ph}]$ = 45 mM	2.9 ± 0.04	45.3 ± 2.7	17.9 ± 0.9
[I] = 100 mM	3.1 ± 0.15	44.2 ± 8.9	15.5 ± 0.8

The characterization of DLS-data prior to dilution, shown in Figure S3 (right), revealed a second mode in addition to the diffusive mode of the monomer. In order to quantify the two modes, a biexponential fit was applied:

$$g_1(\tau, q) = a + b_{mon}\mathrm{e}^{\Gamma_{mon}\tau} + b_{agg}e^{\Gamma_{agg}\tau} \quad \text{(S3)}$$

In eq S3 the parameter a describes the incoherent background, b_i represent the intensity-weighted weighing factor and Γ_i is the corresponding inverse relaxation time of mode i. The calculated hydrodynamic radii for the aggregate mode and the monomer mode for all investigated samples can be found in Table S4.

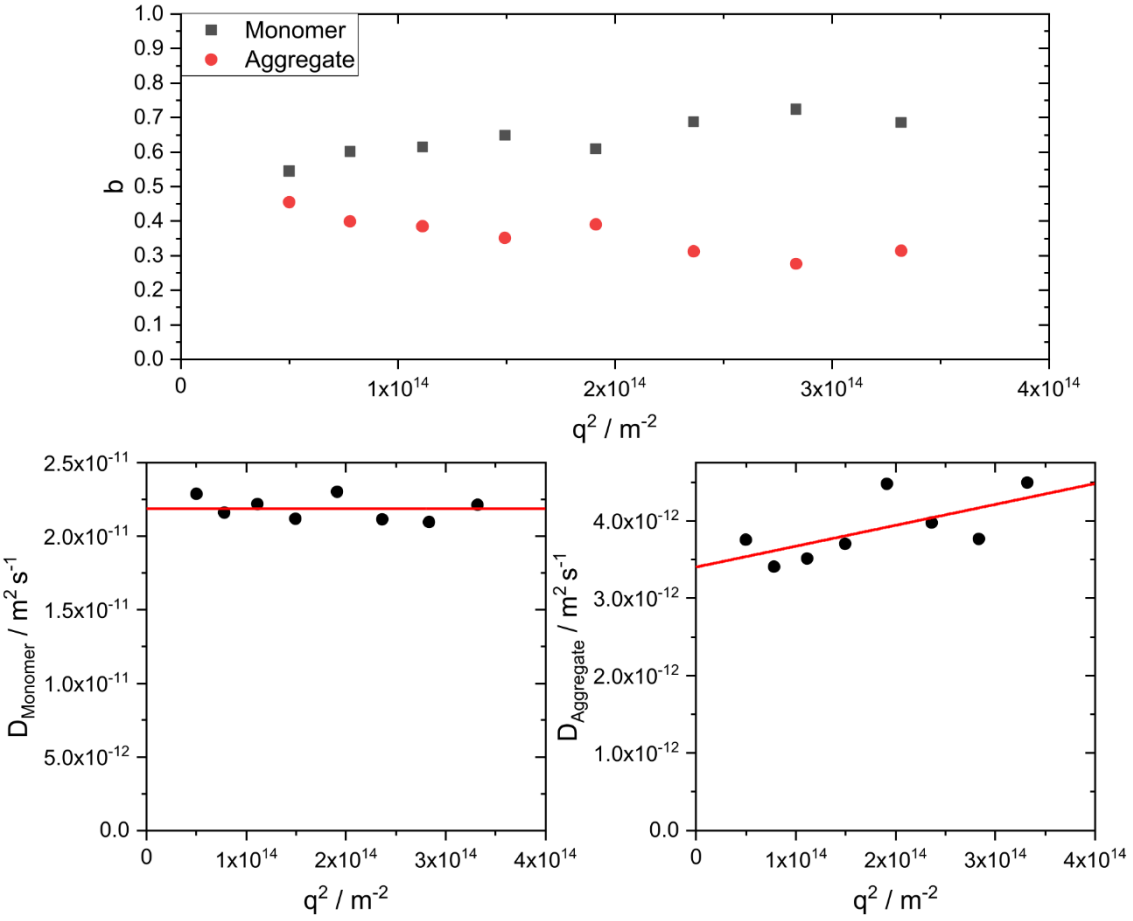

Figure S4. A: Intensity-weighted weighing factors b_i from the fit shown in Figure S3 (right) for the sample with *[I]* = 30 mM and $[I_{Ph}]$ = 0 mM. B and C show the diffusive modes obtained from the biexponential fit. The monomer mode (left) is angular independent whereas the aggregate mode (right) shows an angular dependency.

Table S4. Characterization parameters of the monomer and aggregate mode obtained by the procedure shown in Figure S4.

Sample	$D_{Monomer}$ / 10^{-11} m^2 s^{-1}	$R_{h,Monomer}$ / nm	$R_{h,Aggregate}$ / nm
[I] = 7 mM	2.06 ± 0.01	11.81 ± 0.1	68.36 ± 2.3
[I] = 14 mM	2.06 ± 0.03	11.81 ± 0.2	69.84 ± 3.2
[I] = 30 mM ; $[I_{Ph}]$ = 0 mM	2.18 ± 0.03	11.2 ± 0.1	59.33 ± 2
[I] = 30 mM ; $[I_{Ph}]$ = 7.5 mM	2.08 ± 0.04	11.72 ± 0.2	63.24 ± 2.8
[I] = 30 mM ; $[I_{Ph}]$ = 15 mM	2 ± 0.04	12.18 ± 0.2	66.83 ± 1.6
[I] = 60 mM ; $[I_{Ph}]$ = 0 mM	2.02 ± 0.04	12.07 ± 0.2	74.86 ± 4
[I] = 60 mM ; $[I_{Ph}]$ = 30 mM	2.22 ± 0.04	10.98 ± 0.2	48.42 ± 1.1
[I] = 60 mM ; $[I_{Ph}]$ = 45 mM	2.08 ± 0.03	11.71 ± 0.2	63.34 ± 2.2
[I] = 100 mM	2.04 ± 0.04	11.93 ± 0.2	64.87 ± 5.3
Average	2.08 ± 0.07	11.7 ± 0.4	64.3 ± 7

S5. Mode analysis of DLS data during the aggregation process.

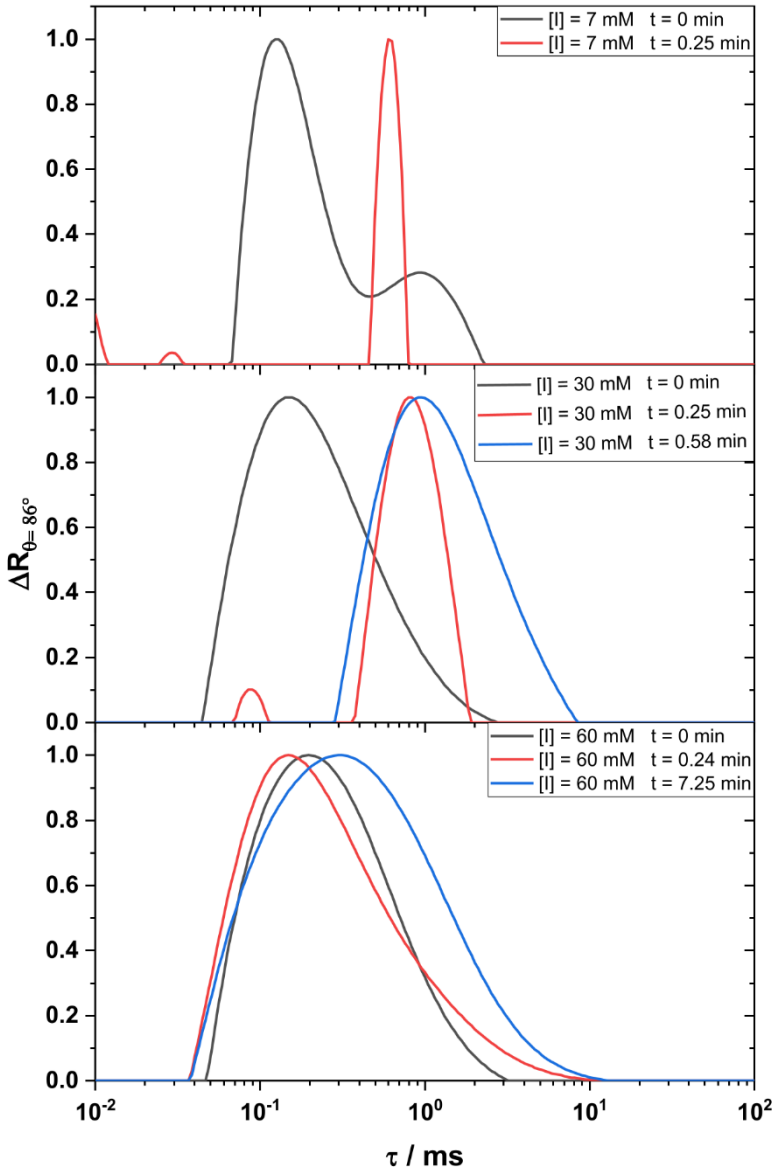

Figure S5. Results of a Contin analysis[1] of three solutions with different ionic strengths and $[I_{Ph}]$ = 0 mM measured at θ = 86°. Black lines indicate the state prior to induction of aggregation (t = 0 min). All other data refer to states after induction of aggregation with the times indicated in the legend. At ionic strengths equal or lower than 30 mM, the monomer mode ($\tau \sim 0.2$ ms) vanishes immediately after dilution. At an ionic strength of 60 mM the process is further slowed down which results in a broad distribution. The extent of aggregation prior to induction of the assembly process (t = 0 min) is noticeable in the regime of $\tau \sim 1$ ms.

S6. Fitting process of the sample with *[I]* = 60 mM based on RLCA.

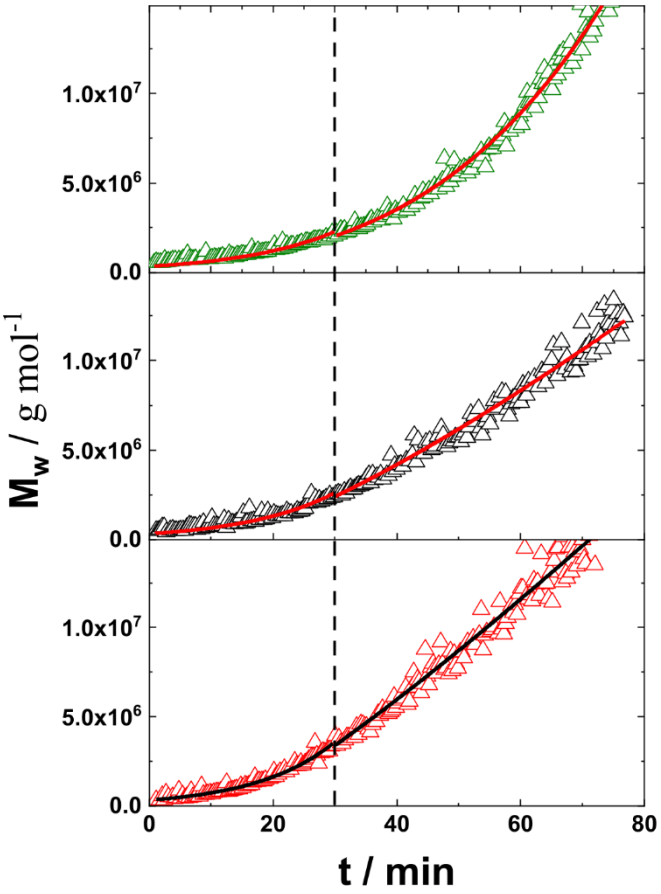

Figure S6. Evolution of the weight averaged molar mass M_w of growing fibrinogen aggregates as a function of time t. All data have an ionic strength of 60 mM but vary in the contribution of the phosphate buffer: 0 mM (green triangles), 30 mM (black triangles) and 45 mM (red triangles). The lines represent fits based on route 2. The transition point at t_t = 30 min marked with the dashed vertical line separates an RLCA approach (eq 16) from a modified von Smoluchowski approach (eq 15) (**Table S5**).

Table S5. Fits to data measured at an ionic strength of 60 mM at variable content of phosphate buffer I_{ph}. The transition point is set to t_t = 30 min.

I_{ph} / mM	t_c / min M_w-data	t_c / min R_g-data	z M_w-data	χ^2 M_w-data
eq 15, 0 < t < 80 min				
45	31.7 ± 0.14	31.4 ± 0.8	2.25	9.69E11
30	43.6 ± 0.2	41.8 ± 0.5	2.41	4.8E11
0	159 ± 0.3	166 ± 0.8	5.8	2.38E11
eq 15, 0 < t < 30 min				
45	247.4 ± 110.4		10.7 ± 4.3	2.82E10
30	63.8 ± 20.3		2.96 ± 0.71	3.62E10
0	19.4 ± 3.8		1.25 ± 0.14	1.82E10
eq 16, 0 < t < 30 min				
	C / min M_w-data	C / min R_g-data		
45	12.7 ± 0.07	12.2 ± 1.5		2.98E10
30	14.7 ± 0.16	13.8 ± 0.7		4.29E10
0	15.7 ± 0.16	17.9 ± 0.7		3.85E10
eq 15, 30 < t < 80 min				
	t_c / min M_w-data	t_c / min R_g-data	z	χ^2 M_w-data[a)]
45	31.5 ± 0.4	28.9 ± 0.4	1.17	1.39E12
30	36.5 ± 0.4	34.9 ± 0.6	1.29	7.4E11
0	144.8 ± 0.5	144 ± 0.9	4.25	3.87E11

[a)] The values of χ^2 refer to the entire time regime including the fit with eq 16, 0 < t < 30 min.

REFERENCES

(1) Provencher, S. W. CONTIN: A General Purpose Constrained Regularization Program for Inverting Noisy Linear Algebraic and Integral Equations. *Comput. Phys. Commun.* **1982**, *27* (3), 229–242. https://doi.org/10.1016/0010-4655(82)90174-6.

5. Mechanism and equilibrium thermodynamics of H- and J-aggregate formation from pseudo isocyanine chloride in water

Reproduced from *Soft Matter*, **2021**, *17*, 8140-8152 with permission from the Royal Society of Chemistry.

DOI: 10.1039/d1sm00979f

Soft Matter

PAPER

View Article Online
View Journal

Check for updates

Cite this: DOI: 10.1039/d1sm00979f

Mechanism and equilibrium thermodynamics of H- and J-aggregate formation from pseudo isocyanine chloride in water†

Benjamin Hämisch and Klaus Huber *

Pseudo isocyanine chloride (PIC) has a strong tendency to self-assemble with a concentration dependent temperature threshold separating a regime with small H-oligomers in equilibrium with monomeric PIC from a regime where large J-aggregates form. In complementing the known set of absorption spectra by the spectrum of a trimer, which represents all H-aggregates with $N \geq 3$, a full description of the sample composition of PIC in the regime of oligomers became possible by means of UV-vis spectroscopy and gave access to the equilibrium thermodynamics of oligomerisation. Successful interpretation of the concentration dependent temperature threshold as a ceiling temperature of J-aggregation made also accessible equilibrium thermodynamics of the formation of J-aggregates together with a full analysis of composition also in the regime of J-aggregates. Evolution of an invariant spectrum for the J-aggregates demonstrates full consistency of the composition analysis. Complementary light scattering experiments led to a comprehensive characterisation of all aggregate species above and below the aggregation threshold. Once initiated, J-aggregates always grow to a final length of 650 nm. Time-resolved light scattering confirmed that the self-assembly of J-aggregates follows a monomer addition process in analogy to a chain growth in polymer chemistry. Initiation and growth of individual aggregates turned out to be always much faster than the progress of aggregation.

Received 1st July 2021,
Accepted 22nd July 2021

DOI: 10.1039/d1sm00979f

rsc.li/soft-matter-journal

Introduction

Cyanine based dyestuffs are able to self-assemble into supramolecular structures under appropriate conditions. Jelley[1,2] observed a sharp absorption band and a sharp fluorescence band for the dyestuff 1,1′-diethyl-2,2′-cyanine chloride (PIC). The absorption and fluorescence band only occurred below a certain temperature threshold, which decreases with increasing dyestuff concentration. Scheibe *et al.*[3–5] attributed the sharp absorption band to supramolecular structures, formed from PIC monomers. Those structures are commonly called J- or Scheibe-aggregates in honor of its discoverers. Temperature induced changes in the absorption pattern of PIC were observed even above the threshold where J-aggregates are forming and were attributed to small oligomers denoted as H-aggregates.[6] Whereas the sharp absorption peak of J-aggregates shows a hypsochromic shift with respect to the monomer spectrum, the signature of H-aggregates is a bathochromic shift.[7] The majority of publications on the topic focuses on the optical behaviour of the molecules and on the supramolecular structure of J-aggregates, with the structural model consisting of six double-stranded chains derived from X-ray diffraction experiments proposed by von Berlepsch *et al.*[8,9] being the most recent one.

The tendency of PIC to form J-aggregates depends on the temperature and on the concentration of PIC, which makes a phase diagram a suitable way to represent the corresponding correlations. Fig. 1 shows such phase diagrams of PIC in pure water and in 0.01 M NaCl solution together with the chemical structure of PIC. Addition of sodium chloride leads to a shift of the phase boundary towards lower concentrations, as it was already observed by Jelley[1] in his pioneering works. States above the threshold correspond to mixtures of monomeric PIC and small oligomers of H-type. Efforts to describe these states above the aggregation threshold[6] by taking into account solely monomers and dimers did not lead to a conclusive interpretation of the experimental results. Cooper[10] mentioned the appearance of trimers and tetramers for the first time, which could be semi-quantitatively verified by the molecular excitonic model. Earlier light scattering on dilute solution of PIC suggests a maximum degree of oligomerization of $N = 4$.[11] However, the composition of solutions above the aggregation threshold shown in Fig. 1 and its variation with temperature and concentration of PIC is not yet known. This is partly due to the lack of a suitable spectrum characterizing the trimers.

Physical Chemistry, Paderborn University, 33098 Paderborn, Germany.
E-mail: klaus.huber@upb.de

† Electronic supplementary information (ESI) available. See DOI: 10.1039/d1sm00979f

This journal is © The Royal Society of Chemistry 2021

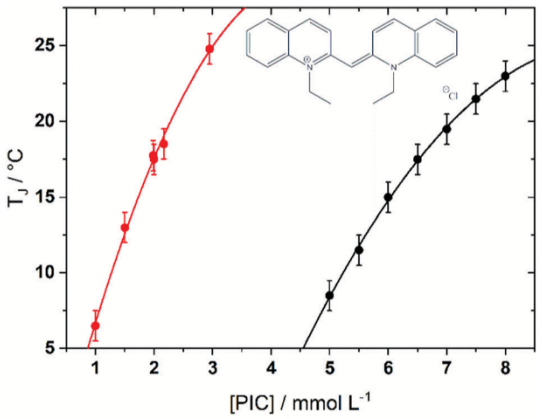

Fig. 1 Phase diagram of PIC in 0.01 M NaCl solution (red) and in aqueous solution (black) together with the chemical structure of PIC. The solid lines serve as a guide for the eye. Data points were generated by temperature dependent measurements of the absorption at $\lambda_{J\text{-Peak}}$ = 573 nm. The temperature at which absorption starts to increase is defined as the aggregation temperature T_J.

As soon as the phase boundary is surpassed, self-assembly of PIC to J-aggregates sets in, which is accompanied by a strong increase in light scattering intensity,[11,12] significant changes in UV-VIS spectra,[13] an emission of fluorescence light[10] and an increased viscosity.[14] A light scattering study in 0.01 M NaCl solution revealed formation of rod-shaped aggregates with a molar mass of 2.55 × 10^5 g mol^{-1} and a fibre length of around 600 nm in 0.01 M NaCl.[12] Daltrozzo *et al.*[15] presented a reaction enthalpy per mole of monomers for their transformation into the state of J-aggregates in water by treating J-aggregate formation as a precipitation process from supersaturated solution. In an effort to provide reference data for a study of the aggregation of PIC in the presence of macromolecular crowding, J-aggregate formation was successfully interpreted as a chain growth polymerisation similar to that found in anionic or radical polymerisation and revealed preliminary data on the equilibrium thermodynamics of J-aggregation.[16] No conclusive set of data exists on the extent of oligomerisation above the threshold of J-aggregate formation and on how this oligomerisation affects the equilibrium thermodynamics of J-aggregates and the underlying aggregation mechanism. Except for a first hint from experiments in 0.01 M NaCl,[12] which suggest a monomer addition process, the mechanism of J-aggregate formation is still awaiting its elucidation. Accordingly, the present study resolves the formation of H-oligomers above and below the threshold line of J-aggregation, complements preliminary thermodynamic data on the formation of J-aggregation and adds new insight on the formation mechanism of J-aggregates in water.

Whereas an analysis of the composition of PIC solutions above and below the threshold requires an in-depth investigation of PIC solutions with UV-vis spectroscopy further insight in the formation of J-aggregates can be expected from an application of multi-angle static (SLS) and dynamic (DLS) light scattering in a time-resolved mode. In short, the following route is pursued to shed further light on the mechanism and thermodynamics of self-assembly of PIC. Spectra from the anticipated species involved in the process are collected and if not yet existing, established in terms of molar extinction coefficients. This led to the spectrum of a trimer representing all oligomers equal to and larger than three monomers. With the spectra from the monomer, dimer and trimer available, the composition of PIC solutions above the threshold is analysed and the outcome successively applied to states below the threshold line resulting in a spectrum for the J-aggregates. Spectral decomposition above the concentration dependent temperature and interpretation of the threshold as a ceiling temperature of J-aggregation made also accessible the equilibrium thermodynamics of PIC self-assembly including the formation of linear J-aggregates. Having a full overview on the composition, time-resolved SLS and DLS is applied to investigate the process of nucleation and growth of the J-aggregates during temperature gradient and adds further information to the mechanism of the self-assembly process. In a previous publication we already showed the great potential of PIC being a protein substitute to mimic self-assembly of proteins under crowded conditions.[16] Therefore, a complete understanding of the mechanisms of H- and J-aggregate formation is also beneficial for using PIC as such a protein substitute.

Experimental section

Materials

1,1′-Diethyl-2,2′-cyanine iodide (PII) was received from Sigma Aldrich (Darmstadt, Germany). 1,1-Diethyl-2,2-cyanine chloride (PIC) with a molar mass of 362.9 g mol^{-1} was obtained from the iodide salt by ion exchange with use of the ion exchanger Amberlite IRA-402 from Sigma Aldrich (Darmstadt, Germany). The procedure of ion exchange is described elsewhere.[17] PIC was stored in the dark to prevent any decomposition. For all investigated samples, LC-MS grade water from Sigma Aldrich (Darmstadt, Germany) was used.

Sample preparation

Experiments were carried out in pure water. Stock solutions of PIC were made by dissolving the dyestuff in water overnight in the absence of light at 50 °C while stirring. The concentration of the stock solution of PIC was set to 7 mM. Lower concentrations were established by respective dilution of the stock solution and stirring at room temperature for at least one hour to ensure equilibrium.

UV-VIS experiments

Recordings of UV-VIS spectra were done with a Lambda-19 spectrometer by PerkinElmer (Waltham, USA). Wavelengths from 400 nm to 600 nm were covered with a scan rate of 60 nm min^{-1} at a slit width of 2 mm. A custom-built copper block was used as the sample holder, which was thermally

 This journal is © The Royal Society of Chemistry 2021

equilibrated by an external thermostat. Demountable cuvettes with a path length of 0.1 mm were used, provided by Hellma Analytics (Mühlheim, Germany). Prior to data accumulation, the cuvettes with samples were equilibrated in the cuvette holder for at least 20 minutes.

Light scattering experiments

Cylindrical quartz cuvettes with a diameter of 25 mm were used for light scattering experiments. They were cleaned by rinsing them with freshly distilled acetone from below for at least 10 minutes. Afterwards, the solutions were filtered directly into the cuvettes by means of PVDF-filters with a pore diameter of 0.22 μm from Millipore (Burlington, USA). Before placing the cuvettes in the goniometer bath, the outer surface of the cuvette were cleaned with an acetone-soaked paper towel.

Time dependent measurements were done with the CGS-3 device from ALV (Langen, Germany). This device is equipped with eight detectors, which are separated by $\Delta\Theta = 8^\circ$, resulting in an angular regime of $25^\circ \leq \Theta \leq 81^\circ$. A helium–neon laser with a wavelength of $\lambda = 633$ nm and a maximum power output of <35 mW was used as the light source. 900 measurements were carried out with a measuring time of 10 s for each data point and a lag-time between two measurements of roughly 10 s needed to adjust the attenuator. Aggregation was initiated by a temperature decrease, which was controlled by an external thermostat of the type F25 from Julabo (Seelbach, Germany). The temperature profile of the time-dependent cooling experiment was a temperature decrease from 25 °C to 16 °C during 5 hours.

Treatment of light scattering data

In static light scattering (SLS) experiments, the recorded scattering intensity is expressed as the excess Rayleigh ratio ΔR_θ of the solute

$$\Delta R_\theta = RR_{\theta,\mathrm{Std}}\left(\frac{r_{\theta,\mathrm{sol}} - r_{\theta,\mathrm{solv}}}{r_{\theta,\mathrm{std}}}\right) \quad (1)$$

with $RR_{\theta,\mathrm{Std}}$ the absolute Rayleigh ratio of toluene used as standard and with $r_{\theta,\mathrm{sol}}$, $r_{\theta,\mathrm{solv}}$ and $r_{\theta,\mathrm{std}}$ the measured scattering signal of the solution, the solvent, and toluene, respectively. Data evaluation was done with a series expansion of the Zimm approximation:[18]

$$\frac{Kc}{\Delta R_\theta} = \frac{1}{M_\mathrm{w}}\left(1 + \frac{q^2 R_\mathrm{g}^2}{3} + Bq^4\right) + 2A_2 c \quad (2)$$

In eqn (2), c is the concentration of PIC in solution, M_w is the weight averaged molar mass, R_g is the radius of gyration, Bq^4 is a term taking into account a curvature of the q^2-dependence and A_2 is the second osmotic virial coefficient. The latter is neglected since determination of A_2 during a time-dependent experiment is not possible. Nevertheless, neglection of A_2 is justified because experiments were conducted in highly diluted samples. The wave vector q is defined as follows

$$q = \frac{4\pi n}{\lambda_0}\sin\left(\frac{\theta}{2}\right) \quad (3)$$

with n being the refractive index of the solvent and λ_0 the laser wavelength in vacuum. The optical constant K is

$$K = \frac{4\pi n^2}{N_\mathrm{A}\lambda_0^4}\left(\frac{\mathrm{d}n}{\mathrm{d}c}\right)^2 \quad (4)$$

with $\mathrm{d}n/\mathrm{d}c = 6.15 \times 10^{-4}$ L g^{-1} the refractive index increment of PIC in aqueous solution.[11]

Dynamic light scattering (DLS) gives access to the field-time correlation function $g_1(\tau)$ which was either evaluated with a cumulant analysis[19] shown in eqn (5) or with a biexponential approach according to eqn (20) in case of data from the onset of aggregation.

$$\ln(g_1(\tau, q)) = C - \Gamma(q)\tau + \frac{\mu_2}{2\Gamma^2}\tau^2 \quad (5)$$

The initial slope of $\ln(g_1(\tau,q))$ gives the mean inverse relaxation time $\Gamma(q)$. Fitting was restricted to the section of g_1 with $g_1(\tau) > 0.3$.

The inverse relaxation time is proportional to the apparent diffusion coefficient $D_\mathrm{app} = \Gamma(q)/q$. A plot of D_app *versus* q^2 gives the z-averaged diffusion coefficient D_z according to eqn (6).

$$D_\mathrm{app} = D_z(1 + CR_g{}^2q^2 + k_\mathrm{D}c) \quad (6)$$

The constants C and k_D are the proportionality factors for the angular and concentration dependency, respectively. The concentration dependency is neglected, as has been done in case of the SLS-data.

The Stokes–Einstein equation[20] is used to obtain the hydrodynamically effective radius R_h, which represents the radius of a sphere with the same diffusion coefficient as the entities under consideration.

$$R_\mathrm{h} = \frac{kT}{6\pi\eta D_z} \quad (7)$$

In eqn (7), T is the temperature, k is the Boltzmann constant and η is the viscosity of the solvent at the temperature T.

Results and discussion

Procedure to decompose UV-Vis spectra of PIC

The procedure outlined in the following is used to describe the sample composition of PIC solutions above the threshold line limiting the formation of J-aggregates. It is assumed that only monomers, dimers and trimers are present in these "non-aggregated solutions" with the trimer representing all species with a degree of oligomerization of $N \geq 3$. Accordingly, UV-Vis spectra of PIC above the aggregation threshold can be described with eqn (8)

$$\frac{A_\mathrm{exp}(\lambda)}{d} = [\mathrm{M}]\cdot\varepsilon_\mathrm{M}(\lambda) + [\mathrm{D}]\cdot\varepsilon_\mathrm{D}(\lambda) + [\mathrm{T}]\cdot\varepsilon_\mathrm{T}(\lambda) \quad (8)$$

with [M], [D] and [T] the molar concentrations of monomers, dimers and trimers respectively. A_exp is the measured absorption, d is the path length and $\varepsilon_i(\lambda)$ are the molar extinction coefficients of monomers, dimers and trimers. The spectra are plotted in Fig. 2. Whereas the spectra of monomers and dimers are well established in literature,[6,21] spectra of trimers (or oligomers with $N \geq 3$) and of J-aggregates, expressed as molar extinction coefficients, are not yet available.

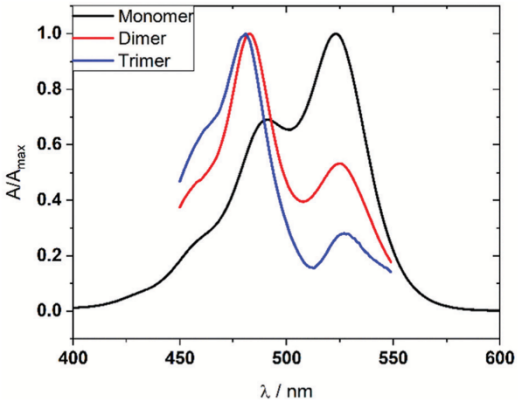

Fig. 2 Absorption spectra of different PIC species present in solution. The monomer spectrum (black) was measured at [PIC] = 3 μM, the dimer spectrum (red) was established by Horng *et al.*[21] Estimation of the trimer spectrum (blue) is carried out in the present work. The trimer spectrum refers to the minimum shown in Fig. 4A and is associated to K_T = 285 000 L^2 mol^{-2}.

The monomer spectrum of PIC is received by a measurement at a low concentration of [PIC] = 3 μM under the assumption that dimer formation according to the monomer–dimer equilibrium is negligible. With a dimerization constant K_D of 179 L mol^{-1} at 25 °C, published by Neumann and Pollmann,[13] the relative monomer content at [PIC] = 3 μM amounts to 99.9%. The dimer spectrum was determined by Horng *et al.*[21] based on the known monomer spectrum of PIC and a set of experimental data at different concentrations.

Determination of the trimer spectrum is outlined in the present work where it is carried out by making use of the known monomer and dimer spectrum[21] and of the dimerization constant K_D.[13] The equilibrium between monomers and dimers with the dimerization constant K_D = 179 L mol^{-1} at T = 25 °C is described with eqn (9).

$$K_D = \frac{[D]}{[M]^2} \Rightarrow [D] = 179\ \text{L mol}^{-1}\ [M]^2 \qquad (9)$$

Formation of trimers is based on the assumption that trimers result from three monomers only. The corresponding equilibrium between those two species can be stated as follows

$$K_T = \frac{[T]}{[M]^3} \Rightarrow [T] = K_T[M]^3 \qquad (10)$$

with K_T the trimerization constant.

Since J-aggregates are absent, the total concentration of PIC [PIC] is the sum of the concentration of monomers, dimers and trimers weighted with their degree of oligomerization.

$$[PIC] = [M] + 2[D] + 3[T] \Rightarrow \frac{[PIC] - [M] - 2[D]}{3} = [T] \qquad (11)$$

Substitution of eqn (9) and (10) into eqn (11) leads to an expression which enables the calculation of the concentration of monomers [M] at a given trimerization constant K_T.

$$\frac{[PIC] - [M] - 2 \times 179\ \text{L mol}^{-1}[M]^2}{3} = K_T \cdot [M]^3 \qquad (12)$$

The resulting value of [M] then allows the calculation of the respective concentration of dimers [D] and trimers [T] according to eqn (9) and (10). Such calculations are performed at variable K_T with K_T ranging from 80 000 L^2 mol^{-2} to 570 000 L^2 mol^{-2}. With the resulting [M] and [D] we are able to calculate a monomer and dimer contribution to the experimentally determined spectrum at the given K_T as follows. At a given K_T the monomer and dimer contributions are subtracted from the experimental spectrum according to eqn (13).

$$\frac{\frac{A_{exp}(\lambda)}{d} - \varepsilon_M(\lambda) \cdot [M] - \varepsilon_D(\lambda) \cdot [D]}{[T]} = \varepsilon_T(\lambda) \qquad (13)$$

The procedure was carried out in a joint mode with seven samples at 25 °C covering a concentration range from 4 mM to 7 mM. The trimer spectra resulting from averaging over all seven concentrations at each K_T respectively are shown in Fig. 3.

Trimer spectra with K_T being below 155 000 L^2 mol^{-2} exhibit negative values around λ = 515 nm and are therefore discarded. Two different parameters are then used to identify the optimum trimer spectrum. First, the standard deviation of the seven trimer spectra at a given K_T is calculated, as stated in eqn (14). With an appropriate value for K_T the trimer spectrum should be independent of the used concentration. Therefore, a low standard deviation indicates a suitable trimer spectrum.

$$\text{stddev}(\varepsilon_T, K_T) = \sum_{i=1}^{i=7} \sum_{\lambda=450nm}^{\lambda=549nm} \sqrt{\left(\varepsilon_{T,i}(\lambda, K_T) - \overline{\varepsilon_T}(\lambda, K_T)\right)^2} \qquad (14)$$

In eqn (14) and (15) the index i represents the seven concentrations. Second, the standard deviation of the differences between the respective model spectrum $A_{model,i}/d$, calculated according to eqn (8), and the corresponding

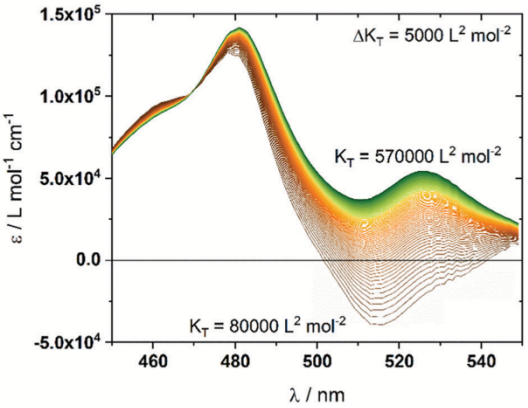

Fig. 3 Calculated mean trimer spectra according to eqn (13) based on a dataset of seven experimental spectra at 25 °C with 4 mM ≤ c(PIC) ≤ 7 mM. K_T ranges from 80 000 L^2 mol^{-2} to 570 000 L^2 mol^{-2} with ΔK_T = 5000 L^2 mol^{-2}.

 This journal is © The Royal Society of Chemistry 2021

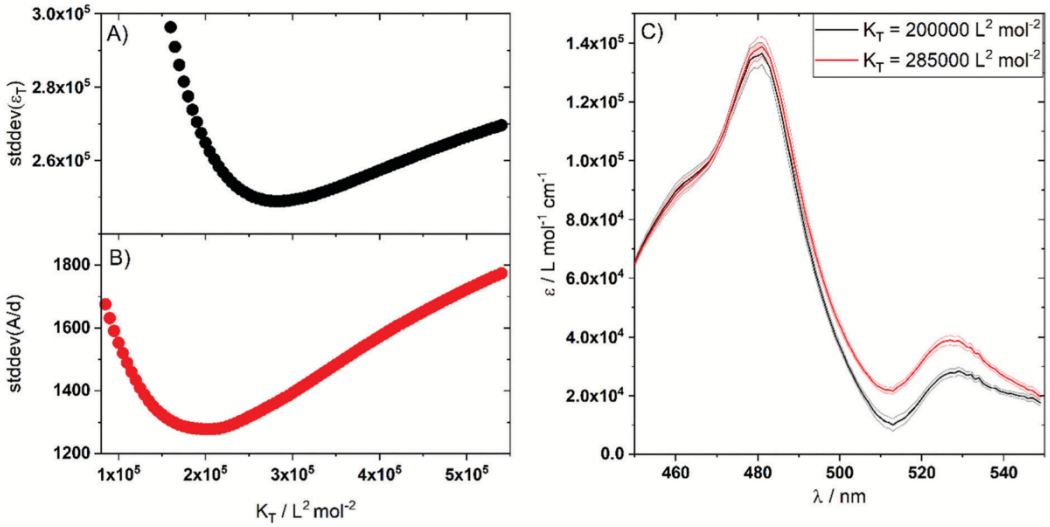

Fig. 4 (A) Standard deviation of the seven trimer spectra in dependence of K_T established with eqn (14). (B) The sum of standard deviations of the seven experimental spectra $A_{experiment,i}/d$ from the model function A_{model}/d established with eqn (15). (C) The two trimer spectra associated with the minima shown in (A) and (B).

experimental spectrum of all seven experiments is calculated at each K_T with eqn (15).

$$\mathrm{stddev}\left(\frac{A}{d}, K_T\right) = \sum_{i=1}^{i=7} \sum_{\lambda=450nm}^{\lambda=549nm} \sqrt{\left(\frac{A_{model,i}(\lambda, K_T)}{d} - \frac{A_{exp,i}(\lambda)}{d}\right)^2} \quad (15)$$

Both parameters are plotted in Fig. 4. The trimer spectrum optimized by eqn (14) is recovered at K_T = 285 000 L^2 mol^{-2}. The trimer spectrum optimized with eqn (15) result in K_T = 200 000 L^2 mol^{-2}. Both trimer spectra, shown in Fig. 4C, are used for further data evaluation and are handled as an upper and lower limit. Digitalized versions of the spectra are given in the ESI† (Section S1). Results which were established with the trimer spectra are then presented as averaged values of both limits throughout the present work.

The sample composition above the aggregation threshold

Having made available component spectra of monomers, dimers and trimers in the preceding section, we will first decompose UV-Vis spectra of PIC samples above the aggregation threshold. The procedure to determine sample compositions in the absence of J-aggregates will later be used to also estimate the composition of dyestuff species below the threshold of J-aggregate formation and, based on this, to develop a spectrum of J-aggregates.

Fig. 5A shows UV-Vis spectra of PIC in aqueous solution with a concentration of 4 mM at temperatures between 25 °C and 11 °C. There is a clear drop in the extinction coefficient at λ = 524 nm with decreasing temperature, which is ascribed to a decrease in monomer concentration since λ = 524 nm is the main peak in the monomer spectrum. Additionally, extinction at the shoulder at λ = 460 nm is increasing while dropping the temperature. Cooper[10] was able to predict the spectral shifts of oligomeric species of PIC with $N \leq 5$ with the molecular exciton model and assigned absorption in this shoulder region to oligomers with $N \geq 3$. Hence, a decrease in temperature leads to an accumulation of trimers.

The peak at λ = 483 nm, mainly representing dimeric species, does not change very much. Only a slight hypsochromic shift with decreasing temperature can be observed. Most likely, these changes can be ascribed to the accumulation of trimers with decreasing temperature, as the trimer spectrum (Fig. 2) also shows a hypsochromic shift with respect to the peak at λ = 483 nm of the dimer spectrum. Fig. 5B shows the standard deviation between experimental spectra and model spectra in dependence of the trimerization constant K_T established at eight different temperatures. A decrease in temperature is accompanied by a shift of the minima in standard deviation which indicates a temperature dependency of K_T. This aspect will be discussed later. At 25 °C the fit with the lowest standard deviation is achieved with K_T = 285 000 L^2 mol^{-2} which is exactly the value attributed to the used trimer spectrum and which underlines the consistency of our procedure.

The results of the analysis of sample composition at different temperatures is shown in Fig. 6A. The percentage of dimers appears to be insensitive to temperature, which results from the underlying model described by eqn (9) and (12) and the concentration regime under consideration. A plot of [D]/[PIC] *versus* [PIC] (see Section S2 of the ESI†) explains this feature as it exhibits an extremely broad maximum of [D]/[PIC] at a regime of 1 mM < [PIC] < 7 mM coinciding with the concentration regime used in the present work. Noteworthy, analysis of the composition along the threshold of Fig. 1 *via* the use of isotherms in Fig. 6A results in unique percentages of all three components within the temperature and concentration regime under consideration.

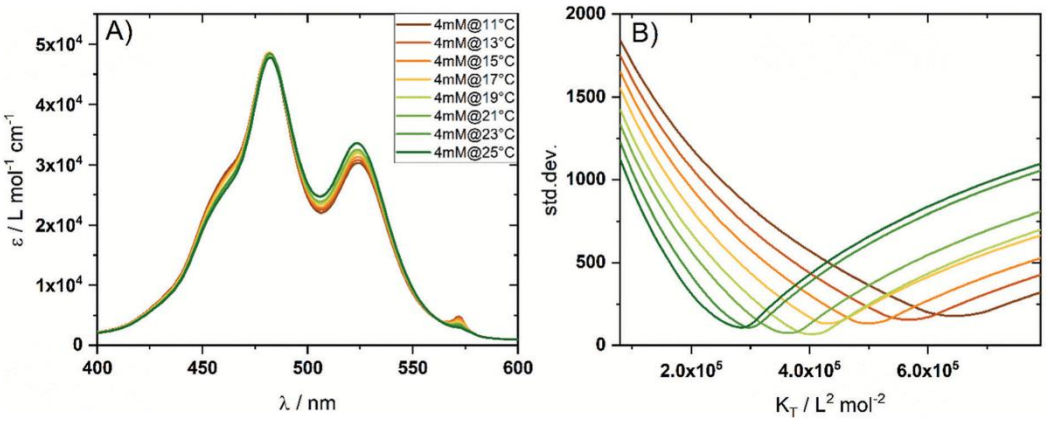

Fig. 5 (A) Extinction coefficients of PIC as a function of the wavelength in aqueous solution at [PIC] = 4 mM at temperatures between 25 °C and 11 °C with ΔT = 2 °C. (B) Resulting standard deviations between experimental spectra shown in (A) and model spectra as a function of the trimerization constant K_T. The model spectra were calculated with the trimer spectrum associated to K_T = 285 000 L^2 mol^{-2} (red curve in Fig. 4C).

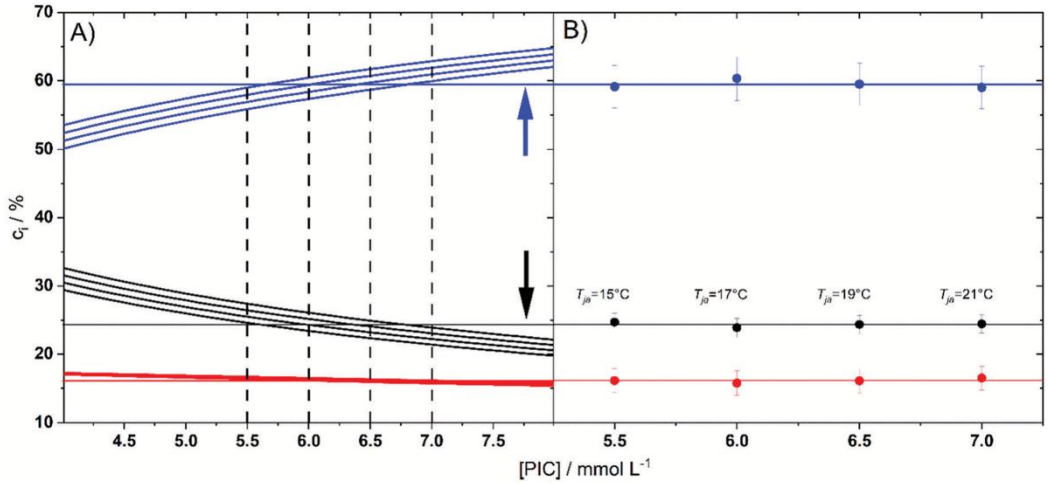

Fig. 6 (A) The dependence of the relative concentration of monomers (black), dimers (red) and trimers (blue) on the total concentration at a temperature of 15 °C, 17 °C, 19 °C and 21 °C calculated with eqn (9), (10) and (12). Arrows indicate how the relative concentrations of monomers (black) and trimers (blue) change with increasing temperature. Horizontal lines represent the relative concentrations determined at the aggregation threshold and the black dashed vertical lines are visual guidelines for the four investigated concentrations. (B) Relative concentrations of oligomeric species of PIC right at the aggregation threshold as a function of the total concentration. The threshold temperature for each data point is given in the plot.

The temperature dependence of K_T determined by the minimum of the standard deviation, as seen in Fig. 5B, makes possible the estimation of the standard enthalpy and entropy of trimerization according to eqn (16).

$$\ln(K_T) = -\frac{\Delta H_T^0}{RT} + \frac{\Delta S_T^0}{R} \qquad (16)$$

The fit shown in Fig. 7 gives $\Delta H_T^0 = -44.8\,\mathrm{kJ\,mol^{-1}}$ and $\Delta S_T^0 = -47\,\mathrm{J\,mol^{-1}\,K^{-1}}$. The results compare well with $\Delta H_T^0 = -40 \pm 8\,\mathrm{kJ\,mol^{-1}}$ and $\Delta S_T^0 = -87 \pm 2\,\mathrm{J\,mol^{-1}\,K^{-1}}$ based on an atomistic simulation by Wilson *et al.*[22] Neumann and Pollmann[13] investigated the thermodynamic parameters of the dimerization of PIC in aqueous solution and found $\Delta S_D^0 = -32.1\,\mathrm{J\,mol^{-1}\,K^{-1}}$ and $\Delta H_D^0 = -22.4\,\mathrm{kJ\,mol^{-1}}$. The standard enthalpy of trimerization is nearly two times larger than of the dimerization, which may be attributed to a larger amount of molecular surface involved in the contact of three PIC molecules as compared to dimers. The change in standard entropy lies within the same order of magnitude for both processes.

The ceiling temperature approach

The knowledge established on the composition of PIC above the aggregation threshold enables us to reconsider the self-assembly of PIC also at and below the aggregation threshold.

 This journal is © The Royal Society of Chemistry 2021

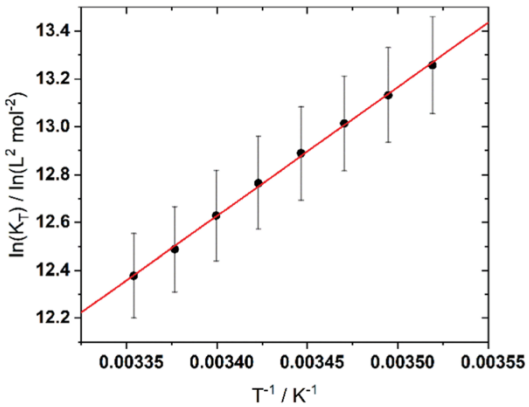

Fig. 7 The natural logarithm of the trimerization constant K_T as a function of T^{-1}. Values of K_T correlate with the minima in standard deviation shown in Fig. 5B. The dataset represents the average of K_T of all investigated concentrations. The red line is a linear fit according to eqn (16) with the y-offset being $-\Delta S_T^0/R$ and the slope being $-\Delta H_T^0/R$.

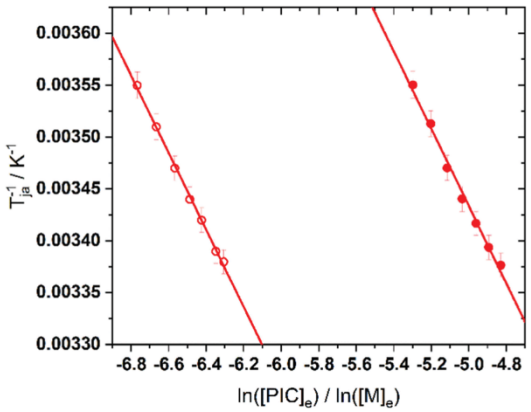

Fig. 8 Application of eqn (18) to the aggregation threshold in aqueous solution shown in Fig. 1. Red filled spheres were established by using the total concentration of PIC for $[PIC]_e$ while the red hollow spheres are based on the concentration of monomers in equilibrium $[M]_e$. Solid lines are linear fits where the slope is $R/\Delta H^0$ and the y-offset amounts to $\Delta S^0/\Delta H^0$.

To this end, it is assumed that decomposition of the oligomers into monomers, dimers and trimers below the aggregation threshold is governed by the same dimerization constant and trimerization constant as determined above the aggregation threshold. As already suggested in previous publications,[16,17] formation of J-aggregates follows a monomer addition process, in close analogy to a chain growth polymerisation in macromolecular chemistry. The equilibrium constant for a chain growth or aggregation *via* monomer addition is

$$K_J = \frac{1}{[PIC]_e} = \frac{e^{\left(-\frac{\Delta G_J^0}{RT_J}\right)}}{1\ \text{mol L}^{-1}} \quad (17)$$

with $[PIC]_e$ the equilibrium concentration of non-aggregated PIC. In the present work states of equilibria are located on the threshold shown in Fig. 1. An application of the ceiling temperature[23] enables calculation of the standard aggregation entropy ΔS^0 and standard aggregation enthalpy ΔH^0, as shown in eqn (18).

$$\frac{1}{T_J} = \frac{\Delta S^0}{\Delta H^0} + \frac{R \cdot \ln([PIC]_e)}{\Delta H^0} \quad (18)$$

This has already been done in a preceding publication,[17] where we recasted the aggregation threshold in aqueous solution from Fig. 1 into a representation obeying eqn (18). However, in that work it was assumed that all PIC molecules are involved in the self-assembly as monomers at the threshold. However, as it has just been established, dimers and trimers coexist above the aggregation threshold with monomers and it is not yet known whether oligomers and monomers or only monomers are involved in the chain growth. The latter would imply that oligomers establish a pool of inactive species, which have to dissociate to active monomers.

With the knowledge developed in the present work on the sample composition above (and at) the aggregation threshold, we are now able to refine that analysis. By taking into account that PIC decomposes into monomers, dimers and trimers and assuming further on that only monomers add to growing J-aggregates, the equilibrium concentration of PIC $[PIC]_e$ in eqn (18) has to be replaced by the equilibrium concentration of monomers $[M]_e$. The plots are shown in Fig. 8 and the resulting parameters are found in Table 1.

Table 1 Equilibrium constants for the self-assembly of PIC *via* monomer addition

Active monomer concentration	K_J (T = 25 °C)/ $L mol^{-1}$	ΔH^0/kJ mol^{-1}	ΔS^0/J mol^{-1} K^{-1}
$[PIC]_e$	118	−22.3 ± 0.9	−35.1 ± 2.2
$[M]_e$	522	−22.4 ± 0.5	−23 ± 1.2

Both datasets are parallel to each other indicating that ΔH^0 is the same for both datasets and amounts to −22.3 kJ mol^{-1}. This value compares with ΔH^0 = −31.2 kJ mol^{-1} established by Daltrozzo *et al.*[15] If all species existing above the threshold contribute directly to the elongation of the aggregate, the standard aggregation entropy ΔS^0 is −35 J mol^{-1} K^{-1}. By including just monomers, ΔS^0 reduces to −23 J mol^{-1} K^{-1}. However, as the arrangement of monomers in H-oligomers differ from that in the J-aggregate,[24] growth of J-aggregates by addition of monomers seems to be more plausible than the addition of monomers and oligomers. To conclude, eqn (17) and (18) make accessible an equilibrium constant for the formation of J-aggregates at variable temperatures.

The J-aggregate spectrum

In order to develop a J-aggregate spectrum in terms of a molar extinction coefficient, an estimation of the J-aggregate concentration at states where spectra get available is necessary. Having

established an equilibrium constant K_J for J-aggregate formation in the preceding section, we are now able to describe the sample composition not only above but also below the aggregation threshold. We only have to assume that the equilibrium constants for dimerization and trimerization developed above the threshold of J-aggregate formation are also valid throughout the regime where J-aggregates are formed. At a given temperature within this regime, the concentration of "non-J-aggregated" PIC, denoted as $[PIC]_{m,o}$, is determined by the equilibrium constants K_D, K_T and K_J at that given temperature. Further PIC being added beyond the threshold value is incorporated in J-aggregates and the concentration of J-aggregates is then the difference between the total concentration [PIC] and $[PIC]_{m,o}$. Decomposition of $[PIC]_{m,o}$ into the respective [M], [D] and [T] by means of the dimerization and trimerization constants determined above the aggregation threshold enables us to calculate the spectra of these oligomers. Subtraction of this monomer and oligomer contributions from the overall spectrum results in a residual, which can be attributed to the J-aggregates, the concentration of which is also known. This procedure has been repeated for five temperatures at 6 mM of PIC, two temperatures at 6.5 mM of PIC and four temperatures at 7 mM of PIC, resulting in eleven different spectra for J-aggregates. The J-aggregate spectra are presented in terms of molar extinction coefficients ε_J. It has to be stressed that ε_J refers to the concentration of PIC molecules incorporated in J-aggregates and not to the concentration of J-aggregates. Fig. 9 shows the averaged J-aggregate spectrum together with the monomer spectrum from Fig. 2 for comparison. All spectra used for forming the average shown in Fig. 9 can be found in the ESI† (Section S3). Overlay of all eleven spectra supports validity of the applied procedure.

The approach just described gives a J-aggregate spectrum in the wavelength regime of 450 nm $\geq \lambda \geq$ 550 nm. In order to extend that wavelength regime to get a full spectrum with the J-peak included, the following approach has been pursued (Fig. S6, ESI†). At first, the decay of the dimer and trimer spectrum at $\lambda \geq$ 550 nm was fitted with an exponential function to get an approximation of the extinction coefficient between 550 nm $\geq \lambda \geq$ 580 nm. Experimental spectra of samples well below the aggregation threshold were then corrected in this extended wavelength regime in terms of the contribution of oligomers/monomers. The resulting extensions of the spectrum were averaged, and the average was merged with the just determined section of the J-spectrum at $\lambda <$ 550 nm. The full spectrum is found in the ESI† (Section S1) in a digitalized format. Noteworthy, the molar extinction coefficient at the J-Peak amounts to ε_J(573 nm) = 250 000 ± 40 000 L mol^{-1} cm^{-1}, which is in good agreement with data from Kopainsky *et al.*[25]

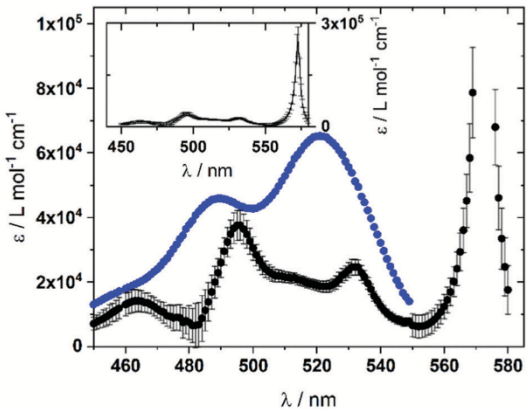

Fig. 9 Calculated averaged J-spectrum (black spheres) together with the monomer spectrum from Fig. 2 (blue spheres). The inlet shows the whole J-spectrum with the maximum of the J-peak at λ = 573 nm included.

Several attempts to establish a spectrum of pure J-aggregates have been already performed in the past. Scheibe mentioned that the absorption characteristics of J-aggregates are not only restricted to the J-Peak at λ = 573 nm pointing to a broad, weak absorption band at around λ = 515 nm.[26] Briggs approximated a bandshape function of monomers and of J-aggregates for a transition which is polarised parallel to the aggregate axis.[27] He observed a similar redshift of the absorption bands of the J-aggregate relative to the monomer band, as it can also be seen in Fig. 9. Neumann and Pollmann[13] provided a J-aggregate spectrum normalized to the J-peak by measuring a spectrum at high PIC concentration (c = 10 mmol L^{-1}) and low temperature (T = 12 °C) assuming that all PIC has been transferred to J-aggregates.

With the knowledge that the molar extinction coefficient of PIC aggregates at λ = 573 nm amounts to approximately 250 000 L mol^{-1} cm^{-1}, the normalized spectrum of Neumann and Pollmann[13] can be transferred to an absolute spectrum. Noteworthy, the resulting absolute spectrum exceeds the spectrum of the present work by a factor of two, if the regime of $\lambda <$ 550 nm is considered, suggesting that a portion of oligomers/monomers still contributes to their J-aggregate spectrum.

In order to further verify the validity of the J-spectrum and the procedure of determining concentrations of "non-J-aggregated" species and J-aggregates *via* the aggregation threshold, the following method has been applied. At first, a new dataset of UV-Vis spectra at three different concentrations of PIC at T = 10 °C has been measured to get new and independent spectra, not involved in the determination of the J-aggregate spectrum. The contribution of J-aggregates on experimental spectra was removed by subtracting the J-aggregate spectrum multiplied with its concentration established with eqn (17) and (18) at T = 10 °C. Since all three samples were measured at the same temperature at T = 10 °C, they all share the same point on the aggregation threshold. Thus, the three resulting excess spectra referring to the oligomer/monomer contribution should overlay. It is shown in the ESI† (Section S3) that indeed, all resulting excess spectra are identical. This perfect overlay does not only confirm consistency of the model introduced in the present work. It also indicates a bimodal nature of the composition below the aggregation threshold including monomers/oligomers as one species in addition to the J-aggregates as the second species, thus supporting a monomer addition process for the formation of J-aggregates.

This journal is © The Royal Society of Chemistry 2021

Temperature dependent dynamic and static light scattering

Static and dynamic light scattering has been carried out in order to gain further insight in the mechanism and kinetics of the J-aggregate formation. Data evaluation shall greatly benefit from the ability to analyse the composition of PIC solutions above and below the aggregation threshold.

The evolution of the weight averaged molecular mass M_w, the radius of gyration R_g and the hydrodynamic radius R_h is analysed during a cooling period with a temperature gradient of -0.03 °C min^{-1} for a PIC sample with [PIC] = 7 mM. As is outlined in Fig. 10, the experiment reveals three distinguishable regimes. (I) At temperatures above the aggregation threshold only small oligomers and monomers exist with the recorded molecular mass M_w constant and R_g and R_h smaller than the detection limit. (II) A decrease in temperature to and beyond a certain threshold triggers the formation of J-aggregates, which is accompanied by an increase in M_w by two orders of magnitude together with the appearance of measurable radii of gyration R_g and hydrodynamic radii R_h. Strikingly, R_g reaches a maximum of R_g = 185 nm at 20 °C and M_w reaches a plateau at slightly lower T. These trends may indicate the establishment of a gel network below T = 19 °C. Light scattering now probes mesh sizes and corresponding collective motions and not anymore individual J-aggregates. (III) At $T < 19$ °C, the increase in M_w levels off and R_g decreases.

In the temperature regime, where J-aggregates are absent, the experimentally determined weight averaged molar mass M_w is constant and amounts to an average of 890 ± 20 g mol^{-1}. Knowledge of $K_D(T)$ and $K_T(T)$ enables calculation of M_w in this regime, which results in M_w = 850 ± 70 g mol^{-1}. Both datasets are plotted in the inlet in Fig. 10 and overlay nicely within experimental uncertainty.

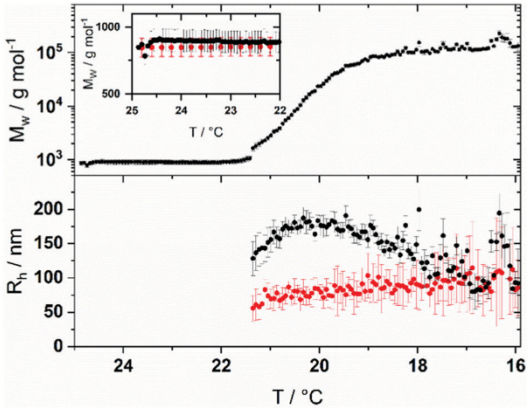

Fig. 10 Evolution of the mass weighed molecular weight M_w (top), the radius of gyration R_g (bottom, black spheres) and the hydrodynamic radius R_h (bottom, red spheres) of a sample with [PIC] = 7 mM while lowering the temperature from 25 °C to 16 °C during a time span of 5 hours. Inset: The weight averaged molecular mass M_w in the non-aggregated regime of the PIC sample (black data points) in comparison to data based on the equilibrium constants $K_D(T)$ and $K_T(T)$, which were used to calculate sample compositions (red data points).

At a threshold temperature of T = 21.4 °C formation of J-aggregates begins. As indicated by an increase in M_w, formation of J-aggregates progresses during the entire temperature gradient following the threshold. This trend shall be interpreted with $K_D(T)$, $K_T(T)$ and $K_J(T)$ established in the previous section of the present work.

In general, the scattering signal, expressed as $\Delta R = KcM_w$, is the sum of the scattering signals of all species present in solution. As a monomer addition process is suggested in preceding works,[12,17] we anticipate the M_w values to be determined by the contributions from monomeric and oligomeric PIC and from PIC J-aggregates, each weighted with its concentration. To simplify matters, we assume a binary system of monomers/oligomers and of J-aggregates. The underlying equation reads as follows:

$$\Delta R = \Delta R_{m,o} + \Delta R_J \quad (19a)$$

$$KcM_w = Kc_{m,o}M_{m,o} + Kc_JM_J \quad (19b)$$

Unfortunately, only the left-hand side of eqn (19a) and (19b) are known from experiment. However, a molar mass of J-aggregates can be estimated under the assumption that the scattering signal of J-aggregates is significantly larger than of the monomer/oligomer mixture. Therefore, at high enough J-aggregate concentrations, the scattering contribution of monomers/oligomers, $\Delta R_{m,o}$, can be neglected and eqn (19b) can be approximated as eqn (19c)

$$KcM_w \cong Kc_JM_J \quad (19c)$$

enabling us to extract M_J in case of known c_J. Neglect of the scattering contribution of the monomer/oligomer mixture in a temperature regime of $T < 20$ °C could indeed be confirmed by means of a temperature dependent composition of the scattering species given by the equilibrium constants $K_T(T)$, $K_D(T)$ and $K_J(T)$ (Fig. S6 in the ESI†). Therefore, the regime between 20 °C and 19 °C in Fig. 10 is most suitable for determining the molar mass of J-aggregates M_J. At 20 °C $< T <$ 19 °C values of $Kc/\Delta R$ are recalculated by replacing the total mass concentration c by the mass concentration of J-aggregates c_J. Determination of c_J is based on $K_T(T)$ and $K_D(T)$ and on correlating the temperature difference between a given threshold temperature and the actual temperature of the respective $\Delta R(T)$ value to a corresponding concentration difference [PIC] − [PIC]$_{m,o}$. The resulting [PIC] − [PIC]$_{m,o}$ can successively be transformed to the concentration of J-aggregates in g L^{-1} as c_J = ([PIC] − [PIC]$_{m,o}$)M_{PIC} with M_{PIC} = 363 g mol^{-1}. Several slightly different approaches are applied to determine a concentration c_J of J-aggregates.

In a first approach, c_J is determined from the aggregation threshold interpolated at [PIC] = 7 mM in the corresponding curve of Fig. 1. The as determined threshold temperature lies at T = 19.7 °C, being 1.7 °C lower than the one identified with the light scattering data from Fig. 10. This inevitably leads to unphysical molar mass values above T = 19.7 °C and induces a strong temperature dependent variation of those data immediately below T = 19.7 °C. Only at low enough temperatures,

molar mass values of J-aggregates approach a regime within 10^6 to 5×10^6 g mol^{-1}, with the actual value depending on the upper and lower error margin of the threshold temperature (see ESI,† Section S4). Mass values recovered from the threshold temperature in the curve of Fig. 1 approach a value of 2×10^6 g mol^{-1}, thus establishing a physically meaningful order of magnitude. Clearly, the actual choice of the threshold temperature determines the extent of the temperature dependence of mass values as well as the overall precision.

To overcome this problem, a slightly modified approach is applied. The temperature differences between threshold and actual temperature established from the experimental data in Fig. 10 are considered to have an acceptable precision independent of the actual location of the threshold curve. Therefore, the threshold line is shifted as a whole to integrate the threshold established by light scattering in Fig. 10, corresponding to a shift of 1.7 °C. The results are shown in Fig. 11, suggesting a molar mass of the J-aggregates close to 1×10^6 g mol^{-1}.

In a third approach, the aggregation threshold was shifted to the point where the standard deviation of the resulting molar masses of J-aggregates M_J in the regime of 20 °C < T < 19 °C adopts a minimum. This corresponds to a threshold temperature at [PIC] = 7 mM of T = 20.55 °C, corresponding to a shift of 0.85 °C. With this threshold value the molar mass of J-aggregates approaches $M_J = 1.48 \pm 0.07 \times 10^6$ g mol^{-1}.

Herzog *et al.*[12] found a value of $M_J = 2.55 \times 10^6$ g mol^{-1} together with a radius of gyration R_g = 200 nm in 0.01 M NaCl solution. In the light of the uncertainty discussed and of the slightly different solvent conditions used in the present work (pure H_2O), compared to 0.01 M NaCl used by Herzog *et al.*,[12] the M_J result shown in Fig. 11A and R_g = 185 nm (from Fig. 10) are compatible with the findings by Herzog *et al.*[12]

Finally, we focus on the initial stage of aggregation, which was deliberately left out in the preceding considerations due to its non-negligible contribution of oligomers/monomers to the scattering intensity. In order to gain further insight into the mechanism of J-aggregate formation during this initial part, an analysis of time-resolved DLS data measured in the temperature regime of 21.4 °C < T < 20 °C was carried out.

Right at the beginning of the aggregation process a pronounced bimodality can be observed in the field-time correlation functions. An example thereof is shown in the ESI† (Section S5). Hence, data is fitted with a bimodal correlation function given by eqn (20), which is based on five fit parameters, the incoherent background A, two weighting factors b_i and two diffusional modes expressed as an inverse relaxation time $\Gamma_i(q)$, one for each species respectively. The fit gives access to the hydrodynamic properties of both modes together with their contribution to the static scattering signal, expressed as normalized intensity weighted coefficients b_i.

$$g_1(\tau, q) = A + b_{m,o}(q) \cdot \exp\left(-\frac{\tau}{\Gamma_{m,o}(q)}\right) + b_J(q) \cdot \exp\left(-\frac{\tau}{\Gamma_J(q)}\right) \quad (20)$$

Fig. 12 shows both parameters for the two modes. The slow mode reveals a constant R_h of 90 nm and shows a gradual increase of its contribution expressed as b_J. We attribute this mode to the J-aggregates. The fast mode results in R_h = 0.5 nm and exhibits a steady decrease in $b_{m,o}$, indicating the consumption of those species. This mode unambiguously corresponds to PIC monomers/oligomers. Invariance of both hydrodynamic radii is striking and underlines the fact that the change in M_w and R_g in Fig. 10 is solely caused by a change in concentrations of J-aggregates and monomers/oligomers.

Proper consideration of $b_i(q)$ from DLS enables partitioning of the experimental $\Delta R(q)$ values from SLS into both modes and hence gives access to the Rayleigh ratio of J-aggregates, $\Delta R_J(q)$,

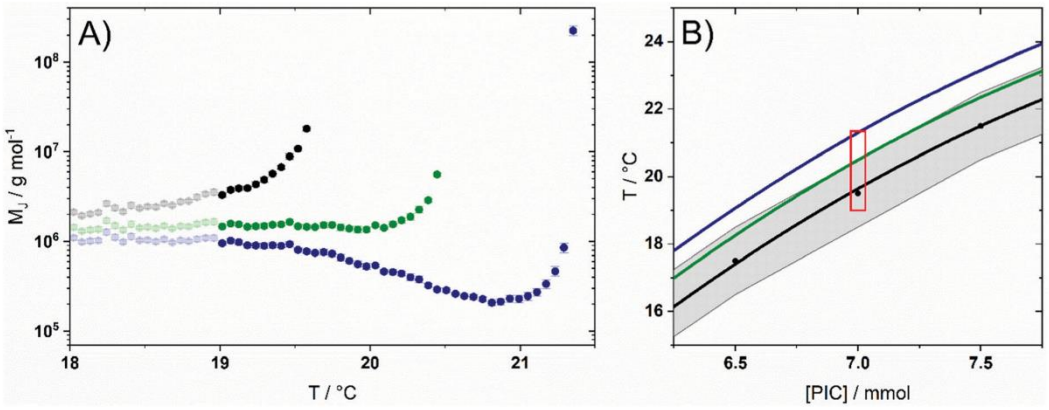

Fig. 11 (A) Determination of the molar mass M_J of J-aggregates. Data are established with eqn (19c). The symbols indicate three different approaches to determine c_J based on different selections of the threshold temperature at [PIC] = 7 mM: (black spheres) T = 19.7 °C as shown in Fig. 1, (blue spheres) T = 21.4 °C corresponding to the threshold temperature determined by light scattering (Fig. 10), (green spheres) T = 20.55 °C resulting in a minimum in the standard deviation of M_J between 20 °C and 19 °C. (B) Aggregation thresholds of the three selections together with the investigated temperature regime marked as a red box. The grey area indicates error margins of the non-shifted aggregation threshold from Fig. 1.

This journal is © The Royal Society of Chemistry 2021

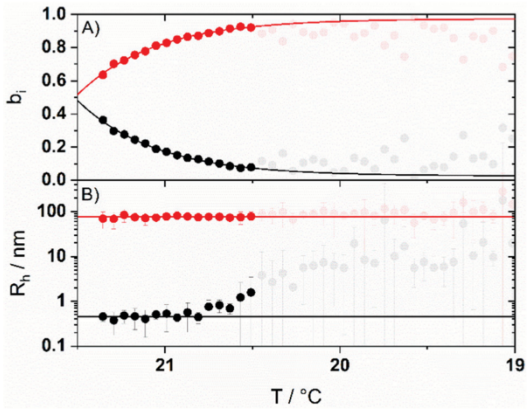

Fig. 12 (A) Evolution of the intensity weighted coefficients b_i of J-aggregates (red) and monomers/oligomers of PIC (black) at the onset of aggregation. The solid lines represent exponential fits of the data and serve as a visual guideline. (B) Hydrodynamic radii R_h of J-aggregates (red) and non-aggregated PIC (black). The solid horizontal lines indicate the average of R_h. Transparent data points below 20.5 °C were not considered for further data analysis.

and of the monomer/oligomer mixture, $\Delta R_{m,o}(q)$. Evaluation of the angular dependency of $\Delta R_J(q)$ and $\Delta R_{m,o}(q)$ is shown in the ESI† (Section S5). Interestingly, $\Delta R_{m,o}(q)$ exhibits no angular dependency, which is physically meaningful since monomers and oligomers are too small to induce an angular dependent scattering intensity. Evaluation of $\Delta R_J(q)$ leads to a constant value of R_g = 188 ± 2 nm for J-aggregates. This value nicely coincides with the plateau value approached at $T \sim 20$ °C (see Fig. 10) corresponding to a regime where the scattering contribution from monomers/oligomers can be neglected. Comparison of the size parameters of J-aggregates R_g established in Section S5 (ESI†) and R_h derived from the slow mode shown in Fig. 12, shows that the ratio between both amounts to 2, indicating the presence of fibrillar structures.[28,29]

Knowledge of the evolution of b_i with time during the initial phase of the aggregation also enables an estimation of the concentrations of both species. This offers an advantage over the determination of c_J *via* the aggregation threshold as it is insensitive towards the actual choice of an aggregation threshold (see ESI,† Section S6). The concentrations calculated with the help of b_i are then used to simulate scattering curves at the initial phase of the aggregation process. The outcome is compared with the corresponding experimental values of M_w and R_g. Agreement of simulated and experimental data is another verification of the underlying monomer addition process. The simulation of scattering curves is described in the ESI† (Section S6). Strikingly, the scattering curves describing the J-aggregation progressing with decreasing temperature can be described with two species, a monomer/oligomer mixture and J-aggregates with a molar mass of $M_J = 1.48 \times 10^6$ g mol^{-1} and a length L of $L = \sqrt{12} \cdot R_g = 650$ nm.

The fact that J-aggregates and non-aggregated PIC monomers/oligomers can be distinguished and identified as the only species present, provides evidence for a monomer addition process or chain growth process as mechanism of the formation of J-aggregates. In case of a step-wise growth process, broad monomodal distribution functions are to be expected, as was observed by us in the context of the self-assembly of the protein fibrinogen.[30] Thus, the formation of J-aggregates can be described as a monomer addition process where at any temperature addressed during the cooling protocol, the formation of fully developed J-aggregates happens faster than the gradual decrease in temperature. Gelation is induced by entanglement of chains once the concentration of those chains exceeds a critical regime.

This feature was further supported with another time-dependent light scattering experiment where the aggregation was triggered by a change of solvent, from pure water to 0.01 M NaCl. This approach has the advantage that it avoids an overlaying variation of equilibrium conditions based on a temperature change with the actual kinetics of J-aggregate formation. As is outlined in the ESI† (Section S7) the abrupt increase of salinity leads to fully developed size parameters within a time span of 30 s, which do not change any more with progressing time. J-Aggregate formation after instantaneous mixing of the two component solutions thus occurs on a time scale, which is not detectable with the multi-angle light scattering device used in the present work.

Having revealed a monomer addition process for the formation of J-aggregates from PIC, we would like to address an issue of potential relevance to the interpretation of the SLS/DLS data just presented. Once size and mass values from growing intermediates can be recorded in a time-resolved manner as it is the case in the present analysis, a correlation of the resulting size values with the corresponding mass values may be of help if it leads to a power law.[31] Such power laws provide structural information on the growing intermediates if those growing intermediates are self-similar like spheres, polymer coils or thin rod-like aggregates. However, it is the outcome of the preceding analysis, based on a decomposition of the DLS data into two modes and on a comparison of experimental curves with simulated scattering curves from binary systems, which clearly demonstrates that such a power law behaviour would be an artefact in the case of the present J-aggregates because size and mass values simply vary due to a variation of a binary composition. While the amount of monomeric material decreases as it is steadily transformed to J-aggregates with a well-defined length, the number of those J-aggregates increases, without changing either species.

Conclusion

The tendency of PIC to form J-aggregates is governed by a threshold curve, shown in Fig. 1. Above the threshold, only monomers and oligomers, so called H-aggregates, are present in solution. The present work is aiming at a comprehensive understanding of the equilibrium thermodynamics of PIC self-assembly in water above and below this threshold and to shed

This journal is © The Royal Society of Chemistry 2021

light on the mechanism of J-aggregate formation leading to the most prominent aggregates PIC is forming. Whereas the information on the thermodynamics is predominantly retrieved from a detailed analysis of the solution composition based on UV-VIS-spectroscopy, SLS and DLS experiments add to a better understanding of the formation mechanism of aggregates.

In order to be able to describe the sample composition in aqueous PIC solutions with the help of UV-Vis spectroscopy, the spectra of all present species are necessary. To this end trimers were considered as the third PIC species in addition to monomers and dimers. Whereas the monomer and dimer spectra were available from literature,[21] the present work had to provide an additional trimer spectrum. Such a trimer spectrum could indeed successfully be established under the assumption that it represents all species with $N \geq 3$. The three spectra made possible a consistent and quantitative analysis of the composition in the regime above the threshold curve, resulting in an equilibrium constant of trimerization of $K_T(25\ ^\circ\mathrm{C}) = 240\,000\ \mathrm{L}^2\ \mathrm{mol}^{-2}$.

Below the threshold curve, solutions could successfully be treated as mixtures of the same PIC species identified already above the threshold and of additional J-aggregates. This approach was made possible by extending the validity of the equilibrium constants of dimerization and trimerization to the regime of J-aggregation and by describing the formation of J-aggregates of PIC with the concept of chain growth polymerisation from living ends originally established in macromolecular chemistry.[23] As a result, the composition also got accessible throughout the entire phase space below the threshold of J-aggregation. With the compositions at variable concentrations and temperatures available, J-aggregate spectra could be established by subtracting the respective contribution of monomers/oligomers from the corresponding experimental spectrum. All resulting spectra turned out to overlay. This does not only confirm consistency of the present approach but for the first time reveals a UV-vis spectrum of PIC J-aggregates expressed as molar extinction coefficient.

Formation of J-aggregates *via* a monomer addition process below the threshold curve justified application of the concept of the ceiling temperature[23] to extract the thermodynamic parameters ΔH^0 and ΔS^0 associated with the formation of J-aggregates. Two approaches were used. The first approach assumed that all monomeric/oligomeric species, including monomers, dimers and trimers, are involved in the self-assembly.[16,17] The second approach took advantage of the successful resolution of the solution composition into monomers, dimers and trimers and assumed that only monomers are incorporated in J-aggregates. A mechanism where only monomers actively polymerize, is supported by the fact that H-dimers or H-trimers would have to reorient while binding to the growing end of a J-aggregate. Both approaches yielded the same value for $\Delta H^0 = -22.4\ \mathrm{kJ\ mol}^{-1}$. However, the standard aggregation entropy ΔS^0 increased from $-35\ \mathrm{J\ mol}^{-1}\ \mathrm{K}^{-1}$ to $-23\ \mathrm{J\ mol}^{-1}\ \mathrm{K}^{-1}$ if only monomers are active in the self-assembly. With these values calculation of an equilibrium constant of aggregation K_J got accessible , leading to $118\ \mathrm{L\ mol}^{-1}$ and $522\ \mathrm{L\ mol}^{-1}$ respectively.

The findings on the sample composition above and below the aggregation threshold were then applied to a quantitative interpretation of a time-dependent light scattering experiment during a temperature gradient. In the regime where J-aggregates are absent (high T), a mass averaged molecular weight of $M_w = 890\ \mathrm{g\ mol}^{-1}$ was measured, in excellent agreement with the molar mass value of $M_w = 820\ \mathrm{g\ mol}^{-1}$ derived from UV-VIS-spectroscopy. At the onset of J-aggregate formation right at the threshold line, bimodal correlation functions were measured by DLS. Evaluation of those correlation functions resulted in weighing factors b_i for both species, together with their hydrodynamic radii R_h. The hydrodynamic radii were constant throughout the regime where bimodality was observed, amounting to 90 nm for the large species representing the J-aggregates and 0.5 nm for the small species corresponding to monomers/oligomers. The weighing factors were further used to split the angular dependent scattering curves from SLS into two component curves. One set of component curves was angular independent again representing the monomers and oligomers. Evaluation of the other set of component curves revealed a constant radius of gyration of $R_g = 188$ nm for the J-aggregates throughout the entire regime under consideration, in line with the value measured deep in the J-aggregate phase. Deep in the regime where J-aggregates are present and where the scattering contribution of monomers/oligomers could be neglected a value of $1.48 \times 10^6\ \mathrm{g\ mol}^{-1}$ was estimated as the molar mass of J-aggregates together with a radius of gyration of $R_g = 185$ nm. These results further verify a monomer addition mechanism or chain growth for the formation of J-aggregates.

The light scattering experiments revealed a formation process of J-aggregates, where in all cases the initiation reaction and aggregate growth process was faster than the time resolution of the instrument. Independent of triggering aggregation instantaneously by addition of salt or gradually by decreasing temperature, an increase of the amount of J-aggregates with $M_J = 1.48 \times 10^6\ \mathrm{g\ mol}^{-1}$ and $L = 650$ nm was observed instead of elongation of aggregates.

Author contributions

The manuscript was written through contributions of all authors. All authors have given approval to the final version of the manuscript.

Conflicts of interest

The authors declare no competing financial interest.

References

1 E. E. Jelley, *Nature*, 1936, **138**, 1009–1010.
2 E. E. Jelley, *Nature*, 1937, **139**, 631–634.
3 G. Scheibe, *Angew. Chem.*, 1937, **50**, 212–219.
4 G. Scheibe, L. Kandler and H. Ecker, *Naturwissenschaften*, 1937, **25**, 75.
5 G. Scheibe, L. Kandler and H. Ecker, *Naturwissenschaften*, 1937, **25**, 474–475.

 This journal is © The Royal Society of Chemistry 2021

6 B. Kopainsky, J. K. Hallermeier and W. Kaiser, *Chem. Phys. Lett.*, 1981, **83**, 498–502.
7 A. H. Herz, *Adv. Colloid Interface Sci.*, 1977, **8**, 237–298.
8 H. Von Berlepsch, C. Böttcher, A. Quart, C. Burger, S. Dähne and S. Kirstein, *J. Phys. Chem. B*, 2000, **104**, 5255–5262.
9 H. von Berlepsch, C. Böttcher and L. Dähne, *J. Phys. Chem. B*, 2000, **104**, 8792–8799.
10 W. Cooper, *Chem. Phys. Lett.*, 1970, **7**, 73–77.
11 B. Neumann, *J. Phys. Chem. B*, 2001, **105**, 8268–8274.
12 B. Herzog, K. Huber and H. Stegemeyer, *Langmuir*, 2003, **19**, 5223–5232.
13 B. Neumann and P. Pollmann, *Phys. Chem. Chem. Phys.*, 2000, **2**, 4784–4792.
14 H. Rehage, G. Platz, B. Struller and C. Thunig, *Tenside, Surfactants, Deterg.*, 1996, **33**, 242–248.
15 E. Daltrozzo, G. Scheibe, K. Gschwind and F. Haimerl, *Photogr. Sci. Eng.*, 1974, **18**, 441–449.
16 B. Hämisch, R. Pollak, S. Ebbinghaus and K. Huber, *Chem. – Eur. J.*, 2020, **26**, 7041–7050.
17 B. Hämisch, R. Pollak, S. Ebbinghaus and K. Huber, *ChemSystemsChem*, 2021, **e2000051**, 1–10.
18 B. H. Zimm, *J. Chem. Phys.*, 1948, **16**, 1093.
19 D. E. Koppel, *J. Chem. Phys.*, 1972, **57**, 4814–4820.
20 A. Einstein, *Ann. Phys.*, 1905, **322**, 549–560.
21 M.-L. Horng and E. L. Quitevis, *J. Chem. Educ.*, 2000, **77**, 637–639.
22 G. Yu, M. Walker and M. R. Wilson, *Phys. Chem. Chem. Phys.*, 2021, **23**, 6408–6421.
23 F. S. Danton and K. J. Ivin, *Nature*, 1948, **162**, 705–707.
24 M. Kasha, H. R. Rawls and M. A. El-Bayoumi, *Pure Appl. Chem.*, 1965, **11**, 371–392.
25 B. Kopainsky and J. K. Hallermeier, *Chem. Phys. Lett.*, 1982, **87**, 7–10.
26 G. Scheibe and L. Kandler, *Naturwissenschaften*, 1938, **26**, 412–413.
27 J. S. Briggs, *Z. Phys. Chem.*, 1971, **75**, 214–218.
28 W. Burchard, *Adv. Polym. Sci.*, 1983, **48**, 1–124.
29 M. Schmidt, *Macromolecules*, 1984, **17**, 553–560.
30 B. Hämisch, A. Büngeler, C. Kielar, A. Keller, O. Strube and K. Huber, *Langmuir*, 2019, **35**, 12113–12122.
31 J. Liu, J. Rieger and K. Huber, *Langmuir*, 2008, **24**, 8262–8271.

This journal is © The Royal Society of Chemistry 2021

Supporting Information

Mechanism and Equilibrium Thermodynamics of H- and J-aggregate Formation from Pseudo Isocyanine Chloride in Water

*Benjamin Hämisch, Klaus Huber**

Physical Chemistry, Paderborn University, 33098 Paderborn, Germany

S1 Datasets of the trimer spectra and the J-spectrum

Table S1. Digitalized versions of the trimer spectra and the J-aggregate spectrum established in the present work.

λ	ε_{trimer} with K_T = 200000 L^2 mol^{-2}	ε_{trimer} with K_T = 285000 L^2 mol^{-2}	$\varepsilon_{J\text{-aggregate}}$
nm		L mol^{-1} cm^{-1}	
450	65642.5	65012.6	7121.0
451	68729.5	68037.0	7606.3
452	71660.4	70907.1	8163.3
453	74300.4	73496.4	8731.6
454	76816.7	75969.2	9236.9
455	79250.3	78347.4	9978.0
456	81449.3	80512.0	10572.7
457	83782.5	82773.9	11241.3
458	85632.0	84612.5	11953.9
460	89537.2	88439.9	13102.9
461	90938.4	89886.3	13558.9
462	92428.3	91377.2	13965.0
463	93322.9	92376.8	14248.2
464	94385.8	93525.0	14224.8
465	95563.4	94782.4	14069.6
466	96820.4	96143.9	13678.3
467	98060.4	97526.2	13548.1
468	99385.9	99056.7	13007.7
469	101541.7	101341.7	12462.1
470	104246.2	104176.1	11704.6
471	107359.4	107429.9	11051.1
472	110644.7	110909.6	10571.2
473	115104.8	115461.7	9577.5
474	118691.2	119303.8	9377.8
475	122915.5	123723.0	8957.9
476	126653.9	127708.5	9079.1
477	130221.3	131538.3	8947.5
478	134109.2	135560.8	7451.4
479	135264.0	137155.8	8015.0
480	135636.4	137877.0	7544.1
481	136439.3	138893.4	6580.5
482	134203.5	137130.4	6592.1
483	131464.3	134761.3	6804.5
484	126369.4	130137.1	8758.4
485	120442.7	124689.3	11302.8
486	114217.5	118868.1	13919.7
487	106828.6	111935.5	16952.8
488	100380.3	105745.1	20036.9
489	93039.5	98759.5	22942.2
490	86404.2	92345.2	25979.7
491	79870.3	85991.2	29493.3
492	73491.1	79802.3	32355.6
493	67847.8	74258.1	34854.4
494	62127.9	68674.9	36702.3
495	57217.3	63829.8	37557.7
496	52550.1	59224.8	37601.2
497	48178.3	54941.9	36444.1
498	44089.4	50955.6	34816.9
499	40280.4	47271.5	32662.9
500	37061.8	44142.8	30439.3
501	33707.4	40967.2	28381.0
502	30284.0	37808.2	26700.8
503	27666.7	35379.8	25158.8
504	24700.6	32737.8	24043.1
505	22193.1	30537.0	23224.2
506	19799.9	28494.9	22539.9
507	17772.2	26821.4	22058.3
508	15332.7	24864.4	21991.4
509	13574.5	23527.1	21842.5

510	12435.2	22763.5	21580.8
511	11304.3	22049.8	21532.1
512	10889.4	21985.9	21293.7
513	10038.5	21584.5	21406.9
514	11085.8	22799.8	20784.4
515	11742.5	23699.3	20558.1
516	12592.7	24780.4	20266.2
517	14128.4	26430.6	19806.7
518	15576.4	27985.6	19538.0
519	17169.9	29648.7	19265.9
520	19114.5	31549.4	19037.5
521	20959.3	33318.8	18819.6
522	22734.1	34962.2	18710.8
523	24126.0	36215.3	18704.2
524	25634.0	37490.9	18776.2
525	26696.8	38314.4	19175.2
526	27369.5	38730.3	19930.7
527	27850.4	38912.5	20897.9
528	27756.8	38548.3	22103.2
529	28474.0	38787.5	22817.7
530	27902.8	37893.0	23802.2
531	26948.0	36631.4	24647.6
532	27274.1	36401.4	24650.8
533	25648.6	34510.2	24594.5
534	26041.7	34274.0	22944.0
535	24204.3	32161.2	21721.8
536	23430.5	30925.9	19745.5
537	22684.3	29698.6	17850.2
538	22620.6	29059.5	15708.6
539	21594.4	27623.5	14219.9
540	21261.2	26777.7	12703.9
541	20834.6	25873.8	11449.8
542	20744.3	25261.7	10353.6
543	20285.1	24378.2	9527.6
544	19922.3	23593.7	8892.0
545	19832.5	23061.1	8344.3
546	19069.3	21995.4	8119.5
547	19384.0	21854.0	7599.7
548	18493.9	20733.2	7611.3
549	17600.5	19639.2	7763.7
550			6620.4
551			6341.2
552			6251.3
553			6318.1
554			6548.7
555			6993.4
556			7610.4
557			8430.6
558			9476.1
559			10801.1
560			12404.9
561			14456.3
562			17009.5
563			20213.0
564			24202.9
565			29345.3
566			36016.0
567			45223.2
568			58466.4
569			78635.8
570			110229.1
571			158822.4
572			225502.1
573			246404.4
574			170129.9
575			106646.2
576			67996.3
577			46131.1
578			33476.4
579			24781.2
580			17610.9

S2 Details on sample composition above the threshold curve

The percentage of dimers as a function of the total PIC concentration shown in **Figure S1** includes a broad maximum, which coincides with the concentration regime applied by the present experiments. The broad maximum offers an explanation for the invariance of the relative dimer concentration.

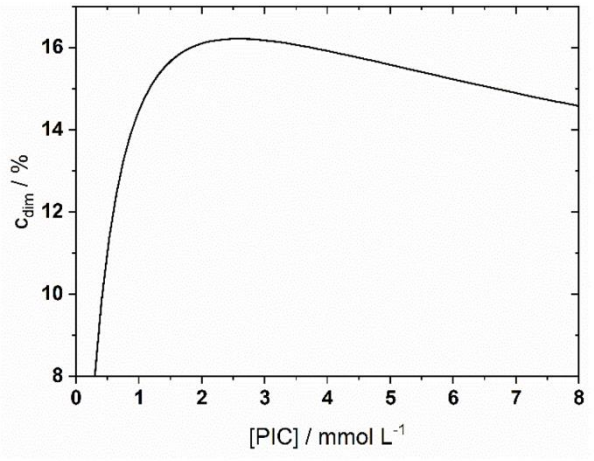

Figure S1. The dependence of the relative dimer concentration on the total concentration, calculated via eqs. 9 and 12.

In **Figure S2** the evolution of the relative concentrations of monomers, dimers and trimers with total concentration and temperature is plotted.

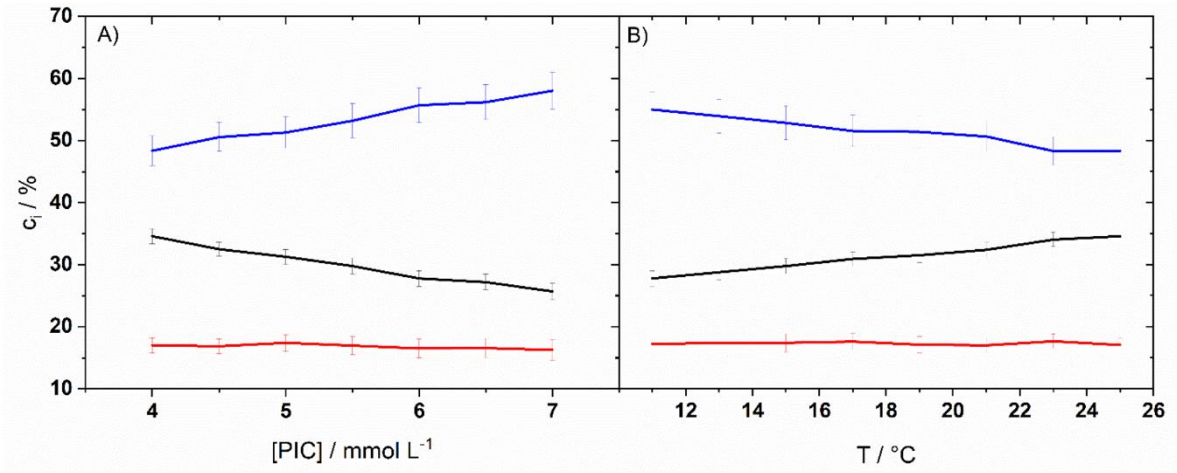

Figure S2. A) Relative concentrations of monomers (black), dimers (red) and trimers (blue) plotted versus the total concentration [PIC] resulting from decomposition of UV-Vis spectra according to eq. 8 at $T = 25$°C. B) Temperature dependence of the relative concentrations of monomers (black), dimers (red) and trimers (blue) resulting from decomposition of UV-Vis spectra according to eq 8 at *[PIC]* = 4 mM.

S3 Determination of the J-aggregate spectrum

Figure S3 shows all J-spectra independently established with three different samples at four temperatures (*[PIC]* = 7 mM), two temperatures (*[PIC]* = 6.5 mM) and five temperatures (*[PIC]* = 6 mM). All twelve spectra were used to form the averaged spectrum in the regime of $\lambda < 550$ nm shown in **Figure 9**. **Figure S4** shows the data used for determining the J-spectrum for $\lambda > 550$ nm together with the whole J-aggregate spectrum. **Figure S5** shows the result of subtracting the J-aggregate contribution from experimental spectra and renormalizing the excess spectra with $[PIC]_{m,o}$.

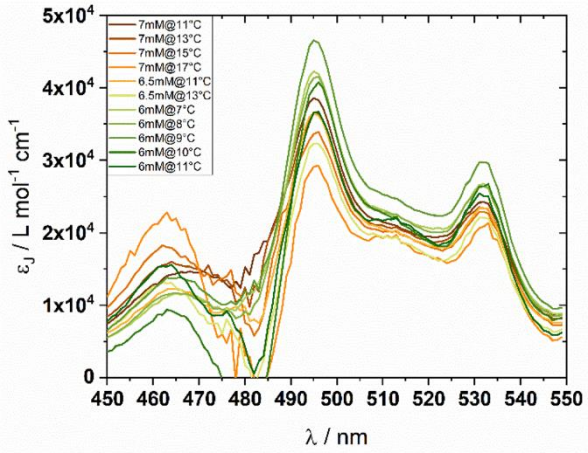

Figure S3. Established J-spectra of all investigated samples which are in the aggregated regime. Experimental spectra were corrected according to the oligomer/monomer contribution and the resulting excess spectra were normalized with the concentration of J-aggregates, which were taken from the aggregation threshold as the difference of the total concentration and the concentration of "non-aggregated" PIC $[PIC]_{m,o}$.

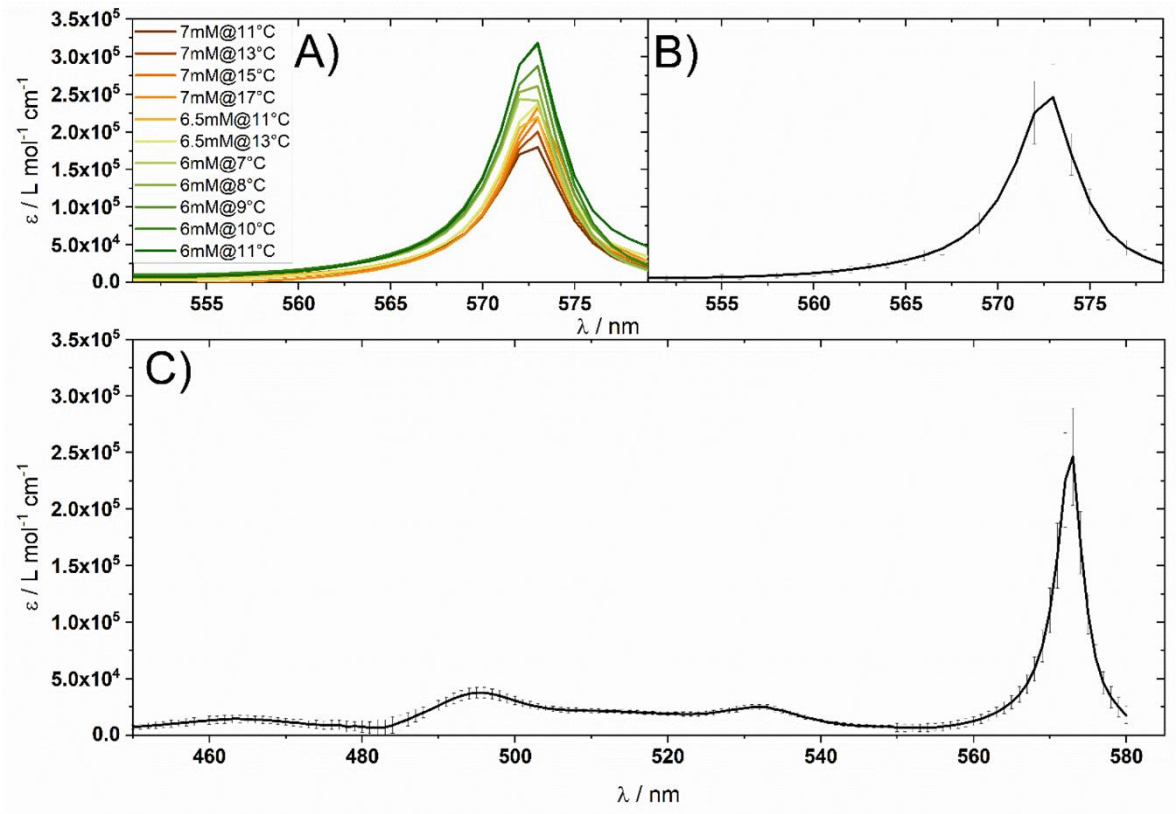

Figure S4. A) Normalized J-peak of experimental spectra below the aggregation threshold after subtraction of the contribution of oligomers/monomers. B) Averaged normalized J-peak of all spectra shown in A). C) The merged J-spectrum. The part below λ = 550 nm is found in **Figure 9** and the part above λ = 550 nm is seen in B).

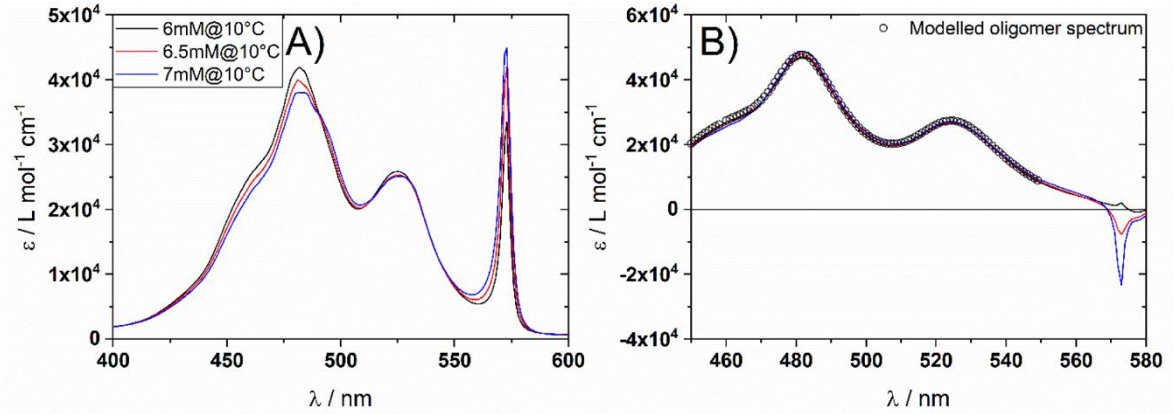

Figure S5. A) Experimental spectra used for verifying the validity of the J-aggregate spectrum. These spectra were not used in the process of determining the J-aggregate spectrum given in **Figure S4**. B) The resulting excess spectra after subtraction of the contribution of J-aggregates from experimental spectra. Additionally, the modelled oligomer spectrum is plotted for comparison.

S4 Determination of the molar mass M_J of J-aggregates

Figure S6 shows the result of calculating the molar mass M_J of J-aggregates with and without taking the scattering contribution of oligomers/monomers into account. The insignificant deviation between both approaches below $T < 20$ °C justifies neglection of the scattering contribution from oligomeric/monomeric PIC in eq 19a.

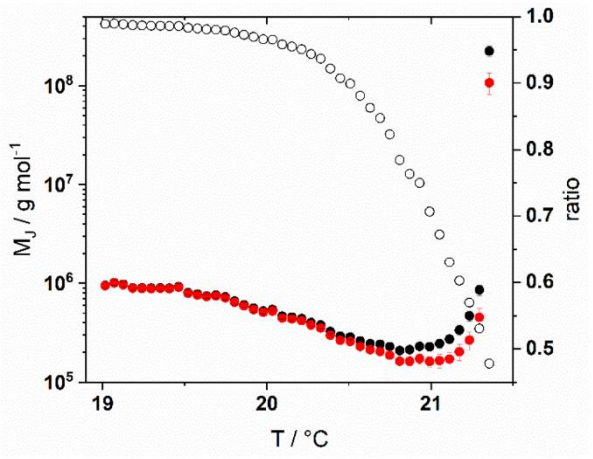

Figure S6. Molar mass M_J of J-aggregates. Black spheres refer to the data points from **Figure 11**, which were calculated by neglecting the contribution of oligomeric/monomeric PIC. Red spheres were established by taking the scattering contribution of oligomeric/monomeric PIC into account. Hollow black spheres represent the ratio of M_J with and without implementing the oligomer/monomer correction.

The result of the calculation of M_J using the aggregation threshold is shown in **Figure S7**. The three different datasets are established by taking either the threshold curve itself or the upper/lower error margin of it to calculate the concentration of J-aggregates.

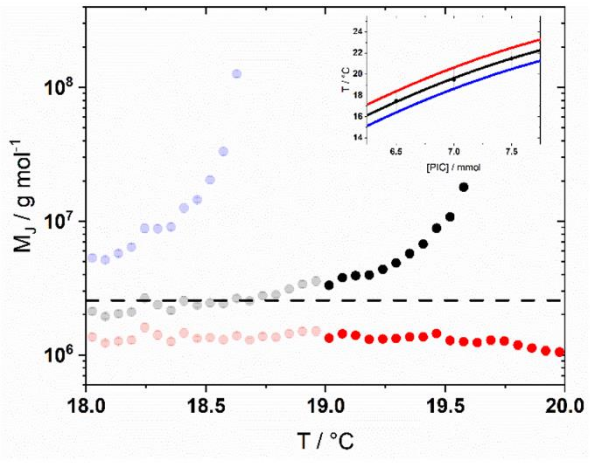

Figure S7. Determination of the molar mass M_J of J-aggregates. Data were established by means of eq 19c with the concentration exclusively of J-aggregates. Black data points were calculated based on the concentration received from the aggregation threshold shown in **Figure 1** at *[PIC]* = 7mM. Blue data points refer to the lower error margin and red data points refer to the upper error margin of the aggregation threshold shown in the inlet. The horizontal dashed line represents the value $M_J = 2.55 \cdot 10^6$ g/mol determined by Herzog et al.[1] in 0.01 M NaCl solution.

S5 Bimodality of field-time correlation functions and resulting SLS curves

Figure S8 shows three examples of bimodal correlation functions which were recorded at the onset of aggregation.

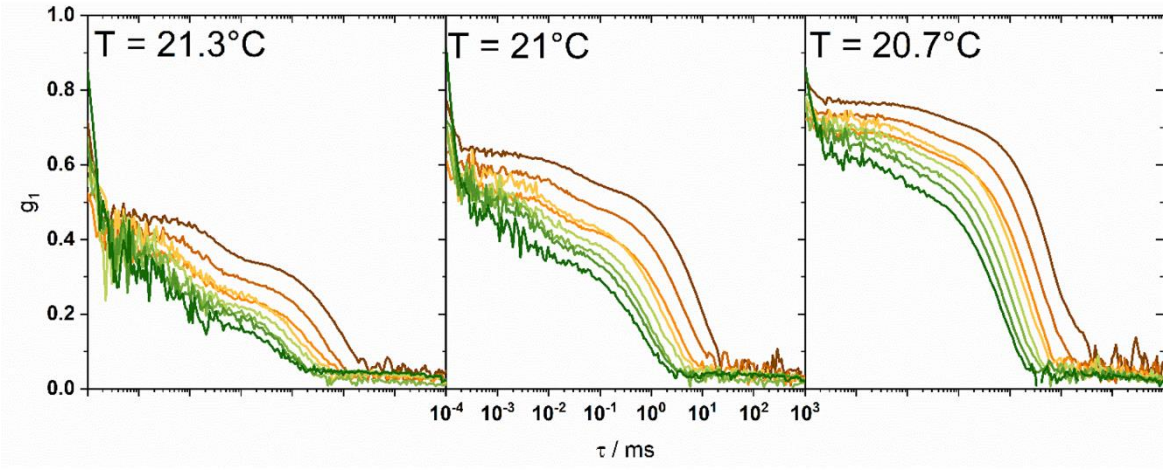

Figure S8. Field-time correlation functions $g_1(\tau)$ at three temperatures close to the threshold value of the formation of J-aggregates. The color index goes from brown to green and represent the scattering angle from 30° to 86° in 8° increments.

In **Figure S9** the scattering curves of the monomer/oligomer mixture and of J-aggregates at the onset of aggregation are plotted.

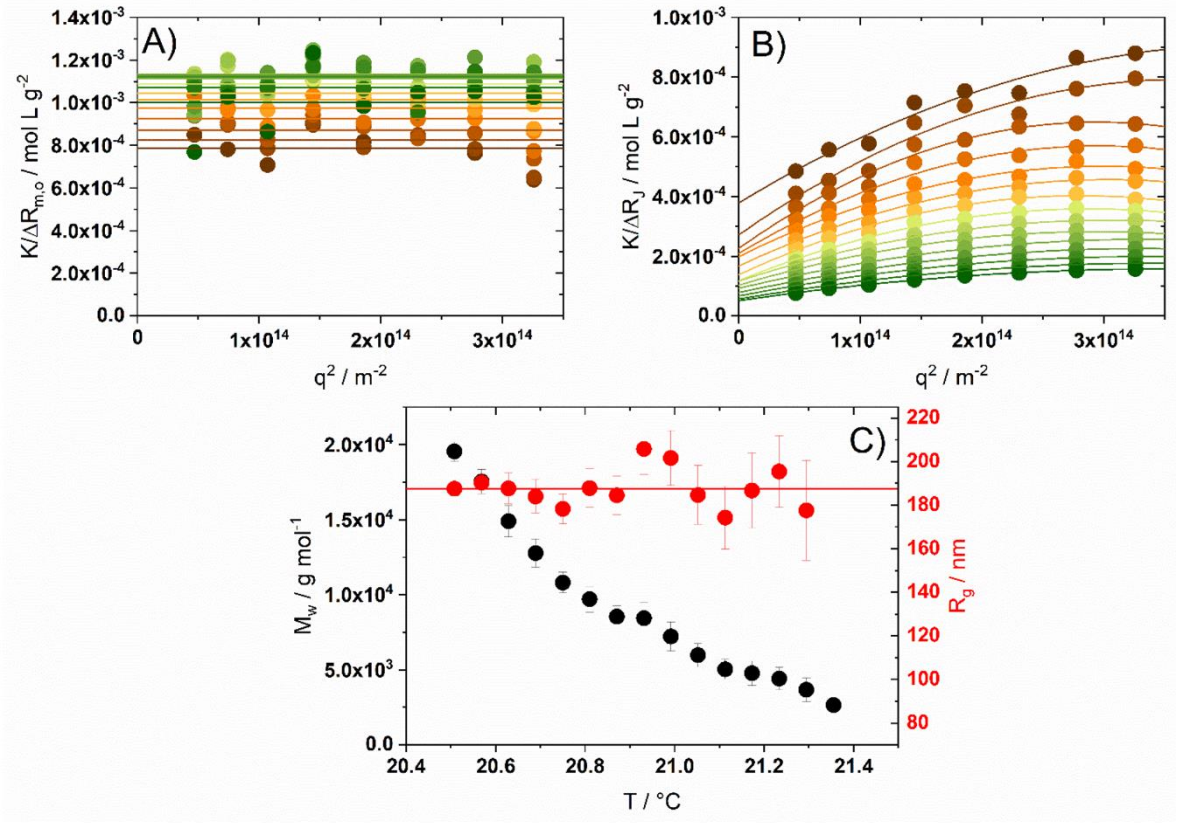

Figure S9. Evaluation of the scattering contribution of J-aggregates at the onset of aggregation. A) Scattering curves of J-aggregates and of B) oligomers/monomers with $\Delta R_i(q) = \Delta R(q) \cdot b_i(q)$. The color index goes from brown to green and represents different temperatures from 21.3 °C to 20.5 °C. C) Results of applying eq 2 on the scattering curves of J-aggregates shown in A) with a dummy concentration of 1 g/L. The increase in M_w with decreasing T indicates an accumulation of J-aggregates. The radius of gyration is constant and amounts to R_g = 188±2 nm.

S6 Simulation of SLS curves based on $M_{m,o}$ and M_J

The evolution of b_i with time shall be used to approximate the concentration of both species. It is shown in **Figure 11** that determination of the J-aggregate concentration c_J depends on the particular choice of the threshold line and thus is charged with an increasing uncertainty while approaching the respective line. One route to circumvent this problem is to approximate the concentrations at the onset of aggregation with help of b_i. These concentrations are then used to predict scattering curves and compare the corresponding R_g and M_w parameters with the experimental values shown in **Figure 10**.

The weighting factors b_i, the molar masses M_i and their mass concentrations c_i are related as follows:

$$\frac{c_{m,o}}{c_J} = \frac{b_{m,o}}{b_J} \cdot \frac{M_J}{M_{m,o}} \qquad \text{(S1)}$$

In order to determine concentrations via b_i, it is in general necessary to know the molar mass of the entities or, if only R_h is known, to know the relationship between R_h and M_w.[2] The molar mass of monomers/oligomers is extracted from the monomer/oligomer phase, shown in the inlet in **Figure 10**, and amounts to 850 g/mol. The molar mass of J-aggregates was set to $M_J = 1.48*10^6$ g/mol corresponding to the best estimate based on **Figure 11**.

Eq S1 is used to calculate the concentrations in g/l of both modes for the aggregation process within the T-regime where the bimodality (shown in **Figure 12**) is unambiguously accessible.

With these concentrations, scattering curves of mixtures of monomeric/oligomeric PIC and J-aggregates were simulated according to the following approach. In case of a multimodal system, the excess Rayleigh ratio ΔR of the sample is approximated as the sum of excess Rayleigh ratios of all species according to

$$\Delta R(q) = \sum_i K_i \cdot c_i \cdot M_i \cdot P_i(q \cdot R_{g,i}) \quad \text{(S2)}$$

In eq S3 K_i is the optical constant defined in eq 4, c_i is the concentration in g/l determined with eq S1, M_i is the molar mass, $R_{g,i}$ is the radius of gyration and $P_i(q)$ is the form factor of species i. In the specific case of the formation of J-aggregates, the system is approximated with distinguishable species. Since both species are based on PIC molecules, the refractive index increment dn/dc, and thus K, the same value is assumed for both species. The first species is monomeric/oligomeric PIC with a molar mass of $M_{m,o}$ = 850 g/mol, derived from the inlet in **Figure 10**. The radius of gyration of this species is too low to be detectable, which results in a form factor of 1 throughout the whole q-regime under consideration. The second species is the J-aggregate with a molar mass of M_J = 1.48*10^6 g/mol and a radius of gyration of R_g = 188 nm, with R_g stemming from the evaluation of ΔR_J shown in **Figure S9**. A form factor of a rod was assumed for the J-aggregate with the length of the rod L determined by means of $L = R_g\sqrt{12}$.[3] Thus, eq S2 transforms to following expression:

$$\Delta R(q) = K \cdot (c_{m,o} \cdot M_{m,o} + (c - c_{m,o}) \cdot M_j \cdot P_{rod}(q \cdot R_g)) \quad \text{(S3)}$$

A comparison of the resulting scattering curves from eq S3 and the corresponding data from the experiment is found in **Figure S10**. Extraction of M_w and R_g from the scattering curves simulated with eq S3 were carried out with the same approach applied to the scattering data from the experiment (See experimental Part for details). Results from eq S3 are compared with the experimental results in **Figure S11**.

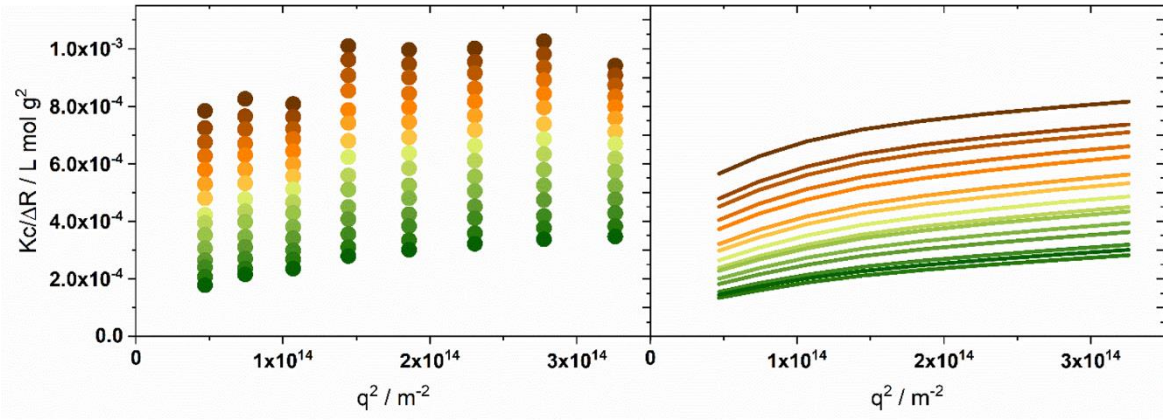

Figure S10. Scattering curves from experiment (A)) and from simulation (B)). The temperature regime corresponds to the data shown in **Figure 12**. Brown data points were recorded at $T = 21.4$°C° and the green data points were recorded at $T = 20.5$°C°.

Evaluation of the simulated scattering curves yields values for M_w and R_g comparable to the values obtained from the experiment, with simulated M_w being slightly larger. The simulated values follow the temperature dependent trend of the experimental data, which suggests a systematic shift as the origin for the larger M_w from simulation. A reason for this deviation could be originated in the uncertainties of $M_{m,o}$ and M_J. Another source of the deviation may be the neglect of the second osmotic virial coefficient A_2 by scattering curves simulated with eq S3. Due to the inherent positive charge of PIC, A_2 is most likely positive, and if known would yield lower values for M_w. In the light of these uncertainties, the small discrepancies between measured and calculated values in **Figure S11** are not considered to be significant and the extent of agreement confirms the applicability of the concept of chain growth on the description of the scattering data.

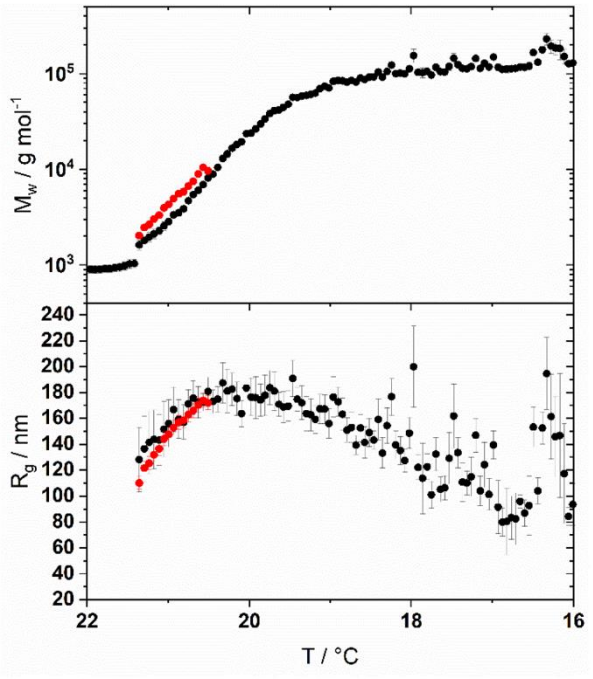

Figure S11. Temperature dependent evolution of the weight averaged molecular mass M_w and the radius of gyration R_g from a light scattering experiment (black) with *[PIC]* = 7 mM. The red spheres represent values for M_w and R_g obtained from the evaluation of simulated scattering curves with mass concentrations extracted from eq S1.

S7 Aggregation experiment triggered by a change in solvent

Figure S12 shows the result of an aggregation experiment recorded with light scattering where the aggregation was triggered by changing the solvent condition from aqueous to 0.01M NaCl solution. For this purpose, 7 mL of a 0.0114M NaCl solution was held at 4°C inside the device. 1 mL of an 8mM PIC solution, which was previously held at 30°C, was added and then mixed for approximately 30 seconds before starting the measurement.

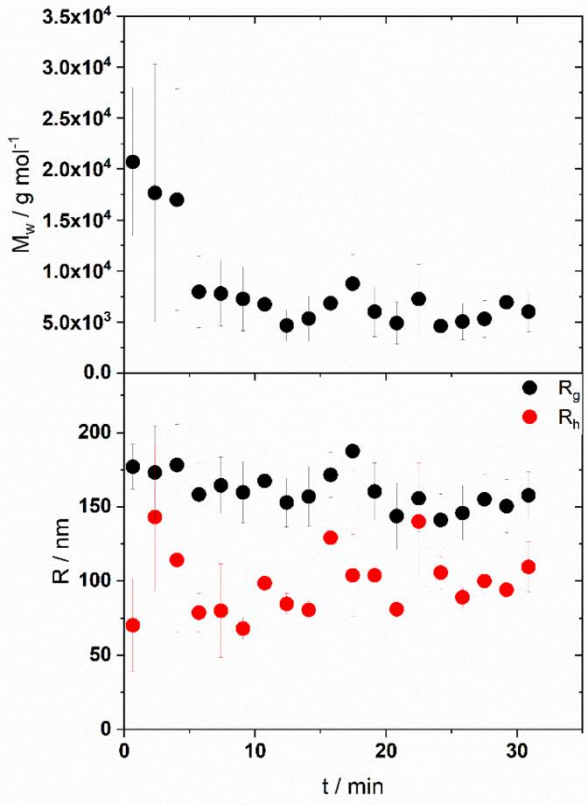

Figure S12. Evolution of the mass weighted molecular weight M_w, the radius of gyration R_g and the hydrodynamic radius R_h for a sample with *[PIC]* = 1 mM in 0.01M NaCl solution at $T = 4$ °C. The aggregation was triggered by changing the solvent from aqueous solution to 0.01M NaCl solution.

REFERENCES

1 B. Herzog, K. Huber and H. Stegemeyer, *Langmuir*, 2003, **19**, 5223–5232.

2 E. A. Litmanovich and E. M. Ivleva, *Polym. Sci. Ser. A*, 2010, **52**, 671–678.

3 A. Guinier, *Small-angle scattering of X-rays*, 1955.

6. Thermodynamic Analysis of the Self-Assembly of Pseudo Isocyanine Chloride in the Presence of Crowding Agents

Reproduced from *ChemSystemsChem*, **2021**, *3*, e2000051.

"Thermodynamic Analysis of the Self-Assembly of Pseudo Isocyanine Chloride in the Presence of Crowding Agents" published in the journal *ChemSystemsChem* by Wiley-VCH GmbH is licensed under CC BY-NC-ND 4.0. No changes have been made.

Copyright 2021 The Authors.

DOI: 10.1002/syst.202000051

ChemSystemsChem

Articles
doi.org/10.1002/syst.202000051

Chemistry Europe
European Chemical Societies Publishing

Special Collection

Thermodynamic Analysis of the Self-Assembly of Pseudo Isocyanine Chloride in the Presence of Crowding Agents

Benjamin Hämisch,[a] Roland Pollak,[b] Simon Ebbinghaus,*[b] and Klaus Huber*[a]

Pseudo isocyanine chloride (PIC) is a water-soluble cationic dyestuff, which self-assembles to fiber-like aggregates below a characteristic temperature threshold. The threshold temperature decreases with decreasing PIC concentration. Macromolecular cosolutes affect this self-assembly of PIC, similar to the impact macromolecular crowding has on the aggregation of proteins in living systems. The present study analyses the impact of triethylene glycol (TEG), polyethylene glycol (PEG), and Ficoll 400 as synthetic macromolecular crowding agents on the self-assembly of PIC. A drastic change in the absorption behavior of visible light by PIC, which accompanies the transformation of monomeric PIC to the aggregate state of PIC, allows to analyze the temperature-dependent self-assembly in detail. Assisted by calorimetric measurements and by an analogy between self-assembly and chemical polymerization, the thermodynamic analysis allowed to interpret the observed tendency of TEG and PEG to suppress and of Ficoll 400 to promote self-assembly of PIC. Whereas the suppression by TEG and PEG can be attributed to preferential interactions between TEG or PEG and PIC, the promoting effect induced by Ficoll 400 is caused by excluded volume effects exerted by Ficoll. The results are in support of PIC as a cheap substitute of proteins in test tube studies of self-assembly and as sensor for crowding effects on self-assembly processes in cells.

1. Introduction

A full understanding of the self-assembly processes of proteins in biological systems is only achieved by a proper consideration of macromolecular crowding. The concentration of solutes within cells or viruses reach 40% by weight,[1] which may alter aggregation patterns of proteins remarkably in comparison to *in vitro* experiments in aqueous solutions. T. C. Laurent was one of the first to observe this discrepancy while studying solubility assay of various proteins in the presence of polysaccharides.[2] One approach to investigate self-assembly processes of proteins in cellular environment is to mimic this environment with synthetic crowding agents. Another approach with a twofold benefit may be established in replacing the self-assembling proteins by alternative compounds like dyestuffs, having a similar tendency to form aggregates as the proteins have. First, self-assembling dyestuffs are less cost intensive to be applied in *in vitro* studies in comparison to proteins and second, dyestuffs in cells responding with a modulated UV-Vis absorption behaviour during aggregation may be useful candidates as sensors for self-assembly *in vivo*.

An interesting candidate capable of acting as a protein substitute is the cationic dyestuff pseudo isocyanine chloride (PIC). An illustration of the molecular structure of PIC is depicted in Scheme 1. Specific patterns of hydrophobic spots, cationic groups and residues suited to form H-binds, together with a marginal solubility in water, typically exhibited by self-assembling proteins, are also provided by PIC. Self-assembly of PIC in aqueous solution is in fact well documented.[3–7] It is typically induced by decreasing the temperature below a characteristic threshold value, which increases with increasing PIC concentration. The assemblies are also denoted as J-aggregates due to a sharp absorption band at 573 nm[7–11]. They adopt a fibrillar shape[3,6] very much like many self-assembling proteins do and, again in contrast to the monomeric species the J-aggregates exhibit a sharp fluorescence band at 577 nm.[8]

A previous study has already addressed the impact of various crowding agents on the fibrillization of PIC.[12] *In vitro* experiments verified that the presence of triethylene glycol (TEG) and polyethylene glycol (PEG) both suppressed the formation of PIC fibrils. Ficoll 400 on the other hand promoted

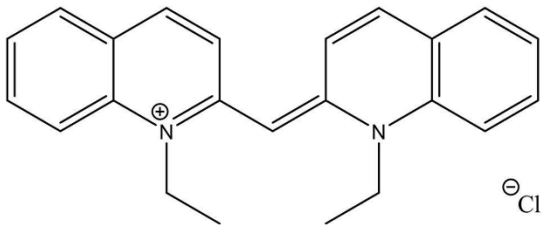

Scheme 1. Molecular structure of pseudo isocyanine chloride (PIC).

[a] *B. Hämisch, Prof. Dr. K. Huber*
Physical Chemistry, Paderborn University
33098 Paderborn (Germany)
E-mail: klaus.huber@upb.de
[b] *R. Pollak, Prof. Dr. S. Ebbinghaus*
Physical and Theoretical Chemistry, TU Braunschweig
38106 Braunschweig (Germany)
E-mail: s.ebbinghaus@tu-braunschweig.de

Supporting information for this article is available on the WWW under https://doi.org/10.1002/syst.202000051

An invited contribution to a Special Collection on Crowded Systems

© 2021 The Authors. ChemSystemChem published by Wiley-VCH GmbH. This is an open access article under the terms of the Creative Commons Attribution Non-Commercial NoDerivs License, which permits use and distribution in any medium, provided the original work is properly cited, the use is non-commercial and no modifications or adaptations are made.

ChemSystemsChem
Articles
doi.org/10.1002/syst.202000051
Chemistry Europe
European Chemical Societies Publishing

the formation of PIC fibrils, whereas sucrose, the corresponding monomeric unit of Ficoll, did not show any effects on fibrillization. *In vivo* experiments, where HeLa cells were exposed to dilute PIC solutions well below the aggregation threshold further supported the use of PIC as a protein substitute to probe how sensitive fibril formation responds to the variation of macromolecular crowding. The dyestuff PIC penetrated the cells and the crowded cellular environment promoted fibril formation, which could successfully be tracked by fluorescence imaging. Exposing the cells to salt-induced osmotic stress increased intracellular crowding and promoted the extent of fibrillization.

In the present work we further elucidate the differences in crowding effects of TEG, PEG, sucrose and Ficoll 400 on the fibrillization of PIC. Therefore, aggregation thresholds are treated as solubility limits (phase diagrams) to enable the evaluation of chemical potential derivatives μ_{23} of PIC denoted as component 2 with respect to a variation of the concentration of synthetic crowders denoted as component 3. The chemical potential derivatives μ_{23} describe preferential or unfavourable interactions of synthetic crowding agents with PIC. Data from Knowles et al.[13] allow a calculation of theoretical values of μ_{23} for TEG and PEG on the basis of water accessible surface areas of PIC with the corresponding group interaction potentials of the crowding agents. To gain the change of entropy, enthalpy and Gibbs free energy of the aggregation process of PIC in the presence of the above introduced crowding agents the concept of the ceiling temperature[14] is employed. As it will be shown, the variation of the Gibbs free energy with the concentration of crowding agents is another method to determine μ_{23}, allowing a comparison with findings from solubility limits and from theoretical values on the basis of water-accessible surface areas. The results provide a physicochemical reasoning for the mode of impact exerted by PEG, TEG and Ficoll 400 on the self-assembly of PIC as a model for proteins.

2. Results and Discussion

At the onset of the present work, the aggregation behaviour of PIC was cast into plots of aggregation thresholds denoted as phase diagrams. The diagrams correlate the temperature of J-aggregate formation with the corresponding concentration of PIC. Figure 1 shows the resulting phase boundaries of PIC in the presence of all investigated crowding agents with concentrations of 2%, 5% and 10% by weight and in pure water as a reference system. Samples above the phase boundary exhibit almost exclusively monomers and H-aggregates. H-aggregates are oligomeric species where the alignment of the transition dipole moments result in a hypsochromic shift in UV-Vis absorbance.[3] As soon as the conditions fall below the phase boundary, J-aggregates are formed and a new sharp peak arises in UV-Vis spectra. In contrast to H-aggregates, the transition dipole moments of PIC molecules within J-aggregates are aligned in such a way that the resulting J-peak is bathochromically shifted relative to the monomer peak.

In the presence of Ficoll 400 a pronounced shift of the phase boundary to elevated temperatures is observed. However, a 2.5-fold increase in the concentration of Ficoll does not further shift the boundary. Only its slope increases slightly, which indicates a stronger dependency on the PIC concentration. Noteworthy, sucrose as the major monomeric building unit of the polymer Ficoll, barely affects the aggregation of PIC. A slight decrease in aggregation temperatures is only observed at a sucrose content of 10% by weight. This strong promotion of the aggregation of PIC by Ficoll 400 compared to the almost inert behaviour of sucrose suggests an interaction exerted by the Ficoll polymers, which is based on excluded volume rather than on chemical interactions between crowder and PIC.

TEG in turn lowers the aggregation threshold of PIC already at a content of 2% by weight, thus hindering the formation of J-aggregates. An increase in the TEG content is accompanied with a further shift of the phase boundary to lower aggregation temperatures. A similar behaviour can be found when exposing PIC to PEG. In contrast to Ficoll 400, interactions of PEG or TEG with PIC cannot be attributed to excluded volume effects

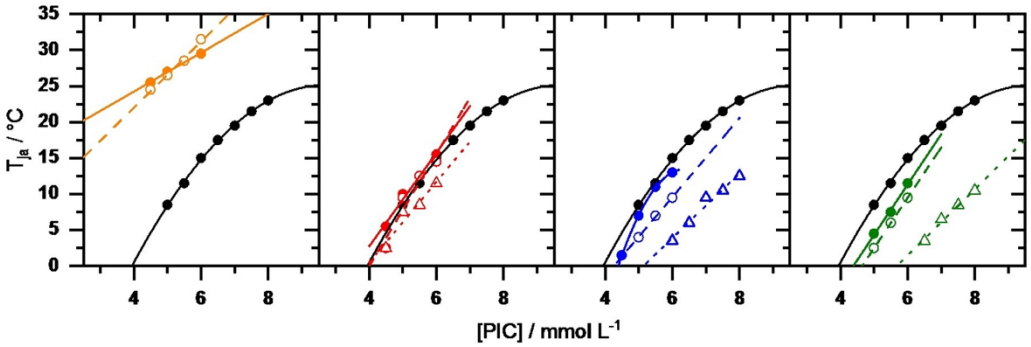

Figure 1. Phase diagrams of PIC in pure water (black) and in the presence of Ficoll (orange), sucrose (red), PEG (blue) and TEG (green). The content of crowding agents amounts to 2% (filled circles), 5% (open circles) and 10% (triangles) by weight. Linear fits of data points are represented by solid lines for 2%, dashed lines for 5% and dotted lines for 10% crowding content by weight.

 © 2021 The Authors. ChemSystemsChem published by Wiley-VCH GmbH

ChemSystemsChem
Articles
doi.org/10.1002/syst.202000051
Chemistry Europe
European Chemical Societies Publishing

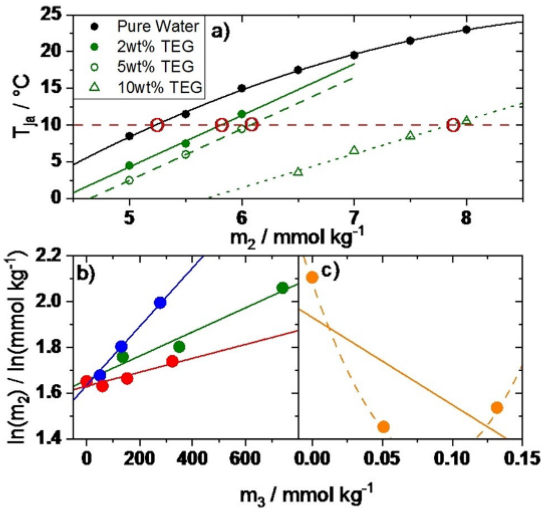

Figure 2. a) Aggregation temperatures as a function of the PIC concentration at variable content of TEG as a crowding agent including pure water as reference. The symbols indicate the content of TEG by weight percent: 0% (black filled circles), 2% (green filled circles), 5% (green open circles) and 10% (green triangles). The red dashed line represents an isotherm at 10 °C, the red circles indicate the respective threshold concentrations m_2. b) ln(m_2) versus m_3 for systems containing TEG (green), PEG (blue) or sucrose (red) at 10 °C and c) for Ficoll (orange) at 25 °C. The linear slope of the fit is used to calculate μ_{23} according to Equation (3).

because of their inhibitory impact on the formation of J-aggregates.

In order to describe these diverse effects on the aggregation threshold of PIC, an approach based on the differential of chemical potentials of the model compound PIC with respect to the different crowding agents is applied. As a starting point, we consider the formation of a precipitate or large aggregate as a reaction, leading to an equilibrium of soluble molecules of a model component 2 with precipitate of 2 defined by the equilibrium constant K_{obs} [Equation (1)]:

$$K_{obs} = \frac{1}{c_{2,ss}} = e^{-\frac{\Delta G^0}{RT}} \quad (1)$$

The equilibrium constant K_{obs} thus represents the solubility product of component 2, with $c_{2,ss}$ the molar concentration of component 2 at the solubility limit, ΔG^0 the standard free energy change during precipitation, R the ideal gas constant and T the temperature. The introduction of a co-solute c_3 alters the solubility product according to Equation (2):

$$\left(\frac{\delta \ln(K_{obs})}{\delta c_3}\right)_{\mu_2,p,T} = -\frac{1}{RT}\left(\frac{\delta \Delta G^0}{\delta c_3}\right)_{\mu_2,p,T} = -\left(\frac{\delta \ln(c_{2,ss})}{\delta c_3}\right)_{\mu_2,p,T} \quad (2)$$

whereby the equilibrium state with its solubility limit $c_{2,ss}$ renders Equation (2) a partial derivative established at constant chemical potential of model component 2.

According to Knowles et al,[13] Equation (2) on a molal scale corresponds to the chemical potential derivative μ_{23} of a model component 2 in the presence of a co-solute 3 [Equation (3)]:

$$\mu_{23} = -RT\left(\frac{\delta \ln m_{2,ss}}{\delta\, m_3}\right)_{\mu_2} \quad (3)$$

where m_2 and m_3 are molal concentrations of component 2 and 3 respectively at constant temperature T and at constant chemical potential μ_2 of component 2. Equation (3) only evolves in this way if the concentration of component 2 is dilute enough to be able to neglect self-interactions (see Supporting Information S2).

This concept is transferred to the solubility of PIC (component 2) in the presence of crowding agents (component 3). The solubility limit of PIC corresponds to the formation of fiber-like J-aggregates. Data evaluation according to Equation (3) was done with the data shown in Figure 1 in a temperature regime of 277 K ≤ T ≤ 285 K (25 °C ≤ T ≤ 30 °C) for Ficoll 400 and in a temperature regime of 298 K ≤ T ≤ 303 K (4 °C ≤ T ≤ 12 °C) for all other crowding agents.

In a first step data from Figure 1 are re-plotted as aggregation temperature versus PIC concentration m_2 and trends are established by fitting these data in a quadratic mode for the system in pure water and in 2 wt% PEG and in a linear mode for all other systems. With these regression curves threshold values m_2 are interpolated at different crowder contents m_3 and a given temperature. The approach is visualized in detail in Figure 2a for TEG as the crowding agent at T = 10 °C. Interpolated data are then plotted as isotherms of $ln(m_2)$ versus m_3, which is exemplarily shown in Figure 2b for TEG, PEG and sucrose at T = 10 °C and in Figure 2c for Ficoll 400 at T = 25 °C. Linear fitting gives a slope which is equal to $-\mu_{23}/RT$. This procedure is repeated at an extended set of isotherms. In all cases, an interval of 0.1 K was used as mesh size for the grid of isotherms.

Figure 3 presents the values for μ_{23} in the specified temperature regime. The temperature dependences of μ_{23} in Figure 3 are negligibly small within experimental uncertainty for all crowders. We therefore discuss differences among crowders in terms of the respective average values. As already indicated by the phase diagrams, sucrose does not strongly alter the phase boundary of PIC. From the values of μ_{23} of all investigated crowders averaged over the whole temperature regime respectively the value from sucrose, which amounts to -160 ± 60 cal mol^{-1} molal^{-1}, is the value closest to zero. The chemical potential derivative of PIC in the presence of TEG exhibits negative values with a mean value of -290 ± 30 cal mol^{-1} molal^{-1}. When PIC is exposed to PEG, the mean value decreases further to -690 ± 40 cal mol^{-1} molal^{-1}. A negative μ_{23} indicates attractive interactions of crowding agents with PIC relative to interactions with water as the reference. PEG and TEG accumulate on the surface of PIC molecules while excluding water molecules. The inhibitory effect of PEG and TEG on the formation of J-aggregates is thus explained by a blockage of binding sites by the crowding agents. J-aggregates are formed when intermolecular forces between PIC molecules

 © 2021 The Authors. ChemSystemsChem published by Wiley-VCH GmbH

ChemSystemsChem
Articles
doi.org/10.1002/syst.202000051
Chemistry Europe
European Chemical Societies Publishing

overcome μ_{23}, which happens at lower temperatures for TEG and PEG than it does in pure water.

Preferential interactions between the lone ion pairs of the oxygen atoms in PEG with cationic charges do not come as a surprise but are well established in literature.[15] Aside from crown ether like assemblies of PEG with lysine residues from *Penicillium* antifungal protein, there is structural evidence for interactions of PEG also with aromatic residues of calix[n]arene molecules.[16] Since aromatic π-systems and cationic nitrogen atoms also occur on PIC similar types of interactions may exist with PEG and TEG with PIC.

The introduction of Ficoll 400 leads to a remarkable increase in aggregation temperature. The corresponding mean value of μ_{23} amounts to $2.1{\cdot}10^6 \pm 1.6 \cdot 10^6$ cal mol^1 molal^{-1}, which is 3 orders of magnitude larger than values typically found for μ_{23}.[13,17] Although the positive sign of the values is compatible with a depletion of Ficoll 400 from the surface of PIC, such an explanation oversimplifies reality as the size of Ficoll 400 is much larger than the size of PIC. Hence, the increased tendency of PIC to form aggregates in the presence of Ficoll mostly originates from an increase in local concentration of PIC because of the excluded volume of Ficoll. In order to estimate the effect of volume exclusion, the occupied volume of Ficoll molecules within a solution is calculated. For this purpose, Ficoll molecules are treated as sphere-like particles impenetrable to PIC molecules with a sphere radius estimated with the hydrodynamic radius of $R_H = 10$ nm, as stated by the supplier. For a solution containing 5 wt% Ficoll 400 the excluded volume amounts to 34% of the overall volume. Therefore, the concentration of PIC is increased by 51%. As it is shown in the Supporting Information S1, this increase in concentration can not be the sole source of the crowding effect as the correction of the concentration by the volume occupied by the crowder still does not suffice to reach the experimentally determined aggregation threshold. Thus, this crude approach underestimates mutual excluded volume effects between PIC molecules and Ficoll 400 polymers.

In order to further support the scheme of preferential attraction between PIC and TEG or PEG, we apply the water-accessible surface area(ASA)-based interpretation of μ_{23} developed by Knowles et al.[13] This approach estimates theoretical values of μ_{23} by the sum of chemical interaction coefficients of the crowding agent with the functional groups of PIC and salt ions present in solution [Equation (4)].

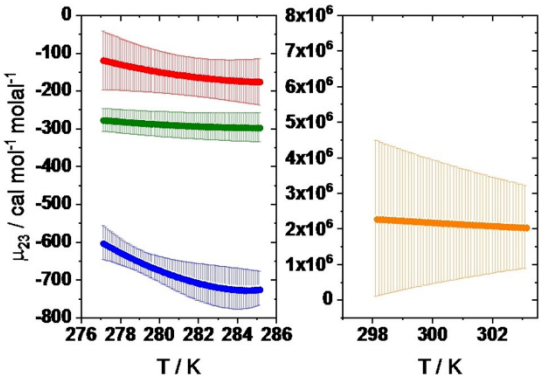

Figure 3. The temperature dependence of the chemical potential derivative μ_{23} of PIC with a) TEG (green), PEG (blue), sucrose (red) and b) Ficoll (orange). Data were established by applying Equation (3) to the phase diagrams shown in Figure 1. An outline of the approach is given in Figure 2.

$$\mu_{23} = \sum_i \alpha_{crowding\ agent,i} \cdot ASA_i^{PIC} + \sum_k \beta_{crowding\ agent,\ k} \cdot \nu_k^{ion} \quad (4)$$

The chemical interaction coefficients α and β of various chemical groups and counterions respectively with TEG and PEG were empirically quantified by Knowles et al.[13] In Eq. 4 ν_k^{ion} is the stochiometric factor of counterion k in solution and ASA_i^{PIC} is the water-accessible surface of functional group i of PIC. The water-accessible surfaces of the chemical groups together with the corresponding chemical interactions coefficients are listed in Table 1. Application of Equation (4) with values stated in Table 1 results in theoretical estimations of the chemical potential derivative μ_{23} of PIC in the presence of TEG of -930 ± 20 cal mol^{-1} molal^{-1} and in the presence of PEG of -2200 ± 340 cal mol^{-1} molal^{-1}. A comparison with experimental data shows that the theoretical predictions exceed experimental values by a factor of 3. However, the ratio of the values of μ_{23} for TEG and PEG is μ_{23}(PEG)/μ_{23}(TEG) = 2.4 for experimentally established data in close agreement with the respective ratio from the theoretically estimated μ_{23}.

A possible cause for the discrepancy between experimental data and theoretical predictions may be the fact that the calculated surfaces in Table 1 are only partly accessible to the respective co-solute, whereas the model assumes that the whole molecular surface is accessible. To bring experimental data in line with the model, one has to assume that only one third of the total surface of PIC is accessible. Since PIC tends to

Table 1. Water-accessible surface areas ASA_i of the chemical groups within PIC estimated with the software *Surface Racer 5.0*. The corresponding chemical interaction coefficients $\alpha_{crowding\ agent,i}$ and $\beta_{crowding\ agent,k}$ for TEG and PEG were taken from Ref. [13].

Chemical group *i* Ion *k*	ASA_i [Å^2]	$\alpha_{TEG,i}$ [cal mol^{-1} molal^{-1} Å^{-2}]	$\alpha_{PEG,i}$ [cal mol^{-1} molal^{-1} Å^{-2}]	$\beta_{TEG,k}$ [cal mol^{-1} molal^{-1} ion^{-1}]	$\beta_{PEG,k}$ [cal mol^{-1} molal^{-1} ion^{-1}]
Aromatic C	371.5	-2.66 ± 0.028	-6.26 ± 0.077	–	–
Aliphatic C	165.5	-0.349 ± 0.029	-0.892 ± 0.092	–	–
Amine N	8.9	-1.67 ± 0.056	-3.64 ± 0.16	–	–
Chloride Cl^-	–	–	–	132 ± 6.8	308.8 ± 21

 © 2021 The Authors. ChemSystemsChem published by Wiley-VCH GmbH

ChemSystemsChem
Articles
doi.org/10.1002/syst.202000051
Chemistry Europe
European Chemical Societies Publishing

form dimers and oligomers, already above the aggregation threshold and especially at the proximity of the threshold, a fraction of the surface of PIC is buried within PIC oligomers and not accessible anymore. Dimerization would for instance decrease the accessible surface by a factor of 1/2 at the most. This factor further decreases the greater the degree of oligomerization gets. An alternative and/or additional explanation for the deviation between experimental and theoretical values may be based on the loss of water-accessible surface area during aggregation. The ASA-approach used in the present work assumes that PIC aggregates establish a separate, precipitated phase with a negligible surface per molecule. Although, the water-accessible surface area per monomer is sharply reduced during self-assembly, the remaining area per PIC monomer exposed to water by the aggregates is far from being negligible. By considering the most recent structure model from von Berlepsch et al.,[3] a loss of water-accessible surface area during aggregation of monomers by a factor of at least 1/2 can be assumed. Therefore, a reduction of the truly accessible surface of PIC by one third of its value under experimental conditions is conceivable.

In a similar approach published recently by Shumilin et al.[18] the impact of sugars has been analysed on the self-association and solubility of caffeine. Caffeine molecules self-assemble towards oligomeric and polymeric stacks, in close analogy to the aggregation of PIC. However, unlike to PIC, the caffeine stacks eventually precipitate. The analysis revealed a preferential adsorption of sugars to caffeine monomers relative to the same units incorporated into the polymeric stacks,[18] similar to the type of interaction of TEG and PEG with PIC monomers revealed in the present work. Although this preferential interaction favors the monomeric state in comparison to the polymeric state in both cases, increasing amounts of a sugar additives decreases the solubility of caffeine leading also to increasing amounts of precipitate, whereas PIC is arrested in its fiber-like state without further precipitation. The origin for the sugar induced promotion of caffeine precipitation, accompanied by an increase of monomer concentration was explained as follows. Caffeine precipitates do not expose a significant surface to the solution as fiber or stack-like polymers would do, thereby entirely avoiding disfavoring contacts between stacks and sugar additives. This does not only promote monomer formation on the expense of destabilized polymers, but also diverts polymeric stacks towards the precipitate state thus decreasing overall solubility of caffeine as the sugar content increases.[18]

In order to obtain additional information on the thermodynamic properties of the systems, concepts from polymer chemistry are applied. As soon as the aggregation threshold is surpassed, monomeric PIC starts to self-assemble to J-aggregates. This process is considered to have a close analogy to a polymerization proceeding via chain growth limited by the ceiling temperature.[14] At equilibrium, monomer addition and monomer liberation at growing chain ends exhibit identical rate constants and no further net growth of chains occurs. A similar situation can be found at the aggregation threshold of PIC. Here, J-aggregates are formed and are in equilibrium with remaining monomeric PIC. Any temperature change would change the equilibrium concentrations and the ceiling temperature is that temperature at which a given monomer concentration starts to form J-aggregates or stops to form J-aggregates, depending on the starting temperature. Thus, the aggregation threshold temperature can be interpreted as a ceiling temperature with the overall PIC concentration *[PIC]* being the equilibrium monomer concentration at the ceiling temperature [Equation (5)].

$$\frac{1}{T_{ja}} = \frac{\Delta S^0}{\Delta H^0} + \frac{R \cdot \ln([PIC])}{\Delta H^0} \tag{5}$$

In Equation (5), T_{ja} is the ceiling temperature here also denoted as the aggregation temperature, ΔS^0 the standard aggregation entropy and, ΔH^0 the standard aggregation enthalpy. A plot of T_{ja}^{-1} versus *ln([PIC])* is then fitted linearly where the slope results in $R/\Delta H^0$ and the y-intercept provides $\Delta S^0/\Delta H^0$. Figure 4 represents all data shown in Figure 1 now

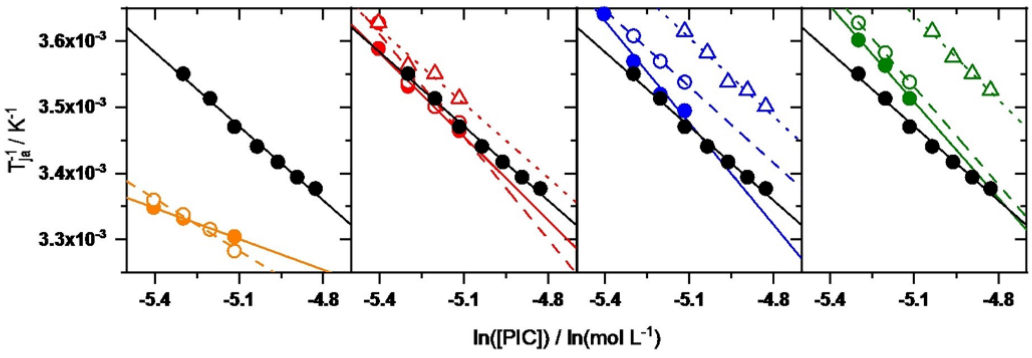

Figure 4. Plots of the inverse aggregation temperature T_{ja}^{-1} versus the logarithmic molar PIC concentration *ln([PIC])* in pure water (black) and in the presence of Ficoll (orange), sucrose (red), PEG (blue) and TEG (green). The content of crowding agents amounts to 2% (filled circles), 5% (open circles) and 10% (triangles) by weight. Linear fits are represented by solid lines for 2%, dashed lines for 5% and dotted lines for 10% crowding content by weight. The y-offset of the resulting fits gives $\Delta S^0/\Delta H^0$ and the slope amounts to $R/\Delta H^0$ according to Equation (4).

© 2021 The Authors. ChemSystemsChem published by Wiley-VCH GmbH

ChemSystemsChem | Articles doi.org/10.1002/syst.202000051 | Chemistry Europe European Chemical Societies Publishing

plotted according to Equation (5). The obtained values for ΔS^0 and ΔH^0 are listed in Table 2.

All obtained values for ΔS^0 and ΔH^0 are negative, suggesting that the formation of J-aggregates decreases the number of monomer arrangements within the solution and is energetically favoured. Daltrozzo et al.[4] investigated the aggregation enthalpy by handling J-aggregates as a slightly soluble salt and obtained $\Delta H = -7500 \pm 500$ cal mol^{-1}, which is in fair agreement with data from this work.

We further validate these results by calorimetric measurements of PIC in pure water at a concentration of $[PIC] = 20$ mM (see Supporting Information Figure S3) and in the presence of 5 wt% PEG, 5 wt% sucrose and 10 wt% sucrose. While decreasing the temperature, a sharp exothermic transition in ΔC_p^{EXP} occurs corresponding to the aggregation of PIC.

Evaluation of the corresponding molar enthalpy is given in Section S4 of the Supporting Information. We find that the molar enthalpy of PIC is -3060 ± 61 cal mol^{-1} in pure water and -2840 ± 57 cal mol^{-1} in the presence of 5 wt% PEG. In 5 wt% and 10% sucrose solutions we find -3080 ± 61 cal mol^{-1} and -2770 ± 56 cal mol^{-1}, respectively. The molar enthalpies measured by DSC are smaller by up to a factor of 2 compared the values given in Table 2. This may be due to the interruption of the aggregation process at the lowest accessible temperature in DSC-thermograms that is not accounted for by the monomer correction (Section S4 of the Supporting Information).

We further observe a significant shift of the aggregation peak for PEG as cosolute. The observed transition at 42 °C at 20 mM PIC in pure water drops to 35 °C in the presence of 5 wt % PEG which is in agreement with the temperature trends shown in Figure 1. Addition of sucrose does not have such an effect, the transition is similar to pure water. This is in line with previous findings, that PEG inhibits formation of J-aggregates while sucrose does not alter the aggregation.

According to the phase diagram shown in Figure 1, Ficoll 400 promotes the self-assembly of PIC. While discussing the respective values μ_{23}, it was already stated that excluded volume effects may be the cause for the promotion of the formation of J-aggregates by Ficoll 400. In order to further underline this statement the scaled particle theory (SPT) was applied.[19,20] With the SPT, activity coefficients of all species involved in a reaction are calculated under consideration of excluded volume effects in order to establish an enhancement factor Γ which describes the ratio of equilibrium constants under crowded and non-crowded conditions. For the system containing 5 wt% Ficoll 400, Γ derived from the present experiments amounts to 1.85 at 298 K. The SPT gives a value of 1.4 to 1.55 (See Supporting Information) which is in fair agreement with 1.85 from the ceiling temperature approach.

The comparison of the reference system in water and systems containing sucrose reveals no significant differences in terms of ΔG^0. Introducing TEG or PEG is accompanied with an increase in ΔG^0 to less negative values, indicating less favoured aggregation of PIC at a given temperature in relation to the reference system in water. The dependence of ΔG^0 on the crowder content is used in the next step to enable a comparison with the results from the chemical potential analysis.

As it is already outlined in Equations (2) and (3), the derivative of ΔG^0 with respect to m_3 can directly be related to μ_{23} in case of a precipitation process [Equation (6)].

$$\mu_{23} = -\left(\frac{\delta \Delta G^0}{\delta m_3}\right) \sim \frac{(\Delta G^0_{m_3} - \Delta G^0_{m_3=0})}{\Delta m_3} \tag{6}$$

This is done by plotting the change in Gibbs free energy of the crowded systems ΔG^0_{m3} versus the molal concentration m_3 of the respective crowding agent with the slope amounting to $-\mu_{23}$.

Figure 5 shows the dependency of ΔG^0 on the crowder concentration. All obtained values are summed up in Table 3. For the system containing sucrose, a value of $\mu_{23} = 60 \pm 300$ cal mol^{-1} molal^{-1} is calculated, which is close to zero and thus in agreement with the fact that sucrose does not alter J-aggregation due to lack of significant interactions with PIC. The system containing TEG gives $\mu_{23} = -230 \pm 130$ cal mol^{-1} molal^{-1}

Table 2. The standard entropy ΔS^0 and standard enthalpy ΔH^0 of J-aggregate formation under all conditions shown in Figure 4. Additionally, the standard Gibbs energy of J-aggregate formation ΔG^0 at $T = 298.15$ K is calculated according to $\Delta G^0 = \Delta H^0 - T \cdot \Delta S^0$.

Crowding agent	Crowder content [wt%]	ΔS^0 [cal mol^{-1} K^{-1}]	ΔH^0 [cal mol^{-1}]	ΔG^0 [cal mol^{-1}]
None (pure water)	0	-8.3 ± 0.7	-5300 ± 210	-2830 ± 300
Ficoll 400	2	-31.8 ± 1.7	-12700 ± 500	-3250 ± 730
	5	-14.6 ± 2.5	-7550 ± 750	-3200 ± 1050
	10			
sucrose	2	-6.1 ± 1.2	-4700 ± 350	-2900 ± 500
	5	-3.1 ± 2.5	-3820 ± 700	-2900 ± 1030
	10	-8.5 ± 3.3	-5300 ± 930	-2770 ± 1350
PEG	2	-3.3 ± 1.7	-3860 ± 470	-2880 ± 690
	5	-8.1 ± 0.6	-5160 ± 160	-2740 ± 240
	10	-7.9 ± 1.6	-5000 ± 440	-2640 ± 650
TEG	2	-4.3 ± 1.5	-4100 ± 420	-2820 ± 610
	5	-4.1 ± 0.3	-4040 ± 80	-2800 ± 120
	10	-6.9 ± 1	-4680 ± 280	-2630 ± 410

 © 2021 The Authors. ChemSystemsChem published by Wiley-VCH GmbH

ChemSystemsChem
Articles
doi.org/10.1002/syst.202000051
Chemistry Europe
European Chemical Societies Publishing

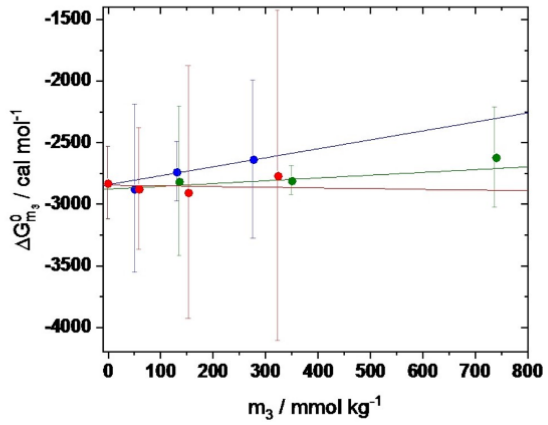

Figure 5. The standard Gibbs energy of J-aggregate formation ΔG^0 versus the molal concentration m_3 of sucrose (red), PEG (blue) and TEG (green). The lines represent linear fits.

and when PEG is introduced, μ_{23} amounts to -730 ± 180 cal mol^{-1} molal^{-1}. Again, the two values are within experimental uncertainty in good agreement with the results from direct evaluation of μ_{23}.

3. Conclusion and Outlook

Pseudo isocyanine chloride (PIC) exhibits a mixture of hydrophobic and hydrophilic spots together with a marginal solubility in aqueous solution, similar to many amyloidogenic proteins. As a consequence thereof (PIC) self-assembles toward fiber-like entities denoted as J-aggregates. The self-assembly of PIC depends on the PIC concentration and temperature. With a preceding work[12] we were able to verify that the self-assembly of PIC is prone to macromolecular crowding, visualised by shifted aggregation boundaries in *in vitro* experiments and supported by a strong aggregation in cellular environment exposed to a supernatant with a PIC content well below the respective aggregation boundary during *in vivo* experiments. This further illustrates close analogies of self-assembly of PIC to self-assembly of proteins in biological systems and identifies PIC to be a suitable model system for mimicking fibril formation of proteins.

In the present work we extended our previous findings by means of an analysis of thermodynamic parameters. In a first step we treated the established phase diagrams of PIC in the presence of various crowding agents as solubility limits with aggregated PIC being a separate phase. Crowding agents could either induce or inhibit the formation of J-aggregates, leading to a lower or higher solubility respectively. Therefore, the chemical potential derivative μ_{23} was calculated to quantify preferential interactions between the crowding agent and PIC. Sucrose does not alter the formation of J-aggregates and thus does not interact with PIC, indicated by a value of μ_{23} near zero. Ficoll, as a copolymer of sucrose and epichlorohydrin, pushes the aggregation threshold towards higher temperatures. In line with this, the resulting values for the chemical potential derivatives μ_{23} are positive and suggest a dominant role of excluded volume interactions which, in the present work, was taken into account by two approaches. In a simple approach the concentration of Ficoll 400 was corrected by the volume occupied by Ficoll polymers and a second approach applied the contribution of mutual excluded volume effects between PIC and crowder by calculating activity coefficients for PIC using the scaled particle theory. When exposing dissolved PIC to PEG or TEG, a decrease in aggregation temperatures can be observed which is accompanied by a negative value for μ_{23}. Those inhibitory effects can be attributed to preferential interactions of TEG and PEG with PIC, blocking binding sites and preventing aggregation. Application of the model of water accessible surface areas[13] for the interactions of PEG and TEG with PIC leads to theoretical values for μ_{23} which are qualitatively in agreement with experimental results. Quantitative discrepancies can be reconciled with only a partial accessibility of the surface of PIC due to oligomerization and or by only a partial obstruction of PIC surface toward water in the aggregate.

As the self-assembly of PIC may bear close similarity to a polymerisation, the concept of the ceiling temperature was applied to gain information on ΔS^0 and ΔH^0 and to be able to calculate ΔG^0. In general, formation of J-aggregates goes along with a decrease in entropy due to the formation of highly ordered structures. The negative values for ΔH^0 furthermore show that J-aggregates are the more stable species and energy is gained during the formation. To be able to compare the results from both approaches, the variation of ΔG^0 with the molal concentration of the crowding agents was used to calculate μ_{23}. A comparison of μ_{23} from the ceiling temperature approach reveals good agreement with μ_{23} from the solubility measurements. The resulting validity of the concept of a ceiling temperature fits well to a chain growth mechanism rather than a step wise growth process as the mechanism underlying the evolution of J-aggregates.

Table 3. The chemical potential derivatives μ_{23} for all investigated systems from the solubility approach based on Equation (3), from data of the ceiling temperature analogy based on Equation (6) and from the ASA-model[13] based on Equation (4).

Crowding agent	μ_{23} Eq. (3) cal mol molal^{-1}	μ_{23} Eq. (6)	μ_{23} Eq. (4)
Ficoll 400	$2.1*10^6\pm 1.6*10^6$		–
sucrose	-160 ± 60	60 ± 300	–
PEG	-690 ± 40	-730 ± 180	-2200 ± 340
TEG	-290 ± 30	-230 ± 130	-930 ± 20

 © 2021 The Authors. ChemSystemsChem published by Wiley-VCH GmbH

ChemSystemsChem | Articles doi.org/10.1002/syst.202000051 | Chemistry Europe European Chemical Societies Publishing

The present analysis together with the preceding work[12] identifies PIC as a suitable candidate for further studies regarding the elucidation of fibril formation in biological systems. The striking change of the absorption pattern of PIC during aggregation gives access to a straightforward data analysis and similarities of self-assembly of PIC and of proteins may allow to transfer established principles of crowding effects on PIC to amyloidogenic proteins.

Experimental Section

Materials

The crowding agents triethylene glycol (TEG), polyethylene glycol (PEG, $M_n = 400$ g mol^{-1}), sucrose, Ficoll 400 ($M_n = 400000$ g mol^{-1}) and 1,1′-diethyl-2,2′-cyanine iodide (PII) were received from Sigma Aldrich (Darmstadt, Germany). 1,1′-diethyl-2,2′-cyanine chloride (PIC) with a molar mass of 362.9 g mol^{-1} was obtained from the iodide salt by ion exchange with use of the ion exchanger Amberlite IRA-402 from Sigma Aldrich (Darmstadt, Germany). PIC was stored in the absence of light to prevent degradation. Sample preparation was done with MS grade water from VWR International (Radnor, USA).

Ion exchange

The ion exchanger was dispersed in Milli-Q water and filled in a column. A solution of 500 mg pseudo isocyanine iodide dissolved in a small amount of dimethyl sulfoxide (DMSO) was prepared. The DMSO-solution was then diluted with Milli-Q water and filled into the column. The column was flushed with Milli-Q water until further eluate was fully decolorized, demonstrating complete elution of the dyestuff from the column. After evaporating part of the water of the eluate under vacuum, ethyl acetate was added which induced precipitation of PIC. Precipitated PIC was filtered and dried in vacuum at 60 °C. The yield was 88% based on the initial amount of PII.

Sample Preparation

Aqueous solutions with 2%, 5% and 10% by weight of crowding agents were prepared. Stock solutions of PIC were made by dissolving PIC either in pure water or in the respective crowding solution to reach a PIC concentration of 6 mM. In some cases, a stock concentration of 8 mM became necessary to facilitate experiments in a suitable temperature regime. The stock solutions were stirred overnight in the absence of light at 50 °C to ensure homogeneity and complete dissolution of PIC. Stock solutions were then diluted with the appropriate solvent to keep the crowding agent concentration constant whilst decreasing PIC concentration in increments of 0.5 mM steps to 4 mM.

Determination of the aggregation threshold via UV-Vis spectroscopy

UV-Vis spectroscopy was carried out with a *Lambda-19* spectrometer from Perkin Elmer (Waltham, USA). The sample holder was a custom-built copper block, which can be thermally equilibrated by an external thermostat. A demountable cuvette with a path length of 0.01 cm, provided by Hellma Analytics (Mühlheim, Germany), was used. A slit width of 2 mm was suitable to keep the primary intensity low enough so that recorded absorptions were below the maximum detector threshold throughout all experiments. Absorption at $\lambda = 573$ nm A_{573} was recorded. Thus, the aggregation temperature T_{ja} at a fixed concentration was determined by observing A_{573} while gradually decreasing the temperature. The experiment was usually started at 25 °C. For samples containing Ficoll 400, the initial temperature had to be set to 35 °C. After the sample was thermally equilibrated, the temperature was decreased by 1 °C while simultaneously recording A_{573} for at least 10 minutes. This step was repeated until a substantial increase in A_{573} was observed. Accordingly, the aggregation temperature was defined as the centre of the temperature interval at which A_{573} increased strongly. If, for instance, the increase occurred between 9 °C and 8 °C, 8.5 °C was set as the aggregation temperature.

Evaluation of μ_{23} via chemical interaction coefficients

Surfaces of the functional groups within PIC were calculated with Surface Racer 5.0[21] with use of the Richards set of van der Waals radii[22] and a probe radius of 1.4 Å for water. The two nitrogen atoms within the quinoline-like system of PIC were both handled as amide groups. This is justified because of the relatively small contribution of those groups to the overall water-accessible surface. The atomic coordinates needed for ASA calculations were obtained by minimizing the interatomic energy according to a mm2 force field[23] within the software Chem3D 16.

Differential Scanning Calorimetry (DSC)

The DSC measurements were conducted using a MicroCal PEAQ-DSC instrument from Malvern Panalytical GmbH with a sample volume of 250 µL. The temperature was scanned from 100 °C to 5 °C at a speed of 60 K h^{-1}. A pressure of 52 psi was applied to prevent evaporation. Three repetitive scans were performed at a concentration of *[PIC]* = 20 mM in aqueous solution without and with two different crowder (5 wt% PEG, 5 wt% sucrose, 10 wt% sucrose) respectively.

Acknowledgements

Open access funding enabled and organized by Projekt DEAL.

Conflict of Interest

The authors declare no conflict of interest.

Keywords: aggregation · crowding · macromolecules · pseudo-isocyanine chloride · self-assembly

[1] S. B. Zimmerman, S. O. Trach, *J. Mol. Biol.* **1991**, *222*, 599.
[2] T. C. Laurent, *Biochem. J.* **1963**, *89*, 253.
[3] H. von Berlepsch, C. Böttcher, L. Dähne, *J. Phys. Chem. B* **2000**, *104*, 8792.
[4] E. Daltrozzo, G. Scheibe, K. Gschwind, F. Haimerl, *Photogr. Sci. Eng.* **1974**, *18*.
[5] G. Scheibe, *Angew. Chem.* **1937**, *50*, 212.
[6] B. Herzog, K. Huber, H. Stegemeyer, *Langmuir* **2003**, *19*, 5223.
[7] F. Würthner, T. E. Kaiser, C. R. Saha-Möller, *Angew. Chem. Int. Ed.* **2011**, *50*, 3376.
[8] E. E. Jelley, *Nature* **1936**, *138*, 1009.
[9] E. E. Jelley, *Nature* **1937**, *631*.

 © 2021 The Authors. ChemSystemsChem published by Wiley-VCH GmbH

ChemSystemsChem | Articles doi.org/10.1002/syst.202000051 | Chemistry Europe European Chemical Societies Publishing

[10] G. Scheibe, L. Kandler, H. Ecker, *Naturwissenschaften* **1937**, *25*, 474.
[11] G. Scheibe, L. Kandler, H. Ecker, *Naturwissenschaften* **1937**, *25*, 75.
[12] B. Hämisch, R. Pollak, S. Ebbinghaus, K. Huber, *Chem. Eur. J.* **2020**, *26*, 7041.
[13] D. B. Knowles, I. A. Shkel, N. M. Phan, M. Sternke, E. Lingeman, X. Cheng, L. Cheng, K. O'Connor, M. T. Record, *Biochemistry* **2015**, *54*, 3528.
[14] F. S. Danton, K. J. Ivin, *Nature* **1948**, *162*, 705.
[15] J. J. Christensen, D. J. Eatough, R. M. Izatt, *Chem. Rev.* **1974**, *74*, 351.
[16] J. M. Alex, M. L. Rennie, S. Engilberge, G. Lehoczki, H. Dorottya, A. Fizil, G. Batta, P. B. Crowley, *IUCrJ* **2019**, *6*, 238.
[17] E. J. Guinn, L. M. Pegram, M. W. Capp, M. N. Pollock, M. T. Record, *Proc. Natl. Acad. Sci. USA* **2011**, *108*, 16932.
[18] I. Shumilin, C. Allolio, D. Harries, *J. Am. Chem. Soc.* **2019**, *141*, 18056.
[19] H. Reiss, H. L. Frisch, J. L. Lebowitz, *J. Chem. Phys.* **1959**, *31*, 369.
[20] A. P. Minton, *Mol. Cell. Biochem.* **1983**, *55*, 119.
[21] O. V. Tsodikov, M. Thomas Record, Y. V. Sergeev, *J. Comput. Chem.* **2002**, *23*, 600.
[22] F. M. Richards, *Ann. Rev. Biophys. Bioeng.* **1977**, *6*, 151.
[23] N. L. Allinger, *J. Am. Chem. Soc.* **1977**, *99*, 8127.

Manuscript received: October 30, 2020
Version of record online: February 3, 2021

 © 2021 The Authors. ChemSystemsChem published by Wiley-VCH GmbH

ChemSystemsChem

Supporting Information

Thermodynamic Analysis of the Self-Assembly of Pseudo Isocyanine Chloride in the Presence of Crowding Agents

Benjamin Hämisch, Roland Pollak, Simon Ebbinghaus,* and Klaus Huber*

Supporting Information

Thermodynamic Analysis of the Self-Assembly of Pseudo Isocyanine Chloride in the Presence of Crowding Agents

Benjamin Hämisch, Roland Pollak, Simon Ebbinghaus, Klaus Huber**

S1. Quantification of excluded volume effects of Ficoll 400

One method to consider the presence of macromolecular crowders on self-assembly of proteins is to rescale protein concentration by taking into account the volume occupied by the crowding macromolecules. The molar mass of Ficoll 400 is M_{Ficoll} ~ 400000 g mol^{-1} and its hydrodynamically effective radius amounts to R_H = 10 nm. Since Ficoll adopts a globular structure, the hydrodynamically effective radius is a suitable parameter to estimate the actual volume excluded to PIC. Accordingly, the molar volume $V_{m,Ficoll}$ of Ficoll 400 amounts to

$$V_{m,Ficoll} = \frac{4}{3} \cdot \pi \cdot R_H^3 \cdot N_A = 2523 \frac{L}{mol} \qquad \text{(S1)}$$

with N_A Avogadro's constant. 10 g of an aqueous solution of Ficoll 400 with a concentration of 5% by weight contains 9.5 g water and 0.5 g Ficoll 400 which corresponds to n = 1.25 µM. The volume of 1.25 µM Ficoll 400 is 3.2 mL. Therefore, Ficoll 400 at a concentration of 5% by weight occupies approximately 3.2ml/9.5ml = 0.34 of the total sample volume.

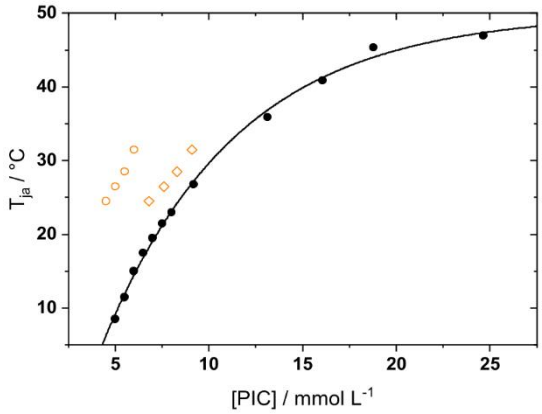

Figure S1: Phase diagram of PIC in aqueous solution (black) as the reference system and in 5wt% Ficoll 400 solution (orange) with hollow spheres representing the weighed-in PIC concentrations and hollow diamonds the PIC concentrations with the volume corrected by the volume excluded by Ficoll. The phase diagram in aqueous solution was extended with data points from Neumann et al.[1] for PIC concentrations greater than 8 mM for a better illustration.

This results in an increase of PIC concentration by a factor of 1.51. The accompanying shift of the aggregation threshold is illustrated in Figure S1.

S2. Volume exclusion of Ficoll 400 based on the scaled particle theory

Another method to take into account volume exclusion effects based on the scaled particle theory[2] was offered by Minton for the self-assembly of proteins[3]. It enables the calculation of activity coefficients of all species involved in a reaction which are then used to calculate the enhancement factor Γ according to eq S2

$$K_{crowded} = \Gamma \cdot K_{non-crowded} \quad \text{(S2)}$$

corresponding to the ratio of the equilibrium constant under crowded and non-crowded condition. Calculation of Γ needs suitable geometrical models for each species. Duncan et al. developed an equation for the case of spherical monomers which build up a spherocylindrical fibril in the presence of a spherical crowding agent[4]:

$$\Gamma = exp\left\{\left[\left(1+\frac{r_p}{r_c}\right)^3 - \left(1+\frac{r_f}{r_c}\right)^2 \frac{3\Delta}{4r_c}\right]\nu c\right\} \quad \text{(S3)}$$

In eq S3 r_p is the radius of PIC monomers, r_f the radius of cylindrical J-aggregates, r_c the radius of Ficoll 400, ν the specific exclusion volume of Ficoll 400 in L g^{-1}, c the concentration of Ficoll 400 in g L^{-1} and Δ the proportionality constant describing the increase in J-aggregate length upon addition of one PIC monomer. The proportionality constant Δ can only be estimated based on the geometrical dimensions of PIC. The length of PIC is the longest axis within the molecule with a value of around 1.4 nm. Since it is known that PIC molecules are not incorporated face-to-face within a fibril, the increase in length upon addition of a monomer to a fibril must be lower than 1.4 nm.[5] Figure S4 shows the change of Γ in a regime of 0 nm ≥ Δ ≥ 1.4 nm for three sets of parameters. It can be seen that Γ amounts to 1.40 to 1.55 at Δ < 1.4 nm. Thermodynamic data received from the ceiling temperature approach, shown in Table 2, can be used to give an estimation of the equilibrium constants according to eq S4.

$$\mathrm{K} = \exp\left(-\frac{\Delta \mathrm{G}}{RT}\right) = \exp\left(\frac{-\Delta H^0}{RT} + \frac{\Delta S^0}{R}\right) \quad \text{(S4)}$$

At 298 K, the ratio of equilibrium constants in pure water and in 5wt% Ficoll 400 solution amounts to 221/119 = 1.85. Therefore, the scaled particle theory gives a good estimate for

the enhancement factor Γ and underlines the assumption that crowding effects of Ficoll 400 are mostly based on volume exclusion effects.

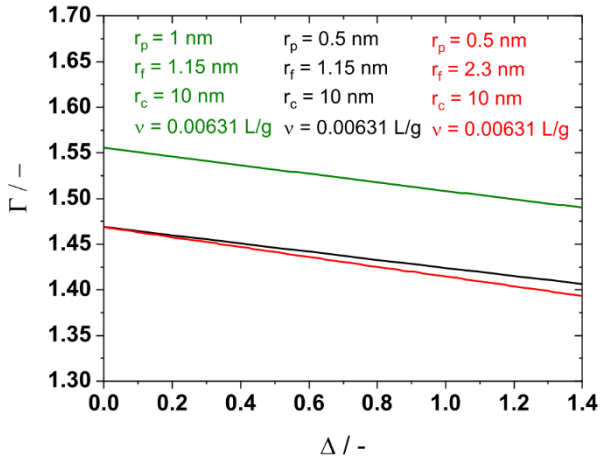

Figure S2: Enhancement factor Γ as a function of Δ at a Ficoll 400 concentration of c = 52.53 g/L, calculated according to eq S3. The respective parameters are shown. The black curve describes eq 3 based on the best parameters of the geometrical dimensions of PIC monomers and PIC fibrils. The red curve shows the effect of doubling the radius of J-aggregates while the green curve shows the effect of doubling the radius of PIC monomers.

S3. Derivation of eq 3

The change of the chemical potential of solute (2) μ_2 with variation of the sample composition is expressed as

$$d\mu_2 = \left(\frac{\delta\mu_2}{\delta m_2}\right)_{m_3} dm_2 + \left(\frac{\delta\mu_2}{\delta m_3}\right)_{m_2} dm_3 \qquad \text{(S5)}$$

with the following two partial derivatives.

$$\mu_{22} = \left(\frac{\delta\mu_2}{\delta m_2}\right)_{m_3} \qquad \text{(S6a)}$$

$$\mu_{23} = \left(\frac{\delta\mu_2}{\delta m_3}\right)_{m_2} \qquad \text{(S6b)}$$

Derivation of eq S5 with respect to m_3 at a constant μ_2 is established by application of the cyclic rule of partial derivatives.

$$\left(\frac{\delta\mu_2}{\delta m_3}\right)_{\mu_2} = \left(\frac{\delta\mu_2}{\delta m_2}\right)_{m_3}\left(\frac{\delta m_2}{\delta m_3}\right)_{\mu_2} + \left(\frac{\delta\mu_2}{\delta m_3}\right)_{m_2}\left(\frac{\delta m_3}{\delta m_3}\right)_{\mu_2}$$

$$0 = \left(\frac{\delta\mu_2}{\delta m_2}\right)_{m_3}\left(\frac{\delta m_2}{\delta m_3}\right)_{\mu_2} + \left(\frac{\delta\mu_2}{\delta m_3}\right)_{m_2} \cdot 1$$

$$\left(\frac{\delta m_2}{\delta m_3}\right)_{\mu_2} = -\frac{\left(\frac{\delta\mu_2}{\delta m_3}\right)_{m_2}}{\left(\frac{\delta\mu_2}{\delta m_2}\right)_{m_3}} = -\frac{\mu_{23}}{\mu_{22}} \tag{S7}$$

Thus, the chemical potential derivative μ_{23} can be described as shown in eq S7.

$$\mu_{23} = -\mu_{22}\left(\frac{\delta m_2}{\delta m_3}\right)_{\mu_2} \tag{S8}$$

Knowledge of μ_{22} enables the calculation of μ_{23}. In the limit of ideal solutions of solute (2), the derivative μ_{22} is

$$\mu_{22} = RT\frac{\delta\ln(x_2)}{\delta m_2} \tag{S9}$$

with x_2 the mole fraction of solute (2). The derivative in eq S9 can be rewritten as shown in eq S10.

$$\frac{\delta\ln(x_2)}{\delta m_2} = \frac{\delta\ln(x_2)}{\delta x_2}\cdot\frac{\delta x_2}{\delta m_2} = \frac{1}{x_2}\cdot\frac{\delta x_2}{\delta m_2} \tag{S10}$$

In the next step, x_2 is written out as $m_2/(m_1+m_2+m_3)$ to be able to solve the remaining derivative in eq S10.

$$\frac{\delta\ln(x_2)}{\delta m_2} = \frac{m_1+m_2+m_3}{m_2}\cdot\frac{\delta\left(\frac{m_2}{m_1+m_2+m_3}\right)}{\delta m_2}$$

$$\frac{\delta\ln(x_2)}{\delta m_2} = \frac{m_1+m_2+m_3}{m_2}\cdot\frac{m_1+m_2+m_3-m_2}{(m_1+m_2+m_3)^2}$$

$$\frac{\delta\ln(x_2)}{\delta m_2} = \frac{m_1+m_3}{m_2(m_1+m_2+m_3)} \cong \frac{1}{m_2} \tag{S11}$$

The approximation in eq S10 holds in the limit of diluted solute (2). Plugging eq S11 into eq S9 then leads to eq S12.

$$\lim_{m_2\to 0}\mu_{22}^{idal} = \frac{RT}{m_2} \tag{S12}$$

Reshaping the last term in eq S8 and inserting the established limit for μ_{22} in dilute, ideal solution in eq S8 then leads to eq 3.

$$\mu_{23} = -\frac{RT}{m_2} \cdot m_2 \cdot \left(\frac{\delta \ln(m_2)}{\delta m_3}\right)_{\mu_2}$$

$$\mu_{23} = -RT \cdot \left(\frac{\delta \ln(m_2)}{\delta m_3}\right)_{\mu_2} \quad \text{(S13)}$$

S4. DSC analysis

The calorimetric enthalpy of the J-aggregate formation from the DSC measurements was calculated by

$$\Delta H_{cal} = \int_0^\infty C_p^{EXC}(T)\, dT \quad \text{(S14)}$$

with $C_p^{EXC}(T)$ the excess heat capacity after baselining the experimental heat capacity $C_p^{EXP}(T)$ with a sigmoidal fit[6]. Due to experimental limitations, thermograms could not be recorded below 5°C (Figure S3).

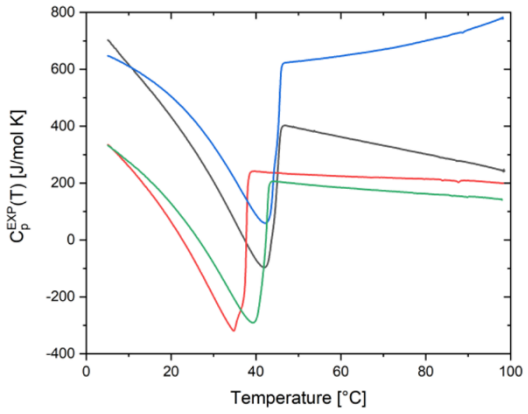

Figure S3: DSC-thermogram of PIC (c=20 mM) in pure water (black), 5wt% PEG (red), 5wt% sucrose (blue), 10wt% sucrose (green).

In order to still estimate a molar enthalpy of the aggregation, the concentration of non-consumed monomers had to be estimated at the cut-off of the DSC-experiment. Estimation was carried out with the help of the thermodynamic parameters given in **Table 1**, which can

be translated into an equilibrium constant according to eq S4. In case of a monomer addition process, *K* can be simplified as shown in eq S15.

$$K = \frac{[P]}{[M] \cdot [P]} = \frac{1}{[M]} \quad \text{(S15)}$$

[P] is the molar concentration of J-aggregates. At 5°C, the equilibrium constant amounts to K = 224 L mol^{-1}, which corresponds to an equilibrium concentration of monomers of [M] = 4.5 mmol L^{-1}. The concentration used to determine the calorimetric enthalpy was therefore corrected by the concentration of non-consumed monomers. Thus, the effective concentration is 15.5 mmol L^{-1} instead of 20 mmol L^{-1}.

References

[1] B. Neumann, P. Pollmann, *Phys. Chem. Chem. Phys.* **2000**, *2*, 4784.

[2] H. Reiss, H. L. Frisch, J. L. Lebowitz, *J. Chem. Phys.* **1959**, *31*, 369.

[3] A. P. Minton, *Mol. Cell. Biochem.* **1983**, *55*, 119.

[4] D. A. White, A. K. Buell, T. P. J. Knowles, M. E. Welland, C. M. Dobson, *J. Am. Chem. Soc.* **2010**, *132*, 5170.

[5] H. von Berlepsch, C. Böttcher, L. Dähne, *J. Phys. Chem. B* **2000**, *104*, 8792.

[6] A. Cooper, M. A. Nutley, A. Wadood, in *Protein-Ligand Interact. Hydrodyn. Calorim.* (Eds: S.E. Harding, B.Z. Chowdhry), Oxford University Press, Oxford New York, **2000**, pp. 287–318.

7. Self-Assembly of Pseudo-Isocyanine Chloride as a Sensor for Macromolecular Crowding In Vitro and In Vivo

Reproduced from *Chem. - A Eur. J.,* **2020**, *26* (31), 7041–7050

"Self-Assembly of Pseudo-Isocyanine Chloride as a Sensor for Macromolecular Crowding In Vitro and In Vivo" published in the journal *Chemistry – A European Journal* by Wiley-VCH Verlag GmbH & Co. KGaA is licensed under CC BY-NC 4.0. No changes have been made.

Copyright 2020 The Authors.

DOI: 10.1002/chem.202000113

Chemistry–A European Journal | Full Paper
doi.org/10.1002/chem.202000113

Analytical Chemistry | *Hot Paper*

Self-Assembly of Pseudo-Isocyanine Chloride as a Sensor for Macromolecular Crowding In Vitro and In Vivo

Benjamin Hämisch,[a] Roland Pollak,[b] Simon Ebbinghaus,*[b] and Klaus Huber*[a]

Abstract: Pseudo-isocyanine chloride (PIC) is a cationic dyestuff that exhibits self-assembly in aqueous solution, promoted either by increasing the PIC concentration or by decreasing the temperature. PIC-aggregates exhibit a characteristic and sharp absorption band as well as a fluorescence band at a wavelength of 573 nm making PIC an interesting candidate to analyze the self-assembly process in various environments. The present work developed PIC-based, synthetic model systems, suitable to investigate how macromolecular crowding influences self-assembly processes. Four synthetic additives were used as potential crowders: Triethylene glycol (TEG), polyethylene glycol (PEG), Ficoll 400 as a highly branched polysaccharide, and sucrose corresponding to the monomeric unit of Ficoll. Combined UV/Vis spectroscopy and time-resolved light scattering revealed a strong impact of crowding based on excluded volume effects only for Ficoll 400. Sucrose had hardly any influence on the self-assembly of PIC and PEG and TEG impeded the PIC self-assembly. Development of such a PIC based model system led over to in-cell experiments. HeLa cells were infiltrated with PIC solutions well below the aggregation threshold in the infiltrating solution. In the cellular environment, PIC was exposed to a significant crowding and immediately started to aggregate. As was demonstrated by fluorescence imaging, the extent of aggregation can be modulated by exposing the cells to salt-induced osmotic stress. The results suggest future use of such a system as a sensor for the analysis of in vitro and in vivo crowding effects on self-assembly processes.

Introduction

Proteins are organic molecules with a variable and often only marginal solubility in water. The marginal water solubility may cause a pronounced tendency to self-assemble toward large filaments often performing distinct tasks in living systems, like the assembly of the cytoskeleton proteins.[1] However, protein self-assembly may also interfere with the proper functioning of living systems like the amyloid formation of (partly) misfolded proteins, which causes amyloidogenic diseases like Alzheimer's dementia.[2,3]

Although analysis of self-assembly processes has become a mature topic in biophysics and biochemistry, the majority of studies in that field were carried out in vitro, under test tube conditions, with purified proteins. Fluorescence dyes, such as Thioflavin T, are commonly used in such studies that show an increase in fluorescence upon binding to amyloid. Kinetic experiments at variable concentration allow to model the aggregation mechanism.[4] Yet, most of those studies discard the fact that the respective processes in living systems usually propagate under crowding conditions.[5] The cytosol of living cells has a solid content of 30%–40% by weight, with proteins establishing more than 50% thereof.[1,5]

Based on excluded volume considerations,[6–9] Minton et al.[10–12] calculated activity coefficients of the monomers at variable contents of cosolutes, herein also denoted as crowders, and predicted a shift of the equilibrium toward assemblies with increasing concentration of crowder if the space occupied by monomeric units is smaller in the aggregate state than in the monomeric state. Assembly and disassembly on the other hand are slowed down the more space is required by the transition states. Experimental work supports the general relevance of excluded volume effects on the self-assembly of proteins. Polyethylene glycole (PEG) promotes dimer formation of pyruvate dehydrogenase,[13,14] in line with predictions based on excluded volume effects,[14,15] but has no effect on the self-assembly of myoglobin.[16] Similar promotion of oligomerization was observed with fibrinogen in the presence of bovine serum albumin (BSA) as crowder and tubulin in the presence of dextran as crowder.[17] Like the formation of oligomers, self-assembly is usually fostered by synthetic as well as natural crowding agents. Dextran enhances amyloid formation

[a] B. Hämisch, Prof. Dr. K. Huber
Physical Chemistry, Paderborn University, 33098 Paderborn (Germany)
E-mail: klaus.huber@upb.de

[b] R. Pollak, Prof. Dr. S. Ebbinghaus
Physical and Theoretical Chemistry, TU Braunschweig
38106 Braunschweig (Germany)
E-mail: s.ebbinghaus@tu-braunschweig.de

Supporting information and the ORCID identification number(s) for the author(s) of this article can be found under:
https://doi.org/10.1002/chem.202000113.

© 2020 The Authors. Published by Wiley-VCH Verlag GmbH & Co. KGaA. This is an open access article under the terms of Creative Commons Attribution NonCommercial License, which permits use, distribution and reproduction in any medium, provided the original work is properly cited and is not used for commercial purposes.

Chemistry–A European Journal | Full Paper doi.org/10.1002/chem.202000113 | Chemistry Europe European Chemical Societies Publishing

of human apolipoprotein C-II.[18] Dextran also promotes formation of actin filaments.[19] In another study, albumin and hemoglobin turned out to act as crowder proteins enhancing the GTP-induced self-assembly of the bacterial cell division protein FtsZ.[20] Use of PEG even led to the formation of bundles of actin filaments mediated by a depletion interaction among the filaments[21] as does Ficoll 70 and dextran with the GTP-induced self-assembly of FtsZ.[22] In all these cases acceleration of the self-assembly can be related to the excluded volume effect of crowders. In the light of the rich patterns of interactions exerted on each other by the large variety of cosolutes, this may come as a surprise. In fact, the impact of cosolutes in general is more complex[23] and further studies showed that the effect of different crowding agents may not be additive[24] and the presence of other cosolutes acting as osmolytes or chaperones may have a significant effect on crowding of synthetic and natural macromolecules.[25] Noteworthy, some species used as crowders do not accelerate but suppress the self-assembly of certain proteins.[25]

As is indicated by this selection of experimental work, it is still difficult to identify systematic trends. This can at least in part be attributed to the large variety of proteins showing self-assembly and to the broad range of cosolutes including species as diverse as polymeric chains, compact proteins and smaller molecules of variable size and chemical nature. In order to make one step forward in classification of crowders, a few representative proteins like human islet amyloid polypeptide (IAPP),[25] MET16,[26] and Ab[27] may be selected to be exposed systematically to different crowding agents. It is at this point where we would like to stress an analogy between proteins and synthetic dyestuffs as this analogy serves as an alternative starting point.[28] Dyestuffs like proteins are organic molecules with usually a marginal solubility in water. A marginal solubility is an important prerequisite enabling proteins and dyes to carry out tasks in nature[1] and in technical applications[29] respectively. Both classes of organic molecules have hydrophobic spots, dipoles, ionic groups and, residues capable of forming H-bonds. Above all, distinct patterns of such residues induce orientated attachment among monomers during self-assembly thereby leading to fibers with long range order in at least one direction. Given these similarities, we suggest to select an appropriate dyestuff molecule exhibiting self-assembly for an analysis of its sensitivity to crowding in solution and thus to address this important aspect of biological systems.

One promising candidate for such a study is pseudo-isocyanine chloride (PIC). PIC was presented almost simultaneously by Jelley[30,31] and Scheibe et al.[32,33] as a cationic dyestuff, which shows a sharp absorption band at the long wavelength of 573 nm, once the dyestuff concentration drops beyond a certain temperature. That temperature threshold increases with increasing PIC concentration. Noteworthy, the appearance of the peak at 573 nm is accompanied by a gradual increase of the viscosity, which was correctly attributed to a self-assembly of the dyestuff molecules[34] with the resulting assemblies denoted as Scheibe- or J-aggregates. Further studies revealed a sharp fluorescence band for J-aggregates at 575 nm close to the J-peak, while PIC monomers hardly show any fluorescence in this wavelength regime.[34,35] The extraordinary interaction of PIC with light pointed to potential applications as photographic sensitizer.[36] A thermodynamic interpretation of concentration dependent UV/Vis measurements indicated that trimers at the least are necessary to generate the characteristic J-peak[37] and that the self-assembly can be interpreted in terms of a chain reaction mechanism based on nucleation and growth.[38] Additionally, dimers were identified as a third component by its own specific UV/Vis spectrum.[39,40] X-ray diffraction[41] in combination with electron microscopy[42] revealed PIC filaments similar to those observed for protein aggregates[43] and gave insight into the alignment of the monomers in those J-aggregates. A detailed light-scattering analysis yielded worm-like aggregates with a persistence length of 500 nm and a final average length of the fiber of 600 nm.[44] The exciton-band responsible for the J-peak turned out to be delocalized over segments limited to a maximum size of a 100 monomers, which makes the final aggregate size much larger than those segments.[45] A suitable way to represent the appearance of the J-aggregates is a phase diagram where the temperature of the onset of aggregation is plotted versus the respective PIC concentration.[44] Accordingly, Figure 1 shows light scattering data from literature[44] in pure water and in 0.01 M NaCl solution. Additionally, UV/Vis spectroscopy data in pure water from Daltrozzo et al.[38] was evaluated as it is outlined in the Supporting Information (Figure S1).

Inspired by these properties, we selected PIC as a protein substitute in order to study two interlinked topics. Reversible self-assembly of PIC will enable us to investigate in vitro fundamental aspects of such self-assembly with and without crowding agents. Once such purely synthetic model systems prove successful, PIC shall be transfected into cells and its self-assembly be analyzed under in vivo conditions. For the in vitro investigation of fundamental aspects, the following additives are applied as crowding agents: Triethylene glycol (TEG), polyethylene glycol (PEG), Ficoll 400 as a highly branched polysaccharide and sucrose corresponding to the monomeric unit of Ficoll. Formation and disintegration of PIC assemblies is triggered via small temperature variations in the presence and ab-

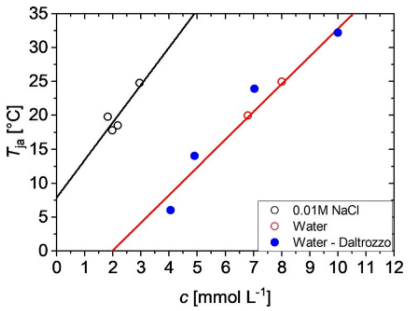

Figure 1. Temperature threshold for aggregation of PIC as a function of PIC concentration determined by means of static light scattering[44] in pure water (red circles) and in 0.01 M NaCl solution (black circles) and by means of UV/Vis spectroscopy[38] in pure water (blue solid spheres).

 © 2020 The Authors. Published by Wiley-VCH Verlag GmbH & Co. KGaA, Weinheim

Chemistry–A European Journal | Full Paper doi.org/10.1002/chem.202000113 | Chemistry Europe European Chemical Societies Publishing

sence of selected crowders. UV/Vis absorption reveals varying amounts of J-aggregates by means of their absorption at 573 nm and time-resolved (TR) light scattering provides the averaged particle mass, squared radius of gyration and hydrodynamic radius of the growing intermediates. Striking effects and differences are established among the different crowders by means of UV/Vis spectroscopy and TR-light scattering to begin with. After a qualitative outline of the major effects, phase diagrams which represent the aggregation threshold temperature as a function of the PIC concentration are established systematically and separately for each of the crowders in comparison to the phase behavior in the absence of crowder. Our focus is then transferred to in vivo experiments. Self-assembly of PIC is carried out in HeLa cells thus providing a realistic scenario for aggregation in living systems. To this end, the cells will be exposed to dilute PIC solutions with their PIC concentration well below the aggregation threshold. Variable conditions are applied in order to learn how such a system responds and whether the responses are suitable to turn in-cell PIC into a sensor for variable crowding conditions.

Results and Discussion

In vitro experiments with synthetic systems

Effect of crowding on PIC aggregation

UV/Vis spectroscopy provides evidence for at least three different species, the monomers, H-dimers and J-aggregates. The prefixes H and J refer to the specific alignment of the monomers in the aggregate, with H denoting a parallel, congruent alignment of the molecular long axis and J indicating a coplanar inclined alignment.[46] Figure 2 compares UV/Vis spectra of PIC in pure water at a concentration of 6 mM, which is well below the threshold concentration of formation of J-aggregates (Figure 1) and with spectra recorded in the presence of 25% by weight of four crowding agents, TEG, PEG, sucrose and Ficoll 400.

Comparison of the spectrum of PIC in pure water and of PIC in solution containing 25 wt% sucrose provides evidence for an almost complete lack of J-aggregates. Both spectra indicate a significant portion of H-dimer, which is noticeable from the fact that the peak close to 485 nm is more intensive than the one appearing at 525 nm (inset of Figure 2). Small differences in the two spectra can be attributed to a slight shift in monomer/H-dimer equilibrium in favor of monomers for the sample containing 25 wt% sucrose. The samples with 25 wt% PEG or TEG differ significantly from the one in pure water but are comparable with that of PIC in pure water at considerably lower concentrations (3 μM, see Figure 2 inset and Figure 3), where PIC is in its monomeric state. Hence, even dimerization or the formation of small oligomers is blocked with PEG or TEG. An entirely different effect is observed once Ficoll 400 is used as a crowding agent. As is outlined in Figure 2, a significant J-peak appears for PIC at a concentration of 6 mM.

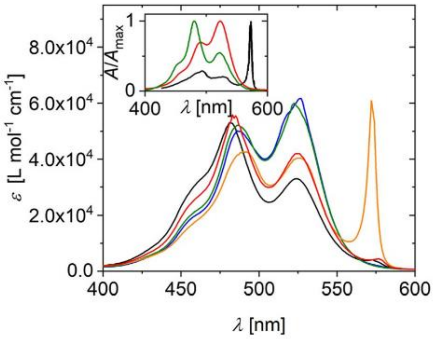

Figure 2. UV/Vis spectra of PIC in aqueous solution at a concentration of 6 mM without and with 25% by weight of crowding agents. The color code indicates absence of crowder (black), TEG (green), PEG (blue), sucrose (red), Ficoll 400 (orange). The inset shows spectra as absorbance normalized to maximum absorbance for J-aggregates (black), H-dimers (green) and monomers (red). The spectrum of J-aggregates in pure water stems from Neumann et al.[47] The monomer spectrum was established in aqueous solution at *[PIC]* = 3 μM and the H-dimer spectrum was replotted from Horng et al.[48] As is outlined in the Supporting Information, the addition of 0.01 M NaCl has no significant influence on the monomer spectrum (Figure S2).

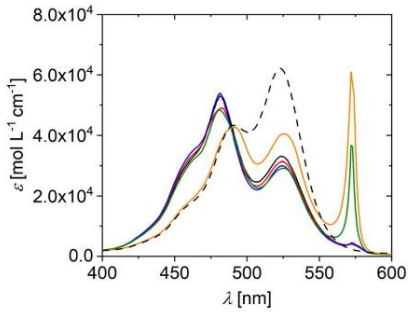

Figure 3. UV/Vis spectra of PIC in aqueous solution at a concentration of 6 mM without crowding agent at variable temperature and with 25% by weight of Ficoll 400 at $T = 25\,^{\circ}C$ (orange). The color code indicates the temperature in the absence of crowder: 10 °C (green), 15 °C (blue), 20 °C (red), and 25 °C (black). The black dashed curve represents a spectrum of PIC in aqueous solution at a concentration of 3 μM at 25 °C.

As already mentioned, self-assembly of PIC is promoted by a decrease in temperature. This is illustrated in Figure 3 for PIC in pure water. Such a trend is a characteristic signature of growth processes proceeding via monomer addition with an exothermic reaction enthalpy and an entropy loss. Such features are for instance observed for many chain reactions in polymer chemistry where this threshold temperature is usually denoted as ceiling temperature.[49] A significant J-peak appears first at a temperature of 15 °C. This may again be compared with the state where 25% by weight of Ficoll 400 is present as a crowder. Strikingly, the effect of adding Ficoll 400 to water is more pronounced than a temperature drop in pure water by 10 °C. Hence, Ficoll 400 strongly promotes formation of J-aggregates.

 © 2020 The Authors. Published by Wiley-VCH Verlag GmbH & Co. KGaA, Weinheim

Chemistry–A European Journal
Full Paper
doi.org/10.1002/chem.202000113
Chemistry Europe
European Chemical Societies Publishing

The induction of PIC self-assembly can be nicely visualized with a TR-light scattering experiment during a gradual temperature decrease. In the presence of PEG, TEG, sucrose and in the absence of crowder as reference experiment T was gradually decreased from 25 °C to 10 °C and in the presence of Ficoll 400 the high threshold temperature made an extension of the temperature gradient to a starting value of 35 °C necessary. Figure 4a represents the evolution of the weight averaged molar mass M_w as a function of time during the respective temperature gradients. In all cases, the PIC concentration was 6 mM and the content of crowder was fixed at 2% by weight. In the absence of a crowding agent, the aggregation sets in at ≈15 °C. The modulations of this threshold by crowders are in agreement with expectations from UV/Vis experiments. Whereas PEG and TEG causes a shift of the threshold toward lower temperatures, sucrose had hardly any impact. Ficoll 400 unambiguously promotes aggregation of PIC as the onset temperature for self-assembly is shifted to higher temperatures by 10 °C.

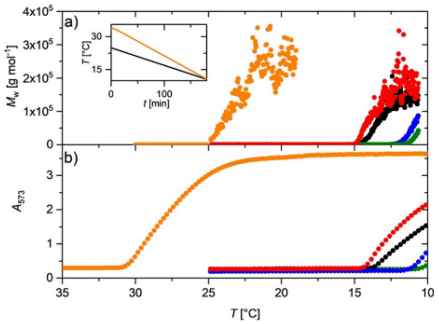

Figure 4. a) Evolution of aggregate mass of PIC in aqueous solution at a PIC concentration of 6 mM with time in the absence (black) and presence of 2% by weight of crowding agents during a temperature gradient of 25 °C→10 °C for PEG (blue), TEG (green), Sucrose (red) and during a temperature gradient of 35 °C→10 °C for Ficoll 400 (orange). Temperature can be transformed to time according to the inset, which shows the temperature gradients applied for the experiments with PEG, TEG, sucrose and without crowding agent (black) and the experiment with Ficoll 400 (orange). b) Evolution of the absorbance A_{573} recorded at a wavelength of 573 nm of a PIC solution with time at a PIC concentration of 6 mM in the absence (black) and presence of 2% by weight of crowing agents during the same temperature gradient as applied in a). The color code indicates the type of crowding agent: Ficoll (orange), TEG (green), PEG (blue), and Sucrose (red).

Additional experiments outlined the Supporting Information (Figure S3a) demonstrate, that the interference of PEG and TEG with the self-assembly of PIC disappears at PEG and TEG contents of 1%. At 25% of PEG and TEG, on the other hand, aggregation of PIC is fully inhibited in the temperature regime investigated. An application of cyclic cooling/heating profiles (Figure S3a and S3b), demonstrates full reversibility of the self-assembly processes.

Analogous trends can be recorded by means of UV/Vis spectroscopy. Based on the fact that the absorbance at a wavelength of 573 nm A_{573} is a characteristic signature of J-aggregates, the process of self-assembly can be followed by time-resolved recording of A_{573} during a temperature gradient. Figure 4b summarizes A_{573} recorded at the same temperature gradients applied for the light scattering experiments with the PIC concentration fixed at 6 mM and the content of crowders fixed at 2% by weight.

All trends show an initial part with a constantly low absorption indicating absence of J-aggregates as long as the temperature is high enough. At a distinct temperature which is characteristic for the respective solvent conditions, the absorbance abruptly increases. As anticipated from the preceding paragraphs, the onset of absorption is shifted to lower temperatures in the presence of PEG and of TEG, with the onset temperature for TEG and PEG close to 10 °C corresponding to the lower limit of the applied gradient. The trend observed in the presence of sucrose is closest to that recorded in pure water, confirming the negligible effect of sucrose on the aggregation of PIC. Strikingly, the onset temperature observed in the presence of 2% by weight of Ficoll 400 is shifted to the opposite direction by a fairly large temperature increment, again indicating that Ficoll 400 promotes the self-assembly of PIC. Agreement of the threshold temperatures determined with the two methods is satisfactory with small discrepancies not exceeding 1 °C, except for the evaluation of the threshold value in the presence of 2% Ficoll, where the uncertainty is slightly larger (details are outlined in Section S3 of the Supporting Information). UV/Vis measurements together with the light scattering experiments confirm that the aggregates shown in Figure 4a are J-aggregates, and the J-aggregates observed in Figure 4b within the uncertainty of the threshold temperature are large aggregates and not small oligomers.

Threshold temperature at variable PIC concentration and crowder content

The onset temperatures extracted from such diagrams are denoted as T_{ja} and plotted in a separate graph as a function of the crowder content in Figure 5. Such a plot provides a comparative overview on the effect of crowding at a distinct PIC

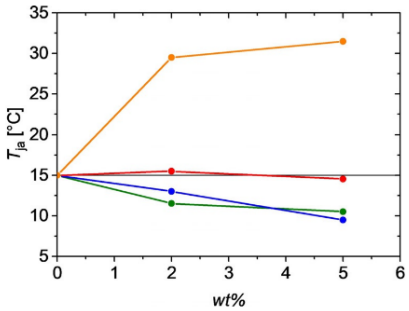

Figure 5. Temperature threshold for aggregation of PIC as a function of crowder content at a PIC concentration of 6 mM and in the absence of crowder. The color code indicates the absence of crowder (black horizontal line), Ficoll 400 (orange), TEG (green), PEG (blue), and sucrose (red).

© 2020 The Authors. Published by Wiley-VCH Verlag GmbH & Co. KGaA, Weinheim

Chemistry–A European Journal | Full Paper doi.org/10.1002/chem.202000113 | Chemistry Europe European Chemical Societies Publishing

concentration. The horizontal line close to 15 °C indicates the threshold in the absence of any crowder serving as a reference. The strongest impact is exerted by Ficoll 400, which intensifies aggregation with increasing concentration of Ficoll 400. PEG and TEG show the opposite effect, with TEG acting as a stronger inhibitor of aggregation. Sucrose shows hardly any effect.

A straightforward extension of this series of experiments leads to a complementing overview, which characterizes the aggregation pattern as a phase diagram generated by a selected concentration of crowder. Now recordings of A_{573} as a function of temperature have to be carried out at a variable PIC concentration at a given crowder concentration. Figure 6 presents the phase diagram for PEG, TEG, sucrose and Ficoll 400 at a crowder concentration of 2% by weight in comparison to the respective trend observed in the absence of crowder. Furthermore, the phase diagram in Leibovitz solution is shown as a reference to the in-cell measurements. A strong shift of the threshold line to lower PIC concentrations is observed, which can at least in part be explained by the physiological amount of sodium chloride of 138 mM in the Leibovitz solution. The presence of sodium chloride promotes aggregation, as it is shown in Figure 1 for 10 mM sodium chloride content.

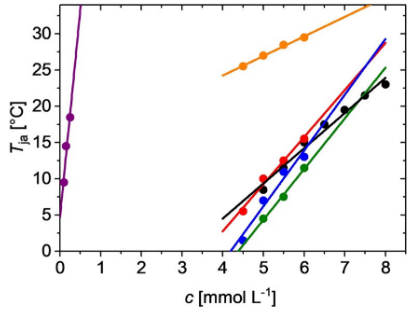

Figure 6. Temperature threshold for aggregation of PIC as a function of PIC concentration at various conditions: Analysis in pure water (black) serves as reference data, Leibovitz solution (purple) is applied as solvent for PIC for the experiments with HeLa cells, and the presence of 2% by weight of PEG (blue), of TEG (green), of sucrose (red) and of Ficoll 400 (orange) illustrate the impact of various crowding agents.

Whereas the threshold temperatures T_{ja} recorded for Ficoll 400 is shifted to lower PIC concentrations, PEG and TEG induces the opposite effect. As is shown in the Supporting Information, increasing the concentration of Ficoll 400 slightly shifts the respective threshold curve to lower PIC concentrations and at the same time slightly decreases its slope (Figure S4).

Among the additives applied as crowding agents in the present work, only Ficoll 400 shows an impact on the self-assembly of PIC, which can be qualitatively reconciled with a crowding effect based on simple excluded volume considerations.[10–12] Ficoll 400 is a branched and hence compact polymer, with sucrose the chemical monomer. Sucrose was therefore used a suitable additive to test for specific interactions between Ficoll and PIC. No significant impact on PIC aggregation could be identified, which excludes significant excess interactions between Ficoll and PIC compared to water and PIC. This supports the hypothesis that excluded volume effects establish the dominating feature exerted by Ficoll 400 on the self-assembly of PIC.

Contrary to the effect of Ficoll 400, PEG and TEG reduce the tendency of PIC to aggregate. This has to be induced by specific interaction of the chemical residues of PEG or TEG with those in PIC. As suggested by Knowles et al.,[50] aromatic C and cationic N indeed interact favorably with (-CH_2-OH) and (-CH_2-*O*-CH_2-) residues compared to the respective interaction with water molecules. These favorable interactions with PEG and TEG likely occur with monomeric PIC and/or with growing ends of PIC filaments, thus nicely explaining the observed impact of PEG and TEG on the interaction of PIC. As a result, PIC is a self-assembling system sensitive to macromolecular crowding based on excluded volume effects. Encouraged by this feature, we decided to transfer PIC into cells in order to study the response of PIC to the crowded environment of the cytosol and its variations. Such experiments are particularly promising as the fluorescence of PIC J-aggregates observed at a wavelength of 573 nm may serve as a powerful tool to analyze self-assembly of PIC in-cell.

In vivo experiments with HeLa cells

Accordingly, we studied PIC aggregation in adherent living HeLa cells to explore how the crowding effect in cells modulates aggregation. Therefore, PIC was dissolved in Leibovitz imaging medium ($c = 50$ μM) and added to the cells before imaging. Initially, no fluorescence was observed and no aggregation occurred in the Leibovitz medium. Surprisingly, we found that fluorescence occurred within a few minutes inside the cells (Figure 7a–d), while the medium in the extracellular space remained non-fluorescent. Confocal microscopy revealed that the fluorescence is mainly observed from bright cytoplasmic speckles and faint regions in the nucleus (Figure S5a and S5b). We independently confirmed the accumulation of PIC in the cell by measuring the change in concentration in the extracellular medium by UV/Vis spectroscopy (Figure S6; see Materials and Methods for further details). The result was that the concentration in the cell is 100 times higher than in the extracellular medium. The accumulation of aggregates inside the cells shows that the cell membrane is permeable for monomeric PIC. The dye aggregates within the cell whereas it does not aggregate at the same temperature in the extracellular space (Figure 6). We summarize these findings in the illustration in Figure 7e.

We then studied the temperature-dependence of in-cell aggregation. The mechanism of aggregation was similar at 12 °C, 21 °C and 37 °C, following the Scheme in Figure 7e, with subtle variations in kinetics at different temperature and subcellular environments (Figure 8). As is outlined in Figure 6, Ficoll 400 shifts the threshold line to much lower PIC concentrations, thereby making aggregation of PIC at higher PIC concentrations insensitive to temperature. A similar effect may be caused by the cellular environment, which locates the states

 © 2020 The Authors. Published by Wiley-VCH Verlag GmbH & Co. KGaA, Weinheim

Chemistry–A European Journal | Full Paper doi.org/10.1002/chem.202000113 | Chemistry Europe European Chemical Societies Publishing

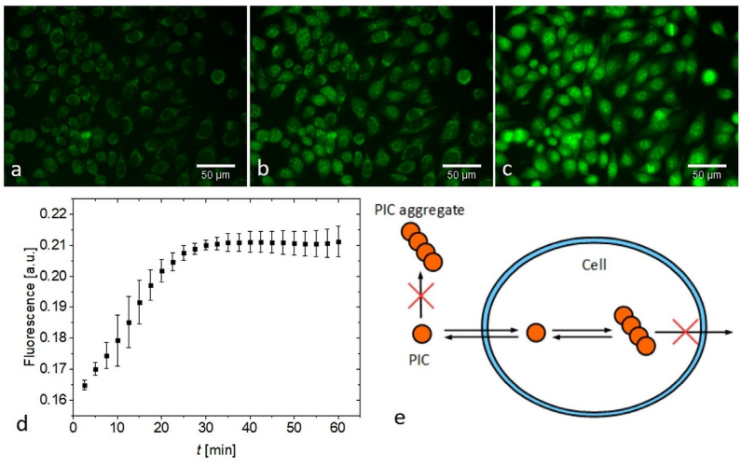

Figure 7. a–c) Exemplary fluorescence images of PIC aggregation in HeLa cells at 21 °C a) 2.5 min b) 10 min c) 40 min after addition of PIC. Scale bar 50 µm. d) Aggregation kinetics of PIC measured by the cell-averaged fluorescence intensities. Three independent measurements were performed and data shown as mean ± s.d. e) Model for PIC aggregation inside cells.

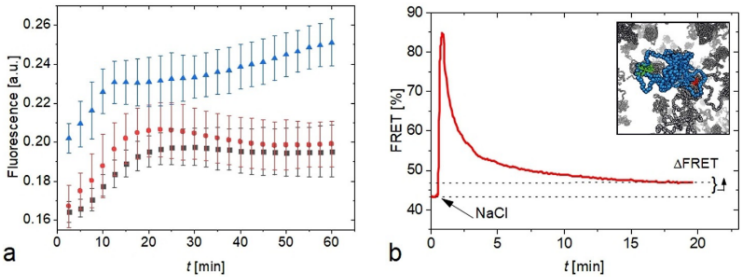

Figure 8. a) PIC aggregation kinetics in HeLa Cells at 0 mM (black squares), 100 mM (red spheres) and 500 mM (blue triangles) concentrations of sodium chloride in the extracellular medium. Three independent measurements were performed and data shown as mean ± s.d. b) Crowding effect in HeLa Cells after osmotic upshift by 100 mM measured by a crowding sensor (inset; PEG shown in blue, FRET dyes in green and red and PEG crowding agents in gray). An increase in FRET corresponds to an increase in crowding. After the osmotic shock that leads to a peak in crowding, cells recover their original volume by regulatory volume increase, except of a residual difference (*ΔFRET*). The data is taken from reference[53] and the graph modified for comparison.

analyzed in Figure S7 deep into the aggregate regime. We also found PIC aggregation in the cells for 5 µM and 0.5 µM PIC solutions. For the 5 µM solution the aggregation kinetics were comparable to the 50 µM solution (Figure S8). In summary, we observed the aggregation of PIC in cells exposed to concentrations well below the aggregation threshold, suggesting that excluded volume effects dominate the in-cell behaviors.

PIC aggregation in cells under osmotic stress

To test if macromolecular crowding in the cell is a cause of aggregate formation we investigated how osmotic stress modulates PIC aggregation. Osmotic stress is an effective tool to modulate the cellular volume and crowding density.[51–54] We used NaCl for an osmotic upshift of the medium leading to a decrease in cell volume and an increase in crowding. The PIC solutions (50 µM) in water were supplemented with NaCl to a final concentration of 100 mM and 500 mM and added to the cell at $t = 0$. Compared to the untreated cells, we found an increase in the overall fluorescence intensity as well as faster aggregation kinetics (Figure 8a).

The strongest increase in fluorescence intensity was observed within the first minutes after the osmotic shock in particular for the 500 mM solution. This is in line with the corresponding strong increase in cellular crowding during this period.

It is known that this increase is caused by an immediate reduction of the cellular volume (due to the osmotic pressure) with invariant cellular biomass.[55] As this leads to detrimental effects, such as protein aggregation,[18,56,57] cells developed different responses to tightly regulate crowding (crowding homeostasis).[58] As a short-term response (within minutes) cells accumulate inorganic salts and a recovery of the cellular volume is observed, leading to the decline in crowding. This

 © 2020 The Authors. Published by Wiley-VCH Verlag GmbH & Co. KGaA, Weinheim

Chemistry–A European Journal | Full Paper doi.org/10.1002/chem.202000113 | Chemistry Europe European Chemical Societies Publishing

mechanism is known as the regulatory volume increase (RVI).[59,60] At longer timescale (up to several hours) the salts utilized for the RVI are replaced by osmolytes to reduce the ionic strength back to a basal level that may otherwise be detrimental to cells.[61,62]

To directly relate PIC aggregation to the changes in crowding for our specific cellular system, we refer to our osmotic upshift experiments in HeLa Cells. In this study,[53] cellular crowding was measured using a previously introduced crowding sensor (Figure 8b, inset).[54] The sensor consists of a 10 kDa polyethylene glycol polymer that was labelled at both ends by Atto488 and Atto565 dyes. In crowded conditions, the sensor adopts more compact conformations, which is measured by an increase in Förster resonance energy transfer. A strong increase in FRET is observed within the first minute after the osmotic shock experiments. This is caused by the cellular volume collapse and the increase in crowding. At longer timescales, the RVI reduces the crowding close to basal level. This is in line with the early modulation of PIC aggregation after the osmotic upshift. However, a significant increase in crowding beyond basal level is also observed beyond 12 min (indicated by the ΔFRET in Figure 8b), which is compensated by the accumulation of osmolytes at longer timescales. The residual increase in crowding could explain the modulation of PIC aggregation at longer times in particular for the 500 μM solution. The osmotic shock experiments confirm that PIC aggregation in cells is particularly sensitive to excluded volume changes.

Conclusions and Outlook

Pseudo-isocyanine chloride (PIC) is a water-soluble cationic dyestuff, which reversibly forms fiber-like aggregates. Aggregation is triggered once the temperature of the solution drops below a certain threshold value, which increases with increasing PIC concentration.[38,45] A characteristic signature of these fiber-like aggregates is a narrow absorption band and a fluorescence band at a wavelength of 573 nm,[34,35] which offers a straightforward and easy to handle tool to track the appearance of aggregates as a function of changing environmental conditions.

In a first step, we dissolved PIC in aqueous solutions at variable crowding contents. Four synthetic additives were used as potential crowders: Triethylene glycol (TEG), polyethylene glycol (PEG), Ficoll 400 as a highly branched polysaccharide and sucrose corresponding to the monomeric unit of Ficoll. Combined UV/Vis spectroscopy and time-resolved light scattering during temperature gradients showed that the formation of fiber-like aggregates coincides with the appearance of the absorption at 573 nm, denoted as J-peak. This enabled us to determine threshold temperatures at variable PIC-concentrations, which can be correlated in terms of a phase diagram. Ficoll 400 is the only additive, for which a drastic promotion of self-assembly is observed. Promotion of self-assembly can unambiguously be attributed to macromolecular crowding dominated by an excluded volume effect. Sucrose, the monomeric unit of Ficoll does not affect the self-assembly thus supporting the excluded volume nature of the crowding exerted by Ficoll. Unlike with Ficoll 400, PEG and TEG shifts the threshold temperature for the self-assembly to lower temperature compared to the phase behavior of PIC in pure water, thereby decreasing the tendency of PIC to form aggregates. These results do not only suggest a use of such synthetic mixtures to scrutinize theoretical predictions on the impact of excluded volume effects on self-assembly processes[10–12] but give rise to an application of PIC in vivo in order to learn if and how PIC responds to changing environmental conditions in cells which lie at the origin of macromolecular crowding.

Accordingly, we exposed HeLa Cells with PIC solutions in Leibovitz medium with PIC concentrations in the range of $0.5\ \mu M < [PIC] < 50\ \mu M$ being significantly smaller than the respective threshold value in the Leibovitz medium. During exposure of the cells to these PIC solutions, the cells were tracked via fluorescence imaging in order to follow the appearance of in-cell aggregation of PIC with the fluorescence band at 573 nm. At PIC concentrations of 5 μM and 50 μM a significant fluorescence developed with time in the cells, clearly signaling PIC aggregation. Analysis of the overlaying Leibovitz medium revealed a loss of PIC via infiltration, indicating a PIC concentration in-cell a 100 times higher than in the overlaying Leibovitz medium. Finally, osmotic stress experiments with excess NaCl salt in the infiltrating PIC medium were applied while analyzing the cells for fluorescence to signal aggregation of PIC. Addition of NaCl in fact further promotes aggregation of PIC in-cell, which can unambiguously be attributed to a temporary compression of the cellular volume and along with this an amplification of crowding. It is these results, which indicate PIC as an extremely promising candidate as a sensor to examine varying cellular conditions with respect to their impact on self-assembly processes of proteins in cells.

Experimental Section

Materials

1,1′-Diethyl-2,2′-cyanine chloride (PIC) was prepared from 1,1′-diethyl-2,2′-cyanine iodide from (Sigma Aldrich) via ion exchange (Amberlite IRA 402 Cl) under exclusion of light. The molar mass of PIC is 362.9 g mol^{-1}. The crowding agents triethylene glycol (TEG), polyethylene glycol (PEG, $M_n = 400$ g mol^{-1}), sucrose and Ficoll 400 ($M_n = 400\,000$ g mol^{-1}) were provided by Sigma Aldrich (Darmstadt, Germany). Leibovitz's L-15 medium was obtained from Thermo Fisher (Waltham, USA). LS-MS Grade water from VWR International (Radnor, USA) was used to prepare the solvents. For the cell culture it was used Dulbecco's Modified Eagle's Medium—low glucose (DMEM), Dulbecco's Phosphate Buffered Saline (DPBS), EDTA, Penicillin-Streptomycin, Fetal Bovine Serum (FBS), Trypsine (0,05 %) EDTA (0,02 %) which were provided by Sigma–Aldrich and sodium chloride obtained from Sigma–Aldrich

Sample preparation

Aqueous solutions of crowding agents with contents varying from 2 wt % to 25 wt % served as solvents. Solvents containing Ficoll 400 were slightly acidic. As Ficoll would undergo chemical decomposition, especially at elevated temperatures, the pH of the solvent thus had to be adjusted to 7 to ensure chemical stability of Ficoll 400. Stock solutions of PIC in the presence of crowding agents had

 © 2020 The Authors. Published by Wiley-VCH Verlag GmbH & Co. KGaA, Weinheim

Chemistry–A European Journal | Full Paper doi.org/10.1002/chem.202000113 | Chemistry Europe European Chemical Societies Publishing

a PIC concentration of 6 mM. Stock solutions in pure water were prepared either at 6 or 8 mM of PIC. In Leibovitz's solution, the concentration of the stock solution was set to *[PIC]* = 0.25 mM. Solutions were then stirred overnight at a temperature of 50° C in the absence of light to ensure complete dissolution without decomposition. For in vivo experiments the stock solution of PIC was diluted to 50 μM.

Cell culture

HeLa Cells were split every 2 to 3 days when reaching a confluency of 80 to 90% in a T-25 flask. The confluency was monitored with a light microscope (Leica). To split the cells, the old growth medium was removed and washed with 1 mL DPBS twice. Trypsine (0.5 mL) was added to detach the cells. Afterwards, growth medium (3.5 mL) was added and the corresponding amount of cell were transferred to a new T-25 flask with additional growth medium (3 mL). To prepare for the experiment, HeLa Cells were split into small Fluorodishes (10 mm diameter, WPI) one day before the experiments. Before imaging the cells were washed twice with DPBS (200 μL) and placed under the microscope. PIC in Leibovitz's solution (200 μL) was added to the samples. For osmotic shock experiments, NaCl was added to the solution to reach a final concentration of 100 μM and 500 μM.

For the absorption spectroscopy, to determine the concentration of PIC in the cells, samples of the same amount of cells were split to 24-well dishes. After 24 h, the cells were washed twice with DPBS (200 μL). PIC solution (200 μL) was added to the cells and incubated for distinct time intervals. Afterwards, the supernatant was removed and analyzed by absorption spectroscopy. The remaining cells were detached from the surface with Trypsine (200 μL) and the population was counted.

Fluorescence microscopy

The cells were imaged with a Zeiss Observer.Z1 wide field microscope. PIC was excited by using an LED with a wavelength of 530 nm. Emission light was detected using the AHF Analysentechnik beam splitter Dual 532/640 ET, the AHF Analysentechnik detector cube H 643 and a Zeiss AxioCam HSm camera. To control the temperature of the samples the Brook Industries Z-HC-K-3112 temperature stage was used. Images were recorded every 2.5 minutes (100 ms exposure time) for 60 min and analyzed using ImageJ. ROIs (Regions of Interest) were set to analyze the average fluorescence intensity in the cytoplasm. A sample size of at least 100 cells was measured and analyzed and the errors determined as standard deviation (s.d.).

Confocal fluorescence microscopy

The cells were imaged using an Olympus FV 3000 confocal microscope. PIC was excited with a wavelength of 532 nm. Emission light was detected using the beam splitter DM405/488/561 and a PMT. The scanning speed was 2 μs/pixel measuring 512×512 pixel. The detection range for the emission light was between 550 and 600 nm. The images were acquired after 30 min of cellular treatment with PIC solution.

Determination of in-cell concentration

PIC concentration was determined using absorption spectroscopy. The absorption coefficient of PIC was determined as $\varepsilon_{525} = 50000\ \mathrm{L\,mol^{-1}\,cm^{-1}}$ using Lambert–Beer's law. The in-cell concentration was then calculated by the loss of PIC in the supernatant [Eq. 1]:

$$c_{loss} = c_{Standard} - c_{Supernatant} \quad (1)$$

$c_{standard}$ is the concentration of PIC that was added to the cells. $c_{supernatant}$ is the remaining concentration after cellular uptake for a specific incubation time. Thereby the concentration of PIC accumulated the cells can be calculated. Thus, the amount of substance in one cell (n_{cell}) can be calculated by [Eq. 2]

$$n_{Cell} = \frac{c_{loss} * V_{Supernatant}}{N_{Cell}} \quad (2)$$

The volume $V_{supernatant}$ is the volume that was used for incubation and N_{cell} the cell count. The concentration of PIC in the cell can be calculated using the average volume of HeLa Cells ($V_{cell} = 2600\ \mu m^3$).[63] [Eq. 3]

$$c_{Cell} = \frac{n_{Cell}}{V_{Cell}} \quad (3)$$

The error was determined using the standard derivation error calculation and comes from the faulty concentration measurement via UV/Vis spectroscopy.

UV/Vis spectroscopy

UV/VIS spectra were recorded with a *Lambda-19* spectrometer from Perkin–Elmer (Waltham, USA). Spectra were recorded from 400 to 600 nm with a scan speed of 120 nm min^{-1} and a slit width of 2 mm. A custom-built copper block was used as a cuvette holder, which can be thermostated externally to enable temperature sensitive measurements. For concentrations of *[PIC]* > 1 mM, a demountable cuvette with a path length of 0.01 cm was used. For samples with a concentration of 0.1 mM ≤ *[PIC]* ≤ 1 mM, cuvettes with a path length of 1 cm were used. The monomer spectrum of PIC at 3 μM was recorded in a cuvette with a path length of 5 cm. All cuvettes were provided by Hellma Analytics (Mühlheim, Germany).

Static and dynamic light scattering (SLS and DLS)

Light-scattering experiments were made with a multi-detection laser light-scattering system *ALV/CGS-3/MD-8* from ALV GmbH (Langen, Germany). A He-Ne Laser with a wavelength of 632.8 nm was used as a light source. The system provides an array of 8 detectors with a shift between two neighboring detectors of 8°, thus allowing simultaneous dynamic and static light scattering in a time-dependent manner. An angular range of $30° \le \theta \le 86°$ was covered, corresponding to a q-range in water of $6.8\times10^{-3} \le q \le 18\times10^{-3}\ \mathrm{nm^{-1}}$ with [Eq. 4]

$$q = \frac{4\pi n}{\lambda_0} * \sin\left(\frac{\theta}{2}\right) \quad (4)$$

as the momentum transfer vector, $n = 1.332$ the refractive index of water at $T = 25\,°C$, θ the scattering angle and λ_0 the laser wavelength in vacuum. For each datapoint, scattered light was recorded for 10 seconds. Cylindrical light scattering cuvettes from Hellma (Mühlheim, Germany) with a diameter of 2.4 cm were used.

To remove dust, the solutions were filtered prior to a scattering experiment by means of *Millex-GV* (PVDF, 0.22 μm) syringe filters from Merck Millipore (Billerica, USA). The solutions were successive-

 © 2020 The Authors. Published by Wiley-VCH Verlag GmbH & Co. KGaA, Weinheim

Chemistry–A European Journal | Full Paper doi.org/10.1002/chem.202000113 | Chemistry Europe European Chemical Societies Publishing

ly equilibrated in the light scattering device for 10 minutes. The starting temperature is 35 °C for the sample containing Ficoll 400 and 25 °C for all other solutions. A measurement was started together with a temperature gradient, during 3 h ending at 10 °C. The gradients were controlled by an external thermostat.

Data from static light scattering were evaluated with the Zimm approximation.[64] Dynamic light scattering was analyzed in terms of a cumulant analysis.[65] A detailed description of both approaches can be found in the Supporting Information (Section 8).

The refractive indices of crowder solutions, which also served as solvents for PIC are required for SLS and DLS data evaluation. Refractive indices of crowder solutions were measured with an Abbe refractometer from Carl Zeiss AG (Oberkochen, Germany) at 25 °C, covering a concentration regime of 1 wt% to 25 wt% of crowder. Each solution was measured three times.

For DLS data analysis, the dynamic viscosities η of the crowder solutions are needed in addition. Dynamic viscosities were determined with an Ubbelohde viscosimeter from Schott AG (Mainz, Germany) at 25 °C at 1 wt% and 5 wt% of crowder content. The viscosity of each solution was determined three times. The slight temperature dependence of the viscosity was taken into account by applying the known relative temperature dependence of the water viscosity on the aqueous solutions of the crowders respectively.

Determination of the aggregation threshold via UV/Vis-spectroscopy

A dilution series of the stock solution of PIC in pure water was prepared, covering a concentration regime from 5 to 8 mM in steps of 0.5 mM. For solutions containing crowding agents, a concentration regime from 4 to 8 mM was covered in steps of 0.5 mM. Absorption at 573 nm A_{573} was then recorded as a function of temperature, which was decreased in increments of 1 °C. The temperature increment during which A_{573} increased at least two-fold was defined as the aggregation threshold temperature. An example of this approach is shown in the Supporting Information (Figure S**1 b**).

Temperature-dependent recording of A_{573}

For all stock solutions of PIC at 6 mM in either pure water or in the presence of crowding agents (2 wt%), the absorption at 573 nm A_{573} was recorded in a time-dependent manner while decreasing the temperature from 25 °C to 10 °C with a linear temperature gradient of 0.375 °C min^{-1}. For the sample containing Ficoll, the starting temperature was increased to 35 °C in order to capture the aggregation threshold. In order to stress the temperature dependence, the time axis was transformed into a temperature axis.

Acknowledgements

B.H. and R.P. carried out all experiments and contributed equally to this work. S.E., and K.H. designed the study. The authors are grateful to Professor W. Schröer, Bremen University, for the donation of an additional sample of PIC.

Conflict of interest

The authors declare no conflict of interest.

Keywords: crowding · in cell · J-aggregates · pseudoisocyanine chloride · self-assembly

[1] B. Alberts, D. Bray, J. Lewis, M. Raff, K. Roberts, J. D. Watson, *The Molecular Biology of the Cell*, Garland Publishers, New York, **1994**.
[2] C. M. Dobson, *Nature* **2003**, *426*, 884.
[3] D. J. Selkoe, *Annu. Rev. Cell Biol.* **1994**, *10*, 373.
[4] S. I. A. Cohen, S. Linse, L. M. Luheshi, E. Hellstrand, D. A. White, L. Rajah, D. E. Otzen, M. Vendruscolo, C. M. Dobson, T. P. J. Knowles, *Proc. Natl. Acad. Sci. USA* **2013**, *110*, 9758.
[5] R. J. Ellis, *Trends Biochem. Sci.* **2001**, *26*, 597.
[6] S. Asakura, F. Oosawa, *J. Chem. Phys.* **1954**, *22*, 1255.
[7] S. Asakura, F. Oosawa, *J. Polym. Sci.* **1958**, *33*, 183.
[8] A. V. Vrij, *Pure Appl. Chem.* **1976**, *48*, 471.
[9] H. N. W. Lekkerkerker, R. Tuinier, *Colloids and the Depletion Interaction*, Springer, **2011**.
[10] A. P. Minton, *Biopolymers* **1981**, *20*, 2093.
[11] A. P. Minton, *Mol. Cell. Biochem.* **1983**, *55*, 119.
[12] R. C. Chatelier, A. P. Minton, *Biopolymers* **1987**, *26*, 1097.
[13] H. J. Bosma, G. Voordouw, A. De Kok, C. Veeger, *FEBS Lett.* **1980**, *120*, 179.
[14] L. W. Nichol, A. G. Ogston, P. R. Wills, *FEBS Lett.* **1981**, *126*, 18.
[15] P. D. Ross, A. P. Minton, *Biochem. Biophys. Res. Commun.* **1979**, *88*, 1308.
[16] J. Wilf, A. P. Minton, *Biochim. Biophys. Acta Protein Struct.* **1981**, *670*, 316.
[17] G. Rivas, J. A. Fernandez, A. P. Minton, *Biochemistry* **1999**, *38*, 9379.
[18] D. M. Hatters, A. P. Minton, G. J. Howlett, *J. Biol. Chem.* **2002**, *277*, 7824.
[19] C. Rosin, P. H. Schummel, R. Winter, *Phys. Chem. Chem. Phys.* **2015**, *17*, 8330.
[20] G. Rivas, J. A. Fernandez, A. P. Minton, *Proc. Natl. Acad. Sci. USA* **2001**, *98*, 3150.
[21] M. Hosek, J. X. Tang, *Phys. Rev. E* **2004**, *69*, 051907.
[22] J. M. González, M. Jiménez, M. Vélez, J. Mingorance, J. M. Andreu, M. Vicente, G. Rivas, *J. Biol. Chem.* **2003**, *278*, 37664.
[23] S. Sukenik, D. Harries, *Prion* **2012**, *6*, 26.
[24] B. Monterroso, B. Reija, M. Jiménez, S. Zorrilla, G. Rivas, *PLoS One* **2016**, *11*, e0149060.
[25] M. Gao, K. Estel, J. Seeliger, R. P. Friedrich, S. Dogan, E. E. Wanker, R. Winter, S. Ebbinghaus, *Phys. Chem. Chem. Phys.* **2015**, *17*, 8338.
[26] S. Sukenik, R. Politi, L. Ziserman, D. Danino, A. Friedler, D. Harries, *PLoS One* **2011**, *6*, e15608.
[27] T. Witte, L. A. Haller, E. Luttmann, J. Krüger, G. Fels, K. Huber, *J. Struct. Biol.* **2007**, *159*, 71.
[28] R. Michels, Y. Hertle, T. Hellweg, K. Huber, *J. Phys. Chem. B* **2013**, *117*, 15165.
[29] D. J. Edwards, A. P. Ormerod, G. J. T. Tiddy, A. A. Jaber, A. Mahendrasingham, in *Physico-Chemical Princ. Color Chem.* (Eds: A. T. Peters, H. S. Freeman), Springer Netherlands, Dordrecht, **1996**, pp. 83–106.
[30] E. E. Jelley, *Nature* **1936**, *138*, 1009.
[31] E. E. Jelley, *Nature* **1937**, *139-140*, 631.
[32] G. Scheibe, L. Kandler, H. Ecker, *Naturwissenschaften* **1937**, *25*, 474.
[33] G. Scheibe, L. Kandler, H. Ecker, *Naturwissenschaften* **1937**, *25*, 75.
[34] G. Scheibe, *Angew. Chem.* **1937**, *50*, 212.
[35] W. Cooper, *Chem. Phys. Lett.* **1970**, *7*, 73.
[36] A. H. Herz, *Adv. Colloid Interface Sci.* **1977**, *8*, 237.
[37] H. Zimmermann, G. Scheibe, *Z. Elektrochem.* **1956**, *60*, 566.
[38] E. Daltrozzo, G. Scheibe, K. Gschwind, F. Halmerl, *Photograph. Sci. Eng.* **1974**, *18*, 441.
[39] B. Kopainsky, J. K. Hallermeier, W. Kaiser, *Chem. Phys. Lett.* **1981**, *83*, 498.
[40] B. Kopainsky, J. K. Hallermeier, *Chem. Phys. Lett.* **1982**, *87*, 7.
[41] H. von Berlepsch, C. Böttcher, L. Dähne, *J. Phys. Chem. B* **2000**, *104*, 8792.
[42] H. Von Berlepsch, C. Böttcher, *J. Phys. Chem. B* **2002**, *106*, 3146.
[43] R. Tycko, *Biochemistry* **2003**, *42*, 3151.
[44] B. Herzog, K. Huber, H. Stegemeyer, *Langmuir* **2003**, *19*, 5223.
[45] H. Fidder, D. A. Wiersma, *Phys. Rev. Lett.* **1991**, *66*, 1501.
[46] M. Kasha, H. R. Rawls, M. A. El-Bayoumi, *Pure Appl. Chem.* **1965**, *11*, 371.
[47] B. Neumann, P. Pollmann, *Phys. Chem. Chem. Phys.* **2000**, *2*, 4784.
[48] M.-L. Horng, E. L. Quitevis, *J. Chem. Educ.* **2000**, *77*, 637.
[49] F. S. Dainton, F. R. S. Ivin, K. J. Ivin, *Q. Rev. Chem. Soc.* **1958**, *12*, 61.

 © 2020 The Authors. Published by Wiley-VCH Verlag GmbH & Co. KGaA, Weinheim

Chemistry–A European Journal | Full Paper doi.org/10.1002/chem.202000113 | Chemistry Europe European Chemical Societies Publishing

[50] D. B. Knowles, I. A. Shkel, N. M. Phan, M. Sternke, E. Lingeman, X. Cheng, L. Cheng, K. O'Connor, M. T. Record, *Biochemistry* **2015**, *54*, 3528.
[51] S. Sukenik, P. Ren, M. Gruebele, *Proc. Natl. Acad. Sci. USA* **2017**, *114*, 6776.
[52] A. J. Boersma, I. S. Zuhorn, B. Poolman, *Nat. Methods* **2015**, *12*, 227.
[53] D. Gnutt, O. Brylski, E. Edengeiser, M. Havenith, S. Ebbinghaus, *Mol. Biosyst.* **2017**, *13*, 2218.
[54] D. Gnutt, M. Gao, O. Brylski, M. Heyden, S. Ebbinghaus, *Angew. Chem. Int. Ed.* **2015**, *54*, 2548; *Angew. Chem.* **2015**, *127*, 2578.
[55] M. B. Burg, *Cell. Physiol. Biochem.* **2000**, *10*, 251.
[56] A. P. Minton, *Front. Phys.* **2014**, *2*, 48.
[57] V. N. Uversky, E. M. Cooper, K. S. Bower, J. Li, A. L. Fink, *FEBS Lett.* **2002**, *515*, 99.
[58] J. Van Den Berg, A. J. Boersma, B. Poolman, *Nat. Rev. Microbiol.* **2017**, *15*, 309.
[59] M. B. Burg, J. D. Ferraris, N. I. Dmitrieva, *Physiol. Rev.* **2007**, *87*, 1441.
[60] E. K. Hoffmann, I. H. Lambert, S. F. Pedersen, *Physiol. Rev.* **2009**, *89*, 193.
[61] P. H. Yancey, M. E. Clark, S. C. Hand, R. D. Bowlus, G. N. Somero, *Science* **1982**, *217*, 1214.
[62] P. H. Yancey, *J. Exp. Biol.* **2005**, *208*, 2819.
[63] L. Zhao, C. D. Kroenke, J. Song, D. Piwnica-Worms, J. J. H. Ackerman, J. J. Neil, *NMR Biomed.* **2008**, *21*, 159.
[64] B. H. Zimm, *J. Chem. Phys.* **1948**, *16*, 1093.
[65] D. E. Koppel, *J. Chem. Phys.* **1972**, *57*, 4814.

Manuscript received: January 9, 2020
Revised manuscript received: February 20, 2020
Accepted manuscript online: March 10, 2020
Version of record online: April 28, 2020

 © 2020 The Authors. Published by Wiley-VCH Verlag GmbH & Co. KGaA, Weinheim

Chemistry–A European Journal

Supporting Information

Self-Assembly of Pseudo-Isocyanine Chloride as a Sensor for Macromolecular Crowding In Vitro and In Vivo

Benjamin Hämisch,[a] Roland Pollak,[b] Simon Ebbinghaus,*[b] and Klaus Huber*[a]

WILEY-VCH

Supporting Information

1. Determination of T_{ja}

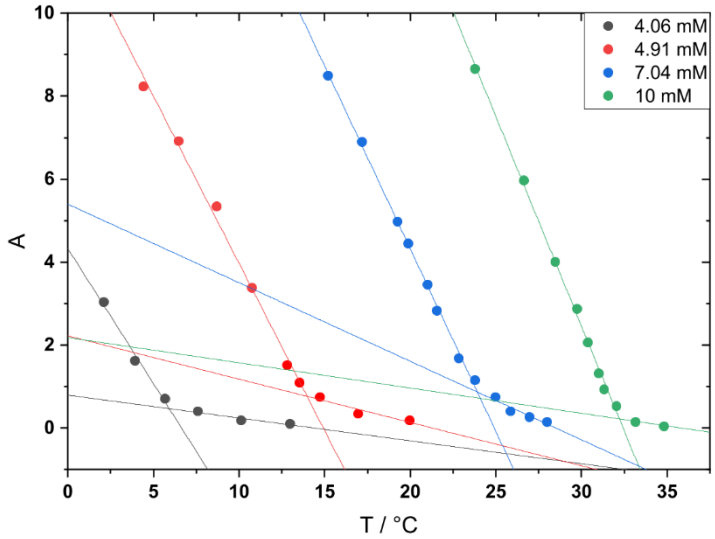

Figure S1a. Absorption at 573 nm at different temperatures for four different concentrations of PIC. The data was digitalized from a publication by Daltrozzo et al.[1] Evaluation of the aggregation threshold was done by linearly extrapolating the regimes below and above the temperature where the sharp increase in absorption occurs. The intersection of both extrapolations gives the threshold temperature for aggregation plotted in **Figure 1** of the manuscript.

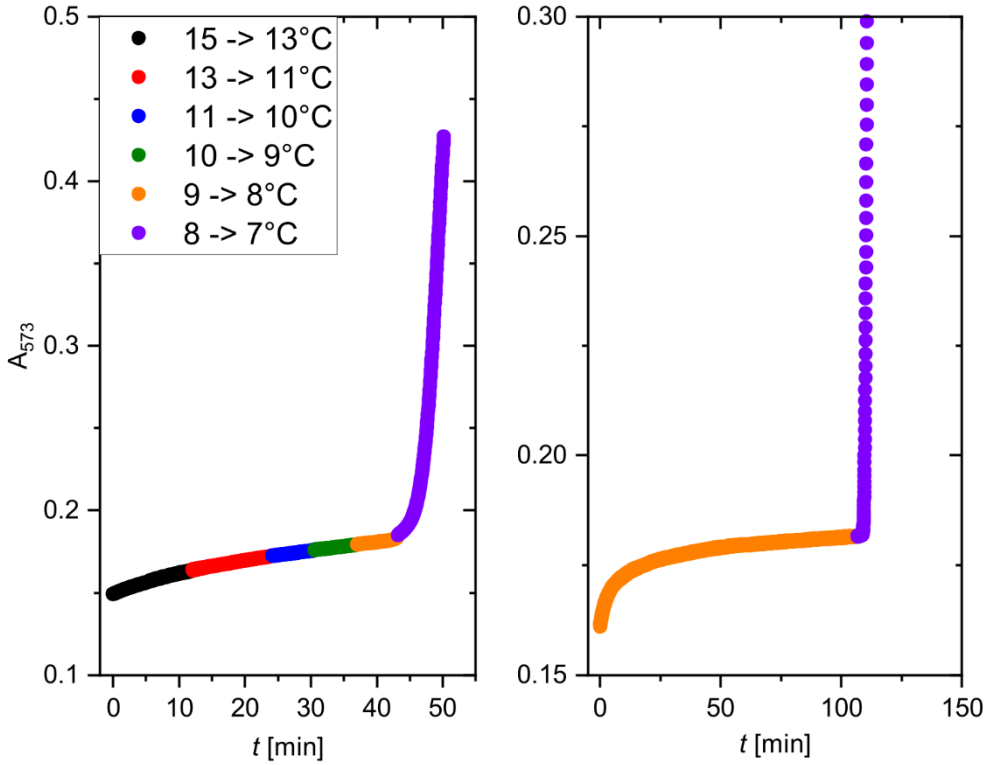

Figure S1b. (Left) Time dependent evolution of absorption at 573 nm for a sample with *[PIC]* = 5.5 mm and 2wt% TEG content while decreasing the temperature as indicated in the legend. The threshold temperature for this sample was defined to T_{ja} = 7.5° C since the absorption at 573 nm drastically increase between 8 and 7° C. The gentle increase of A_{573} during cooling from 15 to 8° C is caused by a marginal increase of the amount of PIC in very small equilibrium J-aggregates prior to reaching the threshold of aggregation. (Right) Time dependent evolution of the absorption at 573 nm while decreasing the temperature from 9 to 8° C recorded during a longer period of time as shown in the graph on the left-hand side. The incremental temperature drop from 9 to 8° C does not lead to an induction of aggregation thus demonstrating that 8° C is still above the threshold temperature for the onset of fiber formation.

2. Monomeric Spectrum of PIC in aqueous solution and in 0.01 M NaCl solution

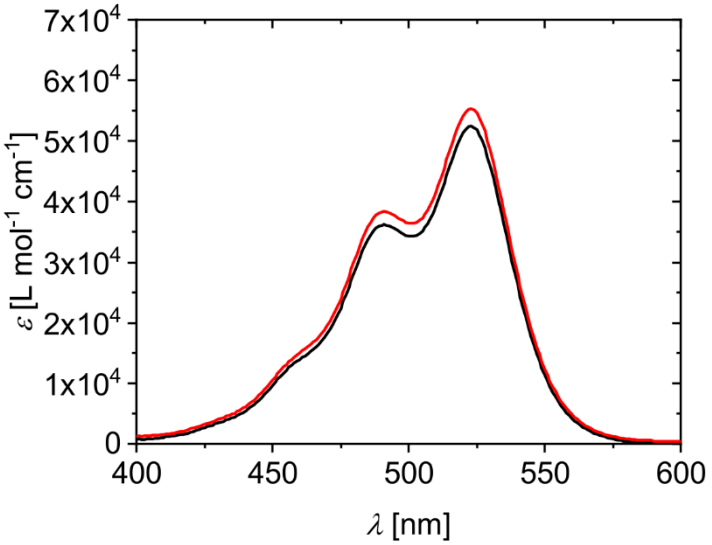

Figure S2. Spectrum of PIC at a concentration of 3 μM in aqueous solution (——) and in 0.01 M NaCl solution (——). At such low concentration, the dimerization of PIC is nearly absent. Thus, these spectra can be seen as the monomer spectrum of PIC.

3. Reversibility of self-assembly, uncertainty of data recorded in the presence of Ficoll 400, and supplementary light scattering data

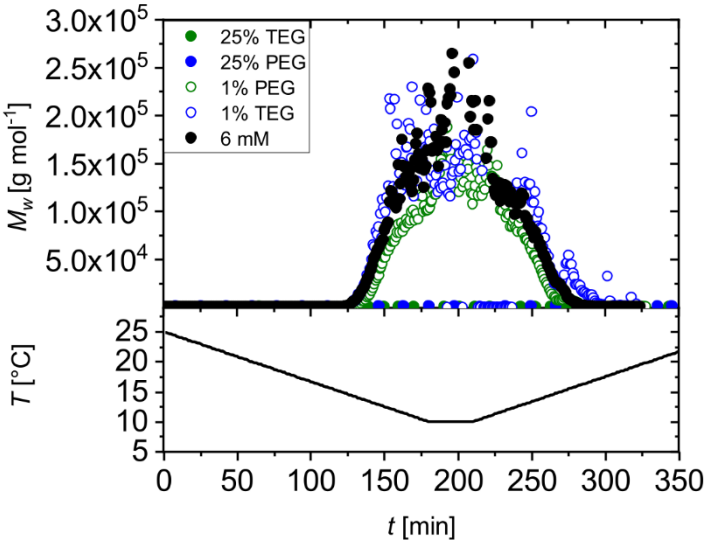

Figure S3a. Evolution of aggregate mass of PIC in aqueous solution at a PIC concentration of 6 mM with time in the absence (●) and presence of 1% by weight (hollow spheres) and 25% by weight (solid spheres) of three crowing agents during a cyclic temperature profile 25° C →10° C → 25° C indicated in the lower graph. The color code indicates the type of crowding agent: TEG (●) and PEG (●).

Figure S3a represents the evolution of the weight averaged molar mass as a function of time during a cyclic time-temperature profile starting at 25° C and reversing at 10° C. PIC concentration in all cases is 6 mM. In the absence of any crowding agent, the aggregation sets in at ~ 15° C with the aggregates disintegrating reversibly once the very temperature threshold is crossed again during re-heating. At weight percentages of 25% of crowding agents, the modulations of this threshold are in agreement with expectations from UV-vis experiments. Whereas PEG and TEG at a content of 25% does not even show any aggregation, 1% of PEG and TEG has hardly any impact.

Figure S3b describes reversibility of PIC aggregation in the presence of 2 % of Ficoll 400 during a cyclic time-temperature profile starting at 35° C and reversing at 10° C. The PIC concentration is 6 mM. The parameters shown are the weight averaged molar mass from SLS and A_{573} from UV-vis spectroscopy. Both techniques clearly demonstrates the reversibility of the formation of J-aggregates..

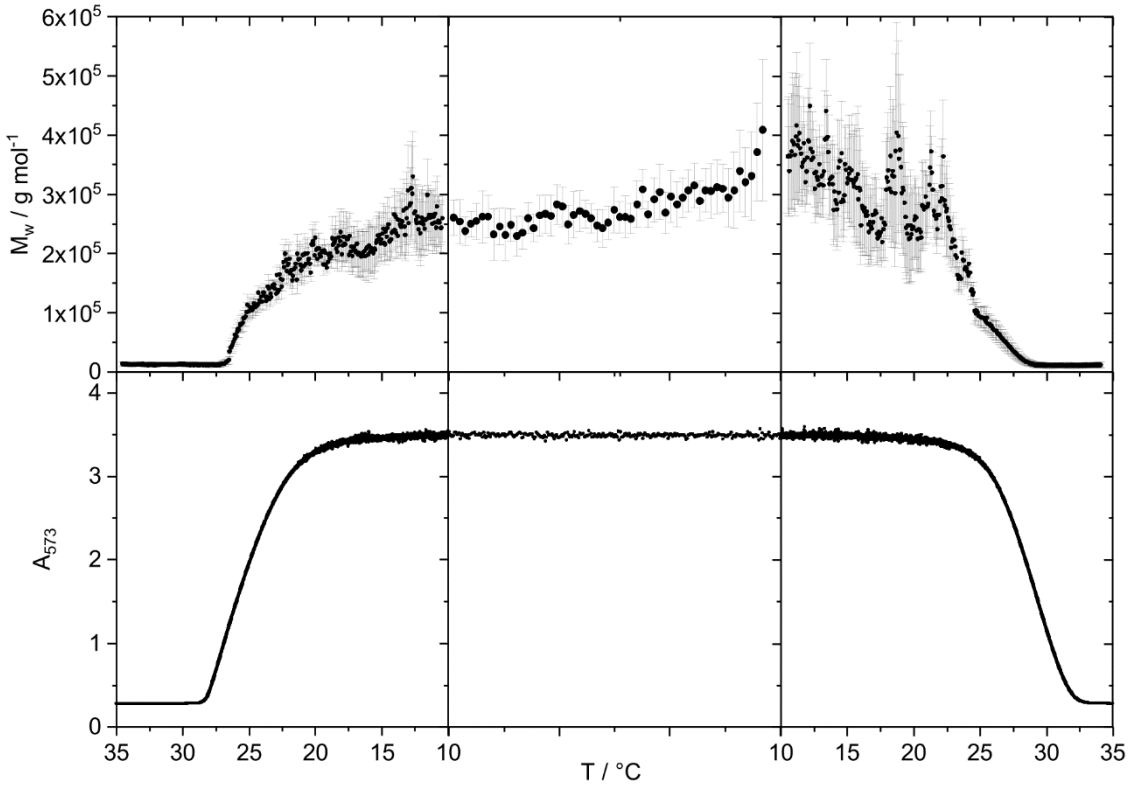

Figure S3b. (Top) Evolution of M_w of a sample with a PIC concentration of 6 mM and 2wt% of Ficoll 400 during a cyclic temperature profile from 35°C to 10°C and vice versa. At 10°C, the temperature was hold for 20 minutes, corresponding to the center part of the plot. (Bottom) Evolution of absorption A_{573} during the same temperature profile as applied for the light scattering experiment shown in the Top graph.

Figure S3c summarizes two time-resolved SLS/DLS experiments on the self-assembly of PIC at a concentration of 6 mM in the presence of 2 % by weight of Ficoll 400. The first experiment is also shown in **Figure 4** of the manuscript and is replotted in **Figure S3c**. The second experiment is part of the temperature cycle shown in **Figure S3b** in order to prove reversibility of the formation of J-aggregates. In both cases, the scattering from the solvent background, which is the corresponding pure Ficoll solution is already fairly large and led us to use the SLS results in the presence of Ficoll 400 in a qualitative manner only.

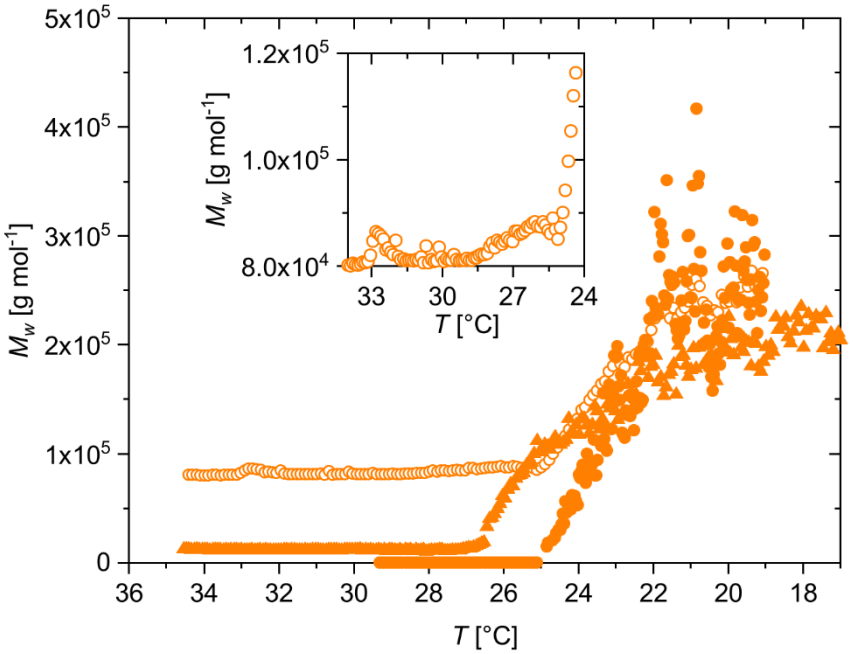

Figure S3c. Temperature-dependent evolution of M_w from SLS of a sample with 6 mM PIC in the presence of 2wt% Ficoll 400. The dataset taken from **Figure 4a** (●) is based on the corresponding Ficoll solution (2 % of Ficoll 400) as solvent background. The same data are also represented with pure water as solvent background (○), thus illustrating the high level of background scattering from the Ficoll 400. The dataset taken from **Figure S3b** (▲) is based on a solution with 2 % Ficoll as solvent background**.**

The two runs reveal threshold temperatures of 25 °C (**Figure 4a**) and 27 °C (**Figure S3b**). In the light of the fact that data stem from two independent experiments, agreement is considered to be satisfactory. The two values compare with the respective thresholds extracted from UV-vis spectroscopy, which are 31 °C and 28.5 °C respectively. Such an offset has not been observed in pure water or in the presence of any other cosolute applied in the present work. Although no conclusive explanation is currently available, it does not affect the result, that Ficoll 400 promotes the formation of J-aggregates by shifting the threshold line in the phase diagram by more than 10 °C.

WILEY-VCH

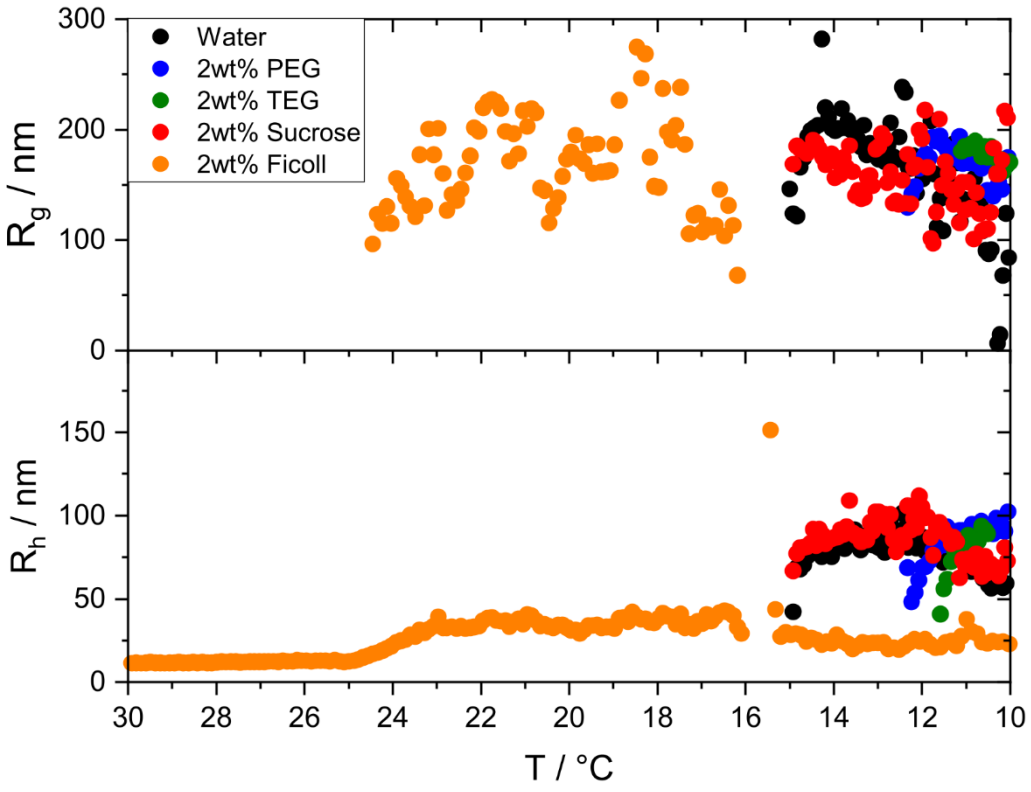

Figure S3d. Evolution of aggregate size in terms of radius of gyration R_g and hydrodynamic radius R_h of PIC in aqueous solution at a PIC concentration of 6 mM with time in the absence (●) and presence of 2% by weight of PEG (●), TEG (●), Sucrose (●) and Ficoll (●) during a temperature ramp from 35 °C to 10° C for the sample containing Ficoll and 25° C to 10° C for all other samples. The shown data stem from the same experiment shown in **Figure 4a**.

Figure S3d shows the evolution of the geometric size (R_g from SLS) and the hydrodynamic size (R_h from DLS) derived from the same experiments as shown in **Figure 4** of the manuscript. All size data show radii larger than 20 nm only once a significant amount of J-aggregates are formed. Lack of any significant growth period suggests that growth progresses via producing an increasing number of aggregates all with the same final size. Formation times of individual fibers are much shorter than the duration of the experiments respectively. Noteworthy, the radius of gyration is significantly larger than the hydrodynamic radius, which is a characteristic signature of fiber formation. However, it has to be emphasized that all parameters evaluated by SLS/DLS are apparent quantities as they are determined at finite concentrations of PIC and as data evaluation did not consider a possible of variations of the scattering contrast of PIC due to the presence of crowding agents.

4. Phase diagram of PIC in the presence of 2wt% and 5wt% crowder content

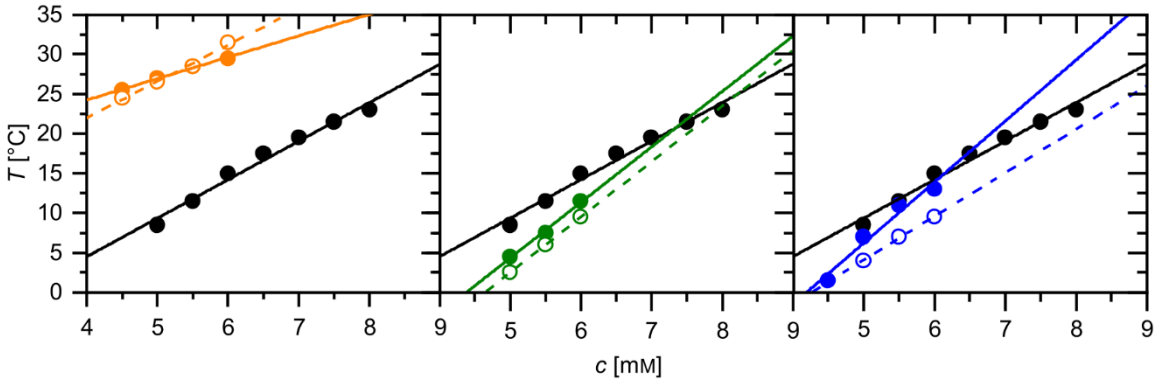

Figure S4. Phase diagram of PIC in the absence of crowder (●) and in the presence of 2wt% Ficoll(●), TEG(●) and PEG (●). The hollow spheres represent samples with 5wt% content of the respective crowding agent.

5. Confocal microscopy of PIC in HeLa cells

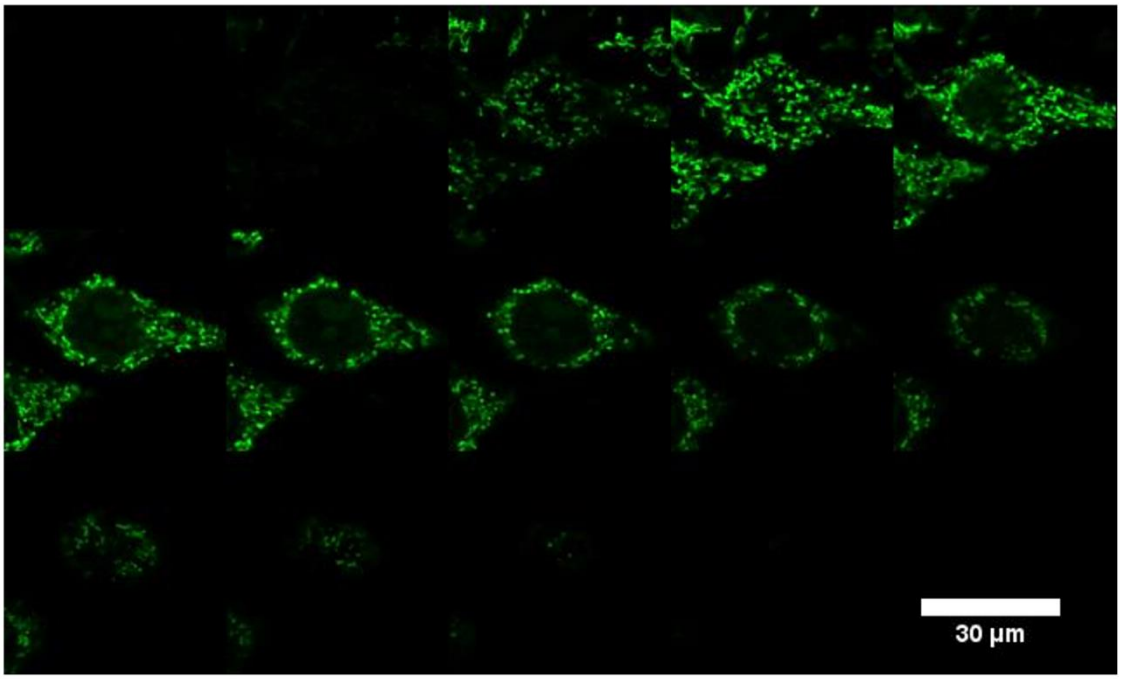

Figure S5a. Fluorescent confocal planes of a PIC containing HeLa cell (bottom to top with 1 µm spacing) after 30 min of 50 µm PIC solution treatment.

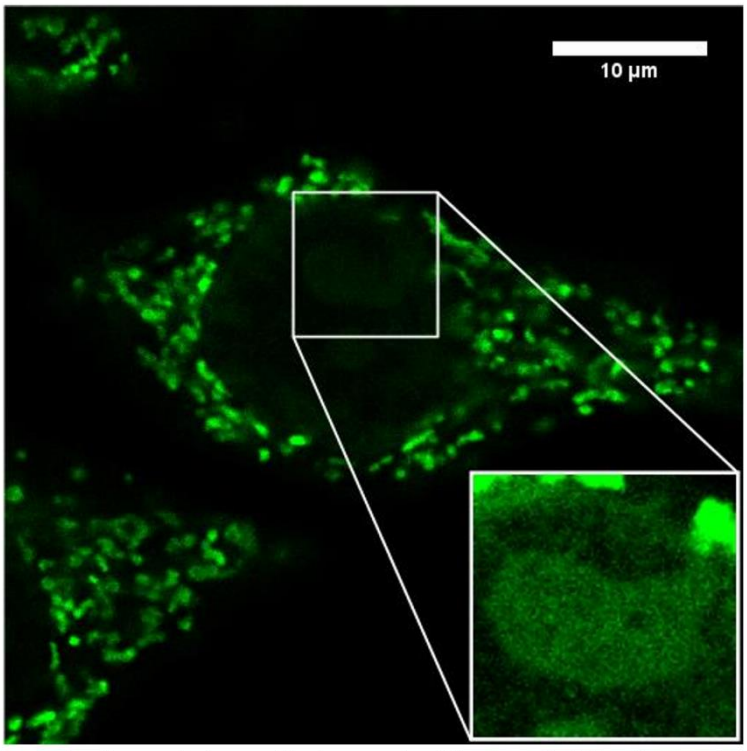

Figure S5b. Enlarged view of the cell shown in **Figure 5.** The inset shows a part of the nucleus with image brightness increased by 250% to visualize the faint fluorescence observed from the nucleus.

6. Concentration measurements via UV/Vis spectroscopy

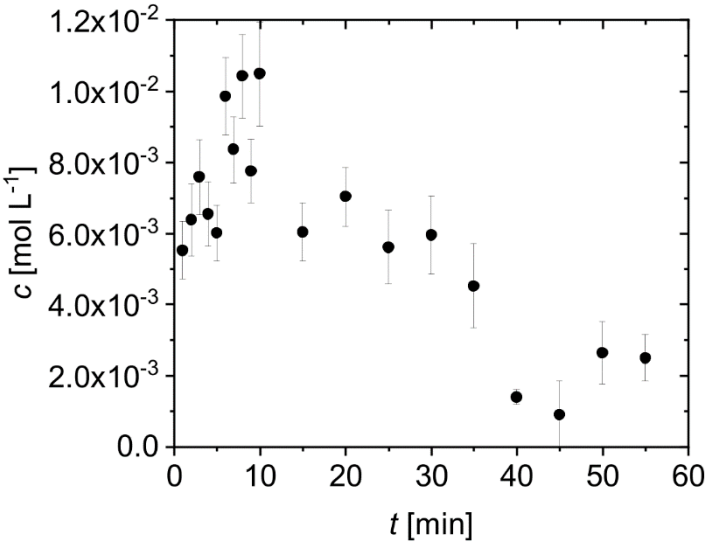

Figure S6. Enrichment of PIC in one cell. 50 μM solution was given onto the cells and the calculated concentration in the cellular environment is 100 times higher. The measurement was performed at 21° C. The error bars represent the standard derivation error.

7. In-cell aggregation of PIC at variable temperature

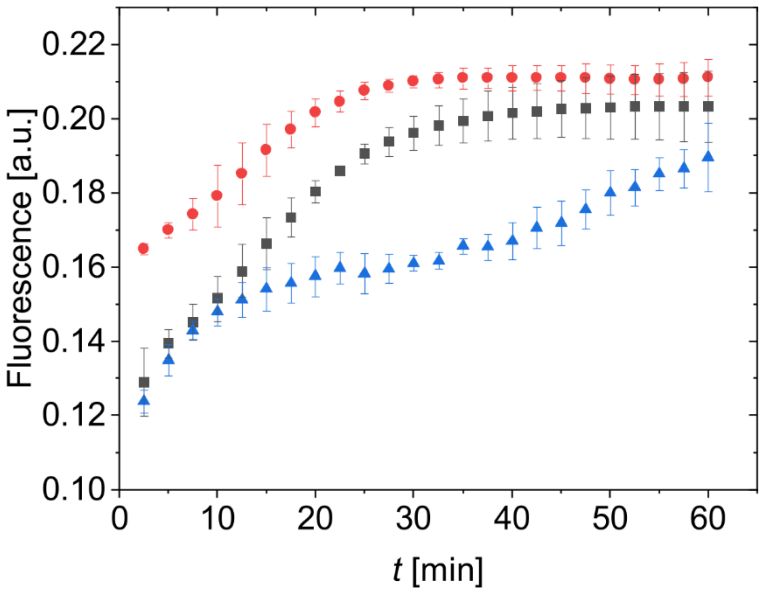

Figure S7. In-cell PIC aggregation kinetics at 12° C (black), 21° C (red) and 37° C (blue). The cells were incubated at $t = 0$ with 50 µM PIC in Leibovitz's solution. The average fluorescence intensity of the cells was measured at different times. Three independent measurements were performed and data shown as plus/minus standard derivation.

8. In-cell aggregation of PIC with a concentration of 5 μM PIC in Leibovitz's solution in the supernatant

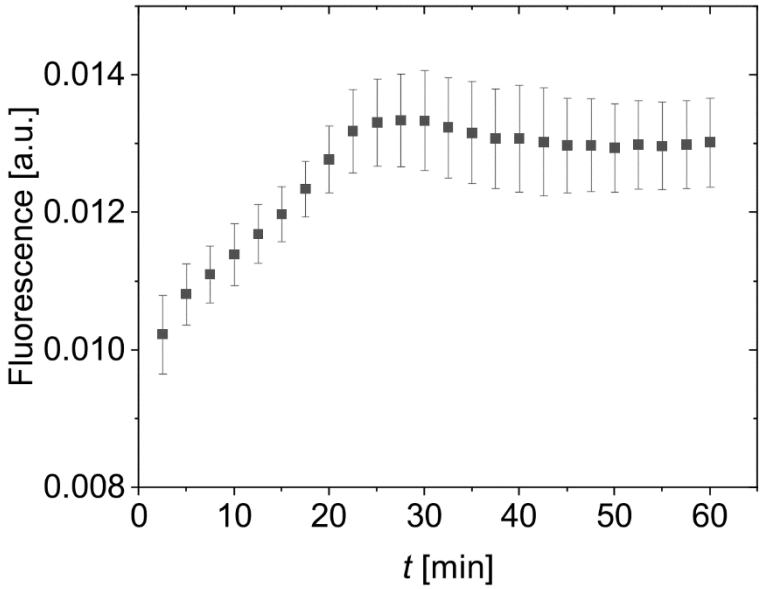

Figure S8. Fluorescence intensity of the HeLa cells incubated with 5 μM PIC in Leibovitz's solution at 21° C. Three independent measurements were performed and data shown as plus/minus standard derivation.

9. Data evaluation of Static and Dynamic light scattering experiments

Static Light scattering experiments provide the excess Rayleigh ratio of the solute

$$\Delta R_\theta = RR_{\theta,Std}\left(\frac{r_{\theta,sol-}\, r_{\theta,solv}}{r_{\theta,std}}\right) \quad \text{(S1)}$$

with $RR_{\theta,Std}$ the absolute Rayleigh ratio of toluene used as standard and with $r_{\theta,sol}$, $r_{\theta,solv}$ and $r_{\theta,std}$ the measured scattering signal of the solution, the solvent, and toluene, respectively.

Data evaluation was done with the Zimm approximation[2]

$$\frac{\mathrm{Kc}}{\Delta R_\theta} = \frac{1}{M_w} + \frac{R_g^2 q^2}{3M_w} + 2A_2 c \quad \text{(S2)}$$

with M_w being the mass averaged molar weight, R_g^2 the z-averaged squared radius of gyration, A_2 the second osmotic virial coefficient and c the concentration of PIC in g L^{-1}. The contrast factor K

$$K = \frac{4\pi^2 n^2}{N_A \lambda^4}\left(\frac{dn}{dc}\right)^2 \quad \text{(S3)}$$

is calculated with the refractive index n of the solvent, with Avogadro's number N_A and with the refractive index increment of PIC in water, which amounts to dn/dc = $6.15 \cdot 10^{-4}$ L g^{-1}.[3] The refractive index n of the solvent depends on the type of crowder and its content. Data are summarized in **Table S1**.

During a time-dependent light scattering experiment recording intermediates of a growth process, an extrapolation scattering curves to $c = 0$ is not possible. Thus, we were forced to neglect the influence of particle-particle interactions, and therefore setting $A_2 = 0$. Neglect of this effect is expected to be negligibly small in the light of PIC concentrations as low as c = 6 mM. However, the obtained values for M_w are apparent in nature due to this simplification.

Dynamic light scattering uses intensity fluctuations of the scattered light due to Brownian motion leading to a field correlation function $g_1(\tau)$. Analysis of $g_1(\tau)$ with a cumulant analysis[4]

$$\ln\big(g_1(\tau,q)\big) = C - \Gamma(\mathrm{q})\tau + \frac{\mu_2}{2\Gamma^2}\tau^2 \quad \text{(S4)}$$

gives the mean inverse relaxation time of diffusive modes *Γ(q)* from the initial slope. *C* describes the signal-to-noise ratio and μ_2 represents a measure of the solute polydispersity. The apparent diffusion coefficient D_z is calculated with *Γ(q)*.

$$D_z(q) = \frac{\Gamma(q)}{q^2} \quad \text{(S5)}$$

A linear extrapolation of D_z toward $q^2 \rightarrow 0$ gives the z-averaged diffusion coefficient D_0.

$$D_z = D_0(1 + q^2 R_g^2 C + k_d C_s) \quad \text{(S6)}$$

In **Equation S6**, C_s is a shape sensitive constant and k_d is a constant, which describes the concentration dependency. This concentration dependency of D_0 is neglected for the same reasons as already mentioned in the context of static light scattering.

With the diffusion coefficient, a hydrodynamically effective radius R_h is calculated with the Stokes-Einstein relationship

$$R_h = \frac{k_b T}{6\pi\eta D_0} \quad \text{(S7)}$$

with k_b the Boltzmann constant, *T* the temperature in Kelvin and η the dynamic viscosity of the solvent. The viscosity depends on the type of crowder and its concentration. Data are summarized in **Table S1**.

Table S1. Dynamic viscosities η and refractive indices *n* of crowder solutions.

Crowder	Content [wt%]	$n_{25°C}$	$\eta_{25°C}$ [mPa s]	Crowder	Content [wt%]	$n_{25°C}$	$\eta_{25°C}$ [mPa s]
PEG	1	1.335	0.96	Sucrose	1	1.334	0.95
	2.5	1.336	-		2.5	1.336	-
	5	1.339	1.22		5	1.34	1.05
	10	1.346	-		10	1.348	-
	25	1.366	-		25	1.372	-
TEG	1	1.334	0.989	Ficoll	1	1.334	1.14
	2.5	1.335	-		2.5	1.336	-
	5	1.339	0.991		5	1.34	2.04
	10	1.345	-		10	1.347	
	25	1.363	-		25	-	-

References

[1] E. Daltrozzo, G. Scheibe, K. Gschwind, F. Haimerl, *Photogr. Sci. Eng.* **1974**, *18*.
[2] B. H. Zimm, *J. Chem. Phys.* **1948**, *16*, 1093.
[3] B. Neumann, *J. Phys. Chem. B* **2001**, *105*, 8268–8274.
[4] D. E. Koppel, *J. Chem. Phys.* **1972**, *57*, 4814–4820.

8. Self-Assembly of Fibrinogen in the presence of Ficoll 400

In nature, the self-assembly of fibrinogen takes place in a crowded environment. Hence, effects of crowding should be considered in the investigation of the process. We shall give an insight on how Ficoll 400 affects the aggregation of fibrinogen. For this purpose, the crowding agent Ficoll 400 was chosen, which is used in literature as typical globular excluded volume crowder.[1] As shown in **Chapter 6** and **7**, Ficoll 400 strongly promotes the self-assembly of PIC towards J-aggregates. Accordingly, light scattering experiments in the absence and presence of 5wt% Ficoll 400 were carried out here with fibrinogen. The results are plotted in **Figure 8.1**.

In the absence of Ficoll 400, M_w increases by two orders of magnitude in a timespan of around 20 minutes. Introduction of Ficoll 400 accelerated the process. The plateau in M_w was reached in approximately 5 minutes while the final value was also slightly bigger than in the absence of the crowding agent. The evolution of the radius of gyration R_g also displays the acceleration of the process via Ficoll 400. There are no striking differences between the values of R_g in the presence and absence of Ficoll 400, but the final values are reached nearly instantaneously after starting the measurement when Ficoll 400 is present.

The hydrodynamically effective radius R_h obtained from dynamic light scattering is growing considerably faster and is reaching higher values in case of Ficoll 400 being present in solution. Interpretation of data is restricted to the first 5 minutes of the measurement because afterwards, the scattering of data points is too big to allow further interpretations.

The experiments indicate that addition of Ficoll 400 has a strongly promoting effect on the self-assembly of fibrinogen, similar to the effect on the formation of J-aggregates of PIC. Strong structural changes of the products were not observed. While the radius of gyration R_g is slightly smaller when Ficoll 400 is present, the hydrodynamically effective radius R_h is considerably bigger. The ratio of both radii, denoted as the structure sensitive parameter $R_g/R_h = \rho$, can be used to make a statement on the geometry of the entities. In the absence of Ficoll 400 ρ amounts to 0.5 to 0.9, depending on the ionic strength of the solution, which represents compact spherical structures. When Ficoll 400 is present, the value of ρ amounts to around 0.8 ten minutes after triggering the aggregation. Regarding the evolution of ρ, one can say that in general the structural characteristics of the aggregates are not altered in the presence of Ficoll 400. Spherical compact structures are obtained in both cases.

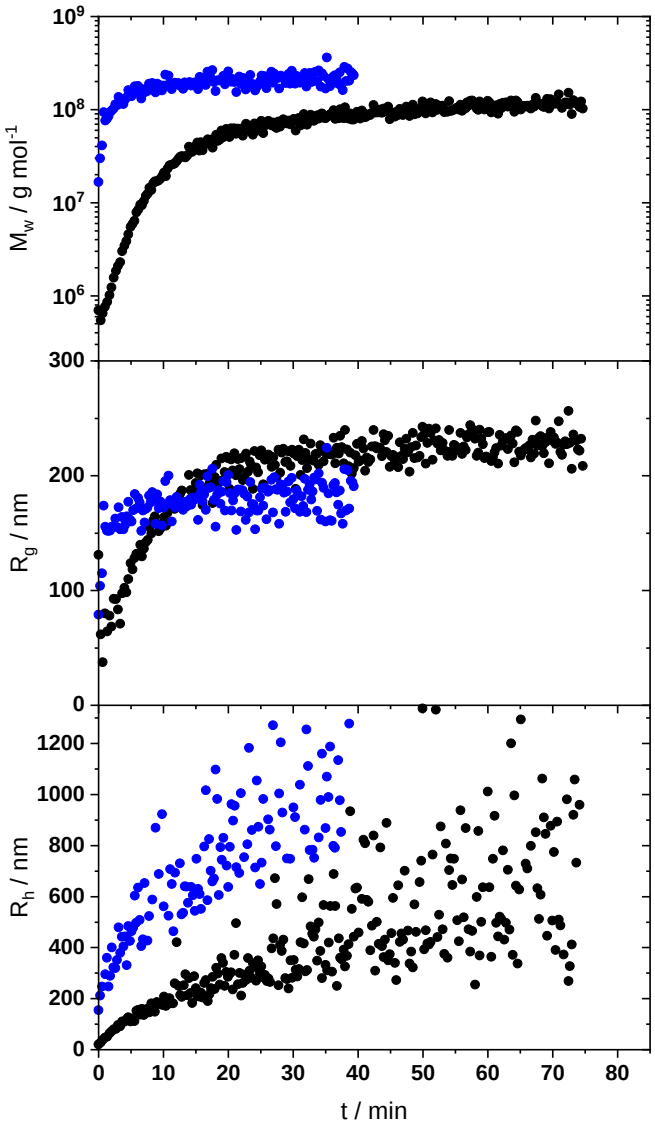

Figure 8.1: Time-dependent evolution of M_w, R_g and R_h of the self-assembly of fibrinogen at an ionic strength of *[I]* = 30 mM. The concentration of fibrinogen amounts to c = 0.075 g L^{-1} for both experiments. The experiment was conducted in the absence (black spheres) and in the presence (blue sphere) of Ficoll 400 with a concentration of 5 wt%. The self-assembly was triggered as described in the experimental section of **Chapter 4**.

References

[1] R. J. Ellis, *Curr. Opin. Struct. Biol.* **2001**, *11*, 114.

9. List of Publications

The present thesis is based on the following publications

- Hämisch, B.; Büngeler, A.; Kielar, C.; Keller, A.; Strube, O.; Huber, K. Self-Assembly of Fibrinogen in Aqueous, Thrombin-Free Solutions of Variable Ionic Strengths. *Langmuir* **2019**, *35* (37), 12113–12122. DOI: 10.1021/acs.langmuir.9b01515.
- Hämisch, B.; Huber, K. Mechanism and equilibrium thermodynamics of H- and J-aggregate formation from pseudo isocyanine chloride in water. *Soft Matter* **2021**, *17*, 8140-8152. DOI: 10.1039/d1sm00979f.
- Hämisch, B.; Pollak, R.; Ebbinghaus, S.; Huber, K. Thermodynamic Analysis of the Self-Assembly of Pseudo Isocyanine Chloride in the Presence of Crowding Agents. *ChemSystemsChem* **2021**, *3*, e2000051, 1–9. DOI: 10.1002/syst.202000051.
- Hämisch, B.; Pollak, R.; Ebbinghaus, S.; Huber, K. Self-Assembly of Pseudo-Isocyanine Chloride as a Sensor for Macromolecular Crowding In Vitro and In Vivo. *Chem. - A Eur. J.* **2020**, *26* (31), 7041–7050. DOI: 10.1002/chem.202000113.

Other publications by the author

- Büngeler, A.; Hämisch, B.; Huber, K.; Bremser, W.; Strube, O. I. Insight into the Final Step of the Supramolecular Buildup of Eumelanin. *Langmuir* **2017**, *33* (27), 6895–6901. DOI: 10.1021/acs.langmuir.7b01634.
- Büngeler, A.; Hämisch, B.; Strube, O. I. The Supramolecular Buildup of Eumelanin: Structures, Mechanisms, Controllability. *Int. J. Mol. Sci.* **2017**, *18* (9). DOI: 10.3390/ijms18091901.
- Hansch, M.; Hämisch, B.; Schweins, R.; Prévost, S.; Huber, K. Liquid-Liquid Phase Separation in Dilute Solutions of Poly(Styrene Sulfonate) with Multivalent Cations: Phase Diagrams, Chain Morphology, and Impact of Temperature. *J. Chem. Phys.* **2018**, *148* (1). DOI: 10.1063/1.5006618.
- Stolzenburg, P.; Hämisch, B.; Richter, S.; Huber, K.; Garnweitner, G. Secondary Particle Formation during the Nonaqueous Synthesis of Metal Oxide Nanocrystals. *Langmuir* **2018**, *34* (43), 12834–12844. DOI: 10.1021/acs.langmuir.8b00020.
- Sistemich, L.; Kutsch, M.; Hämisch, B.; Zhang, P.; Shydlovskyi, S.; Britzen-Laurent, N.; Stürzl, M.; Huber, K.; Herrmann, C. The Molecular Mechanism of Polymer Formation of Farnesylated Human Guanylate-Binding Protein 1. *J. Mol. Biol.* **2020**, *432* (7), 2164–2185. DOI: 10.1016/j.jmb.2020.02.009.
- Gräfenstein, A.; Rumancev, C.; Pollak, R.; Hämisch, B.; Galbierz, V.; Schroeder, W. H.; Garrevoet, J.; Falkenberg, G.; Vöpel, T.; Huber, K.; Ebbinghaus, S.; Rosenhahn, A. Spatial Distribution of Intracellular Ion Concentrations in Aggregate-Forming HeLa Cells Analyzed by μ-XRF Imaging. *ChemistryOpen* **2022**, *11*, e202200024, 1-9. DOI: 10.1002/open.202200024.